Microstructural control of Al alloys using intrinsic oxides

Akash Verma

St Cross College

DPhil thesis submitted to University of Oxford

Trinity term, 2015

Abstract

Currently, there is not enough information available on the effect of inclusions on extrusion alloys. Theoretical calculations in the past demonstrated the probable role of oxides in Fe-intermetallic phase selection **(Cao et al., 03)**. However, no concrete evidence can be found in the literature to support this argument. This study investigates the role of in-situ oxides in intermetallic phase selection. Various Mg oxides (spinel and MgO) were formed in-situ by adding different levels of Mg. A special intermetallic extraction process was used for 3D analysis. SEM, EDS and XRD analysis were used for qualitative and quantitative analysis. Dry and wet surfaces of the oxide bi-films were observed with the wet surfaces highly associated with MgO and spinel particles. MgO particles had spherical morphology and there average diameter was observed to be in the range 200nm-400nm, whereas spinel particles had octahedral morphology with average length of the side in the range 1-2µm. MgO was found in locations which appear to be the most probable nucleation points of α-AlFeSi intermetallics and Mg_2Si. These results provide a new and more distinctive perspective on the actual morphology of Fe-rich intermetallics and Mg oxides than the ones that exist in the literature. It also provides direct evidence of the role of inclusions (oxides) in intermetallic phase nucleation. This information can be utilised to improve the surface properties in 6xxx extrusion alloys.

DECLARATION OF ORIGINALITY

This thesis is an account of work carried out by the author in the Materials Department, University of Oxford from October 2010 to August 2014 under the supervision of Dr Keyna O'Reilly and Prof. Patrick Grant. This thesis is submitted for the degree of Doctor of Philosophy at the University of Oxford. Where the work of others has been drawn upon this is duly acknowledged in the text, and a list of references is presented at the end of the thesis. No part of this thesis has been submitted towards the completion of another degree at the University of Oxford or elsewhere. Parts of this thesis have been submitted to or published in the following scientific journals or conference presentations:

Journal articles

A. Verma, S. Kumar, P.S. Grant, K.A.Q. O'Reilly, Influence of cooling rate on the Fe intermetallic formation in an AA6063 Al alloy, Journal of Alloys and Compounds, Vol 555, 2013, 274-282

A. Verma, S. Kumar, P.S. Grant, K.A.Q. O'Reilly, 3D Characterisation Of In-situ Nano-Oxides and Oxide Bi-Films in Al-Fe-Si-Mg Alloys, 2014, in preparation

A. Verma, S. Kumar, P.S. Grant, K.A.Q. O'Reilly, Influence of Mg on intermetallic formation, 2014, in preparation

Conference proceedings

A. Verma, S. Kumar, P.S. Grant, K.A.Q. O'Reilly, ICAA: 13th International Conference on Aluminum Alloys, 2012, Pittsburgh, USA

A. Verma, S. Kumar, P.S. Grant, K.A.Q. O'Reilly, 3rd National Student Conference in Metallic Materials (NSCMM 2013), 2013, Brunel, U.K.

S. Kumar, A. Verma, P.S. Grant, K.A.Q. O'Reilly, Fifth International Conference on solidification science and processing (ICSSP5), 2012, Bhubaneswar, India

Conference papers

A. Verma, S. Kumar, P.S. Grant, K.A.Q. O'Reilly, Intermetallic Phase Formation in TP-1 and DC Cast Billet of an AA6063 Al Alloy, ICAA13: 13th International Conference on Aluminum Alloys, 2012, Wiley online library, Pittsburgh, USA

ACKNOWLEDGEMENTS

I am deeply grateful to the Felix Scholarship for financially supporting my education at Oxford; it would not have been possible without their support. I am very thankful to St Cross College for providing an amazing and relaxing social life. I also thank the Department of Materials and St Cross College for supporting me financially at difficult times.

I thank Dr Keyna O'Reilly for her wonderful guidance and kind support. I very much appreciate, the time she spent on thought provoking discussions, for her everlasting patience, understanding and tips for a happy life. Her availability even at short notices helped a lot in the smooth running of my research. I can't thank her enough for her awesomeness. I thank Prof. Patrick Grant for his time and kind support and allowing me to use the laboratory facilities even at tough times.

I am very much obliged for the wonderful support from Dr Kumar Sundaram. He has helped me at every stage of my DPhil and pushed me to work harder when I was lazy. I am grateful for his intellectual inputs when I get stuck, quick feedbacks on numerous occasions and encouragement at every step.

I would like to thank Mr Trevor Knibbs for his kind help and amazing support for my experiments at high bay. I am grateful to Mrs Gabriella Chapman for training me on SEM's and helping me with the analysis. I am grateful to N-Tec for helping me with the prefil experiments. I thank Laurie Walton for training me on different

instruments in the workshop. I very much appreciate the efforts from Marion Beckett, Adrian Taylor, Barry Fellows, Ian Sutton, and Paul Warren for various forms of assistance.

I would like thank my collegues, Tahsina for training me on IEA, XRD sample preparation and for fascinating tips on photography and life at Oxford; Figo for the amazing ‘discussions’ we had in the office and most importantly for realising me that I have six packs somewhere but they are hidden; Xia for constantly reminding me of my big tummy; Stella for organising all the amazing group outings; Amogh for being such a kind experiment and lunch buddy; Laura for organising the lab perfectly and of course for orange Wednesdays. I thank Meijia, Chen, Amogh, Shermin and Fiona for bringing all the happiness of the world. You guys are the best!!!

Finally, I thank my family for their continuous love. I am blessed with an amazing family in my life which supported me at every point. This thesis, which none of you will ever read, is unsurprisingly dedicated to you. ☺

Table of Contents

1. INTRODUCTION

1.1 Background

According to the International Aluminium Institute, aluminium (Al) alloy production has increased from 2 million tons to 50 million tons (for 2014) over the last five decades. Al alloys are widely used for a number of engineering structures or components where light weight or corrosion resistance is required, for example aerospace industry, automobiles, food packaging, electrical appliances and many more. Since 6xxx series Al alloys are one of the most commonly used alloys with a broad range of applications, this thesis focuses only on 6xxx Al alloys. The major process for producing 6xxx Al alloy ingots/billets is direct-chill (DC) casting, a semi continuous process, which has been developed for high volume Al alloy extrusion **(Grandfield et al., 93)**. The need for better billet quality, to improve extrusion manufacturing efficiency, has led to significant technological and process development in DC billet production.

6xxx Al alloys are Mg and Si based alloys. These alloys are designed to be solutionisable and then age hardenable. It is the Mg/Si ratio that plays a major role in deciding the mechanical properties of the alloy. Generally, Mg/Si ratio is kept close to 2:1 (atomic ratio) or Si on the higher side for better response to age hardening. Other elements like Cu, Cr and Mn are added sometimes to enhance the strength. Fe in 6xxx series Al alloys is usually present as an impurity and

have low solid solubility in Al i.e. 0.04% and so have a tendency to partition out of the primary α-Al phase during solidification and form a variety of intermetallic phases in the as-cast microstructure (**Kuijpers et al., 03**). Sometimes Fe is deliberately kept at higher levels to generate a matte surface for less demanding structural applications. Numerous factors such as cooling rate, temperature gradient, non-equilibrium solute partitioning, inclusions (oxide particles) and type of grain refiner govern the formation of particular intermetallic phases in Al alloys **(Eskin et al., 04) (Jarrett et al., 03) (Tanihata et al., 99)**. The most commonly observed Fe-rich intermetallic phases in 6xxx Al alloys are cubic α_c-AlFeSi (α-AlFeSi) and monoclinic β-AlFeSi (**Paray et al., 96**). α-AlFeSi often exhibits a dendritic morphology and β-AlFeSi possesses a needle like or plate like morphology (**Paray et al., 96**).

Both α-AlFeSi and β-AlFeSi are brittle and are harmful for the mechanical properties (ductility and toughness) of the alloy. The intermetallics in extrusion also adversely affect the surface quality because of the pick-up phenomenon from the die bearing surface. However, past studies have shown α-AlFeSi to be much less deleterious than β-AlFeSi **(Zajac et al., 96) (Allen et al., 96)**. As a result, to transform the as-cast β-AlFeSi intermetallics to α-AlFeSi, homogenisation is used. During this solid state phase transformation, β-AlFeSi is broken and fine α-AlFeSi particulates are formed. Homogenisation results in a lower percentage of β-AlFeSi and higher percentage of α-AlFeSi in the alloy **(Kuijpers et al., 05)**. A small amount of Mn (~0.05%) will favour this solid

state transformation by stabilizing the α-AlFeSi. Higher amount of Mn (~0.5%) is added to obtain better toughness but will stabilise as-cast α-AlFeSi which is deleterious for the surface properties.

Inclusions exist in nearly all liquid metals (mainly MgO, Al_2O_3 in Al alloys) and alloys exposed to air or even under protective atmospheres **(Miller et al., 06)**. The inclusions cause's problems like rapid die wear during extrusion and deteriorate mechanical properties if present in excess but only in shape casting. Currently, extensive research is being done to make positive use of oxides for refining microstructures in Al alloys. Theoretical calculations have previously demonstrated the probable role of oxides in Fe-intermetallic phase formation **(Cao et al., 03)**. However, no direct evidence can be found in the literature to support this argument.

The main objective of this study is to investigate the influence of in-situ formed oxide particles on intermetallic phase formation in 6xxx series Al alloys. Mg:Si ratio in the 6xxx alloy is chosen to achieve certain mechanical properties after extrusion and subsequent ageing, which also plays an important role in intermetallic phase formation. The ratio of Mg:Si influences the stability of metastable phases, i.e. when the Mg/Si ratio is less than about 1, the Si phase is stabilized, when it is greater than 1, Mg_2Si is stabilized (**Chakrabarti et al., 04**). Also, various Mg oxides are present in Al alloys as inclusions. In order to form different types of in-situ oxides, 0-5 wt% Mg additions were used. Following

that the nucleation sequence of various intermetallic phases due to Mg and Mg oxides has been studied during the solidification of the Al-alloys.

Chapter-2 discusses in detail the morphologies of different types of intermetallics in 6xxx Al alloys observed in the literature. Chapter-2 goes on to discuss the DC-casting and homogenisation processes. Chapter-3 describes the experimental procedures followed to produce different alloys and to analyse different aspects of the microstructure. A phase extraction technique is being used to facilitate the detailed characterisation of intermetallic phases and their interaction with extrinsic and intrinsic alloy additions. Chapter-4 and Chapter-6 provides quantitative and qualitative results of the different features of the microstructure observed for various alloys i.e. 2D and 3D morphology of the grains and intermetallics as well as quantification of the size, type and interconnectivity of the intermetallics and grains. Chapter-4 starts with a discussion of the effect of the homogenisation process on the Fe-intermetallics to get an idea of the reference microstructure. Chapter-4 then moves on to study the effect of cooling rate on intermetallics in different sections of TP-1 samples and then to verify the similarity of the intermetallic morphologies in as-DC cast samples and TP-1 samples at the 38mm section. **(TP1, 90)**.

Chapter-5 discusses the theoretical calculations of phase prediction for different alloy compositions using MTDATA software. These calculations played an important role in interpreting the results for alloys with different Mg

compositions that were used for inclusion and intermetallic analysis via prefil and TP-1 experiments. Chapter-6 discusses the 2D and 3D morphologies of Mg oxides, intermetallics and different inclusions in Al-Fe-Si-Mg alloys with the help of prefil experiments. Chapter-6 then analyses the intermetallic phase formation behaviour in TP-1 samples. Lastly, Chapter-7 provides the conclusions of this study i.e. how the inclusions (Mg oxides in particular) effect the formation of intermetallics.

2. Literature review

2.1 Recycling of Al

Al production is an energy intensive process. Recycling of Al is gaining popularity in the current industrial world as Al is a sustainable material and can be recycled again and again**.** Raw material for recycling of Al is generated from a number of sources such as machining of casting resulting in the generation of scrap (5% of casting weight), beverage cans, foils, sheets etc. Recycling of Al scrap is very energy favourable, as it requires only 5% of the energy required for producing primary Al **(Verran et al., 08)**. As a result, recycling of Al scrap is environmentally friendly, as it conserves primary resources i.e coal, coke etc. which are used to generate electricity and hence reduces pollution (gases and smoke generation) **(Legarth, 96)**.

Although recycling of Al scrap is associated with economic and environmental benefits, there are a number of concerns in maintaining the quality standards mainly due to contamination from the scrap mixed with virgin metal. For example some paints and coatings are harmful for re-melting furnace or poor refractory coatings on melt handling steel tools will result in Fe contamination. Also, scrap from different sources will consist of different alloying elements so it is very important to carefully segregate them. In order to maintain the high quality standard, Al scrap recovery uses high environmental impact fluids and fluxes during the Al dross recovery process and leaching process

(Shinzato et al, 05). Puga **(Puga et al., 09)** categorises the different steps required to maintain high quality standards for Al scrap. The first steps are to de-coat the scrap if coated and send to the melting furnace. Steps after that involve treating the molten metal i.e. fluxing with salts or gas to remove inclusions, degassing to remove hydrogen and filtration. It is after these steps that a DC ingot is produced. The only different process between producing new Al and recycled Al is de-coating. This operation is usually low cost as the burning of the coating preheats the metal.

A major problem with recycling of Al is caused by the presence of impurities predominantly Fe. Fe is an undesirable impurity as it deteriorates the mechanical properties of the casting, particularly ductility and toughness **(Fang et al., 07)**. Extensive efforts are made to keep the Fe level to a minimum, given economic constraints. However, Fe is deliberately added for etched and anodised alloys to generate matte surface finish **(Ramanan et al., 08)**. For commercial alloys the Fe level varies from <0.1% in aerospace alloys to 0.4% in extruded product depending on application **(Davis et al., 93) & (Gale et al., 04)**. The detrimental effect of Fe is due to its low solubility and tendency to form Fe containing intermetallic compounds **(Fang et al., 07)**, which will be discussed in detail in section 2.2.3.2. As 6xxx series alloys have Mg and Si added to them for strength, the Fe levels in the alloy need to be kept low in order to maintain an appropriate Fe/Si ratio (governing factor for intermetallic formation). These compounds are brittle and are prone to grow as long needles/plates during solidification, which are very harmful for mechanical properties of the alloy. These intermetallic

particles can deteriorate the properties and make the alloy unsuitable for extrusion, which will be discussed in Section 2.2.5. As a result to supress the negative effects of intermetallics a number of techniques such as addition of particular elements (for example Mn, Cr) or homogenisation (section 2.5) are used **(Eskin, 08)**. This review will focus on the formation of intermetallics (section 2.4) in 6xxx Al alloys (section 2.2). Effect of important manufacturing processes like DC casting (section 2.3) and homogenisation (section 2.5) on intermetallics is also discussed. This review will also discuss the effect of various parameters like cooling rate, alloying elements, inclusions on the intermetallic phase formation (section 2.4). The effect of melt conditioning on inclusions and microstructure is also discussed in short (section 2.6). Lastly, this review will discuss various characterisation techniques available for analysing the intermetallics.

2.2 6xxx Al alloys

2.2.1 Introduction

According to the world Al organisation, over the past five decades total Al production has increased from 2 million tons to 50 million tons (as of 2014). Today more Al is produced each year than all other non-ferrous metals combined**.** As a result, continuous research is being done on improving the properties of Al alloys and one of the ways this can be done is by improving the understanding of the underlying solidification theory **(Parson et al., 89)**. The major process for producing wrought (i.e alloys that are mechanically worked after casting) 6xxx Al alloys is direct-chill (DC) casting, a semi continuous process, which is used to manufacture high volume Al alloy billet or ingot for further processing by extrusion or rolling. About 30% of overall Al alloys consumed are extruded products and 90% of these are 6xxx series alloys **(Reiso, 04)**. Hence 6xxx series alloys are also known as high speed extrusion alloys.

2.2.2 Types and uses of 6xxx Al alloys

The main alloying elements in 6xxx Al alloys are Mg (0.35% – 1.5%) and Si (0.35% - 1.7%). Copper (Cu), manganese (Mn), chromium (Cr), zinc (Zn), boron (B), lead (Pb) and bismuth (Bi) are also added to 6xxx alloys to improve specific properties **(Springer Handbook, 05).** Chemical compositions of some 6xxx alloys are given in Table 2.1**.**

Table 2.1 Chemical compositions of various 6xxx Al alloys **(Springer Handbook).**

6xxx	Si %	Fe %	Cu %	Mn %	Mg %	Cr %
6003	0.35 – 1	0.3-0.6	0.1	0.8	0.8 – 1.5	0.35
6005	0.6 – 0.9	0.1-0.35	0.1	0.1	0.4 – 0.6	0.1
6053	0.5 – 0.8	0.1-0.35	0.1	-	1.1 – 1.4	0.15 – 0.35
6061	0.4 – 0.8	0.3-0.7	0.15 – 0.4	0.15	0.8 - 1.2	0.04 – 0.35
6063	0.2 – 0.6	0.1-0.35	0.1	0.1	0.45 – 0.9	0.1
6066	0.9 – 1.8	0.1-0.5	0.7 – 1.2	0.6 – 1.1	0.8 – 1.4	0.4
6070	1 – 1.7	0.1-0.5	0.15 – 0.4	0.4 – 1	0.5 – 1.2	0.1
6101	0.3 – 0.7	0.1-0.4	0.1	0.03	0.35 – 0.8	0.03
6201	0.5 – 0.9	0.1-0.5	0.1	0.03	0.6 – 0.9	0.03
6463	0.2 – 0.6	0.1-0.15	0.2	0.05	0.4 – 0.9	-

6xxx series Al alloys are relatively medium strength alloys and are heat treatable. They have moderate mechanical strength (150-380 MPa) however much lower than 2xxx/7xxx/8xxx series. 6xxx series Al alloys have good formability, weldability and higher resistance to corrosion than traditional aerospace alloys (2xxx and 7xxx) **(Davis, 99)**. 6xxx series Al alloys are soft at high temperatures and are easily extrudable in comparison to 2xxx/7xxx series Al alloys due to low flow stress. This combination of good properties results in their widespread use in various sectors such as transportation (automobiles, railcars etc), architectural (windows, ladders etc), marine (ships) etc **(Altenpohl et al., 98)**, where many of the components are extruded.

The DC casting process is mainly used for producing 6xxx billets, which then undergo homogenisation treatment in order to improve composition uniformity and to dissolve any Mg_2Si into solution prior to extrusion. Subsequent heat treatment of the extruded product is used to re-precipitate Mg_2Si to increase the strength of the product **(Jarrett et al., 03)**.

2.2.3 Influence of different alloying elements in 6xxx Al alloys

This section discusses the effects of the different alloying elements on the microstructure of the 6xxx Al alloys. The particular intermetallics which form and their effects on the material properties will be discussed in the next section.

2.2.3.1 Mg and Si

Mg and Si are the major additions to 6xxx series al alloys and play a very important role in deciding the mechanical properties of the alloy. The variation of Mg and Si composition within 6xxx Al alloys is shown in Table 2.1. The ratio of Mg:Si influences the stability of some metastable phases, which in turn determines the strength of the alloy via precipitation hardening **(Chakrabarti et al., 04)**. Si is added to this alloy as it is solutionisable and combines with Mg to form hardening phase Mg_2Si that provides strength in these alloys (usually Mg/Si ~ 1.73). Chakrabarti et al also observed that when the Mg/Si ratio is less than about 1, the Si phase is stabilized, when it is greater than 1, Mg_2Si is stabilized. Mg_2Si intermetallic phase precipitates incoherently from the

matrix to provide increased strength **(Meyveci et al., 10)**. Excess Si (Mg/Si <1.73) is added sometimes to achieve higher strength and reduce strengthening response time during aging **(Gupta et al., 01)**, however it has a negative effect on ductility due to segregation at the grain boundaries **(Aucote et al., 78).** Also, an increase in Si content leads to a decrease in the transformation rate of β-AlFeSi to α-AlFeSi during the homogenisation process **(Parson et al., 02)**. It has been reported that higher Mg content increases the yield stress while decreasing the ductility **(Kashyap et al., 93)** and fracture toughness **(Murali et al., 92)**. Caceres et al. observed only β-AlFeSi phase in low (0.4 wt%) Mg alloys **(Caceres et al., 99)**. Also, the probability of formation of $Al_{13}Fe_4$ phase increases with the increase in Mg concentration **(Hsu et al., 01)**. This is because Mg reduces the solubility of Si in solute and forms Mg_2Si. Fe present in the alloy then has no Si to react with and forms $Al_{13}Fe_4$. This phase shift is discussed further in chapter-5.

2.2.3.2 Mn and Cr

In 6xxx alloys Mn and Cr are added to prevent recrystallization and/or control grain growth during processing **(Murat et al., 03).** Both Mn and Cr have similar influence on alloy properties, have low diffusivity in Al matrix and forms homogeneously distributed fine dispersoids **(Murat et al., 03)**. Large amount of Mn addition in these alloys (Mn>1%) lead to increase in strength and toughness. This is because Mn forms dispersoids which affect the recrystallization behaviour and result in fine grain structure. Addition of small amount of Mn has a great influence on the transformation rate of β-AlFeSi to α-AlFeSi during the

homogenisation process **(Mondolfo, 76)**. It was observed that for low Mn concentrations (<0.01 wt%) the transformation rate of β-AlFeSi to α-AlFeSi is quite slow. For higher Mn concentrations (> 0.05 wt%) the transformation rate increases and cubic α_c-AlFeSi (α-AlFeSi henceforth) is the stable phase **(Zajac et al., 94)**. Also, excess Mn supresses the β-AlFeSi phase and encourages α-AlFeSi phase formation (as-cast), but it also leads to defects such as hard spots which lead to difficulties in machining **(Taylor et al.)**.

2.2.3.3 Cu

Addition of Cu in 6xxx series Al alloys alters the precipitation pattern and is an alternative to adding excess Si to increase the strength **(Chakrabarti et al., 99)**. The addition of Cu results in the formation of various metastable phases. The Al-Mg-Si-Cu family of alloys is formed when Cu is added. The most frequent phase observed is designated as Al-Cu-Mg-Si phase, commonly known as the Q ($Al_5Cu_2Mg_8Si_6$) phase **(Dix et al., 32)**. Chakrabarti et al observed strengthening effects in Al-Mg-Si-Cu alloys due to the lath morphology of Q$^{/}$ ($Al_4Cu_2Mg_8Si_7$) phase (precursor of Q phase) **(Chakrabarti et al., 04)**.

2.2.3.4 Fe

Fe has the most significant impact on the mechanical and surface properties of the alloy. It is usually present as an undesirable impurity in the primary ingot due to the difficulty of removing it completely from molten metal **(Murat et al., 03)** but is also picked up from casting equipment made of steel **(Lu et al., 05)**. Fe levels

in the alloy is kept as low as possible due to its low solubility in Al and tendency to form number of intermetallic compounds, which adversely affect the toughness and are also associated with formation of porosity. Fe/Si ratio governs the phase formation behaviour which in turn determines the pick-up defects and surface quality of the alloy. It is interesting to note that higher levels of Fe are deliberately added particularly in etched and anodised alloys to increase the etch pit density and to obtain a uniform matte finish on the surface **(Ramanan et al., 08)**. Higher Fe levels (0.7 wt%) enhance the tendency to form the β-AlFeSi phase, which is very detrimental for the properties of the alloy **(Lu et al., 05)**. The β-AlFeSi phase is reported to have sharp edges and needle-like morphology, which results in stress build up in the matrix. For high Mg:Si ratio alloys, Fe is present in the form of $Al_{13}Fe_4$ (2.2.3.1) which causes pitting and reduces corrosion properties **(Wang et al., 95)**.

2.2.4 Intermetallic phases

In the 6xxx Al alloys many elements (including Mg, Si and Fe) tend to partition out of the primary Al solid solution during solidification as they have low solubility in Al and partition coefficients < 1 **(Kuijpers et al., 03)**. Fe and Si are the most important among these because they react with other alloying elements and form a number of ternary Al-Fe-Si phases of slightly different stoichiometries (Table 2.2) as listed in the literature **(Sha et al., 03) & (Allen et al., 00)** and including nonequilibrium variants of the Al-Fe-Si system **(Jarrett et al., 03) & (Mulazimoglu et al., 96)**. Some of the different

stoichiometries and crystal structures of the iron bearing phases reported in the literature are described below in Table 2.2.

Table 2.2 Crystallographic data for some commonly reported Fe-containing intermetallic phases in dilute Al alloys **(Kuijpers et al., 05), (Mondolfo, 76)** and **(Sha et al., 01)**.

Phase	Stoichiometry	Bravais Lattice	Space Group	Lattice Parameter (Å)
	$Al_{13}Fe_4$	C-centred monoclinic	C2/m	a = 15.49, b = 8.08, c = 12.48, β = 107.8°
	Al_mFe	Body centred tetragonal	I42m	a = 8.84, c = 21.6
	Al_9Fe_2	Monoclinic	unknown	a = 8.90, b = 6.35, c = 6.32, β = 93.4°
	Al_6Fe	C-centred orthorhombic	Ccmm	a = 6.49, b = 7.44, c = 8.79
	Al_xFe	unknown	unknown	unknown
α_c-AlFeSi	Al_8Fe_2Si	Body centred cubic or simple cubic	Im3 or Pm3	a = 12.56 (BCC) or 12.52 (simple cubic)
α_h-AlFeSi or α'-AlFeSi	Al_8Fe_2Si	Hexagonal	P63/mmc	a = 12.30, c = 26.20
α''-AlFeSi	unknown	C-centred orthorhombic	unknown	a = 27.95, b = 36.2, c = 12.7
α_T-AlFeSi	unknown	C-centred monoclinic	unknown	a = 27.95, b = 30.62, c = 20.73, β = 97.74°
β-AlFeSi	Al_5FeSi	Monoclinic	A2/a	a = 6.16, b = 6.17, c = 20.8, β = 90.4°
	Al_3FeSi	C-centred monoclinic	unknown	a = 17.80, b = 10.25, c = 8.90, β = 132°
	Al_4FeSi_2	Tetragonal	unknown	a = 6.14, c = 9.48

Composition is one way to differentiate these intermetallics and Fig. 2.2 shows the reported windows of composition range for the formation of various Fe-intermetallic phases **(Langsrud, 90)**. Langsrud obtained this data by determining the amount of Si that dissolves in the Al matrix and precipitates in the intermetallics and measuring the fraction and composition of Si containing intermetallics. The measured experimental data was then compared with a macroscopic model to get the phase distribution. It is very difficult to get the accurate composition of an in-situ intermetallic particle as the interaction volume of the x-rays used in energy dispersive x-ray (EDX) analysis is greater than the size of the particles. Also, for extracted intermetallic particles there could be more than one intermetallic particle in the analysed area.

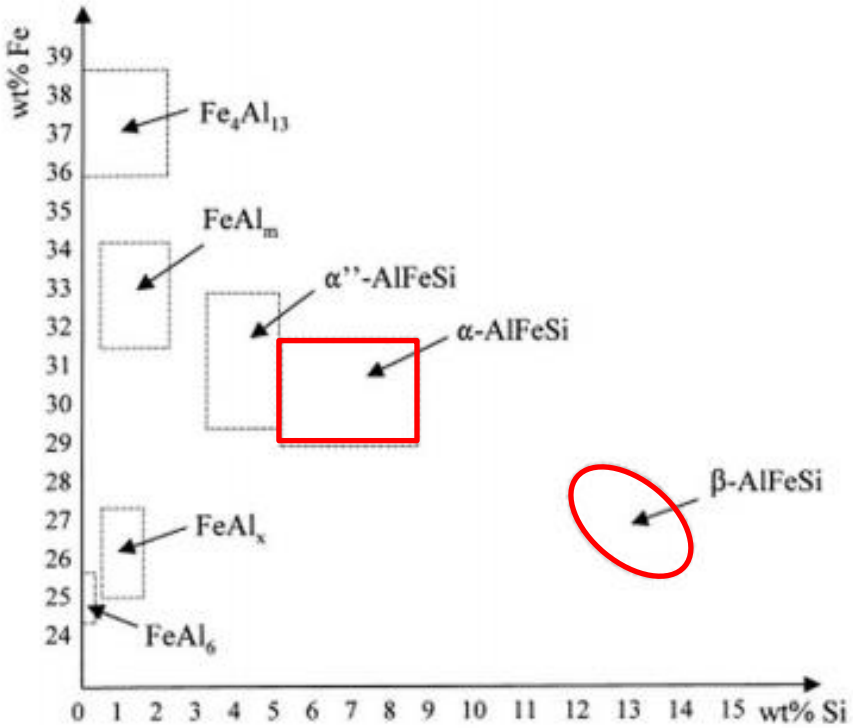

Fig. 2.2 Composition map of the common binary and ternary intermetallic phases found in dilute Al-Fe-Si alloys **(Langsrud, 90)**.

As α-AlFeSi (α_c-AlFeSi or Al_8Fe_2Si) and β-AlFeSi (Al_5FeSi) are the most common intermetallics observed in 6xxx Al alloys and have significant effect on the properties of the extruded alloy **(Zajac et al., 96)**, this section will mainly focus of these two intermetallics (as shown by red markings in Table 2.2 and Fig. 2.2).

Mg:Si play an important in the AlFeSi intermetallic formation. At high Mg:Si ratio (less likely in 6xxx series), all Fe forms the $Al_{13}Fe_4$ phase (2.2.3.1) and at low Mg:Si ratio β-AlFeSi phase become dominant **(Belov et al., 05)**. Belov et al. also observed that binary eutectic reactions containing Fe and Si phases take place after the primary α-Al crystals are formed. The liquidus path in Fig 2.3 below gives an idea of the various intermetallics that can form in the Al-Fe-Si system **(Mondolfo, 76)**. It shows the effect of Fe/Si ratio on the intermetallic phase formation i.e. if Fe/Si >1, α-AlFeSi is stable whereas if Fe/Si<1 β-AlFeSi is more stable.

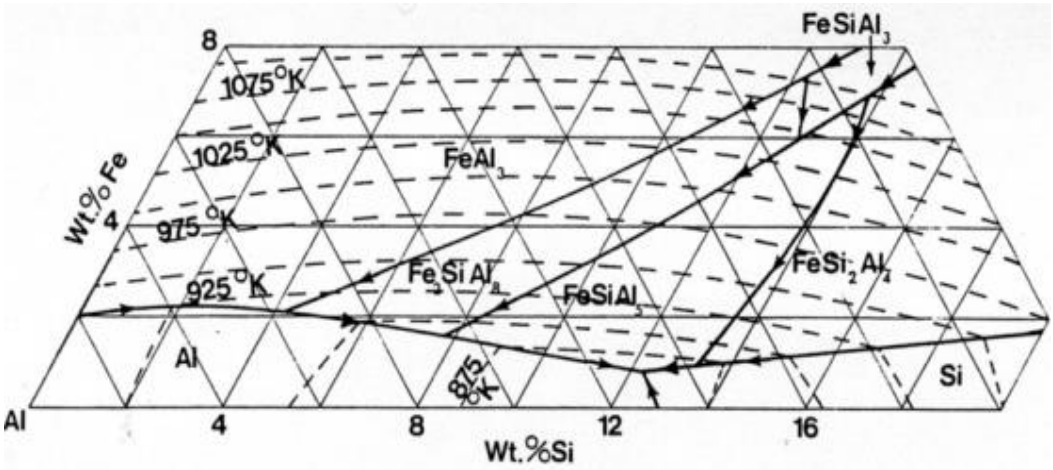

Fig 2.3 The liquidus path in the Al corner of the Al-Fe-Si phase diagram **(Mondolfo, 76)**.

Table 2.3 shows the formation of α-AlFeSi and β-AlFeSi intermetallic phases and Mg_2Si via different reactions that occur during solidification. It also shows how the reaction temperature changes with the cooling rate. During the homogenisation process, phases containing Mg dissolve (Mg_2Si in particular), whereas Fe containing phases remain **(Kuijpers et al., 03)**. Therefore in order to control the phase selection, it is very important to understand the formation and behaviour of Fe rich intermetallic phases. Fig. 2.4 shows the morphology of β-AlFeSi intermetallics and Mg_2Si observed in Al-Mg-Si system **(Liu et al., 99)**.

Table 2.3 Solidification reactions under non-equilibrium conditions in a 6063 alloy (0.43 wt% Mg, 0.39 wt% Si, and 0.2 wt% Fe) **(Backerud et al., 86)**.

	Temperatures (^{0}C) at a Cooling Rate	
Reaction	**0.5 K/s**	**15 K/s**
L → (Al)	655-653	654
L → (Al) + α(AlFeSi)	618-615	617
L + α(AlFeSi) → (Al) + β-AlFeSi	613	610
L + α(AlFeSi) → (Al) + βAlFeSi + Mg_2Si	576	576
Solidus	576	576

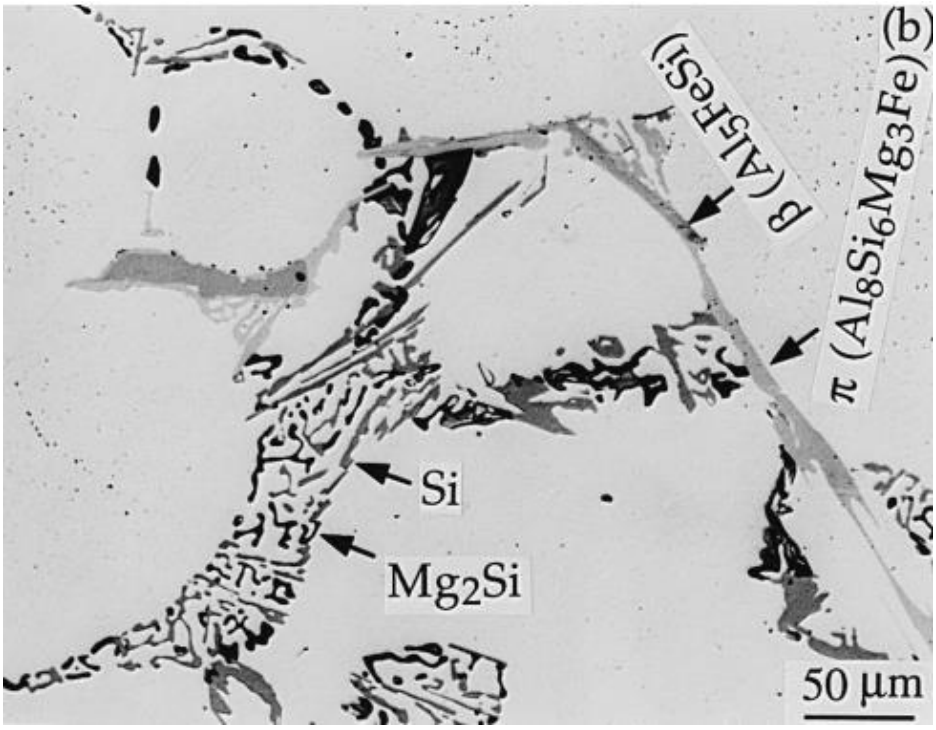

Fig 2.4 As-cast microstructure of an Al-Mg-Si alloy showing different intermetallics **(Liu et al., 99)**.

2.2.5 Effects of intermetallic phases

Intermetallic phases have a marked influence on the downstream processing and physical properties of Al alloys. Their type, size and shape greatly affect the downstream processing **(Hamerton et al., 00)** and hence the surface appearance of the extruded material. All the intermetallic particles have different unit cell structures, different morphologies and mechanical properties, which causes inhomogeneity in the microstructure and properties of the alloy **(Allen et al., 98)**. Such materials cause problems during extrusion and further processing. As the volume fraction and number density of intermetallic particles

increases with the amount of Fe content, this also result in reduction in toughness and ductility and extra wear of the extrusion die during processing.

β-AlFeSi intermetallic particles in particular, affect the extrusion surface in a number of ways for example surface gloss, streaking etc. β-AlFeSi intermetallics reduce the grain size, randomize the texture, cause etching pits and hinder the recrystallization process **(Hanliang et al., 09)**. The β intermetallic particles also increase the flow stress during the extrusion process **(Zajac et al., 94)**. Similar phenomenon is proposed for as cast α-AlFeSi, however there is no supporting hard evidence reference. This increase in flow stress will result in drop in productivity.

The presence of β-AlFeSi platelets has proven to be deleterious for the extrusion properties of the material by causing an increase in the initial work hardening rate, and a sharp decrease in ductility and toughness and initiating cracks due to decohesion at the particle/matrix interface **(Zajac et al., 94)**. β-AlFeSi particles are highly faceted and hence severely degrade mechanical properties **(Yi et al., 04)**. They also cause pick up of debris and die lines on the extruded surface **(Hamerton et al., 00)**.

Also, Fe rich intermetallic particles (α-AlFeSi and β-AlFeSi) tend to fracture more easily under tensile load than the Al matrix, hence creating micro-cracks

and easy paths for macro-cracks **(Zajac et al., 96)**. On the same note, α-AlFeSi intermetallic particles proved to be much less deleterious in comparison to β-AlFeSi as α-AlFeSi was reported to have a more spherical morphology which improves the ductility and reduces the likelihood of inducing any micro-cracks **(Zajac et al., 96)**. The presence of transformed α-AlFeSi also decreases pick-up defects in the extruded material **(Hamerton et al., 00) & (Allen et al., 96),** however as cast α-AlFeSi result in higher pick-up defect.

It is interesting to note that Fe is deliberately added in order to generate products with hard wearing decorative finish. This is because the intermetallic particles act as nucleating site for etch pits, which generates a matte surface finish on etching. However, Fe levels have to be kept low for a bright surface finish.

Various solute elements such as Mg, Si, Mn, Cr, Cu and Fe have significant effects on the intermetallic phase selection in 6xxx series Al alloys. In this chapter we have seen how different intermetallic phases are formed depending on the initial chemical composition of the alloy. This review will now focus on the commercially most used process for Al alloys i.e. DC casting which will be described in the next section.

2.3 DC Casting

The major process for producing wrought Al is direct-chill (DC) casting, a semi continuous process, which is used to manufacture high volume Al alloy billet or ingot for further processing by extrusion or rolling **(Jarrett et al., 03)** and **(Grandfield et al., 93)**. DC casting is a very important process for producing ingots, rolling sheet ingots, billets, etc. The process consists of a water cooled mould which provides primary cooling of the melt, to form a solid shell followed by direct cooling of this shell with water sprays outside the mould. There are a number of advantages in using DC casting over other processes **(Jarrett et al., 03):**

a) reduced centreline segregation;
b) productivity, very high heat transfer by direct water sprays
c) increased density in central portion of the billet;
d) finer and more homogeneous structure, hence better mechanical properties;
e) better surface properties;
f) lower operation costs.

2.3.1 Process

The standard DC casting process uses melting furnaces which are charged with scrap Al, prime Al and hardeners. Melt is transferred to holding furnaces before casting as this maximises the efficiency, and is then poured from the top into a short, open, water cooled mould, which is initially closed from the bottom with

the help of a starter block **(Eskin, 08)**. The block is connected to a hydraulic lowering system, which comes into play when the melt reaches a certain level. This downward movement of the ram results in extraction of the solid part of the billet or ingot. The melt level in the mould is kept constant by adjusting the melt flow rate and the casting speed **(Eskin, 08)**. As the bottom of the mould moves down, water jets spray water onto the solid shell (as seen in the left side of Fig. 2.5). Since it is a semi continuous process, as soon as the ram reaches its lowest position, casting is stopped and the billet is removed **(Jarrett et al., 03) & (Eskin, 08)**. Cooling pits filled with water are used for safety purposes i.e. if there is a run out or to dip the billet into water after it's been cast for some time.

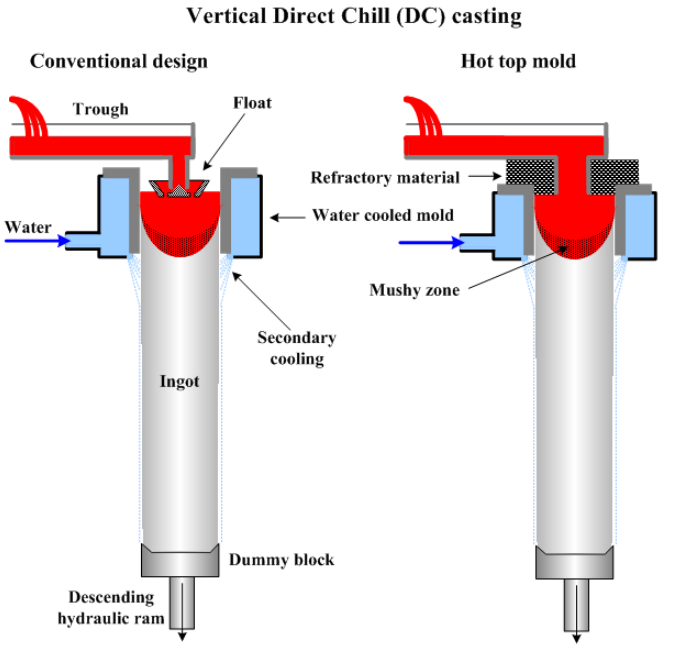

Fig 2.5 Conventional and hot top mould DC casting processes **(www.substech.com)**.

A hot top mould helps to protect the melt from oxidation, requires much less flow control and reduces heat losses (see Fig. 2.5).

2.3.2 Microstructure of the ingot

During casting the microstructure can be divided into a number of zones including fully solid, mushy zone and fully liquid. The phase formation in these zones depend on the temperature distribution of the system which in turn depends on a number of factors like melt temperature, melt flow, chemical composition and the cooling conditions **(Eskin, 08)**.

Solidification rate and cooling rate are two prominent factors affecting the structure and hence the properties of the ingot. Maximum solidification rates are achieved at the periphery and at the centre of the billet because of the flat solidification front, whereas the minimum solidification rate occurs at approximately the mid-radial position where the solidification front is steepest as shown in Fig. 2.6a **(Eskin et al., 04)**.

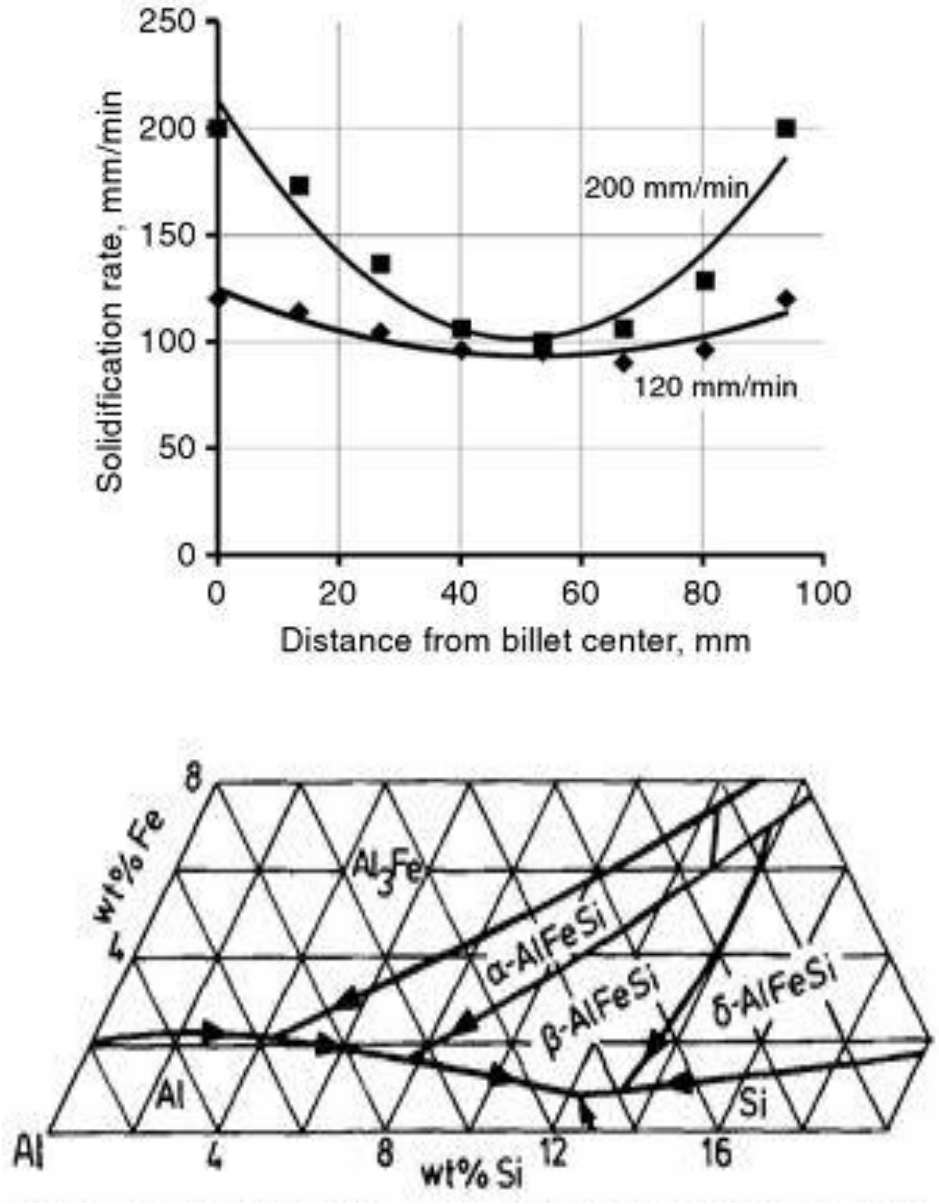

Fig. 2.6 a) Variation of solidification rate with distance from the centre of the billet **(Eskin et al., 04)** and b) liquidus projection **(Skerpje, 87).**

The other important phenomenon in a DC cast billet is micro-segregation which is typically associated with faster solidification rates. The faster the solidification rate, the lesser the time solute has to get homogenized via diffusion, resulting in

solute rich liquid. As a result of micro-segregation, a number of non-equilibrium reactions occur resulting in different non-equilibrium phases **(Eskin, 08)**. This can also be seen in the liquidus projection in Fig. 2.6b i.e. as the Fe:Si ratio decreases, the phase formation path changes. The quantity of non-equilibrium phases in the billet is at a minimum in the centre of the billet, which indicates more solute enrichment in the periphery than in the centre **(Cefalu et al., 03)**. This also correlates with the fact that on increasing the cooling rate, the number of non-equilibrium phases formed increases. The cooling rate in DC casting typically varies from 1K/s in the centre to 20K/s at the periphery **(Aliravci et al., 98).** Lozano et al observed that the volume fraction and particle density for the Mg_2Si and AlFeSi intermetallics in 6063 Al alloy increases by three folds from centre to periphery in a DC cast billet **(Lozano et al., 14).** During the later stages of solidification, the highly solute enriched liquid in the centre is pushed towards the periphery due to high metallostatic pressure which results in the solute enrichment of liquid at the outer surfaces **(Gruzleski, 00).** Such large scale inhomogeneous distribution of alloying elements during solidification is commonly referred to as inverse segregation **(Nadella et al., 08)**. This back diffusion in the centre of the billet compared to the periphery also reduces the amount of non-equilibrium phases at the centre **(Cefalu et al., 03)** and **(Vusanovic et al., 05)**. They also observed that negative macrosegregation also helps in reducing the amount of non-equilibrium phases.

α-AlFeSi (α_c-AlFeSi / Al_8Fe_2Si) has been observed to form via peritectic and eutectic reactions for the typical DC casting cooling rate. Other researchers also

suggested that during industrial cooling rate (~5K/s) and Fe:Si ratio <1, β-AlFeSi forms preferentially over α-AlFeSi **(Tanihata et al., 99)** & **(Lassance, 06)**. This can also be attributed to lower atomic ratio of Fe:Si (1:1) in β-AlFeSi particles in comparison with higher Fe:Si (2:1) in α-AlFeSi. The liquidus projection as shown in Fig. 2.6b also shows β-AlFeSi as the more stable phase than α-AlFeSi for low Fe:Si ratios.

A zone of fine grains with fine dendrites is formed at the surface of the billet in the region of direct contact with the mould **(Eskin, 08)**. The average grain structure coarsens toward the centre of the billet, as the structure changes from fine grained at the periphery to a zone of columnar grain and then to equiaxed grains in the centre **(Nadella et al., 08)**. Since most of the castings are grain refined, only equiaxed grains are observed. Varying the cooling rate affects nucleation and growth of grains, hence on increasing the melt temperature and decreasing the casting speed coarser grains are observed towards the centre of the billet **(Jarrett et al., 03)**. This phenomenon can be explained by competitive nucleation and growth. As the cooling rate at the periphery is high, more Al grains can nucleate due to higher undercooling and lesser time is available for grains to grow which result in finer grain size. Whereas in the centre, lower cooling rate due to limited convection and released latent heat result in lower undercooling and more time for grains to grow, thus resulting in coarser grain size.

At high casting temperatures, factors such as the casting speed and cooling rate affects the amount of non-equilibrium phases in the centre of the billet. The fraction of these phases decreases with an increase in cooling rate, whereas it increases with an increase in casting speed **(Eskin et al., 05)**. However, at low casting temperature, the effect is reversed. Higher concentrations of non-equilibrium phases were observed when casting at high melt temperature **(Du et al., 05)**. Also, the amount of non-equilibrium phases formed increases for more highly alloyed billets. Interestingly, the degree of formation of these phases at the centre of the billet reduces significantly in less alloyed billets **(Eskin et al., 04).** This can be attributed to inverse segregation or back diffusion of solute enriched liquid (explained earlier in this section). In low alloyed billets, even smaller migration of solute rich liquid will reduce the amount of non-equillibrium phases and shift the liquid composition to lower end of Al corner (as shown in liquidus projection Fig. 2.6b) where non equilibrium phases are not formed. Commercial 6xxx Al alloys generally can have β-AlFeSi (Al_5FeSi) and α-AlFeSi (Al_8Fe_2Si) coexisting in the structure **(Mondolfo, 76)**.

2.4 Factors governing intermetallic phase selection during solidification

The main alloying elements for 6xxx alloys are Si and Mg. In the solidified alloy, elements are partly in solid solution in the primary α-Al matrix, and partly present in the form of intermetallic phases **(Eskin et al., 04)**. Due to non-equilibrium reactions, it is very difficult to predict the phases in the as cast structure. Cooling rate, trace elements, temperature gradient, non-equilibrium solute partitioning, impurities, inclusions and other factors affect the local chemistry and consequently the intermetallic phases formed **(Eskin, 08).** Therefore, an understanding of factors that govern phase selection is very important, as changing one factor can lead to a different phase. Metastable as well as equilibrium intermetallic phases are formed depending on local alloy composition, growth rate and cooling rate **(Jarrett et al., 03)**.

2.4.1 Effects of local composition, cooling rate and growth velocity on intermetallic phase selection

As discussed earlier, Fe present as an impurity in 6xxx Al alloys forms mainly α-AlFeSi (α_c-AlFeSi/Al_8Fe_2Si) and β-AlFeSi (Al_5FeSi) intermetallics **(Khalifa et al., 05)**.

Nucleation of β-AlFeSi takes place in a region where the liquid is enriched in Si due to partitioning into the interdentritic liquid, whereas nucleation of α-AlFeSi is favoured by high cooling rate as it reduces the partitioning

(Khalifa et al., 05). It has been found that when the Fe/Si ratio is greater than 1, then α phase is more stable and when it is less than 1, β phase is favourable **(Tanihata et al., 99)**.

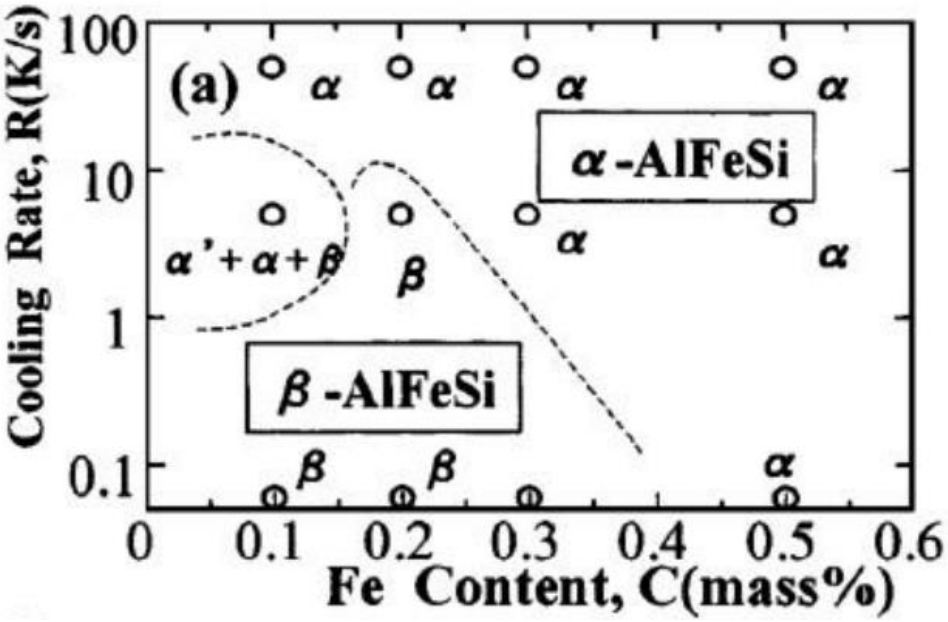

Fig 2.7 The range of relative amounts of AlFeSi intermetallics in the 6063 as-cast ingot material **(Tanihata et al., 99)**.

Cooling rate during DC casting plays a crucial role in the formation of intermetallic phases. At higher cooling rates, particles with lower Si content i.e. α-AlFeSi phase forms and at lower cooling rates particles with high Si content i.e. β-AlFeSi phase form as shown in Fig 2.7 **(Tanihata et al., 99)**. This is because at higher cooling rate less Si is partitioned which result in high Fe/Si ratio. The liquidus projection in Al-Fe-Si system (Fig. 2.2a) also shows that when Fe/Si is high α-AlFeSi is more stable than β-AlFeSi. Birol **(Birol, 98)** observed that β-AlFeSi particles form predominantly at the boundaries of

dendrites, whereas α-AlFeSi particles form at the triple points of the grains (because of lower Si/Fe ratio).

It has been observed **(Langsrud, 90)** that α-AlFeSi and β-AlFeSi phases can form in the solid state after solidification, although according to the equilibrium phase diagram only α_h-AlFeSi should have been formed. The reason being the shift to the metastable phase field due to an increase in the cooling rate. It has also been suggested that β phase can form via a quasi-peritectic reaction from α-AlFeSi to β-AlFeSi **(Hsu, 99)**, as shown in (5) below.

According to the phase diagram, the following reactions can be expected during solidification and melting of 6xxx alloys **(Allen et al., 98) & (Hsu, 99):**

$L \rightarrow \alpha\text{-Al}$ (1)

$L \rightarrow \alpha\text{-Al} + Al_{13}Fe_4$ (2)

$L + Al_{13}Fe_4 \rightarrow \alpha\text{-Al} + \alpha_c\text{-AlFeSi}$ (3)

$L \rightarrow \alpha\text{-Al} + \alpha_c\text{-AlFeSi}$ (4)

$L + \alpha_c\text{-AlFeSi} \rightarrow \alpha\text{-Al} + \beta\text{-AlFeSi}$ (5)

$L \rightarrow \alpha\text{-Al} + \beta\text{-AlFeSi} + Mg_2Si$ (6)

All of the reactions except the first (which forms primary α-Al), form intermetallic phases. It has been shown that as the non-equilibrium nature of

solidification increases, the tendency to form α_c-AlFeSi phase via eutectic reaction (4) increases over the peritectic reaction (3) **(Sha et al., 01)**. It has been suggested that β-AlFeSi forms via a peritectic reaction at higher cooling rates **(Hsu, 99).** This will result in low β-AlFeSi as peritectic reactions are time dependent and so the reaction would be incomplete at high cooling rate. This is also in accordance with Fig 2.7 **(Tanihata et al., 99)** which shows β-AlFeSi as more stable phase during low cooling rates.

Earlier studies show that $Al_{13}Fe_4$ is not a stable phase **(Backerud et al., 86)** and **(Mulazimoglu et al., 96)**. Backerud **(Backerud et al., 86)** suggested that $Al_{13}Fe_4$ particles are formed but easily transform into α-AlFeSi, while Mulazimoglu **(Mulazimoglu et al., 96)** proposed that $Al_{13}Fe_4$ does not form at all because it is difficult to nucleate at high cooling rates. The presence or absence of $Al_{13}Fe_4$ phase will govern the solidification path (either reaction (3) or (4)) and hence the morphology of α_h-AlFeSi. α_h-AlFeSi formed via peritectic reaction has faceted morphology **(Mulazimoglu et al., 96)**.

Si which is not in solution in the Al matrix or contained in any intermetallic, solidifies to form Mg_2Si **(Tanihata et al., 99)**. The intermetallic particles size and Al columnar grain size both reduce with an increase in growth velocity. Al grains are formed through reaction (1) at high temperature. With high growth velocities, the size of the Aluminium grains decreases which result in fine intermetallic particles. It has been shown that the proportion of α-AlFeSi

(α_c-AlFeSi) increases and β-AlFeSi decreases with an increase in growth velocity **(Sha et al., 01)**. This is because at high growth velocities, α-AlFeSi forms mainly through eutectic reaction (4) and not from quasi-peritectic reaction (3), whereas β-AlFeSi forms through both eutectic reaction (6) and quasi-peritectic reaction (5). Since peritectic reactions are time dependent, they are preferred for slow growth velocities. It is also important to note that the initial growth velocity increases with the initial undercooling and the actual phase selection is defined by the complex interaction between the two and not solely by one of them **(Bongo et al., 14)**. The other possible reason for α-AlFeSi being preferred at high growth velocities could be the non-faceted growth mode in comparison with faceted growth mode of β-AlFeSi, as the latter faces more hindrance from space adjustments **(Adam et al., 72)**. Also during competitive growth, the dominance of one phase increases over another phase if that phase has a higher growth temperature than the other and during competitive nucleation, one phase can dominate the other phase if the nucleation temperature of that phase is higher than the other **(Eskin, 08)**.

2.4.2 Effect of transition elements on intermetallics

Additions of small amounts of transition elements can greatly affect the nucleation of intermetallic phases. Impurities present at ppm levels are sufficient for the formation of metastable phases **(Cantor et al., 97)**. Transition elements such as V, Cr, Mn, Cu, Mo and W promote the formation of metastable cubic α-AlFeSi over the equilibrium hexagonal α_h-AlFeSi **(Pennors et al., 98)** and

(Gustafsson et al., 86). Higher amounts of Fe not only favour the formation of β-AlFeSi but also change its morphology to coarse needles, whereas lower Fe levels produce small needle-like β-AlFeSi **(Lu et al., 05)**.

Of all of the transition elements, Mn has the most significant effect on the β-AlFeSi to α-AlFeSi transformation rate during homogenisation which will be discussed in Section 2.5.3. Effect of addition of Mn is discussed in section 2.2.3.2. Alloying 6xxx Al alloys with 0.9% Mn, results in fragmentation of the β-AlFeSi needles **(Shabestari et al., 02)**. At higher Mn the plate-like morphology of the β-AlFeSi needles was replaced by $Al_{15}(Fe,Mn)_3Si_2$ dendrites in the form of plate, polyhedral or star-like shapes **(Shabestari et al., 02 & 04)**.

Also, the detrimental effect of β-AlFeSi can be reduced with the addition of small amounts of Cr and Co **(Mahta et al., 05)**. Coarse Chinese script dendrites are promoted when the Fe:Cr ratio is close to 3. Also, a Fe:Co ratio close to 1, suppresses the formation of β-AlFeSi needles **(Mahta et al., 05)** and **(Gustafsson et al., 86)**. Sr at lower levels (0.03%) hinders the positive effect of Mn, whereas at higher levels (0.3%) dendritic morphology is promoted **(Pennors et al., 98)** and **(Shabestari et al., 02)**. S.Murali **(Murali et al., 96)** suggested that Be could completely neutralise the deleterious effect of Fe (0.93% Fe) by forming a Be-Fe phase in 6xxx alloys.

2.4.3 Effect of oxides

There are different types of inclusions present in commercial Al alloys such as oxides, carbides, chlorides, grain refiners, refractory materials etc. However, this study will only analyse the effect of oxides and oxide bi-films on secondary phase formation. Re-melting of secondary Al is always associated with the formation of oxides and oxide bi-films. Al and Mg are active metals and form oxides on their surface when heated. Dispinar et al. suggested that if the molecular volume of the oxide is greater than the atomic volume of the metal contained in the compound, a continuous film is formed, whereas a discontinuous film is formed if it is less than unity. This is because if the oxide particles have smaller molecular volume, they will be loosely packed and oxygen can easily seep through them which will result in a discontinuous layer, whereas if the oxide particles are large they will form a continuous protective film **(Dispinar et al., 05)**. These surface oxides when entrained in the bulk liquid through actions like pouring or stirring, form a bi-film as shown in Fig. 2.8 **(Campbell et al., 03)** and **(Dispinar et al., 04)**. During this action the oxide film is folded over from dry side to dry side due to turbulent flow i.e. 2.8d to 2.8e **(Dispinar et al., 04)**.

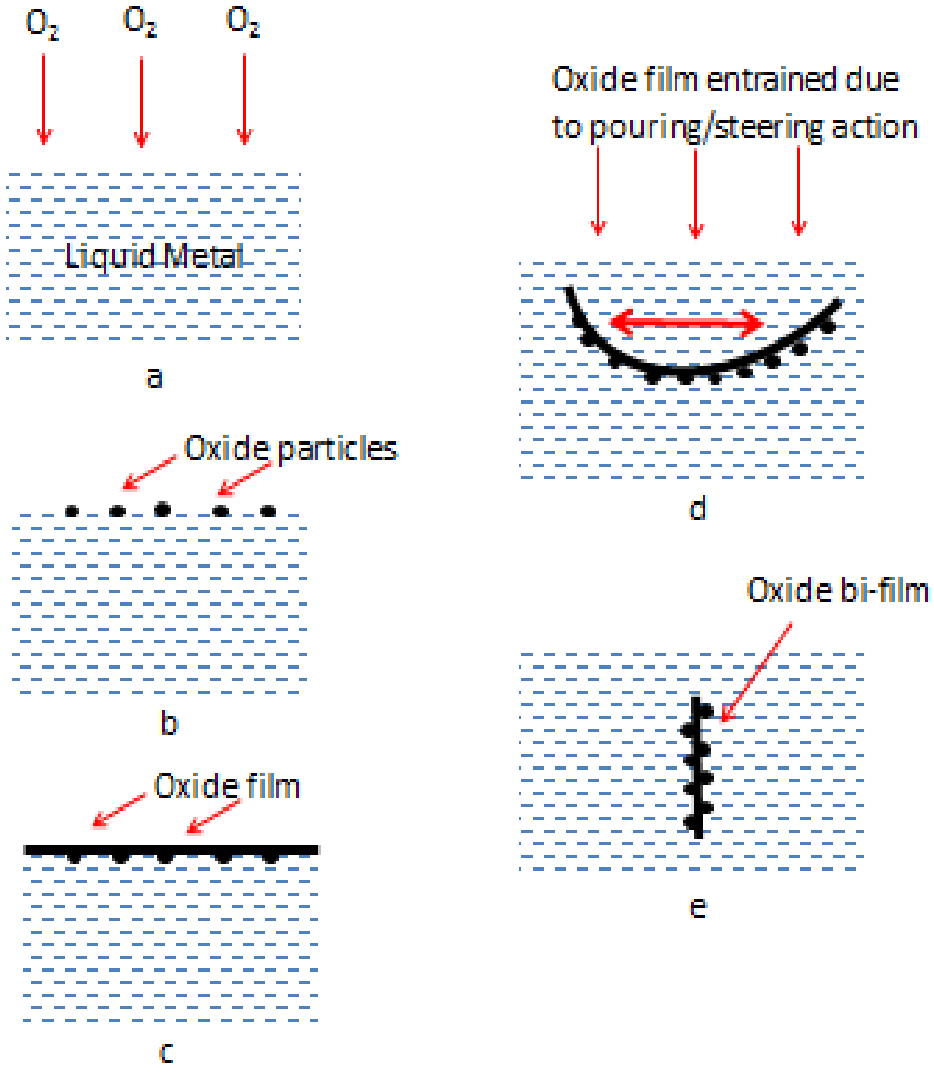

Fig. 2.8 Different stages of the formation of oxide bi-film **(Campbell et al., 03)** and **(Dispinar et al., 04).**

These bi-films have some air trapped between their two halves and appear as cracks in the alloy due to negligible bonding between the dry surfaces facing each other **(Campbell et al., 03)**. As the film grew on the melt, the top side of

the film is exposed to air whereas the underside of the film is in contact with other oxide molecules or phases.

The top surface is also known as the dry side (not exposed to liquid metal) and the surface underneath as the wet side (exposed to liquid metal), where the wet side is expected to have good bonding with Fe-rich intermetallic phases or the Al matrix based on theoretical calculations and therefore may support the nucleation and growth of Fe rich intermetallics **(Cao et al., 05)**. Simensen **(Simensen et al., 97)** et.al observed the nucleation of π-phase on the oxidised melt surface of Al-17.6Si-7.6Mg-1.0Fe alloy. Also, β-AlFeSi phase can cause cracking along the centre line of the oxide film if it grows on both sides of an oxide film, or can cause decohesion from the matrix if it grows on one side **(Tian et al., 02)** and **(Shabestari et al., 02)**.

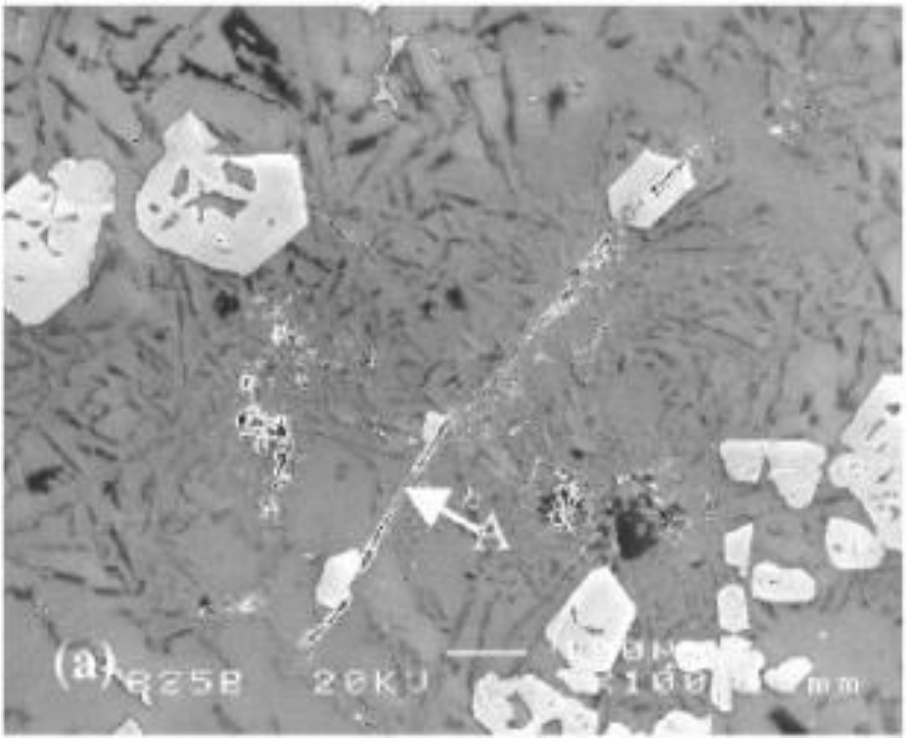

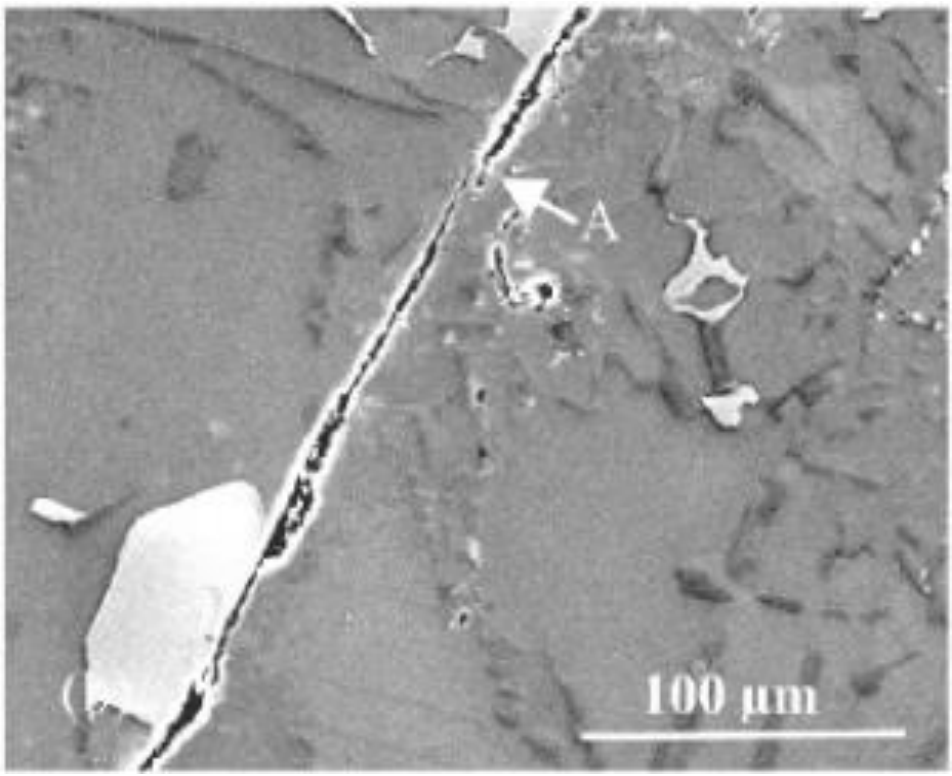

Continued overleaf…

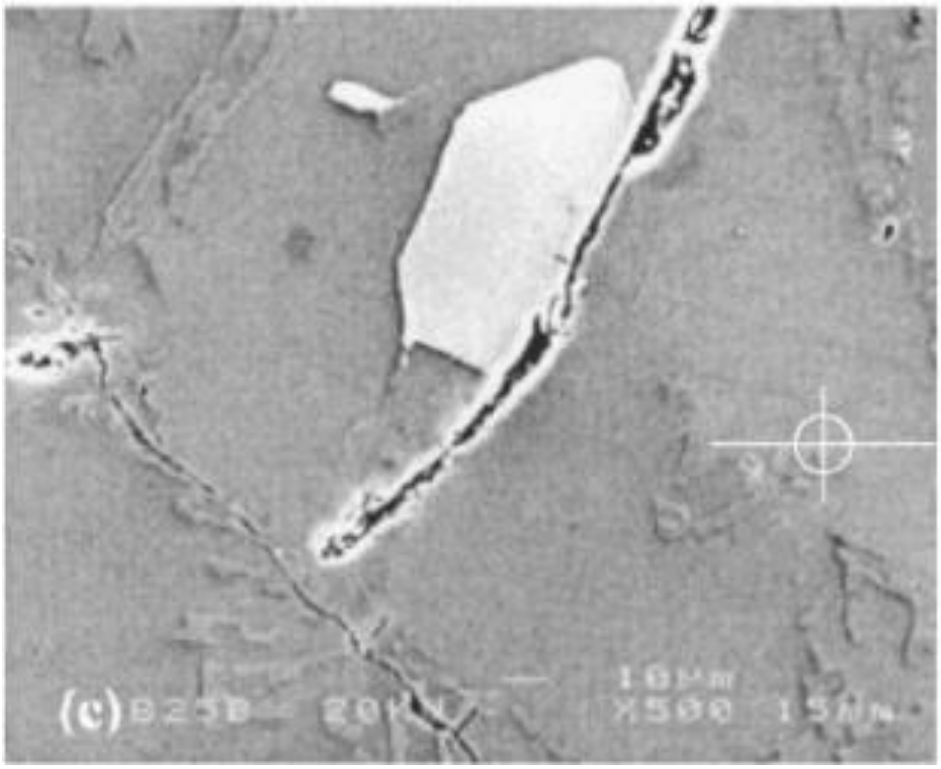

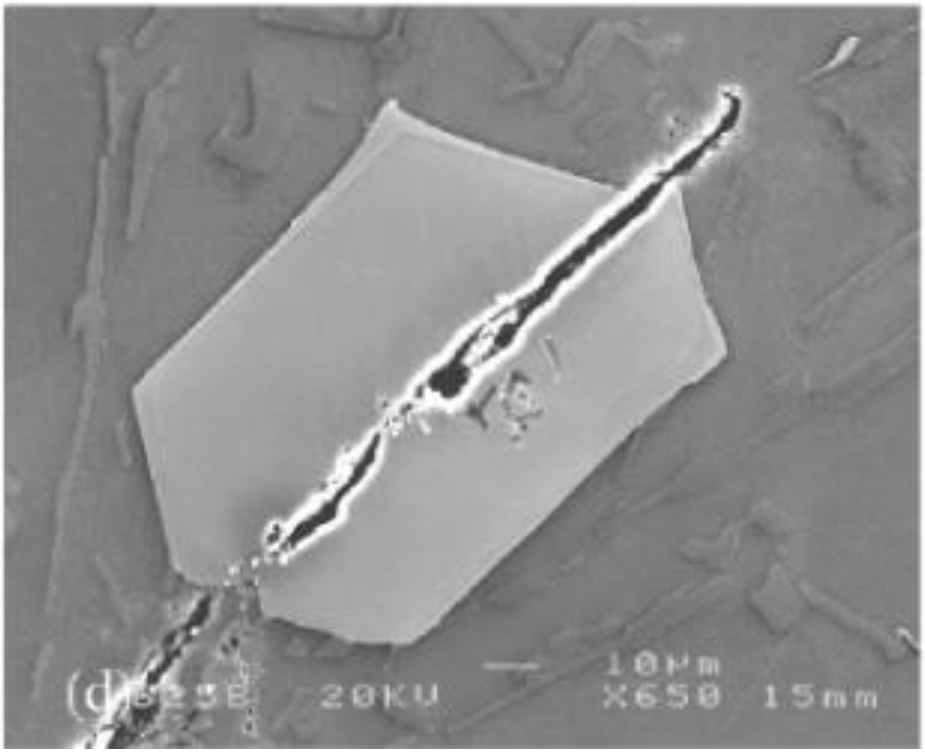

Continued overleaf…

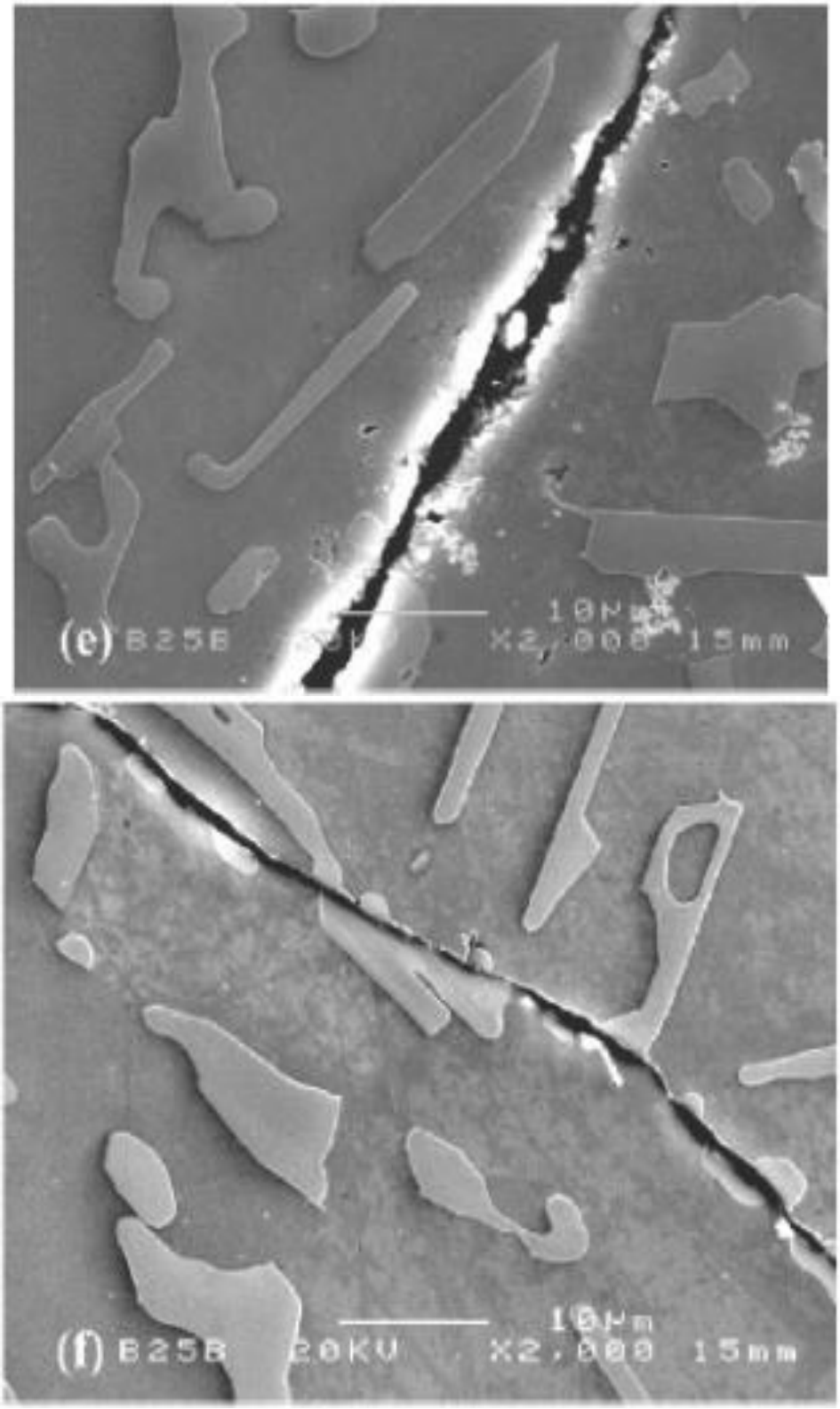

Fig 2.9 Secondary electron images showing association between $Al_{15}(FeMn)_3Si_2$ particles and entrained oxide films **(Cao et al., 03).**

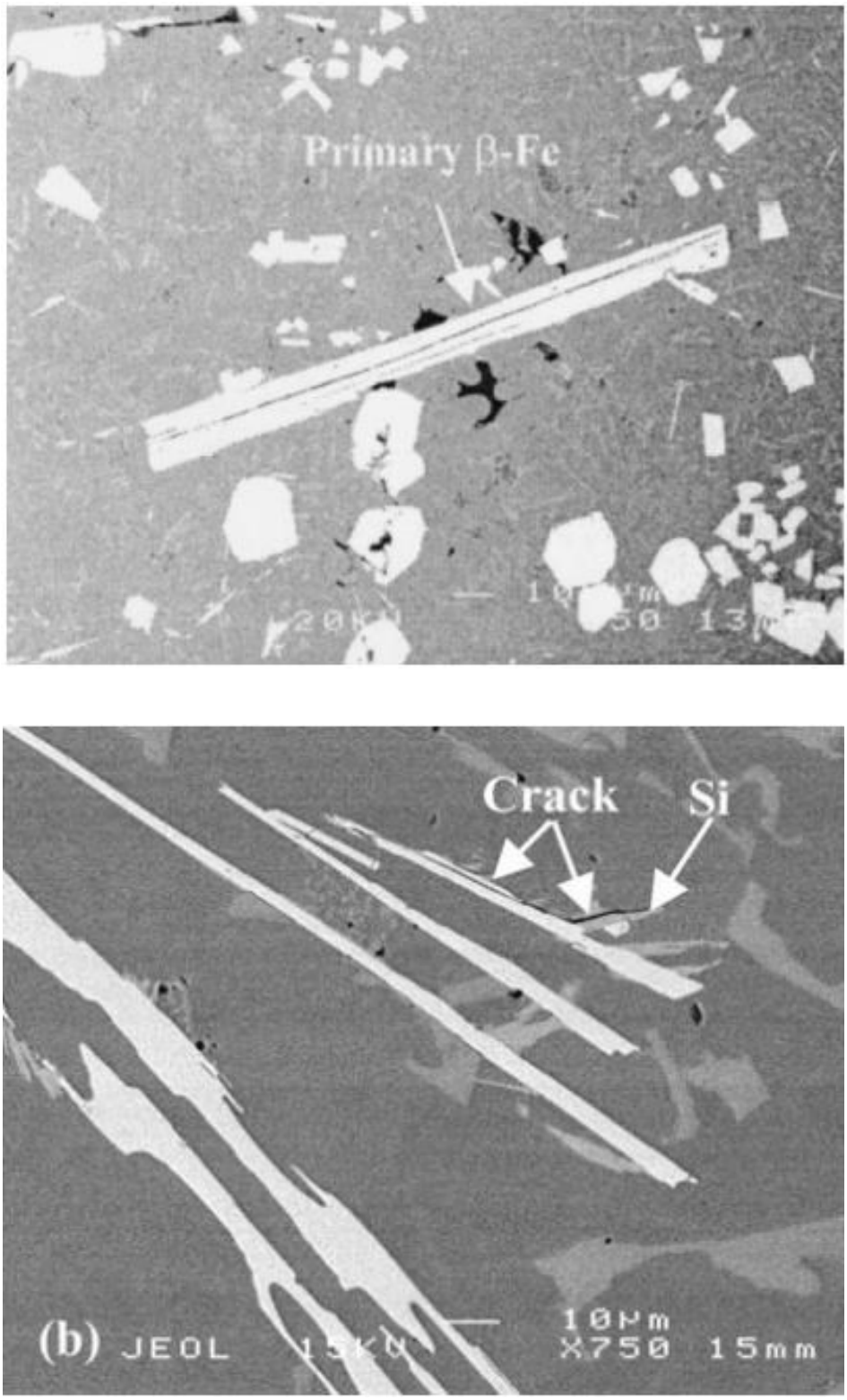

Fig 2.10 Backscattered electron images showing primary β-AlFeSi phase containing cracks **(Cao et al., 03)**.

Fig 2.9 shows the association of α-AlFeSi intermetallic particle with an entrained oxide film. The cracks observed in Fig 2.9 are due to the gap between the dry sides of a double oxide film and are due to a complete lack of bonding between fold planes **(Cao et al., 05)**. Nucleation of intermetallic on the oxide indicates good atomic contact between them. Therefore, the bonding between the outer wetted surface of the oxide and the intermetallic is likely to be strong. Fig 2.10 shows the association of β-AlFeSi phase with the cracks, with cracks propagating through the length of β-AlFeSi platelets **(Cao et al., 03)**. Cao et al. showed that oxide films can be suitable nucleants for α-AlFeSi and β-AlFeSi intermetallics. Fig 2.11 shows how Fe-intermetallics can grow on the surfaces of some typical oxides like α-Al_2O_3 and ϒ-Al_2O_3 present in the 6xxx Al alloys.

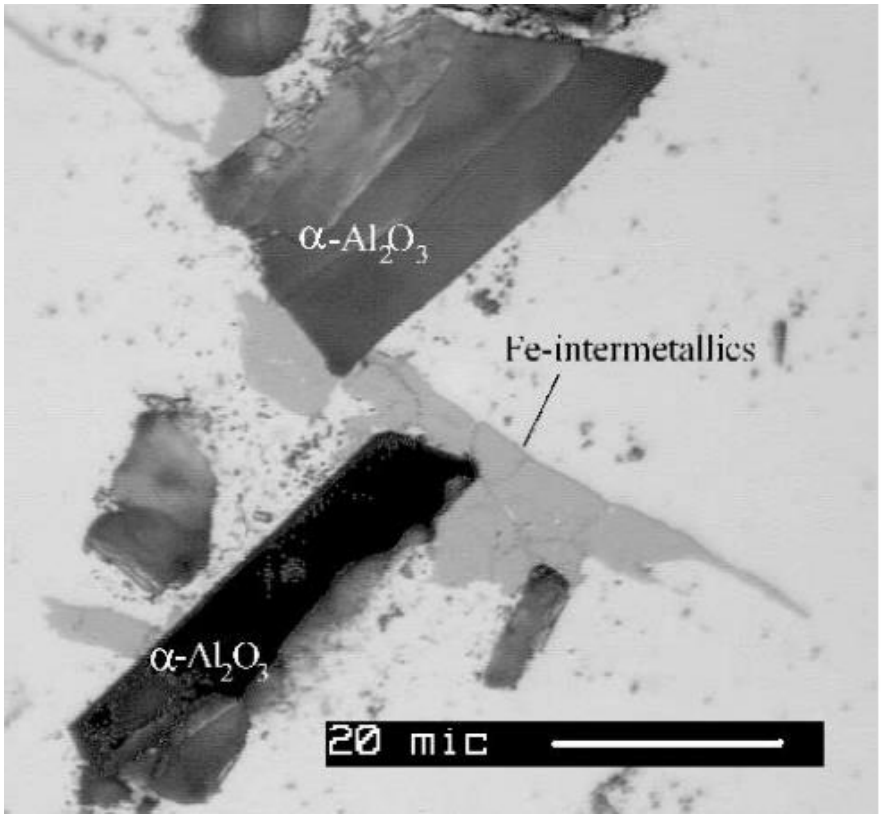

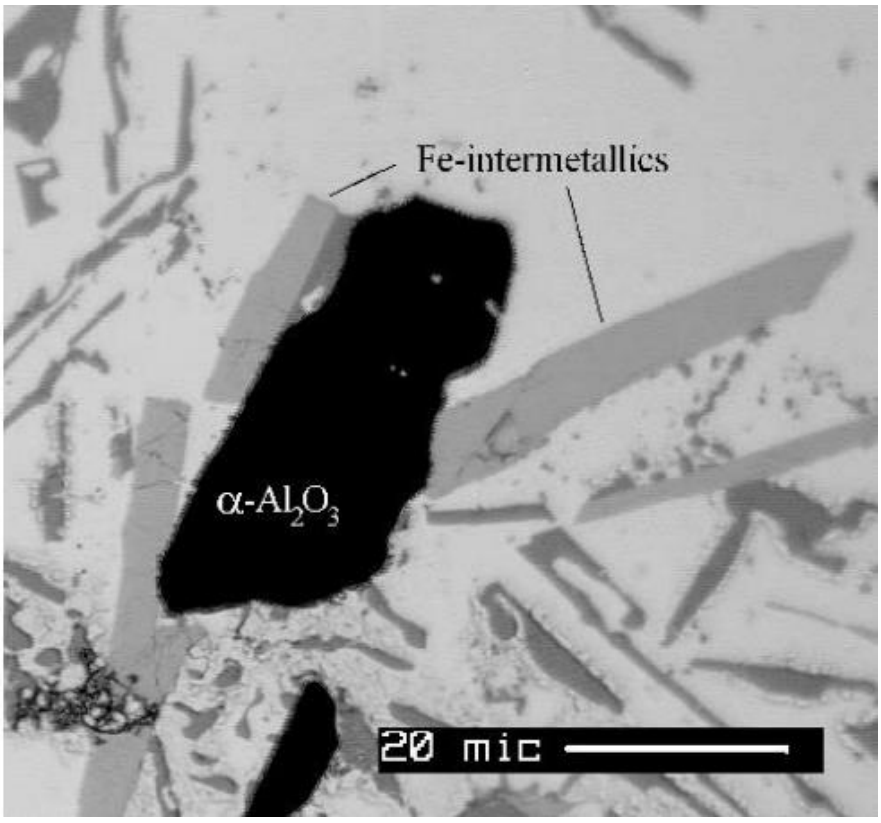

Continued overleaf…

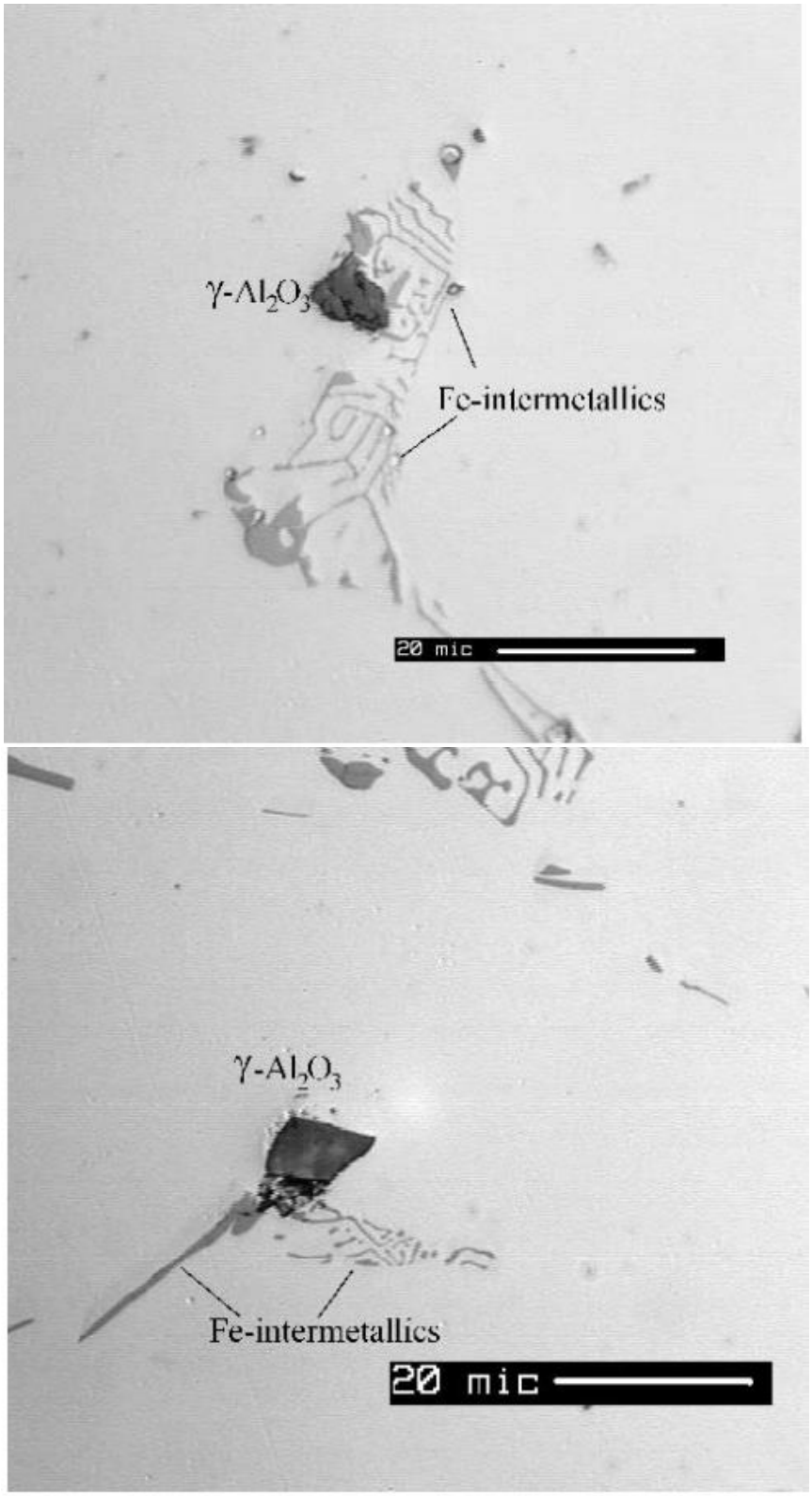

Fig 2.11 Examples of nucleation of Fe intermetallics on the surfaces of ϒ-Al_2O_3 and α-Al_2O_3 **(Khalifa et al., 05)**.

Lattice mismatch between two phases is important in understanding the likelihood of nucleation. Cao **(Cao et al., 03)** analysed the effectiveness of nucleation of α-AlFeSi phase on oxide in 6xxx Al alloys by a parameter called planar disregistry. Planar disregistry (mismatching) is the degree of mismatch between the lattice parameters of low index planes of the nucleated solid (solid lines) and the substrate (dotted lines) as shown in Fig. 2.12.

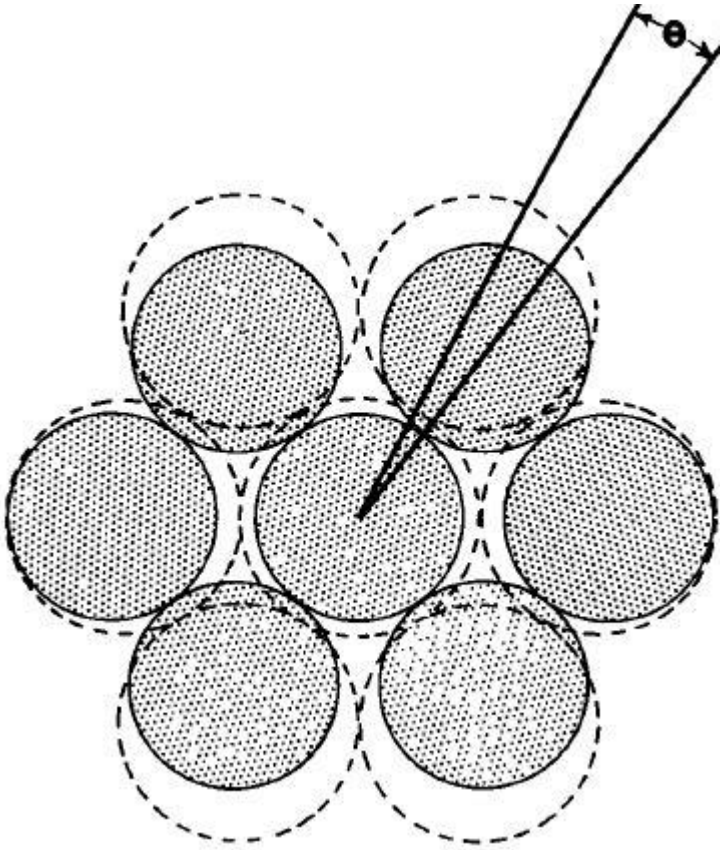

Fig. 2.12 shows the planar mismatch between two planes **(Bramfitt, 70)**

Planar disregistry is given by equation (2.1) assuming that the substrate will remain solid to act as heterogeneous nucleation site **(Bramfitt, 70)**:

$$\delta^{(hkl)_s}_{(hkl)_n} = \sum_{i=1}^{3} \frac{\left|\left(d^{i}_{[uvw]_s} \cos\theta\right) - d^{i}_{[uvw]_n}\right|}{d^{i}_{[uvw]_n}} \times \frac{100}{3} \quad (2.1)$$

Where $(hkl)_s$ = a low-index plane of the substrate,

$[uvw]_s$ = a low-index direction in $(hkl)_s$,

$(hkl)_n$ = a low-index plane in the nucleated solid,

$[uvw]_n$ = a low-index direction in $(hkl)_n$,

$d_{[uvw]n}$ = the interatomic spacing along $[uvw]_n$,

$d_{[uvw]s}$ = the interatomic spacing along $[uvw]_s$ and

θ = the angle between $[uvw]_s$ and $[uvw]_n$.

The value i = 1 to 3 represents the disregistries (δ) calculated along the three lowest indexed directions within a 90^o quadrant of the planes of the nucleated solid and substrate.

Table 2.4 Planar matching (δ < 12%) and mismatching (δ > 12%) between typical oxides and α-AlFeSi phase based on disregistry values calculated by Cao **(Cao et al., 03)**.

Oxide	Oxide plane	Matched α-AlFeSi	Mismatched α-AlFeSi
MgO	(100)	(100) , (111)	(110)
	(110)	(110) , (111)	(100)
	(111)	(111)	(100) , (110)
$MgO.Al_2O3$	(100)	(100) , (111)	(110)
	(110)	(110)	(100) , (111)
	(111)	(110) , (111)	(100)
Υ-Al_2O_3	(100)	(100) , (111)	(110)
	(110)	(110)	(100) , (111)
	(111)	(110) , (111)	(100)
α-Al_2O_3	(0001)	(100) , (111)	(110)
	$(10\bar{1}0)$	----	(100), (110), (111)
	$(\bar{1}101)$	----	(100), (110), (111)

Bramfitt **(Bramfitt, 70)** calculated the planar disregistries for different planes and on comparing them with their characteristic supercooling suggested that if the value of planar disregistry is less than 12% then the nucleating agent may be potent as it achieves the required supercooling. However it is important to note that other factors like interfacial free energy, electrostatic potential between phases and chemical nature of the substrate also play a significant role in heterogeneous nucleation. Table 2.4 shows the potency of different planes in different oxides with respect to the nucleation of α-AlFeSi phase in 6xxx Al alloys **(Cao et al., 03)**.

The oxides present in the alloy were MgO, $MgO.Al_2O_3$ and Υ-Al_2O_3 having face-centred cubic structures and α-Al_2O_3 having a hexagonal structure, whereas α-AlFeSi phase has a body centred cubic structure. Planar disregistries between some oxides (MgO, $MgO.Al_2O_3$, Υ-Al_2O_3 and α-Al_2O_3) and α-AlFeSi indicate that they are potentially good substrates for the nucleation of α-AlFeSi phase **(Cao et al., 03)**.

Table 2.4 shows the planar match and mismatch between different planes of typical oxides found in an Al-11.5Si-0.4Mg alloy and α-AlFeSi phase. Although the disregistry between (111) planes of $MgO.Al_2O_3$ and Υ-Al_2O_3 and (111) planes of α-AlFeSi phase is small, the chances of nucleation and growth of α-AlFeSi phase is poor. This is because the disregistry values for the above mentioned planes were calculated using the multiplicative factor of 2 and 3 and not for a single lattice. This can be visualised as the planes for substrate and nucleating solid (as shown in Fig. 2.12) are repeated twice and thrice and then superimposed on each other to calculate the disregistry. It is then the above calculated low disregistry values would be effective **(Cao et al., 03)**. As the probability of 2 or 3 planes to participate together in the nucleation is low, the low disregistry value is not the true representation of nucleation capability of that particular plane. Bramfitt **(Bramfitt, 70)** suggested other factors such as their interfacial energy, superheat and trace impurities of active elements such as Sr or Na can also affect the nucleation of Fe-rich phases.

2.4.4 Effect of grain refiners

Addition of grain refiner can play an important role in phase selection of an intermetallic. Grain refining is also beneficial for reducing hot cracking tendency **(Spittle et al., 83)**. Studies done previously showed **(Allen et al., 98)** and **(Mckay et al., 00)** that nucleation of Fe-rich intermetallic phases was enhanced with the addition of Al-Ti-B grain refiners, as it changes the solidification conditions thereby stabilising one phase over other **(Allen et al., 98)**. The addition of Al-Ti-B grain refiner (containing TiB_2) to different wrought Al alloys, containing Fe and Si, promoted the nucleation α-AlFeSi in Al-0.2Fe-0.1Si **(Maggs et al., 95)** and other phases. Fig 2.13 shows the association of TiB_2 with α-AlFeSi intermetallic phase.

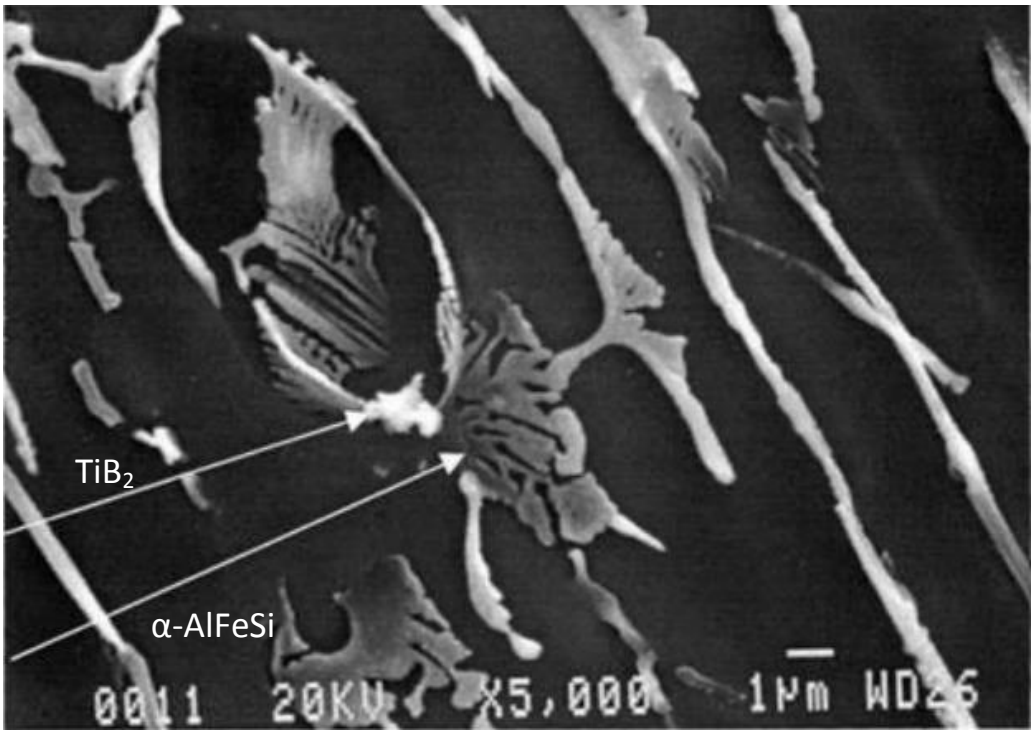

Fig 2.13 TiB_2 particles associated with α-AlFeSi particles **(Merdith et al., 99)**.

Favourable crystallographic orientation was considered to be the most important parameter for the nucleation of intermetallic on a substrate. However, Khalifa **(Khalifa et al., 05)** suggested that the effect of nucleation temperature is much more significant than crystallographic fit for competitive nucleation between any two phases in 6xxx alloys. In 6xxx Al alloys TiC and Al_4C_3 particles have also been observed to be potent nucleants for α-AlFeSi and δ-AlFeSi as shown in Fig. 2.14 **(Khalifa et al., 05)**.

Low lattice mismatch between hexagonal TiB_2 particles and cubic α-AlFeSi and Al_mFe has also been observed **(Maggs et al., 95)**. In addition, a number of orientation relationships have been found between TiB_2 and β-AlFeSi **(Sha, 01)**:

$$[100]_{TiB2} // [010]_{\beta\text{-AlFeSi}}$$

$$(100)_{TiB2} // (001)_{\beta\text{-AlFeSi}}$$

$$(010)_{TiB2} // (001)_{\beta\text{-AlFeSi}}$$

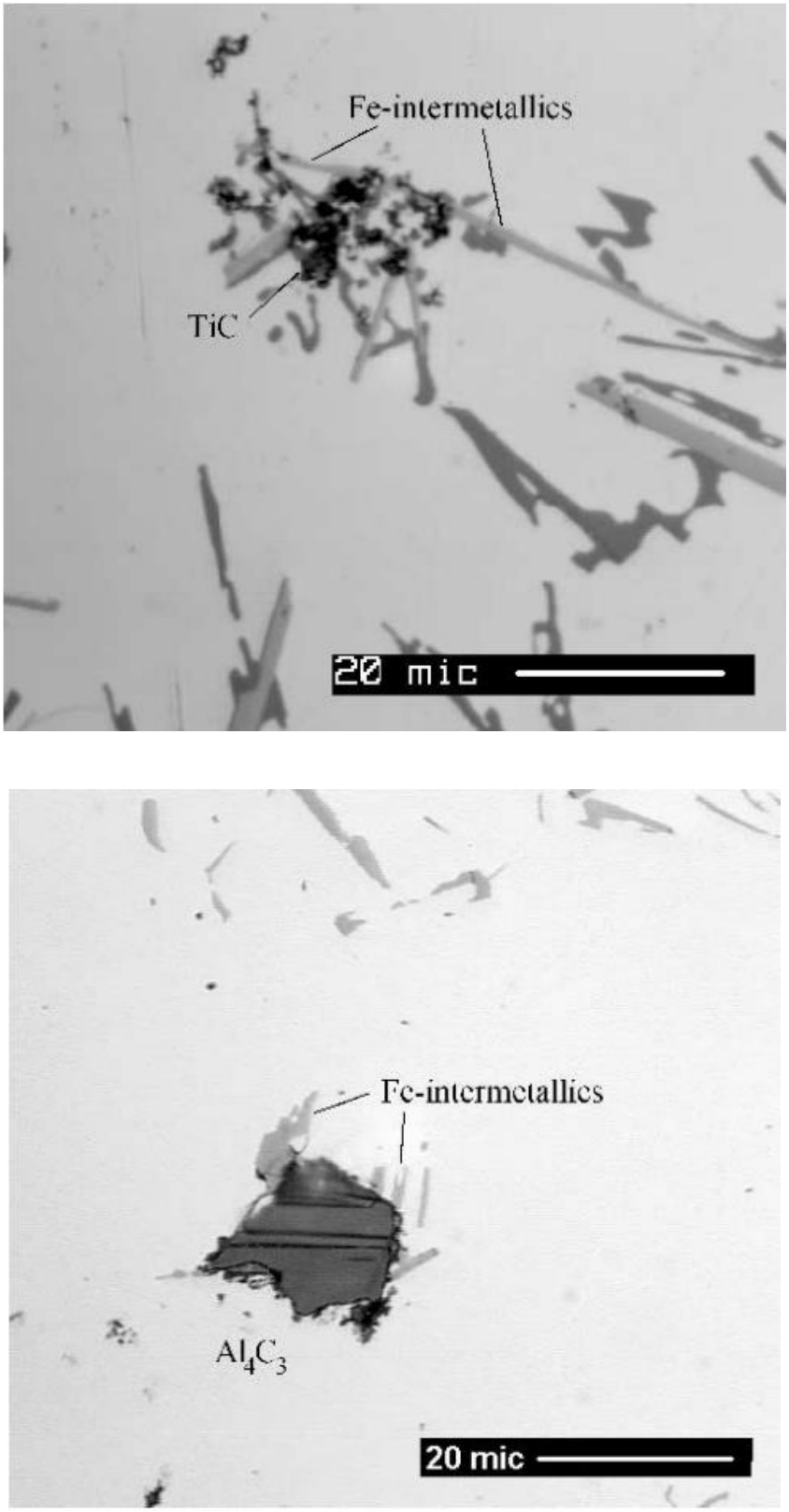

Fig 2.14 TiC and Al_4C_3 particles acting as potential nucleation sites for the formation of Fe-intermetallics **(Khalifa et al., 05)**.

To summarise, grain refiners significantly affect the phase selection of the intermetallics. However, in some cases the intermetallics remained invariant even on addition of grain refiner **(Merdith et al., 99)**. It is still not clear whether all the TiB_2 particles take part in the nucleation process or not.

2.5 Homogenisation

Homogenisation is the process of heating the as-cast Al-Mg-Si billets to a particular temperature, holding at that temperature for a certain amount of time and then cooling in order to make them extrusion favourable **(Veki et al., 85)**. Homogenisation greatly affects the intermetallic phases and hence the extrusion properties of the material, which is discussed in the subsequent sections.

2.5.1 Advantages of homogenisation

The as cast materials possess a number of inhomogeneities such as microsegregation, grain boundary segregation, supersaturated solutions of alloying components etc **(Laue et al., 76)**. Homogenisation helps to avoid cracking or tearing during hot working by removing non-equilibrium low melting point eutectics, particles and segregation gradients **(Samaras et al., 07)** and to uniformly distribute the alloying elements in solid solution **(Dons, 01)**. The advantages of homogenisation process are:

- dissolve the coarse Mg_2Si located at grain boundaries into the solution and avoids speed cracking during extrusion which could otherwise only be avoided by reducing extrusion speed (reducing productivity) **(Zajac et al., 96)**.
- eliminate micro-segregation which result in uniform local chemical composition and phase formation behaviour (see section 2.3.2 for more details) **(Dons, 01).**

- transform as-cast β-AlFeSi to α-AlFeSi (section 2.5.4) which improves the surface quality of the extruded product by eliminating surface defect like 'pick up'**(Kuijpers et al., 03)**.
- helps in the precipitation of fine dispersoids containing elements like Mn and Cr in structural alloys which otherwise are super saturated in as-cast state. This also improves the toughness of the alloy **(Zajac et al., 02)**.
- controlled cooling during homogenisation allows the Mg and Si in the solution to re-precipitate in the form of fine Mg_2Si **(Birol, 04)**. This is because faster cooling will lead to all the Mg and Si in the solution which will increase the extrusion pressure, whereas slower cooling will form large Mg_2Si particles which will result in precipitation hardening. Thus the size of the Mg_2Si formed during controlled cooling is chosen such that it dissolves during the heat generated during extrusion process to minimize extrusion pressure.

2.5.2 Process

The most important parameters for the homogenisation process are time and temperature. However, the microstructural evolved during the homogenisation treatment of Al alloys also depends on the distribution and geometry of the intermetallic phases, and alloy composition as the degree of homogenisation is governed by diffusion of alloying elements and initial matrix concentration profiles of the alloying elements **(Vermolen et al., 98)**.

The homogenization temperature should not exceed the melting point of the lowest melting point phase in the alloy as it is necessary to avoid local melting which may lead to the formation of voids, segregation, swelling of the surface, and cracks, which cannot be removed **(Zajac et al., 02)**. For 6xxx Al alloys, the temperature for homogenisation is in the range 550^{o}C to 590^{o}C and the time for homogenisation is kept between 4 hours and 6 hours **(Grazyna et al., 05)**. Also, step-cooling to 250-300^{o}C for 2h for 6063 alloys is the other option available apart from continuous cooling **(Birol, 04),** however it might be inconvenient to implement.

2.5.3 Effect of homogenisation on intermetallic phases and properties

One of the purposes of the homogenisation process is to remove microsegregation and to improve surface quality of extruded product by eliminating surface defects like 'pick up'. During homogenisation of most of the 6xxx Al alloys, a phase transformation takes place i.e. acicular β–Al_5FeSi to cubic rounded α-AlFeSi (α_c-AlFeSi / Al_8Fe_2Si) **(Kuijpers et al., 03)** and **(Zajac et al., 96)**. These intermetallics and the interconnectivity between them are deleterious for the mechanical and surface properties of the extruded alloy **(Narayan et al., 95)** and **(Kumar et al., 14)**. This improves the extrudability of the alloy as β-AlFeSi particles can induce surface defects and initiate local cracks **(Kuijpers et al., 05)**.

In addition to the phase transformation, homogenisation also reduces the interconnectivity of the intermetallics (as shown in Fig. 2.15), which is more favourable for extrusion **(Tanihata et al., 99), (Kuijpers et al., 02a)** and **(Griger et al., 96)**. Recently it was observed that homogenisation breaks interconnected networks and modifies the secondary phases to a more equiaxed morphology which result in more successful downstream deformation processing **(Kumar et al., 14)**. This is because the elongated intermetallic particles tend to become smaller and globular during homogenisation to minimize their surface area per unit volume and thus to minimize their surface energy.

The homogenised alloy has improved ductility from the spherodised morphology of the α-AlFeSi intermetallic phase as the chance of inducing micro-cracks is reduced compared to the planar β-AlFeSi intermetallic phase. Addition of a small amount of Mn to alloys significantly accelerates the homogenisation process **(Zajac et al., 94)**. Reduced levels of solute (Fe and Si) in the Al solid solution were found in a homogenised alloy as compared to a non-homogenised alloy **(Birol, 08)**.

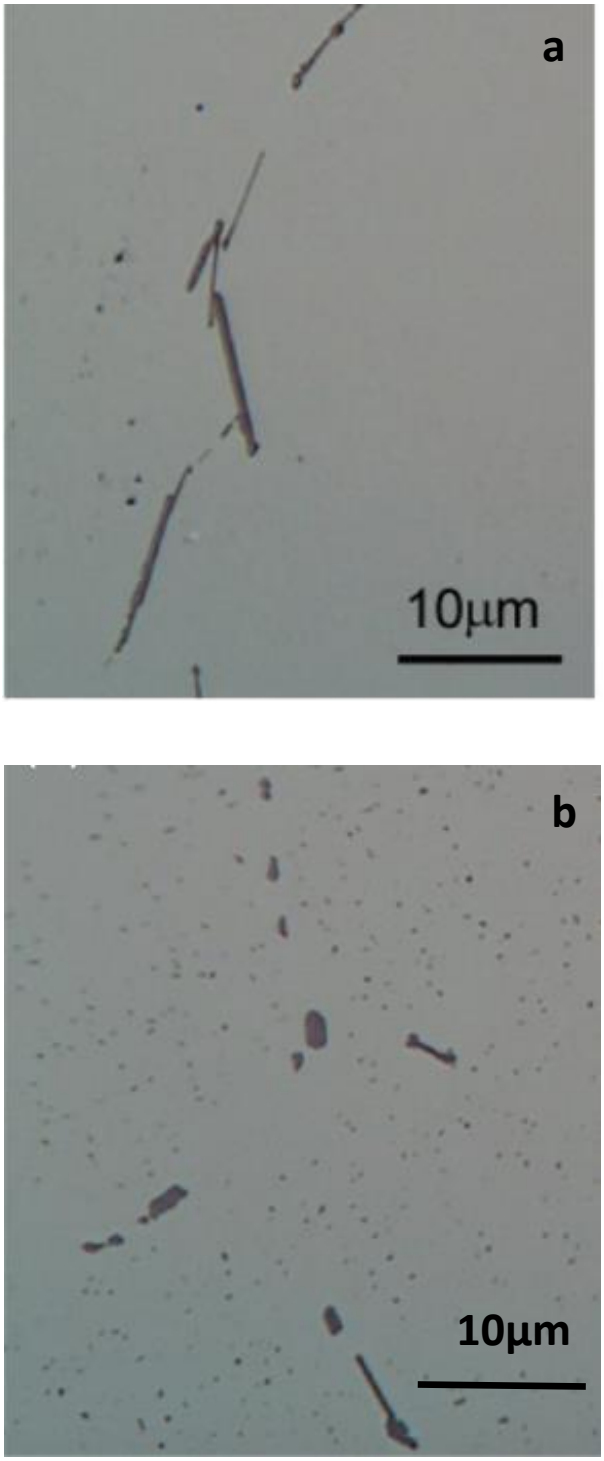

Fig 2.15 The β-AlFeSi to α-AlFeSi transformation in an Al-Mg-Si alloy (AA 6005A). (a) β-AlFeSi particles in the as-cast state (b) transformed α-AlFeSi particles after homogenisation **(Kuijpers et al., 03)**.

Apart from the dramatic effect on Fe rich intermetallic phases (particularly α-AlFeSi and β-AlFeSi), homogenisation also effects other phases to a great extent. In the process of homogenization the supersaturated solid solution decomposes **(Zajac et al., 02)**. Homogenisation leads to the dissolution of the coarse Mg_2Si particles during holding at high temperature **(Zajac et al., 96)**. This dissolution is very advantageous for the extruded product as it gives out maximum age hardening potential **(Kuijpers et al., 02)** and **(Kuijpers et al., 03)**.

The retained Mg and Si (which is not a part of Fe-intermetallic or Mg_2Si) increases the flow stress of the billet material, retards recrystallization and causes problem for the extrusion die by increasing the stress level on the die **(Akhtar et al., 09)**. Controlled cooling during homogenisation provides re-precipitation of the dissolved phases and lower flow stress, without forming coarse and stable Mg_2Si particles which are very difficult to solutionize during subsequent heating processes **(Birol, 04).** Also, Mg_2Si dispersoid free zones are formed in precipitation hardened alloys along grain boundaries after homogenization **(Lorimer et al., 66)**. Homogenised billets were found to have higher tensile strength than non-homogenised billets due to finely dispersed Mg_2Si precipitates **(Kuijpers et al., 05)**.

2.5.4 Transformation of β-AlFeSi to α-AlFeSi during homogenisation

One of the main purposes of homogenisation is to transform needle-like β-AlFeSi (Al_5FeSi) particles to spheroidal shaped α-AlFeSi (Al_8Fe_2Si) particles, as it improves the ductility of the material and leads to a reduction in pickup defects on the extruded surface **(Zajac et al., 96)**. A number of investigations have been carried out on how the fraction of β-AlFeSi to α-AlFeSi transformation varies as a function of time and temperature. Table 2.5 **(Kuijpers et al., 02b**) shows the fraction of α-AlFeSi formed with respect to time and temperature of homogenisation process. It can be concluded that the time required to partially transform β-AlFeSi to α-AlFeSi at a lower temperature of homogenisation (~540^oC) is much longer than the time required for the complete transformation of β-AlFeSi to α-AlFeSi at a higher temperature (~590^oC).

Zajac **(Zajac et al., 96)** observed that α-AlFeSi particles nucleate on β-AlFeSi particle boundaries and gradually replace them. Birol **(Birol, 98)** observed that Si concentration was higher in the matrix after the homogenisation process and this increase in Si concentration could be attributed to the dissolution of the Mg_2Si phase and the transformation of β-AlFeSi to α-AlFeSi which is given by reaction (1).

$$2\beta\text{-}Al_5FeSi \rightarrow \alpha\text{-}Al_8Fe_2Si + [Si]Al + 2Al \quad (1)$$

where, [Si]Al is Si in solution in the Al matrix.

In the early stages of the transformation β-AlFeSi is mainly in the plate-like structure and α-AlFeSi was observed to nucleate on the top and on the rim of β-AlFeSi plates **(Lodgaard et al., 00)**. The phase transformation may occur via peritectoid reaction of the β-AlFeSi intermetallic particles and the aluminium matrix to give α-AlFeSi intermetallic particles **(Birol, 03)**. The instabilities caused by differences in chemical potential at the boundary may cause morphological changes in the intermetallics i.e. coarsening and spheroidisation **(Grazyna et al., 05)**.

Table 2.5 The conditions and fraction transformed from β-AlFeSi to α-AlFeSi for a 6005A Al alloy **(Kuijpers et al., 02b)**.

Homogenisation time (min)	0	30	480	60	1920	1920
Temperature of Homogenisation (^{o}C)	none	540	540	590	540	590
Fraction of α-AlFeSi (%)	5	20	50	80	80	100

2.6 Melt Conditioning/Shearing

Melt conditioning is a laboratory technique of conditioning the alloy melt before solidification processing. The most common way for melt conditioning is by intensive shearing of the liquid melt **(Fan et al., 09a)**. A number of other methods such as ultra-sonication **(Eskin, 08)** electromagnetic stirring **(Gabathuler et al., 92)** and hydrodynamic stirring **(Vives, 92)** have also been suggested for conditioning the liquid.

2.6.1 Process and Advantages

For conditioning the alloy melt, liquid metal is commonly fed into a twin screw machine, in which a pair of rotating and intermeshing screws is rotated inside a heated barrel with temperature control, as shown schematically on Fig 2.16 **(Scamans et al., 09)** and Fig 2.17 **(Haghayeghi et al., 10)**. There is a large interfacial area between the melt, the screws and the barrel, ensuring efficient heat transfer that provide uniform temperature throughout the melt. However it is important to note that molten aluminium is sheared using graphite based or molybdenum disilicide coated rotary devices to stop any reaction with molten aluminium or to avoid contamination.

The operating temperature can be above the alloy liquidus for conditioning liquid or below the alloy liquidus for semisolid slurries **(Haghayeghi et al., 10)**. The melt undergoes a high shear rate and high amount of turbulence and can then be poured into a high pressure die casting (HPDC) or in a DC casting unit

(Barekar et al., 09) & (Fan et al., 09a & 9b). It can either work as a continuous process or as a batch process depending on the requirement of the casting industry.

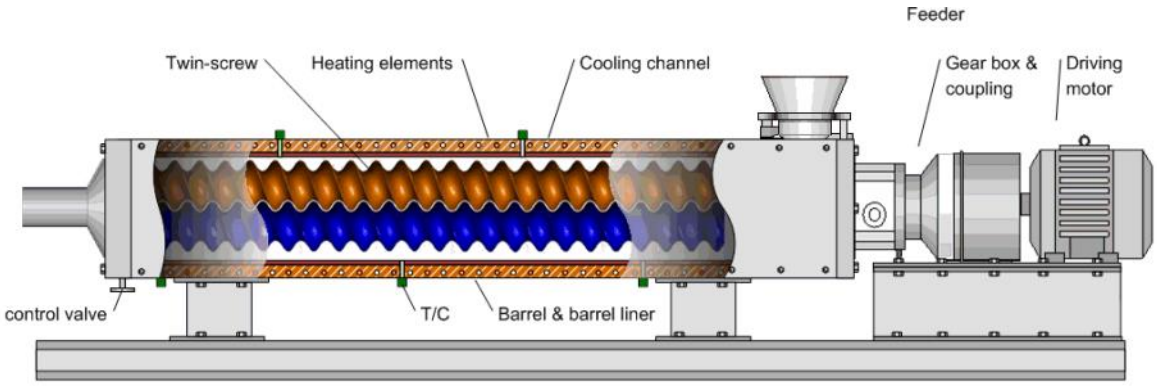

Fig 2.16 Schematic of melt conditioning by advance shear technology **(Scamans et al., 09)**.

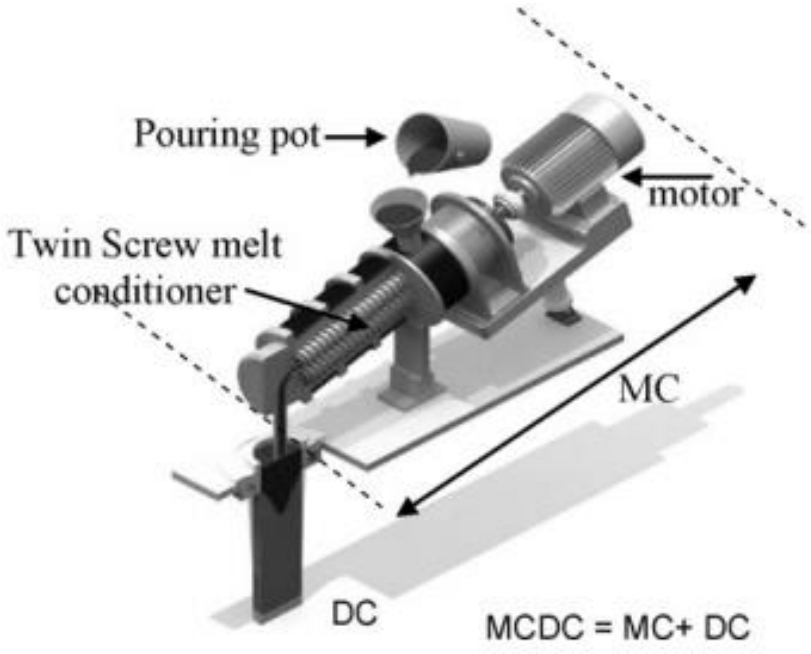

Fig 2.17 Schematic of the melt conditioning DC casting process **(Haghayeghi et al., 10)**.

Fan **(Fan et al., 09b)** showed that melt conditioning has many advantages over conventional casting without introducing any adverse effects on downstream processing for eg. increased tolerance for impurities like Fe. It provides uniform microstructure throughout the ingot, solves the problems of columnar grains and macrosegregation and helps in reducing the volume fraction and size of porosity **(Turchin et al., 05)**. The intensive melt shearing promotes nuclei formation throughout the liquid and enhances their participation capability in refinement, whereas in conventional casting the nuclei formed might remelt/dissolve if transferred to high temperature region **(Fan et al., 09b)**.

It has a number of advantages over conventional DC casting. Since the liquid is not poured at high temperature, thermal stresses are reduced. Also, due to lower viscosity in the melt conditioning process, the melt flows more smoothly and the problems of segregation and columnar grains are reduced **(Turchin et al., 05)**. Melt shearing also has a degassing effect on the melt, as it drives out H_2 from Al alloys with the help of argon gas **(Zuo et al., 11)**. The final microstructure was free from defect bands and porosity, which lead to better mechanical properties in Mg alloys **(Tzamtzis et al., 10)**.

2.6.2 Control of intermetallics by melt conditioning

Melt conditioning can greatly affect the formation of the intermetallic particles. Fan **(Fan et al., 09a)** showed that melt shearing of the Mg alloy AZ91D (9% Al, 0.15% Mn, 0.5% Zn, 0.1% Si, balance Mg) results in grain refinement of the primary α-Mg and Al_8Mn_5 intermetallic particles. Fang **(Fang et al., 07)** showed that melt conditioning of LM24 (8% Si, 3.5% Cu, 3% Zn, 3% Mg, 1% Fe, 0.5% Mn, 0.5% Ni, balance Al) and LM25 (7% Si, 0.1% Cu, 0.4% Mg, 0.5 Fe, 0.3% Mn balance Al) alloys with the help of intensive shearing before solidification, promotes the formation of α-AlFeSi compound with a compact morphology. It has also been shown that intensive shearing of LM24 and LM25 also plays an effective role in spheriodising the primary α-Al phase, reducing the formation of dendritic microstructures and promoting the formation of equiaxed α-AlFeSi intermetallic phase **(Fang et al., 07)**. This could also be attributed to uniform composition throughout the sample due to high turbulent mixing.

Melt conditioning also hinders the formation of faceted features, detrimental to the material properties. Melt shearing reduces the aspect ratio of β-AlFeSi, enhancing the formation of short bars rather than long needles i.e. reducing the aspect ratio **(Fan et al., 09a)**. The process breaks up clusters of oxide inclusions into fine particles and disperses them uniformly with the help of forced convection **(Haghayeghi et al., 10)**. These fine particles are then believed to act as potent nucleating sites for intermetallic phases or primary α-Al phase, which is discussed in the subsequent section.

2.6.3 Effect on inclusions

Recycling of Al is a very big industry and recycled Al always have impurities and inclusions. Oxide inclusions enter the material during melt preparation and the filling process **(Miller et al., 06)**. Presence of oxide inclusions can influence the castability of the material, affects the quantity of defects and hence the mechanical properties of the material **(Dai et al., 03)**. When a liquid melt is subjected to intensive shearing and turbulence during melt conditioning, the clusters and oxide films are broken into fine particles with a narrow size distribution. These fine oxide particles present in the melt are completely wetted and uniformly distributed in the melt with the help of forced convection, and hence can then act as potent sites for heterogeneous nucleation of primary phase or intermetallic phases **(Fan et al., 09a)**.

2.7 Characterisation and quantification techniques for intermetallic phases

A number of intermetallic phases form during the non-equilibrium solidification of 6xxx Al alloys, the important ones being α-AlFeSi and β-AlFeSi phase. For some 6xxx Al alloys, during the homogenisation process β-AlFeSi phase transforms to α-AlFeSi phase, and so there is a need to calculate the volume fraction transformed. There are a number of ways such as optical microscopy **(Valle et al., 98)** (OM), scanning electron microscopy (SEM) along with energy dispersive spectroscopy **(Nilsen et al., 00)** and **(Alexander et al., 02)** (EDS), transmission electron microscopy (TEM), x-ray diffraction **(Sha et al., 00)** and **(Minoda et al., 98)** (XRD), focused ion beam (FIB), electron back scattered diffraction (EBSD) and X-ray synchrotron for characterising and quantifying these phases.

2.7.1 Optical Microscopy (OM)

The simplest way of characterising the intermetallic phases is OM. OM gives a good idea about the distribution and connectivity of the intermetallic phases in the material. The 2D morphology of β-AlFeSi phase is needle-like (as shown by red arrows in Fig 2.18 a) **(Paray et al., 96)** and that of α-AlFeSi is Chinese script (as shown by black arrows in Fig 2.18 b) **(Paray et al., 96)**. In OM the morphology of the particles (aspect ratio R) is the primary criterion used to distinguish α-AlFeSi and β-AlFeSi phase, which is not reliable. It is also used to give an idea about the changes in the 2D microstructure after homogenisation as

shown previously in Fig 2.15. Quantification of intermetallic phases can only be carried out using their differences in grey scale with the matrix i.e. the Al matrix appears very light grey, whereas the intermetallic phases are dark grey in the micrograph.

However, this information is not very reliable and cannot accurately differentiate intermetallic phases due to their similar grey levels **(Kuijpers et al., 03)**. Moreover, information obtained from OM is incomplete as it gives only 2D information about the intermetallic particles, and not 3D. It cannot show the 3D morphology and connectivity of the intermetallic particles.

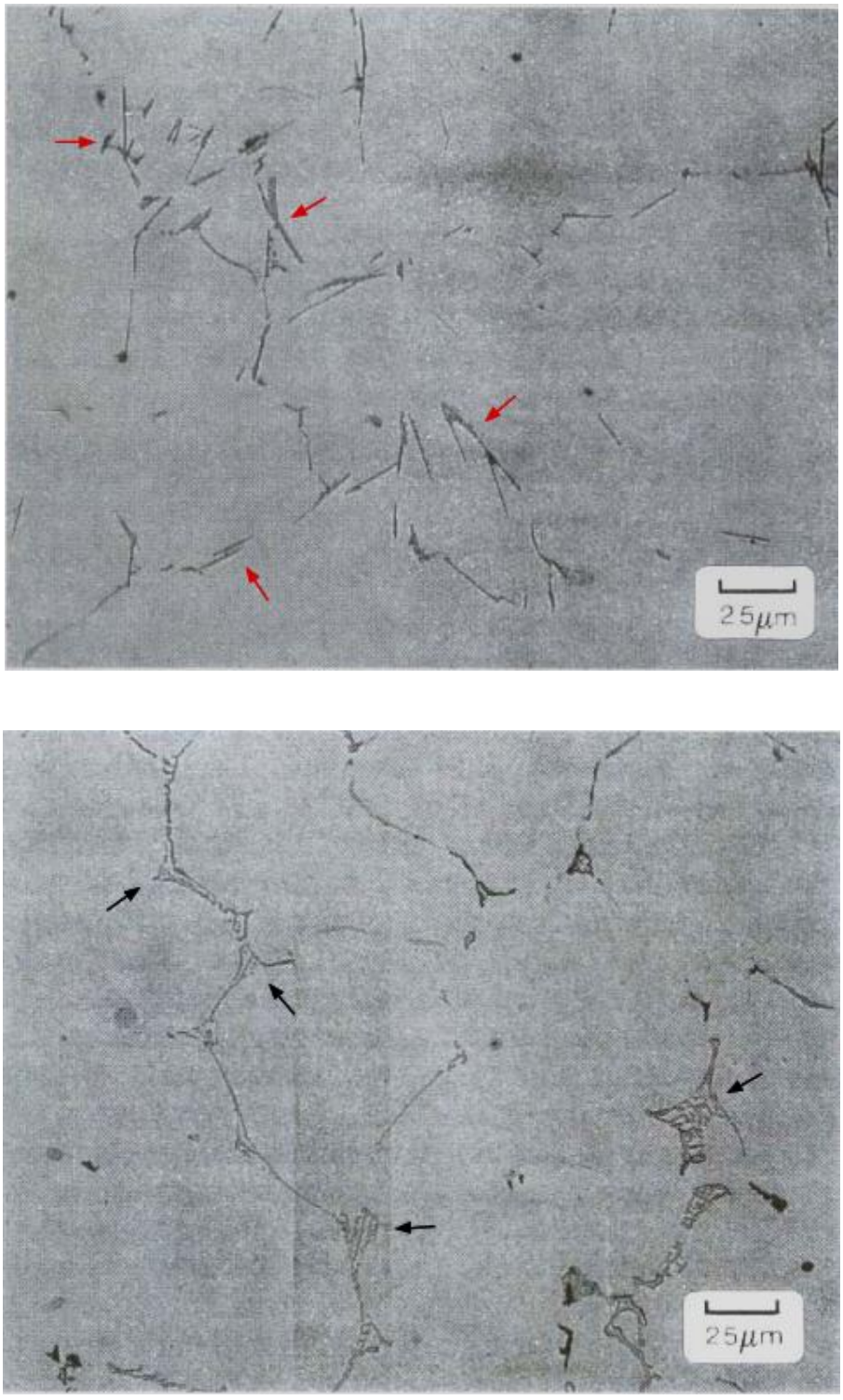

Fig 2.18 Optical micrographs of 6xxx Al alloy a) red arrows showing needle-like morphology of β-AlFeSi phase b) black arrows showing chinese script morphology of α-AlFeSi phase **(Paray et al., 96)**.

2.7.2 Scanning electron microscopy (SEM)

SEM has proven to be an effective way to characterise and differentiate intermetallic phases.

2.7.2.1 2D analysis

2D refers to the microstructure observed in normal samples along x and y axis only. SEM gives similar information on the 2D distribution of intermetallic particles in the matrix to OM but with better quality. Higher resolution images can be obtained in SEM as compared to OM. But similar to OM, 2D characterisation does not gives a complete picture regarding the orientation and connectivity of intermetallic particles **(Kuijpers et al., 02b)**.

2.7.2.2 3D analysis

3D refers to the microstructure observed in extracted intermetallic samples (section 3.5) along x, y and z axis. SEM gives a clear picture of 3D morphology and connectivity of different intermetallic phases. For differentiation purposes only the particle morphological features are used. However, Kuijpers **(Kuijpers et al., 03)** showed that SEM with EDS is a better technique for the quantification of intermetallic phases. It has also been shown **(Kuijpers et al., 03)** that the ratio (Mn+Fe)/Si (α-AlFeSi ~3 and β-AlFeSi ~1) is one of the most important parameters for accurately calculating relative fraction transformed. SEM alone cannot give any compositional analysis; it has to be combined with EDS in order to get more accurate differentiation of intermetallic phases **(Kuijpers et al., 02b)**.

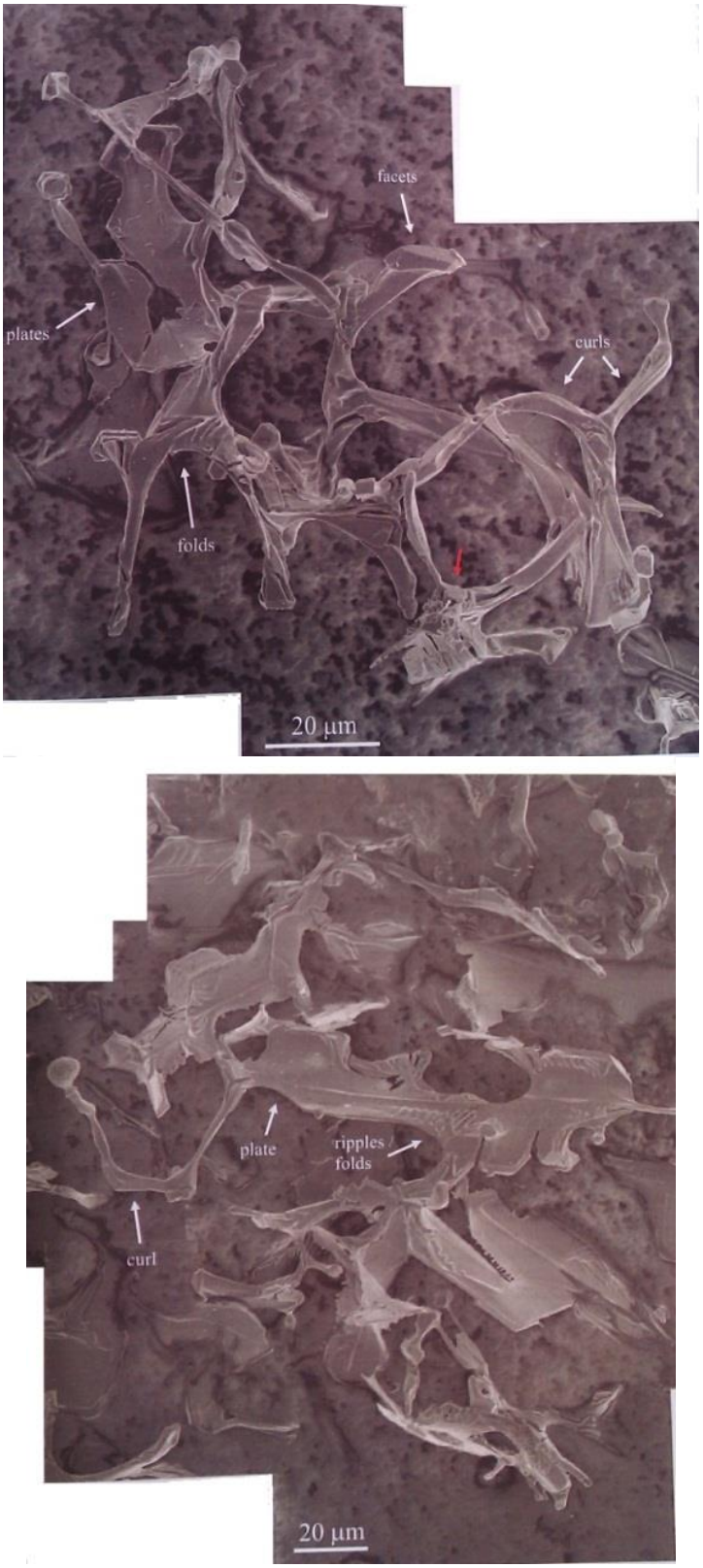

Fig 2.19 Montage SEM images of extracted intermetallic particles from as DC cast Al billet **(Lui, 05)**.

Fig 2.19 shows the connectivity and 3D morphology of intermetallic particles. However, SEM has some limitations. It cannot quantify the fraction of different intermetallic phases present in the alloy.

2.7.3 X-ray diffraction (XRD)

XRD cannot be used to quantify the amounts of intermetallic phases present in bulk samples as the intermetallics are usually present in volume fractions below the detection limit of this technique. Hence for XRD analysis, intermetallic particles are extracted from the material matrix, XRD patterns generated from the extracted intermetallics are compared with the JCPDS and XRD patterns in the literature. For example Fig. 2.20a and Fig. 2.20b shows the XRD patterns from extracted intermetallics and the reference XRD patterns for α-AlFeSi and β-AlFeSi used by Lui **(Lui, 05)**. The intensities of different peaks are measured and can be used to quantify the different phases with the help of a regression curve generated using samples of known identity on a specific XRD machine, which is a machine specific equation **(Sha, 01)**. Please refer to section 3.6.4 for more details on regression curve and Appendix I for XRD reference patterns used for the current study. XRD is one of the best techniques for quantification of different intermetallic phases, but it cannot provide morphological information.

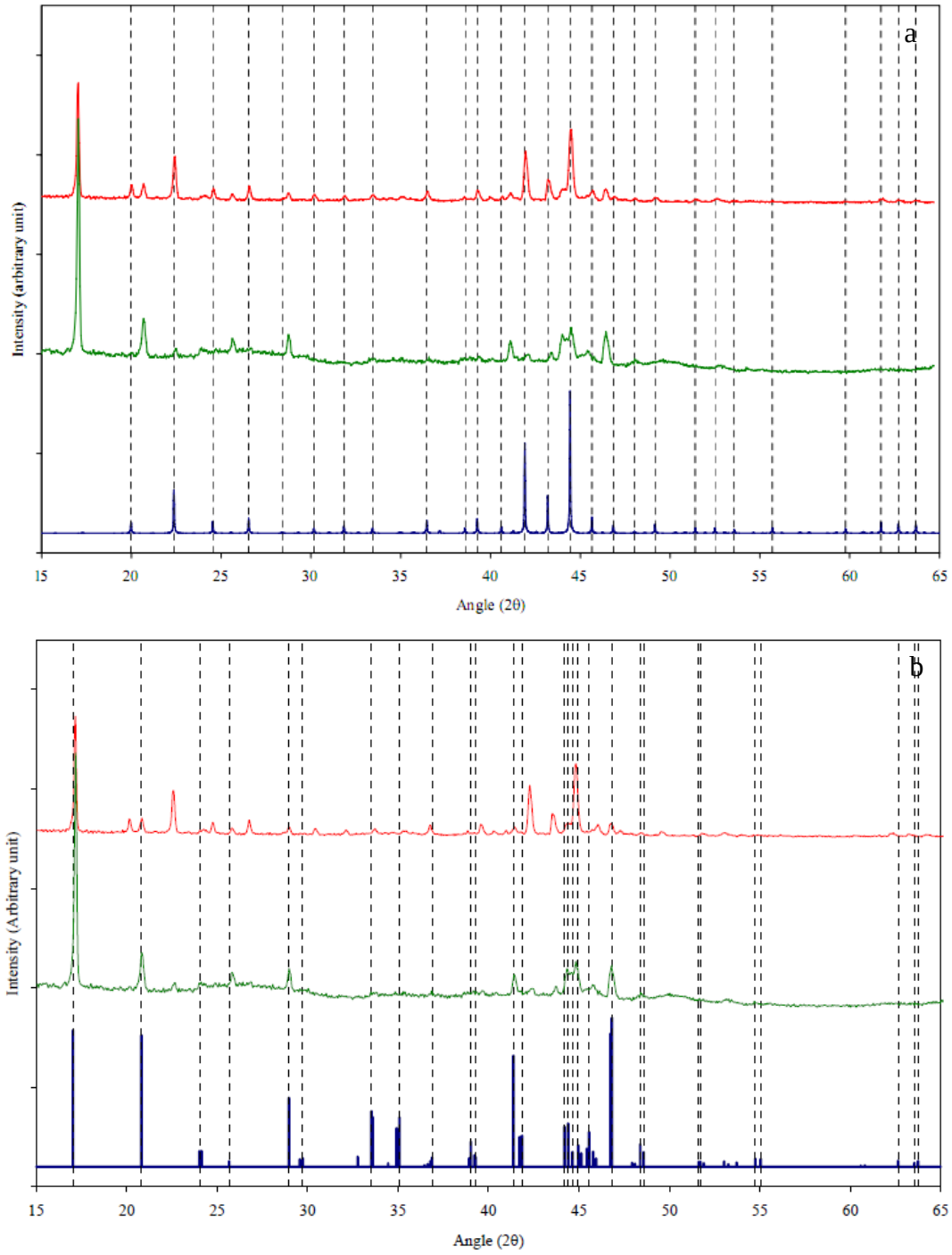

Fig 2.20 Two XRD diffraction patterns (red and green) from the extracted intermetallics and compared with reference pattern (blue) for a) α-AlFeSi and b) β-AlFeSi **(Lui, 05)**.

2.7.4 Focused ion beam (FIB)

FIB is used for quantification and examining the 3D morphology of the intermetallic particles.

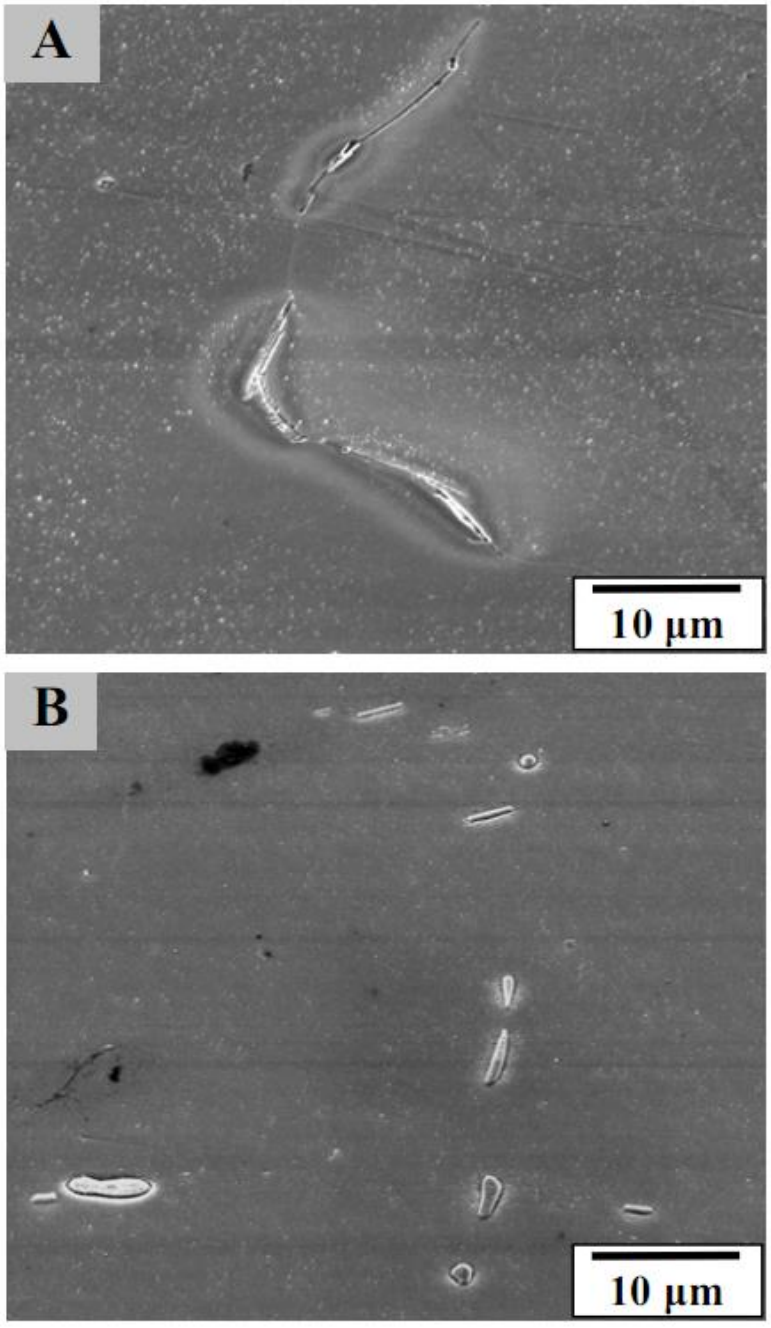

Fig. 2.21 SEM images **(Claves et al., 04b)** of features of interest at surface. A) β-$Al_9Fe_2Si_2$ and B) α_c-Al_8Fe_2Si.

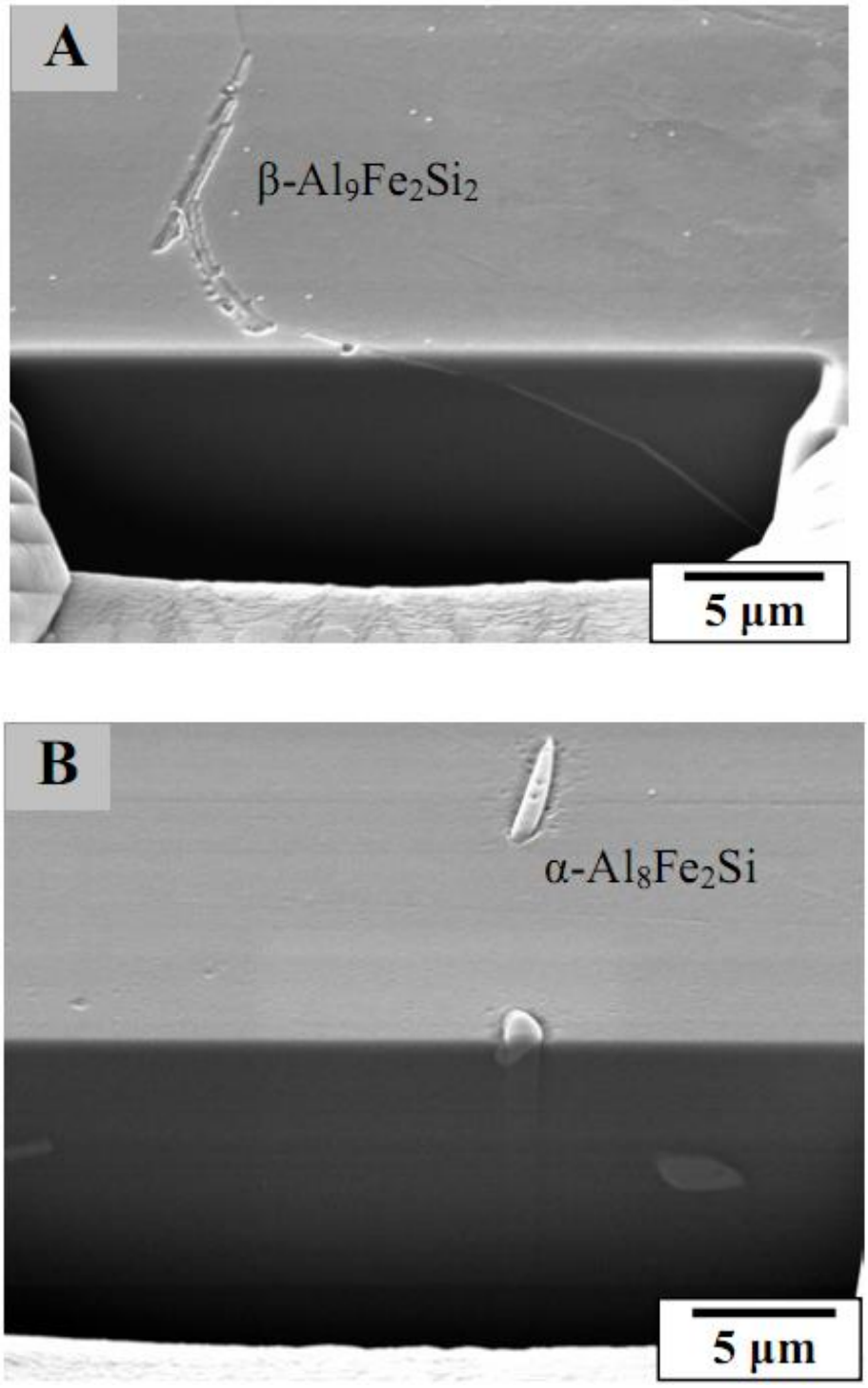

Fig 2.22 Two perpendicular planes are observable after FIB milling **(Claves et al., 04b)**.

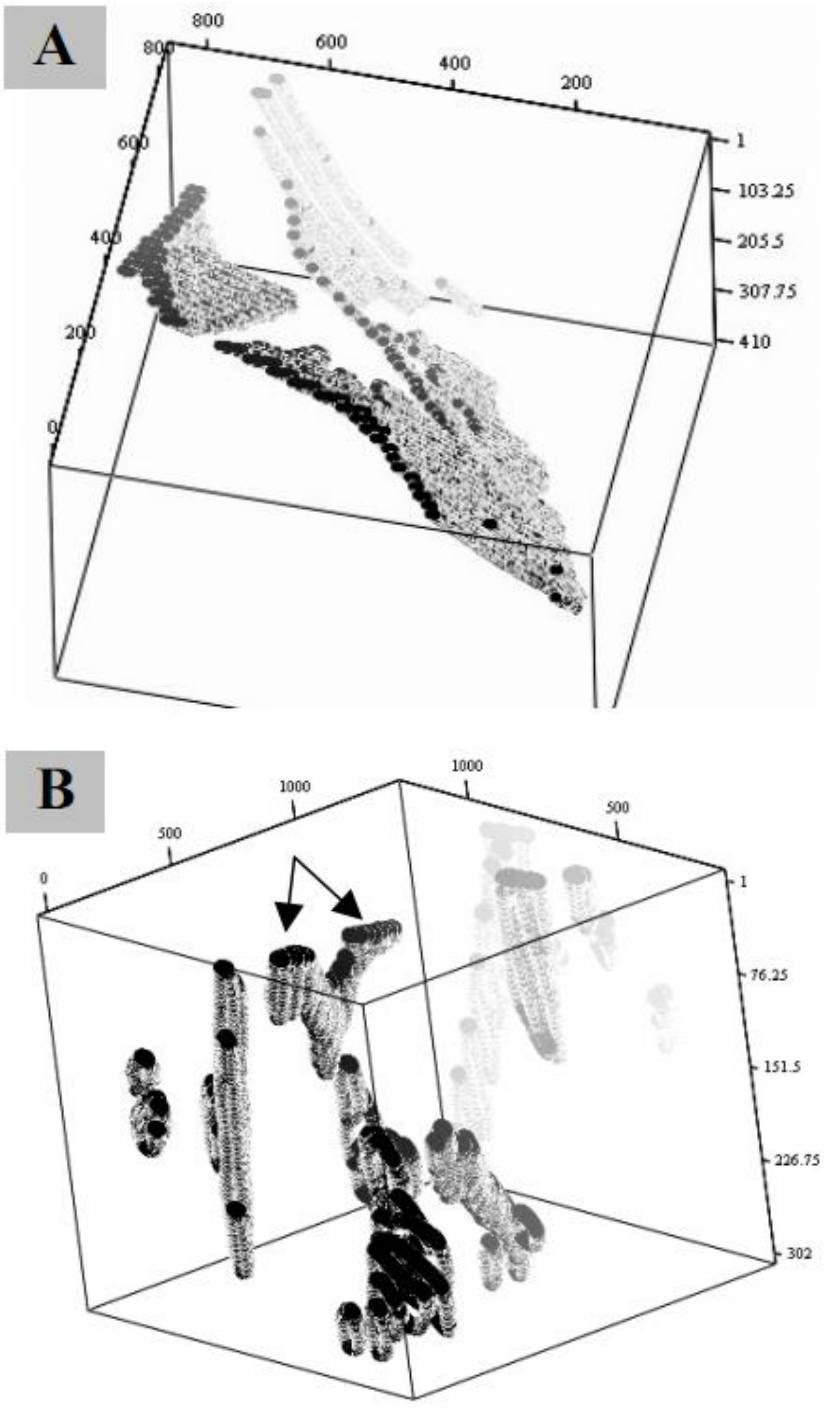

Fig 2.23 3D reconstructions of AlFeSi particles analysed from the preceding images **(Claves et al., 04b)**.

Fig 2.21A and 2.21B shows the SEM images of the area of interest for inspection. FIB uses consecutive electron beams to acquire images as the ion beam removes material from the examined face **(Claves et al., 04a).** Fig 2.22A and 2.22B shows the concurrent viewing of two perpendicular faces **(Claves et al., 04b)**, generated with precise ion milling, for accurate 3D re-construction **(Claves et al., 04a)**. It can be seen that β-AlFeSi actually has plate-like morphology which appears as needle-like in 2D images. Once the data from the 2D serial sections is collected, it is then analysed quantitatively using MatLab and 3D reconstruction is conducted using MatCad. Fig 2.23A and Fig. 2.23B show the reconstructed 3D intermetallic phase structure.

Particle matrix interface data can be extracted from the above images, which can also be used for quantification analysis. However, FIB uses very small cross sections so quantification may not be representative of the bulk sample. Also, there is the possibility that imaging may spoil the sample for subsequent analysis.

2.7.5 Energy dispersive X-ray spectroscopy (EDS)

This process analyses x-rays emitted from a sample undergoing electron bombardment. The resulting x-ray spectrum can be displayed as a function of energy **(Garratt et al., 03)**. These data can then either be analysed to give an indication of which elements are present in the sample (qualitative), or in a much more rigorous process, a precise and accurate (quantitative) chemical analysis

(Garratt et al., 03). This process does not give any morphological information. Intermetallic phases present in 6xxx Al alloys can be identified using this technique and Fig 2.3 based on the Fe/Si ratio.

2.7.6 Transmission electron microscopy (TEM)

TEM provides 3D (not so good as the sample is very thin) imaging and excellent diffraction data with very high spatial resolution for crystals **(Williams et al., 05),** which helps in identification of different intermetallic phases. However, the biggest limitation with TEM is the sample preparation. Quantification of intermetallic phases can be carried out using TEM but cannot be generalised, as the analysed area is small. Figure 2.24 a) is a TEM image showing the highly facetted nature of β-AlFeSi and 2.24 b) is a diffraction pattern indicating multiple (001) growth twins parallel to the growth direction **(Mulazimoglu et al., 96)**.

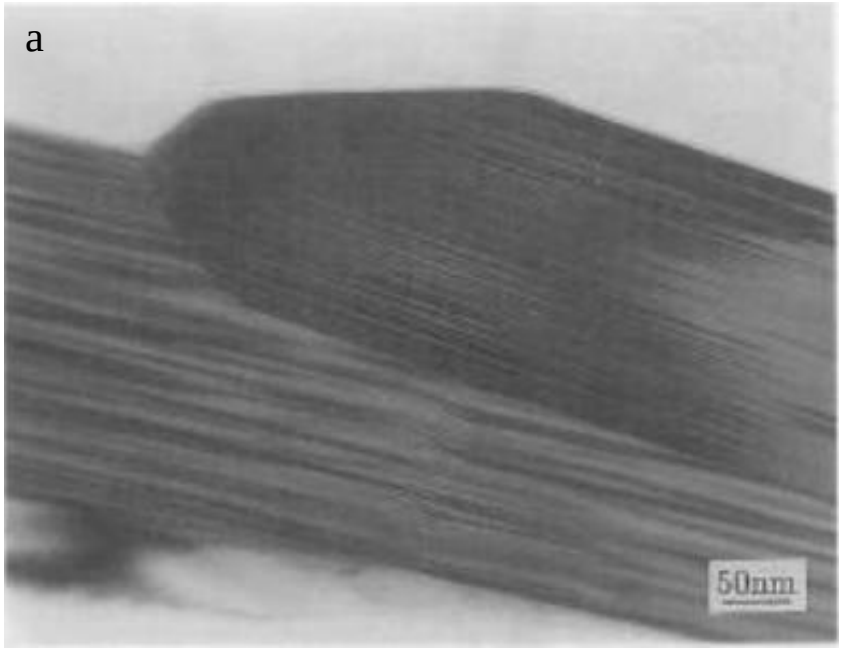

Continued overleaf…

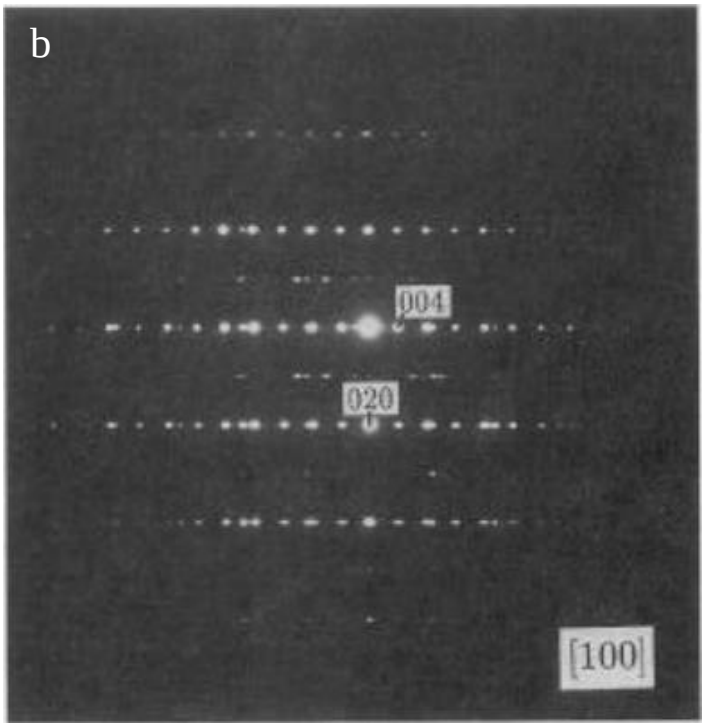

Fig 2.24 shows a) TEM image of a β-particle b) electron diffraction pattern **(Mulazimoglu et al., 96)**.

2.7.7 Electron backscatter diffraction (EBSD)

EPMA analysis is a faster technique than TEM for determining the 3D orientation of a crystal. However, it too requires special sample preparation, and results are better only for small scanning area **(Schwartz et al., 00)**. EBSD is also a useful technique for the identification of micron-size phases because the electron backscattering patterns can be obtained from the individual particles **(Schwartz et al., 00)**.

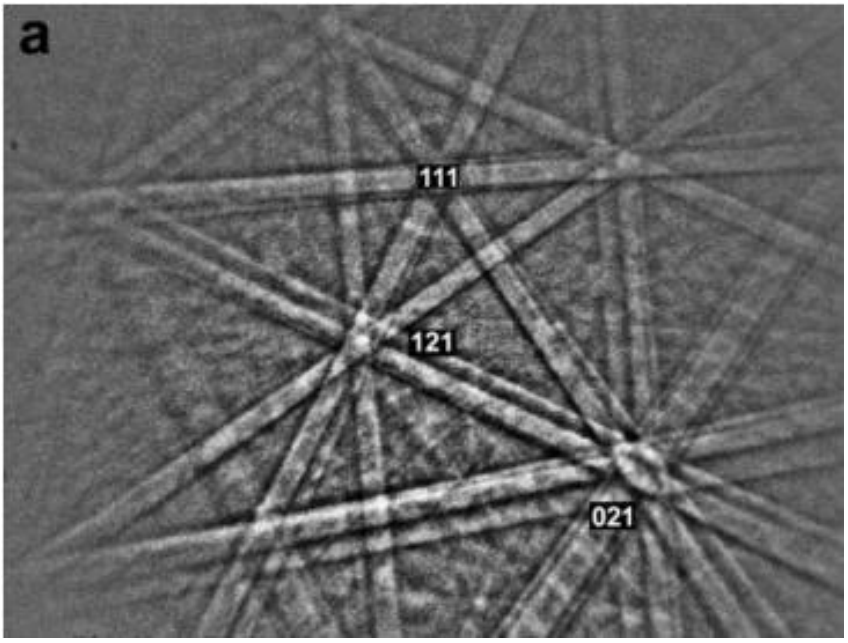
a
111
121
021

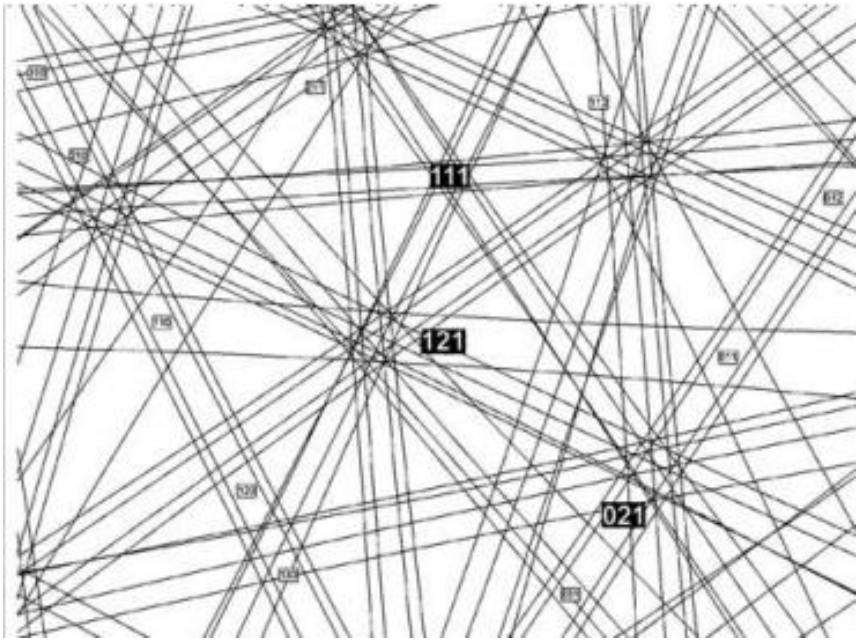
111
121
021

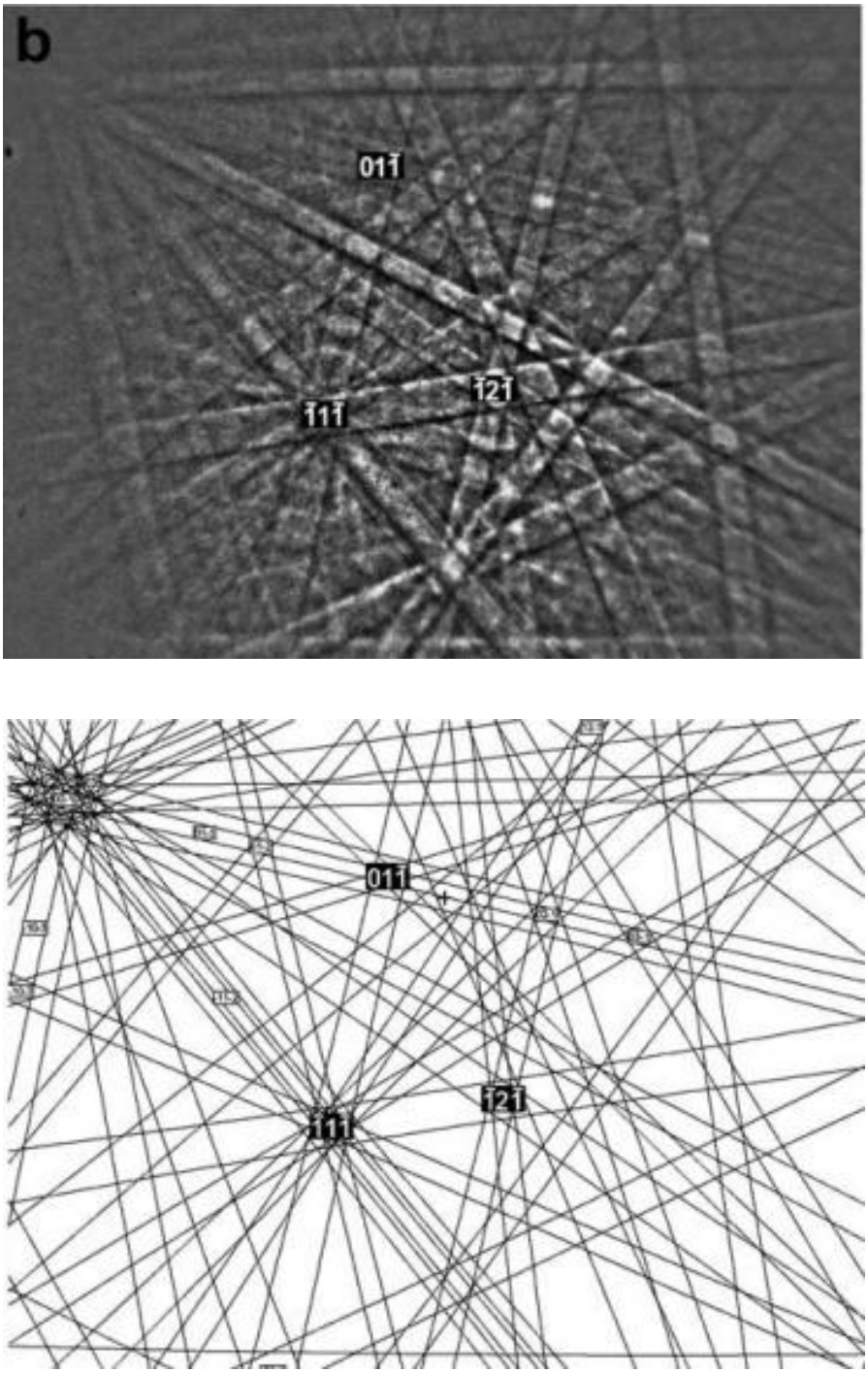

Fig 2.25 Representative experimental EBSD patterns with HKL Channel 5 simulations (a) the α-AlFeSi phase indexed as $Al_{19}(Fe,Mn)_5Si_2$ and (b) the β-AlFeSi phase indexed as $Al_3(Fe,Mn)Si_2$ **(Kral et al., 04)**.

This technique uses diffracted electrons from atomic layers to generate kikuchi bands. They give direct information about the crystalline structure and crystallographic orientation of grains **(Schwartz et al., 00)**, and can be used to identify particular intermetallic phases. Fig 2.25 shows the kikuchi pattern obtained from α-AlFeSi and β-AlFeSi intermetallic phases using EBSD. EBSD has been widely used for phase identification in the literature. For example, Yongshi **(Yongzhi et al., 10)** has identified the π phase, Sweet **(Sweet et al., 11)** has identified the α-AlFeSi and β-AlFeSi phases, Cheng **(Cheng et al., 11)** has identified various τ-AlFeSi phases.

2.7.8 Electron probe microanalysis (EPMA)

EPMA can be used to characterise the distribution of different intermetallic particles by using a mapping technique. The technique is capable of high spatial resolution (~1μm) and relatively high analytical sensitivity (<0.5% for major elements) and detection limits (~100 ppm for trace elements) **(Lavrent et al., 04)**. It can also acquire digital secondary-electron and backscattered-electron images as well as digital x-ray maps. Quantitative analysis can also be performed with EPMA but it is time consuming. Yoshio **(Osada, 04)** used this technique along with Monte Carlo simulation to differentiate between various intermetallic phases.

Table 2.6 summarises the information which can be obtained from the different techniques. Due to the complex structure of the intermetallics and

interconnectivity between them, it is very hard to identify a particular type of intermetallic. Also, 2D analysis provides only incomplete information. In this study a phase extraction technique will be used for quantitative and qualitative analysis of 3D morphology of intermetallics and the microstructure with the help of optical microscopy, SEM, EDX and XRD. Also, the morphologies of different intermetallics reported in the literature will be considered for identification.

Table 2.6 Information that can be obtained from various characterisation techniques

Characterization Technique	2D analysis	3D analysis	Quantitative analysis
Optical Microscopy	Yes	No	Yes (inaccurate)
SEM	Yes	Yes	No
XRD	No	No	Yes
FIB	No	Yes	Yes
EDS	No	No	Yes
TEM	No	Yes	Yes
EBSD	No	Yes	Yes
EPMA	No	No	Yes
Synchrotron X-Ray	No	Yes	Yes

2.8 Problem definition and approach

From the above literature review it can be inferred that intermetallics affect the properties (ductility and toughness) in 6xxx Al alloys. Also, it is a well-known fact that intermetallics affect the quality of extrusion. The literature review discussed past research which demonstrated the effect of inclusions on the primary Al and intermetallic formation through theoretical calculation and experimental observations (limited to 2D). It has been proposed that in-situ oxides can be utilised for selective nucleation of secondary phases **(Cao, 01)**. However, there is no concrete evidence which proves this theory. Therefore this research work will investigate the role of inclusions (Mg oxides) in the formation of secondary phases. Since using only 2D analysis can provide misleading information, for this study an extraction process was employed to reveal the 3D morphologies of the secondary phases and their association with inclusions for the first time.

From the literature it can be seen that only a little knowledge is available on the role of inclusions (particularly oxides and oxide bi-films) on the intermetallic phase formation. Therefore it was planned to analyse their 3D morphology. Since the amount of inclusions present in the commercial Al alloys are minute, a pressure filtration technique was planned to be used to increase their number density. TP1 test was utilised in this study to replicating the commercial casting conditions in an ergonomic way (see section 3.1.1 for more details on TP1 test). Though from the literature it can be seen that, TP1 test was used for grain refiner assessment, this study will also assess the intermetallic phase formation in TP1 test with respect to DC cast billet.

3. Experimental details

This study mainly analyses Fe-rich intermetallics and inclusions present in 6xxx Al alloys. The source of the 6xxx Al alloys in this study varies from commercial samples to in-house cast samples. Samples were mainly produced using the Aluminium Association's TP-1 grain refiner test **(TP1, 90)**. The inclusions were concentrated using the pressure filtration (PreFil) technique. The composition of the casting was checked regularly using optical emission spectroscopy. Different characterisation techniques were used to characterise different features of the microstructure. A special process was used to extract intermetallic particles for 3D characterisation. Optical microscopy, SEM and EDS techniques were used in order to identify the intermetallic particles and to analyse their 2D and 3D morphologies and interconnectivity between intermetallic and inclusion particles. XRD (appendix I) was used for the quantitative analysis of the intermetallic and inclusion particles.

3.1 Material and material preparation

3.1.1 TP1 test

In order to understand the preparation of the samples for different sets of experiments, it is important to understand the TP1 test. Fig. 3.1 shows the different components used in a TP1 test. The first step of the test was the preparation of the TP1 ladle. The TP1 ladle was sand blasted to remove any rust or dirt on the mould. It was then coated with boron nitride (inside and outside)

and kept in a furnace for drying for 24 hours at 300^{o}C. Once the alloys were molten, the TP1 ladle was dipped completely into the liquid metal with a melt temperature of 720^{o}C for about 30 seconds so that the ladle reaches the temperature of the molten alloy and did not result in a temperature gradient. The ladle was then withdrawn vertically and then subsequently lowered vertically into the retaining ring of the quench tank with the water flow rate fixed at one gallon (3.8 liters) per minute for three minutes. After that the sample was taken out of the ladle and allowed to cool to room temperature. The TP1 ladle was placed back in the furnace for drying.

Fig. 3.1 TP1 setup showing different components of the equipment

A 3 mm thick disc was sliced at a height of 38 mm from the bottom of the TP1 cast samples. This section of the TP1 sample has been characterised and

provides similar cooling rate to the centre of a commercial 7" DC-cast billet **(TP1, 90)**. The TP1 test is simple and economical to conduct when compared to expensive and complex DC casting. The centre parts of the discs were then used for microstructural analysis and extracting intermetallic particles for 3D analysis and XRD analysis.

3.1.2 Commercial alloys

Commercially homogenised billet of 7" diameter was provided by the SAPA group. Due to the company's policy the exact homogenisation conditions were not disclosed. However, the composition was verified using OES and lies well in the range for 6xxx series Al alloys (see Table 3.1). An in house (at Oxford) as DC-cast alloy (non-homogenised) of almost similar composition (except Si) and diameter was utilised for comparison between homogenised and non-homogenised billets. The composition of the alloy used can be seen in Table 3.1. The errors in composition for Mn and Ti were in third decimal places and hence were not reported. It is important to note that the difference in the compositions of the two alloys (section 2.2.3) particularly Si. The lower value of Fe/Si ratio in as DC-cast alloy in comparison to homogenised alloy might result in relatively higher amount of β-AlFeSi than what will be expected. Also, the lower Mg:Si ratio in as DC-cast might result in less amount of Mg_2Si precipitates after homogenisation.

Table 3.1 Composition of the commercial alloy used

Alloy	Si wt%	Fe wt%	Mg wt%	Mn wt%	Ti wt%	Al wt%
Homogenised	0.44±0.02	0.19±0.01	0.53±0.02	0.05	0.01	98.76±0.05
As DC-cast	0.52±0.02	0.21±0.01	0.52±0.02	0.05	0.01	98.67±0.05

A 10mm thick and 18cm in diameter discs were sliced from the homogenised and as DC-cast Al billets. Small sections (~5mm x 5mm x 5mm, 0.42 gms) were cut out from centre and edge of each disc, which were used in the intermetallic extraction apparatus (IEA) for extracting intermetallic phases. The remaining parts of the discs were used for metallography purposes.

3.1.3 In-house modelled alloys

For this study majority of the samples were produced in Oxford laboratories, as it is not always possible to get hold of the required samples from commercial sources in time. It is important to note that molten metal can get contaminated very easily. As a result, a number of precautions were taken to prevent the ingress of any unexpected impurities. For example, equipment like ladle, stirrer, tongs, TP1 moulds were sand blasted to remove any dirt and rust. Also all the experiment apparatus mentioned above along with ceramic crucibles were coated with boron nitride and dried before using in the experiment.

3.1.3.1 Samples for studying the influence of cooling rate and for comparison of microstructures formed during DC casting and TP1

In order to analyse the influence of cooling rate on different sections of TP1 samples, the as DC-cast alloy mentioned in section 3.1.2 was re-melted in a heat resistance furnace at 750^{o}C and a TP1 test was performed. Table 3.2 shows the composition at different sections of the TP1 sample and as DC-cast alloy. Elements such as Zn, Cu and Ni were present in amounts less than 0.01 wt. %. Also, the errors in composition for Mn and Ti were in third decimal places and hence were not reported.

The same as DC-cast alloy was utilised to compare the intermetallic formation in DC casting and at the 38mm section of TP1 (cast after re-melting the same as DC-cast alloy) as they have similar cooling rate (see section 3.1.1). The DC-cast alloy has 0.015% of grain refiner in it. Hence further addition of 0.015% Al-5Ti-B grain refiner was required for TP1 casting (the samples are called TP-1 with additional grain refiner (GR)), as the grain refiner was not effective after re-melting (see section 4.3 for results).

A 3 mm thick disc was sliced at heights of 12.5 mm, 25 mm, 38 mm and 50 mm from the bottom of the TP1 cast samples as shown in Fig. 3.2. The centre parts of the discs were then used for microstructural analysis and extracting intermetallic particles for 3D analysis and XRD analysis.

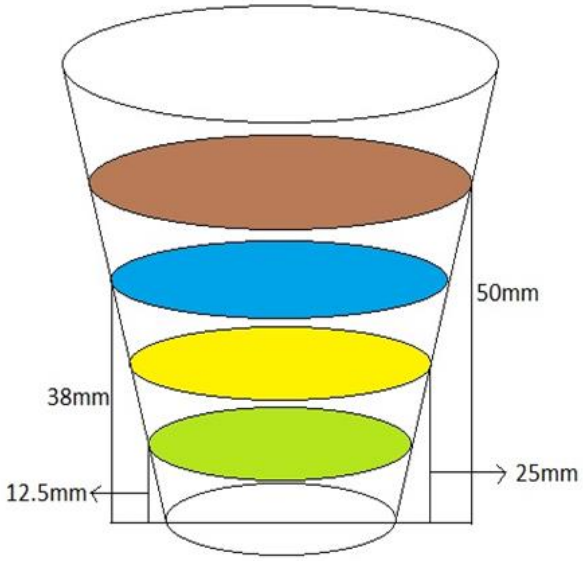

Fig 3.2 Sections analysed at different heights from the bottom of the TP1 sample

Table 3.2 Elemental composition at different sections of the TP1 sample and DC cast billet.

Distance	Si wt%	Fe wt%	Mn wt%	Mg wt%	Ti wt%	Al wt%
12.5 mm	0.53±0.02	0.20±0.01	0.05	0.55±0.02	0.01	98.60±0.05
25 mm	0.52±0.03	0.20±0.01	0.06	0.56±0.01	0.01	98.61±0.05
38 mm	0.55±0.02	0.21±0.01	0.06	0.56±0.02	0.01	98.58±0.05
50 mm	0.57±0.02	0.21±0.01	0.06	0.55±0.01	0.01	98.59±0.05
DC-cast	0.54±0.01	0.21±0.01	0.05	0.54±0.02	0.01	98.65±0.04

Generally, in order to measure the chemical composition of an alloy, a mushroom mould was used as shown in Fig. 3.3. However, a sectioned disc from the DC-cast billet was utilised for the composition measurement. While

preparing the TP-1 sample for a particular alloy, a part of the melt was taken and poured into a mushroom mould. Six different areas of this sample were used to measure the composition and there average was reported with the measured error.

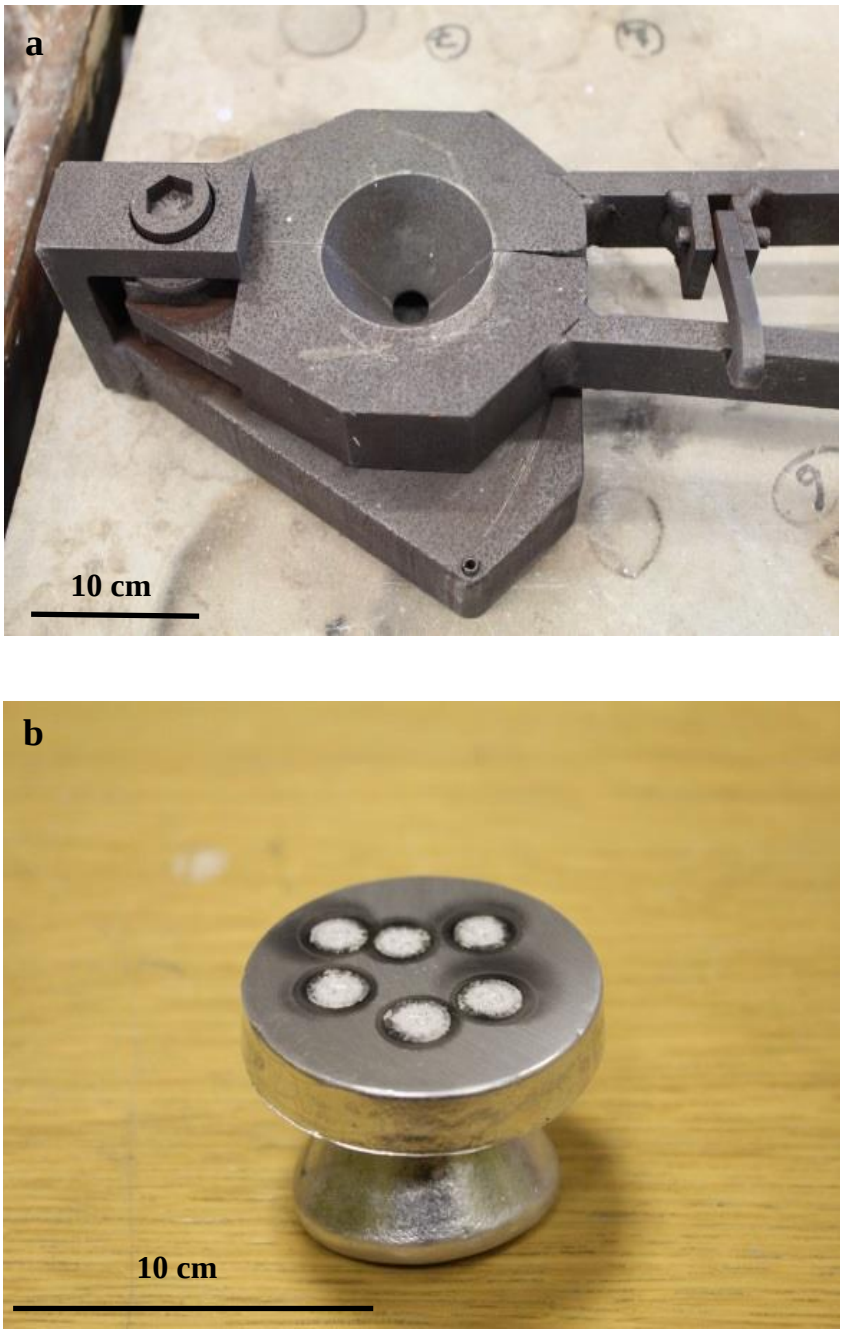

Fig. 3.3 a) Mushroom mould and b) mushroom cast with sparks from OES

3.1.3.2 MTDATA calculations for phase formation in different alloy compositions

MTDATA is a software tool to calculate phase equilibria and thermodynamic properties for a multicomponent system. It can be used for numerous applications like alloy development, extraction, metallurgy, refractories, corrosion, chemistry, pollution control etc. It helps us to have improved understanding of the process as a whole using reliable and powerful databases, software modules for critical assessment of the data to evaluate thermodynamic functions and equilibrium/non equilibrium calculations. MTDATA differs from other phase calculation software because it uses the principles of chemical and phase equilibria **(Bale et al, 90)** to calculate true minimum Gibbs energy **(Dinsdale et al., 89)** in order to perform various types of complex calculations in a binary, ternary, multicomponent system and predominance area diagrams**.** MTDATA is capable of performing both equilibrium and scheil calculations. In scheil calculations, local equilibrium is assumed with complete diffusion in the liquid and no diffusion in the solid, whereas in equilibrium calculations infinite diffusion in the solid is assumed **(Flemings, 74).** Both the calculations represent extreme cases and the real solidification lies somewhere in the middle. For this study, MTDATA- Ver. 5.10 and validated NPL Aluminium Database-Ver. 6.10 were utilised. This data set contained thermodynamic information about various elements like Al, Mg, Si, Fe, Cu, Ti, Mn etc. as well as binary and ternary interactions between them. Also, lever rule calculations were performed for this study. This data was utilised while analysing the pressure filtration samples and samples for studying the influence of oxides on intermetallics. The temperature range for the solidification simulation in this study was 300^0C - 700^0C at atmospheric pressure. Also, only the frequently

observed phases like α-AlFeSi, β-AlFeSi, Mg_2Si and $Al_{13}Fe_4$ were allowed to form and all the other phases were suppressed. Please see Chapter-5 for the detailed results of the MTDATA calculations.

3.1.3.3 Pressure filtration samples (prefil alloys)

The main purpose of pressure filtration (prefil) samples was to study/identify the morphologies of different inclusions or extra additions (eg. Zr) commonly present in Al alloys. As prefil increases the density of inclusions to ~10,000 times it will be relatively easier to study different types of inclusions. The additional advantage was that the intermetallics were formed in a region highly rich with inclusions and their density was also increased by many folds. However, prefil has much smaller solidification rate as compared to the DC casting and will not provide very reliable data for intermetallic formation. Therefore, this data will be very useful to identify different inclusions in TP1 samples when inclusions are scarce. Hence, for this investigation a commercially pure Al was chosen instead of high purity Al as it had different elements like Fe, Mg, Si, Ti, Zr etc. already present in it. This experiment was not utilised to study the intermetallics in detail as the prefil setup has completely different solidification process in comparison to DC casting. About 12Kgs of base alloy of composition Al-0.3Fe-0.5Si-0.1Mg was prepared. Fe and Si content in this base alloy were chosen well within the 6xxx range. In order to prepare the base alloy, commercially pure Al (99.7 wt% Al, 0.1 wt% Fe, 0.1 wt% Si, 0.1 wt% Mg) was melted in a heat resistance furnace at 750^{o}C and binary alloys Al-50Si and

Al-80Fe were added. The melt was stirred frequently and held for four hours at 760^{o}C and then cast. Extra care was taken while adding Mg to the melt. As Mg has the tendency to float on the surface, small cubes of pure Mg were wrapped in an Al foil and dipped in the molten alloy with the help of a boron nitride coated tong until completely dissolved (~3-5 minutes). Argon was constantly supplied to the molten metal surface during this procedure to avoid the reaction between oxygen and Mg floating on the surface. This will provide more realistic Mg oxides content in the alloy and not more than normally expected. After the addition of pure Mg to the base alloy, the melt was held for another four hours in each case. Four alloys were produced using the base alloy and pure Mg giving compositions of 0.1 wt% Mg, 0.5 wt% Mg, 1.3 wt% Mg and 5.1 wt% Mg respectively. A wide range of Mg was chosen in order to study the morphology of different Mg oxides.

A pressure filter machine called Footprinter was used for this experiment as shown in Fig. 3.4a. Fig. 3.4b shows the top and bottom parts of the reusable ceramic crucible and the filter. Before the experiment, the filter holder was screwed to the bottom of the crucible. The ceramic crucible was preheated to 300^{o}C using a resistance heater and 2 kgs of the melt was poured into it after placing it in the pressure chamber (see Fig. 3.4a). A thermocouple is inserted to measure the desired temperature for filtration, which was 680^{o}C for this study. An overpressure of 30psi was applied to the melt and the melt was forced to pass through the ceramic filter on to the weight balance. The pressure was applied until the mass on the weighing scale reached 1.4 kg as shown in the PODFA

curve (Fig. 3.4d). As a result, the top of the filter becomes the maximum density zone for inclusions as shown in Fig. 3.4c. Table 3.3 shows the elemental compositions of the different alloys produced for this study. The compositions of the different alloys were verified using the OES. The errors in composition for Cr, Ni, Cu, Zn, Zr, Mn and Ti were in third decimal places and hence were not reported.

Table 3.3 Compositions of the different alloys produced for PreFil experiment.

Mg wt%	Fe wt%	Si wt%	Ti wt%	Cr wt%	Mn wt%	Ni wt%	Cu wt%	Zn wt%	Zr wt%	Al wt%
0.13±0.01	0.31±0.01	0.52±0.02	0.09	0.05	0.03	0.01	0.03	0.02	0.02	98.79±0.05
0.52±0.01	0.29±0.01	0.51±0.01	0.09	0.04	0.02	0.01	0.04	0.01	0.01	98.46±0.05
1.33±0.02	0.32±0.01	0.51±0.02	0.08	0.05	0.02	0.01	0.03	0.01	0.02	97.62±0.05
5.15±0.03	0.29±0.01	0.49±0.02	0.1	0.05	0.02	0.01	0.03	0.02	0.02	93.82±0.05

Prefil plots in Fig. 3.4d shows that the time taken to reach the 1.4 Kg value increased with the Mg content. This can be due to increase in the density of inclusions particularly the Mg oxides (MgO and spinel ($MgAl_2O_4$)) as more Mg is added.

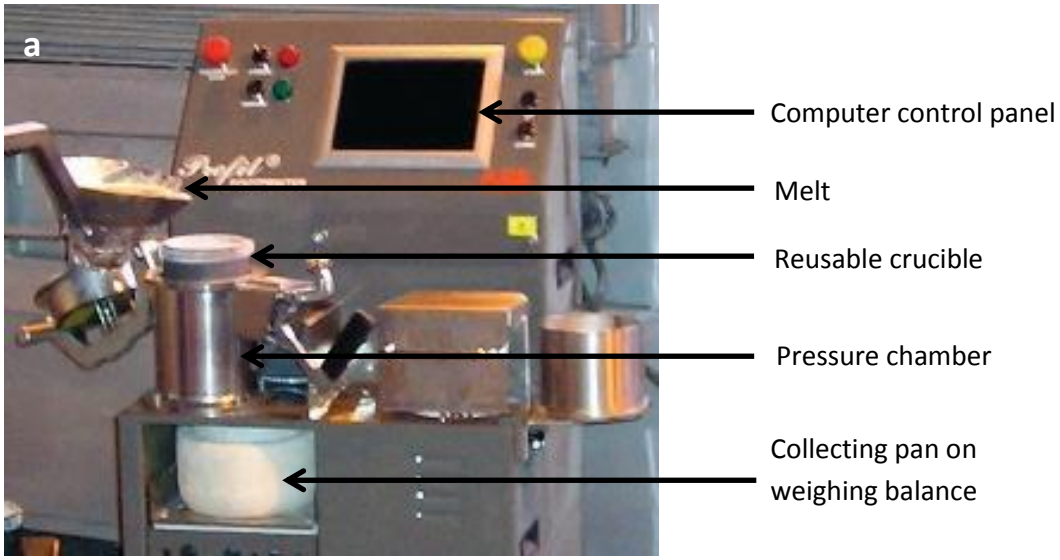

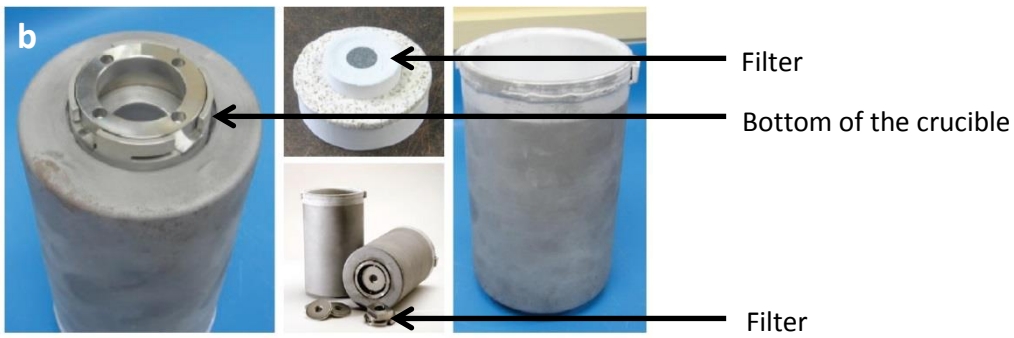

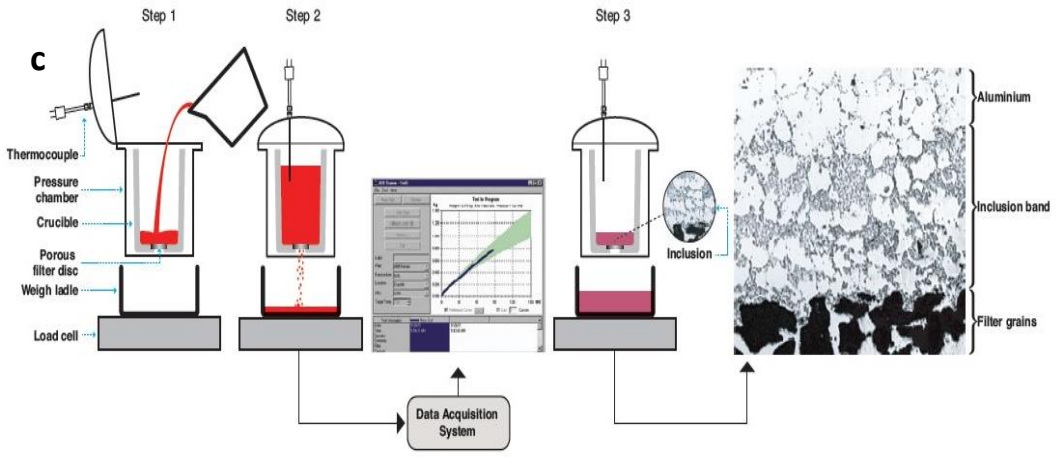

Continued overleaf…

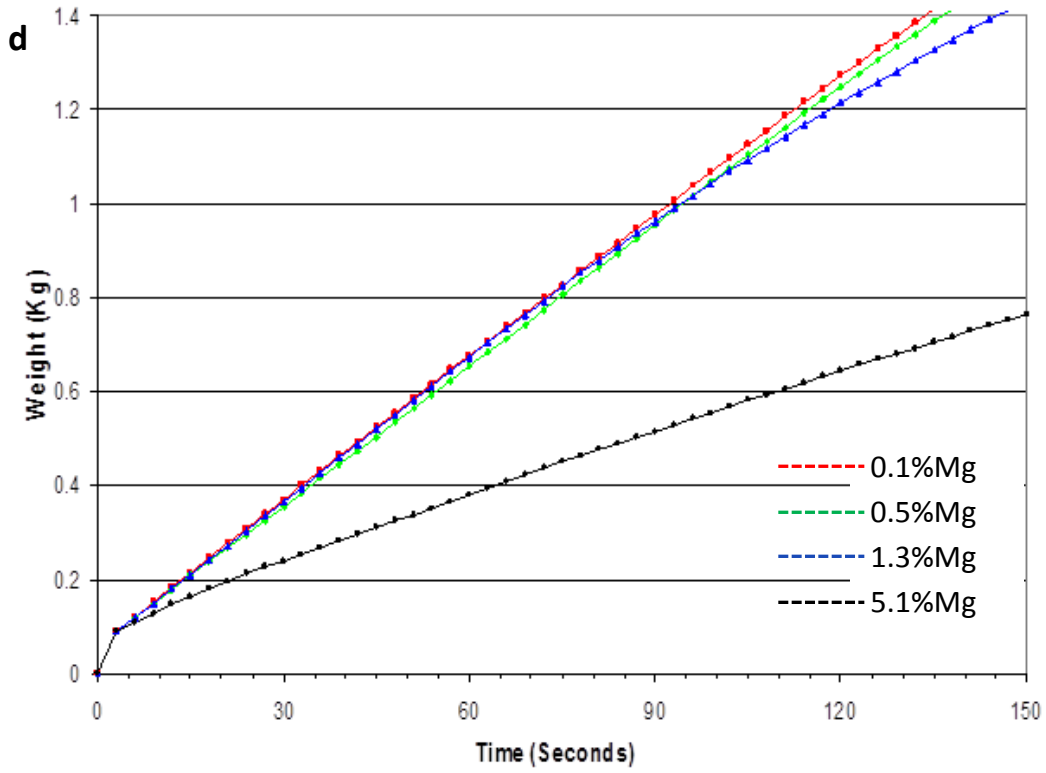

Fig.3.4 a) Prefil foot printer setup, b) crucibles and filters used during prefil experiment, c) operation principle of prefil footprinter **(Enright, 87), (Enright et al., 96)** and **(www.abb.com)** and d) PODFA curve for different prefil alloys**.**

3.1.3.4 Samples for studying the influence of oxides on intermetallics

In order to prepare the samples for studying the effect of oxides on intermetallic formation, about 14 Kgs of base alloy of composition Al-0.2Fe-0.4Si was prepared. Fe and Si content in this study were close to average value in 6xxx series Al alloys. The slightly lower value of Fe and Si from the prefill experiment (3.1.3.3) will make no difference in the solidification route

(Belov et al., 05). This was also confirmed using MTDATA analysis (see chapter-5 for more details). For the preparation of the base alloy, high purity Al (99.95 wt%) was melted in a heat resistance furnace at 750^{o}C and binary alloys Al-80Fe and Al-50Si were added. The composition of the base alloy was confirmed using OES.

Approximately 1.5Kgs of base alloy was then re-melted for each Mg composition in a heat resistance furnace at 750^{o}C before adding pure Mg to it. Mg was added to the melt in a similar manner as for prefil alloys (section 3.1.3.3). The Mg content added resulted in the following compositions: 0.4%, 0.8%, 1.2%, 1.6%, 2%, 2.5%, 3% and 5 wt% Mg. Table 3.3 shows the compositions of the different alloys produced. Other elements like Cu, Ni, Cr, Mn, Ti and Zn were present in quantities less than 0.001wt% and hence are not reported. The melt was held at 750^{o}C for four hours and was frequently stirred before casting via TP1 tests. Four samples were cast for each of the different Mg compositions and the master alloy without Mg. The compositions of all the samples were verified using OES. The diverse range of Mg content was added to generate a range of in-situ MgO/$MgAl_2O_4$ in the alloy. High Mg content (even in 5xxx Al alloys range) was added to check the effect of saturation of in-situ MgO on the intermetallic formation. It is also important to note that alloys with high Mg (>1.2 wt%) are not in 6xxx Al alloys range and are not age-hardening or extrusion alloys.

Table 3.4 Compositions of the different Mg alloys produced using TP1 test.

Alloy (aimed)	Si wt%	Fe wt%	Mg wt%	Al wt%
0 wt% Mg	0.43±0.01	0.23±0.01	0	99.31±0.03
0.4 wt% Mg	0.41±0.02	0.22±0.01	0.39±0.01	98.95±0.05
0.8 wt% Mg	0.39±0.02	0.21±0.01	0.79±0.01	98.57±0.05
1.2 wt% Mg	0.40±0.02	0.21±0.01	1.16±0.02	98.22±0.05
1.6 wt% Mg	0.41±0.02	0.22±0.01	1.64±0.02	97.69±0.05
2 wt% Mg	0.42±0.01	0.20±0.01	2.05±0.02	97.3±0.05
2.5 wt% Mg	0.40±0.02	0.22±0.01	2.48±0.02	96.87±0.06
3 wt% Mg	0.40±0.02	0.21±0.01	3.08±0.03	96.28±0.06
5 wt% Mg	0.42±0.01	0.21±0.01	4.94±0.04	94.41±0.08

3.2 Polishing

Samples were mounted in conductive and non-conductive phenolic resin. Mounting was conducted using a Metkon Ecopress 200 press. The samples were then ground and polished using a Metkon Forcipol polishing unit and SiC paper of 120, 240, 600, 800, 1200 and 1400 grit progressively. After completion of the first step of polishing, six of the samples were mounted simultaneously on the counter rotating head and polished using 5μm and 3μm diamond paste on a Metkon Forcimat automatic machine. The surface was regularly checked under the optical microscope at each stage for any major marks/scratches. Lastly, all the samples were polished using 0.06 μm colloidal silica to achieve an even finer mirror-like polish. In order to remove the silica from the sample surface, the

samples were thoroughly washed under de-ionised water using soap solution and dried immediately using methanol and a hot air blower to avoid water marks.

3.3 Anodising

Anodising was conducted to reveal the grain structure. As oxide growth is a function of crystallographic orientation, the birefringence effect gave rise to coloured grains. In order to have a good anodised microstructure, it is important to mount the sample in non-conductive phenolic resin. Half of the sample was coated with silver dag and dried for 15-20 minutes. A conducting wire was attached to the silver coated part of the sample and the positive socket of the Kristall 620 equipment (blue hole). A second conducting wire was connected between the metallic cup containing Barker's reagent (1.4 gm boric acid, 9ml of tetrafluoroboric acid and 194 ml of water) and negative socket of the machine (red hole). For anodisation, the sample was dipped in Barker's reagent for the duration of one minute. A potential difference of 20V was applied through conducting wires for that duration the using Kristall 620 as shown in Fig. 3.5. Samples were then washed with ethanol and dried with an air blower. The anodised microstructure was then cross checked under the cross-polarised light using a Polyvar optical microscope.

Fig. 3.5 Shows Kristall 620 machine which was used to pass current for anodising.

3.4 Macro-etching

To prepare macro-etched samples to reveal the grain structure, TP1 castings were vertically sectioned in half as shown in Fig 3.6. The flat surface of the sample was grounded (1200 grit) to make it smooth. The etchant used for this purpose was Tucker's reagent (HNO_3 (15%) + HCl (45%) + HF (15%) + H_2O (25%)). A small quantity of the etchant was gently rubbed on the flat surface of the sample using a cotton bud for about 8-10 mins. After the macrostructure was revealed, the sample was washed thoroughly with ethanol, water and dried. An example of the etched surface is shown in Fig 3.6.

Fig 3.6 Macroetched vertical section of 0.8% Mg sample

3.5 Extraction of intermetallic phases

Intermetallic extraction apparatus (IEA) involves using butan-1-ol (butanol) to dissolve away the Al matrix of Al alloys whilst keeping the intermetallic phases intact. Fig 3.7 shows the intermetallic extraction setup. In order to remove any moisture in the butanol, it was first refluxed and dried in the distillation apparatus (evacuated and purged with argon) using pure Al metal swarf for 3 hours.

Four Sartorius steel pressure filtration holders (autoclaves) each with 200 ml capacity with maximum working pressures of 10 bar were used. They were ultrasonically cleaned in de-ionised water and left in the oven at 150 ^{o}C for 2 hours. They were each fitted with a poly-tetrafluoroethene (PTFE) filter membrane (47 mm diameter, pore size of 0.2µm) and thoroughly dried at 150^{o}C for another 2 hours so that the filter paper was properly fixed in place.

Fig 3.7 Intermetallic extraction setup showing manifold and refluxed butanol

Small Al alloy sections taken from the centre and edge of a billet were reduced to 0.42 gm (maximum mass of sample for the autoclave described above) using a hacksaw and grinding paper. Each specimen was cleaned with the help of an etchant (40 vol% HPO_3, 5 vol% H_2SO_4 and 2.5 vol% HNO_3) at ~60^{o}C for about

3 minutes to remove the oxide layer. Simultaneously, a Schlenk glass tube was cleaned using methanol and vacuum dried. Immediately after etching, the specimen was washed in ethanol and placed inside the argon purging Schlenk tube which had been dried again in vacuum. The sample was then stored under argon gas in a clean glass Schlenk tube until the autoclaves were dry.

A stainless steel manifold of Swagelok system was used to connect the distillation apparatus, vacuum system and argon gas. The autoclave was attached to the manifold where it was evacuated and leak tests were conducted to check the stability of the vacuum inside the autoclave before filling with argon gas. 80 ml of dried butanol was measured and tapped into the autoclave before the specimen was inserted. The lid was fitted and the autoclave was placed into an oven at 150^{o}C. The above process was repeated three more times for another three samples.

The following reaction takes place inside the autoclave:

$$2Al + 6\ C_4H_9OH \rightarrow 2Al\ (C_4H_9O)_3 + 3H_2 \qquad (1)$$

Fig. 3.8 Extracted intermetallic particles on a PTFE filter paper

The gaseous hydrogen produced in this reaction causes the pressure within the autoclaves to increase. Stabilisation of the pressure indicates the completion of the reaction and dissolution of the whole of the Al matrix. This normally takes approximately 4 hours, but varies with alloy composition. The autoclaves were removed from the oven and all the butanol was drained out with the help of the pressure built-up. They were washed with ethanol in order to collect the intermetallics sticking inside the autoclaves and put back in the oven (not allowing any pressure to built-up). They were taken out after 10 minutes and allowed to cool down and were dismantled. The filter membranes were removed from the autoclaves and were left to dry overnight. Fig 3.8 shows the extracted intermetallics collected on a PTFE filter paper.

3.6 Characterisation techniques for microstructural analysis

3.6.1 Optical microscopy

Optical microscopy is the first step for characterising the bulk microstructure. After final polishing using colloidal silica, it is the most convenient way to check for any imperfections or quality of the polished surface before moving to a higher characterisation technique. Optical microscopy was conducted using a Zeiss Axioplan 2 microscope. Objective lenses of 5x, 10x, 20x, 50x and 100x along with eye piece lens of 10x were used to capture the images. Techniques such as differential interference contrast (DIC) and white digital imaging along with Zeiss pro software were used to analyse the images of the 2D morphologies of the intermetallics and anodised microstructures.

The information obtained from the optical microscope is quite important, however very limited. For example, it is very suitable for characterising the grain size and dendritic arm spacing (DAS) in an anodised microstructure. In order to measure the average grain size and average DAS, the line intercept method was used. Also, it is reasonably effective for calculating the percentage of secondary phases using area fraction analysis with the help of grey scale calculations. However, the information obtained about intermetallics and other features of the microstructure is very restricted in 2D analysis and has relatively poor resolution.

3.6.2 SEM and EDS

The polished samples (conductive mount) were used for determining the 2D morphology and distribution of intermetallic phases within the microstructure. In order to prepare an SEM sample from the extracted intermetallics, a carbon sticky tab was put on a 12mm Al stub which was gently touched on to different parts of the filter membrane in order to stick the extracted intermetallics to it. An aerosol duster was used to remove any excess particles piled over one another. Examination revealed that the particles were sufficiently rigid and made good contact with the tab (to avoid charging). However, particles rich in oxides and inclusions needed to be coated with two coats of platinum of 2nm each at 90^{o} to each other to avoid charging.

Two microscopes were mainly used to study intermetallics i.e. JEOL 840A (tungsten filament) and JEOL 840F (field emission gun). For image capture using the 840A, the accelerating voltage used was 10 kV, probe current ~5 nA and working distance varied from 8-20mm. However, in order to detect Fe peaks (K_{α} at 6.39kV) in the phase and for optimised EDS analysis on JEOL 840A it was necessary to use 20 kV and ~4-6 nA. For 840 F, the voltage was fixed at 5kV, current at 5 nA and the working distance varied from 8-20 mm. Both SE and BSE images of the same place were taken to collect complete information.

3.6.3 Image analysis

Image analysis was used to measure the phase area fraction in 2D images, the length of the intermetallics, the interconnectivity between the intermetallics and the interdentritic arm spacing in grains and intermetallics. Freely available software called Image J was used to measure the area fraction of a phase using grey scale analysis. For example, in Fig 3.9 the area fraction of the phases Mg_2Si and Fe-intermetallics were measured to be 1.7% and 3% respectively using grey scale analysis. Zeiss pro software was used to measure lengths, as the scale used was by default calibrated with the scale in the image.

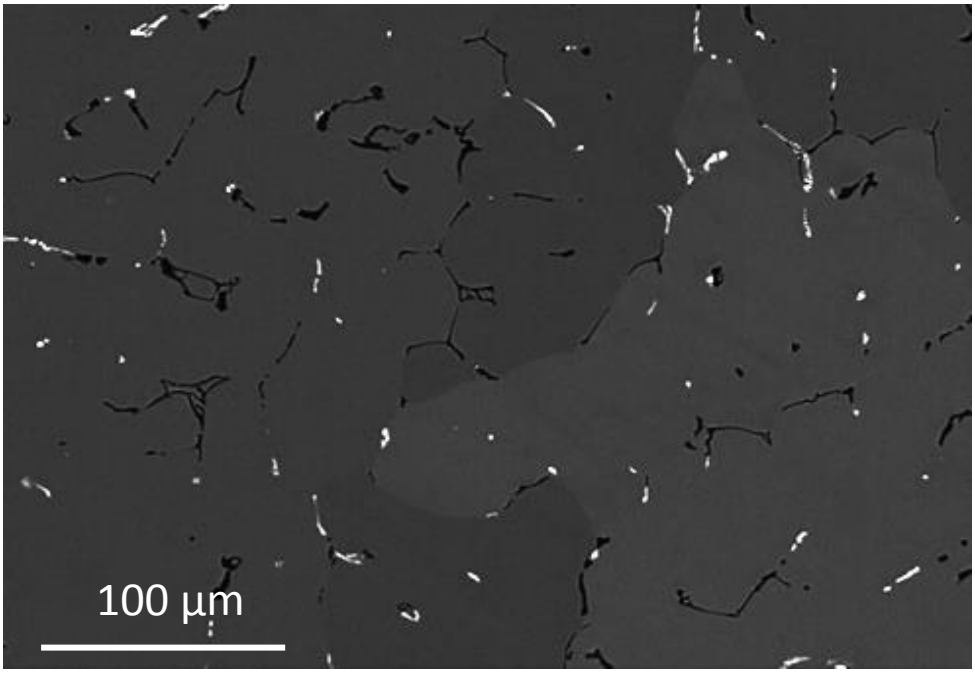

Fig 3.9 2D SEM image showing microstructure of 5 wt% Mg sample

3.6.4 X-Ray diffraction

The preparation for XRD samples was a bit more complicated. To prepare sample for X-ray diffraction analysis, the extracted particles along with the PTFE filter membrane were dipped in some amount of methanol for a couple of minutes. The extracted particles were softly scraped off the filter paper using the stainless steel spatula. The resultant suspension was transferred to an agate mortar which was then heated gently to evaporate the methanol. The extracted particles were simultaneously stirred using an agate pestle (to avoid sticking of particles on the surface of agate mortar) and the resulting powder was collected into a gelatine capsule for storage. It is important to note that stirring, although gentle, might introduce texture (preferred crystallographic orientation) in the sample due to stress from agate pestle. This texture might result in the unexpected high peaks i.e. high peak for usually low intensity peak. The reflective surface of a silicon wafer was uniformly coated with vacuum grease and the collected powder was carefully spread in the centre of the wafer before mounting in the XRD machine.

XRD was performed using a Philips 1700 X-ray diffractometer. A Cu-Kα X-ray source was used ($\lambda = 1.54\acute{A}$) at a voltage of 35kV and a current of 50 mA. The range of 2θ was between 15^o and 65^o, with a step size of 0.05^o and exposure time of 12.5 seconds per step. The 2θ range was chosen between 15^o and 65^o as all the major peaks (top 9 intensities) for intermetallics and inclusions (top 5 intensities) lie within this range. The XRD spectrums generated were compared with the

reference patterns provided by the International Centre for Diffraction Data. All the peaks were normalised with respect to the highest peak to make the traces more uniform. This also provides accurate comparison of peak intensities and removes any error caused by the amount of sample used for XRD. The reference code for files for different compounds is tabulated in Table 3.5. The XRD patterns for these compounds can be seen in the Appendix I. The XRD pattern for α-AlFeSi used in this study has been taken from the literature **(Davidson, 06)** as this was the only reference pattern available was for α-AlFeSi (see Appendix I). Davidson calculated this XRD pattern using the theoretical analysis from **(Cooper, 67)**.

Table 3.5 shows the reference code for files for different compounds

Compound	Reference Code for XRD file
α- AlFeSi	**(Davidson, 06)**
β- AlFeSi	00-049-1499
Mg_2Si	00-034-0458
$Al_{13}Fe_4$	00-029-0042
MgO	00-045-0946
$MgAl_2O_4$	00-021-1152
Al_2O_3	00-046-1212
TiB_2	00-035-0741

A regression curve was used to quantify the relative fractions of α-AlFeSi and β-AlFeSi from XRD spectra. This curve was calculated using the XRD spectra obtained from known mixtures of pure α-AlFeSi and β-AlFeSi i.e. 10-90wt% of α-AlFeSi and β-AlFeSi. After setting the baseline, three peaks of α-AlFeSi (2θ = 22.37°, 26.53° and 36.44°) and β-AlFeSi (2θ = 17.03°, 20.81° and 28.96°) were chosen to calculate the nine ratios of β-AlFeSi:α-AlFeSi peak intensities. The peaks were chosen such that they were not overlapping or obscured.

The average of these nine ratios is given by R (average XRD peak height ratio):

$$R = 1/9 \sum_{i,j=1=3} I_{\beta i} / I_{\alpha i}$$

R's for different known wt% α is plotted and Fig. xxx shows the variation of wt% α with respect to R. After regression analysis, the equation for the best fit is calculated. As the wt% α in this derivation varied in the multiples of 10 (eg. 20%, 30% and so on), the error in calculating the wt% α from this equation is ±10%.

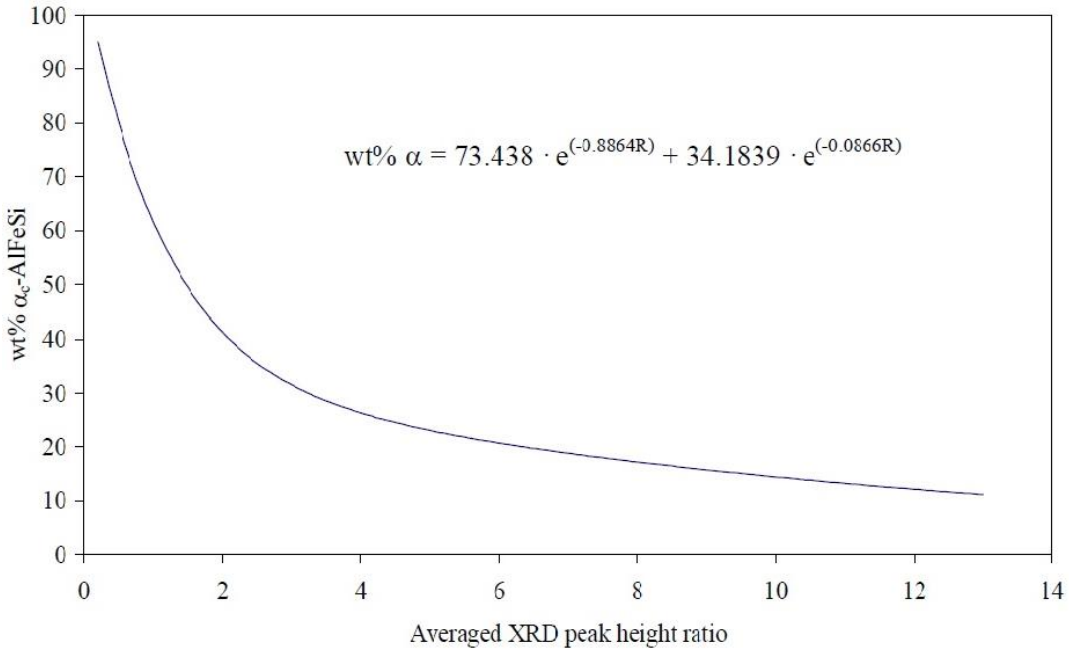

Fig 3.10 Regression curve for converting average XRD peak height ratio (R) into wt% α-AlFeSi **(Sha, 01)**.

The regression curve for the above curve is given by equation (1) **(Sha, 01)**.

$$wt\%\ \alpha\ (\alpha\text{-AlFeSi}) = 73.44 \cdot e^{(-0.8864R)} + 34.18 \cdot e^{(-0.0866R)} \quad \text{.....(1)}$$

where R is the average of peak intensity ratios.

3.6.5 Optical emission spectroscopy (OES)

OES was used to measure the composition of the alloys and to check for macrosegregation effects for all the commercial and non-commercial samples. A Spectrolab LAVFAO 5A instrument was used for this purpose. For this purpose,

a disc of 6-7cm diameter was cut out from the castings or mushroom moulds (Fig. 3.3) were used for in-house cast samples. The disc/mushroom mould sample was ground (1200 grit) to obtain a flat and contamination free surface. Five readings were taken from different areas of the ground surface and the average composition was reported. The least count for this technique was 0.001wt%.

3.7 Measurement of intermetallics

Due to the complex 3D structure of intermetallics, it was very hard to measure the size of the intermetallics. Most of the time an intermetallic was observed to overlap/entangle with other intermetallics. Therefore, only isolated intermetallics were measured for this study. SEM micrographs of extracted intermetallics (3D) were used for this measurement as 2D micrographs gave misleading information. The quantification techniques used for different intermetallic features are described below.

3.7.1 Measurement of α-AlFeSi

During SEM analysis, α-AlFeSi was observed mainly with a flower-like morphology. In order to measure the size of α-AlFeSi, the length of the petals of this flower-like particle were measured as shown by the black lines in Fig 3.11. About 50 particles were measured during each analysis and their average was calculated.

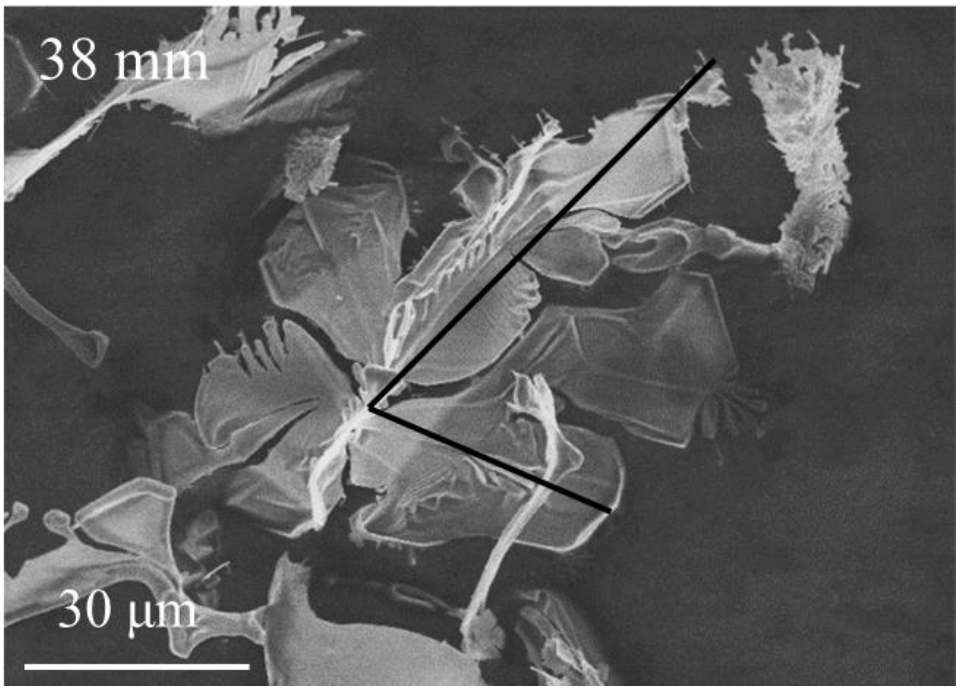

Fig 3.11 SEM micrograph of α-AlFeSi showing the lengths of petals measured (black lines)

3.7.2 Measurement of β-AlFeSi

During SEM analysis, β-AlFeSi was observed mainly with a faceted morphology. In order to measure the size of β-AlFeSi, the length of the longest faceted side of each particle was measured as shown by black lines in Fig 3.12. About 50 particles were measured during each analysis and their average was calculated.

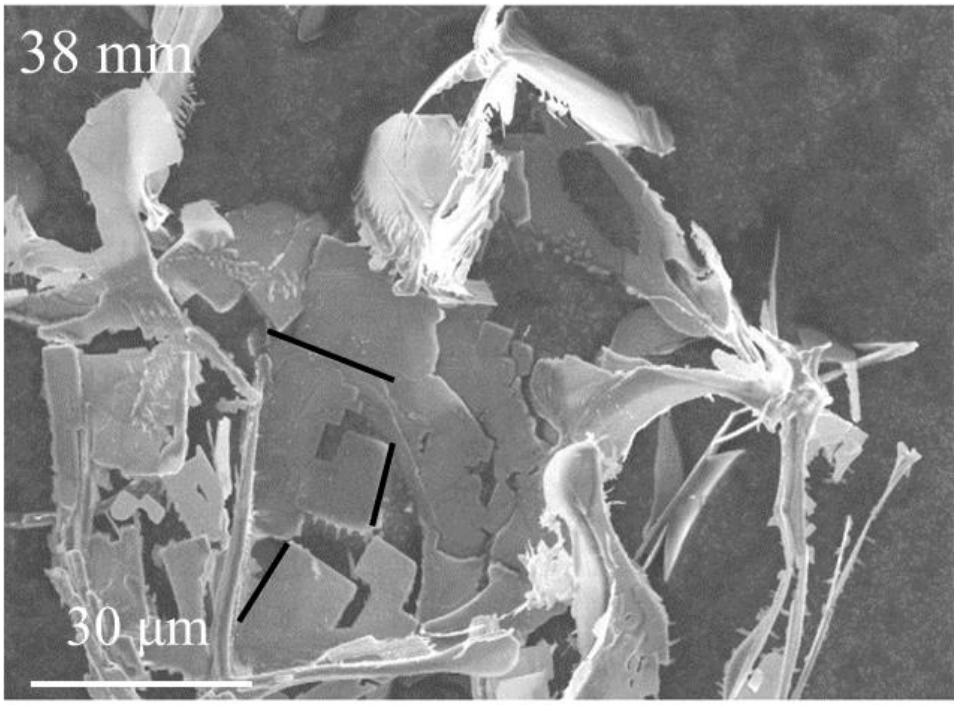

Fig 3.12 SEM micrographs of β-AlFeSi showing the lengths of the maximum faceted side measured (black lines)

3.7.3 Measurement of interconnectivity

The interconnectivity of intermetallics provides vital information about the solidification mechanism in the alloy. The method of measuring this complex data is shown in Fig 3.13. The length of various interconnected intermetallics was measured as shown by black lines. The length of each black line was summed to get the total length of interconnectivity, which forms one data point. About 50 such interconnectivities were measured and their average was calculated.

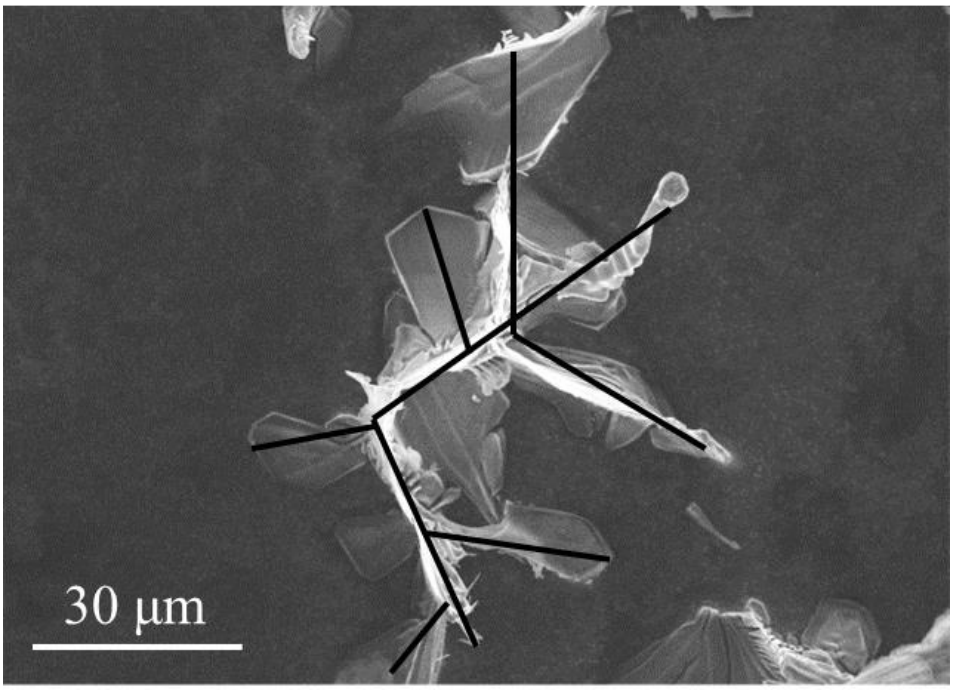

Fig 3.13 SEM micrograph showing interconnectivity between intermetallics (black lines)

3.7.4 Measurement of intermetallic dendritic arm spacing

Intermetallics dendritic arm spacing (I-DAS) also provides vital information about the solidification mechanism in the alloy. The method of measuring this complex data is shown in Fig 3.14 by the red line. The total length of the red line was measured and divided by the number of I-DAS in that line. About 50 such measurements were made on different particles and their average was calculated.

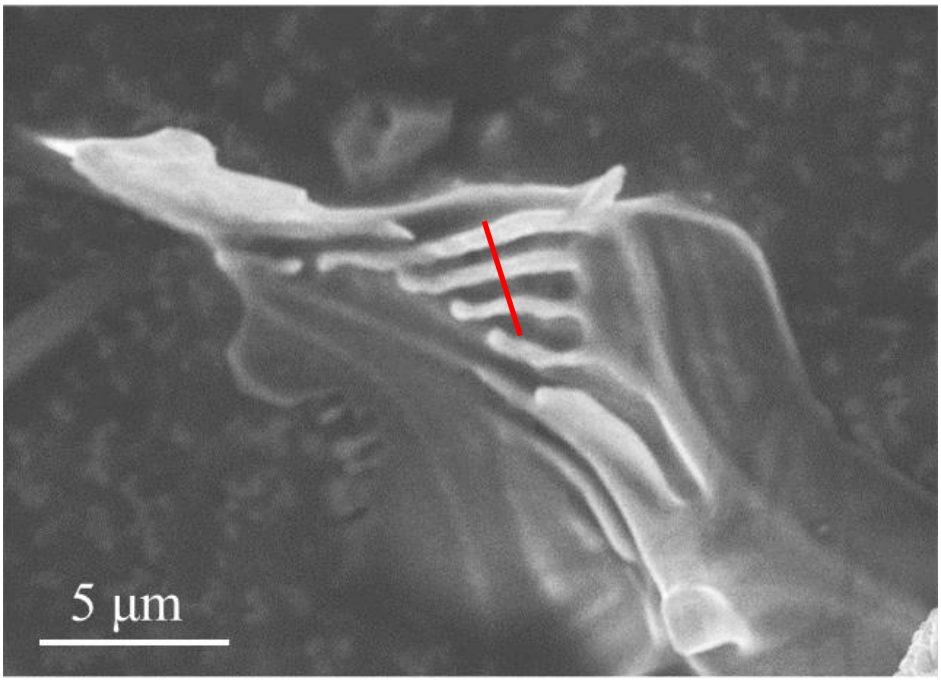

Fig 3.14 SEM micrograph showing dendritic arm spacing in intermetallic

4. Results and discussion I

4.1 Analysis of as-cast and homogenised 6xxx Al alloy

This study was conducted in order to analyse the effect of homogenisation on the microstructure with particular emphasis on intermetallics. In order to do so, two alloys of nearly similar composition, one as DC-cast and the other commercially homogenised, were chosen (please see section 3.1.2 for composition details). Grain size and the 2D and 3D microstructures of intermetallics in these alloys were studied in depth with the help of techniques such as optical microscopy, SEM, EDX and XRD. Center and edge sections of the billet as shown in Fig. 4.1 were also compared.

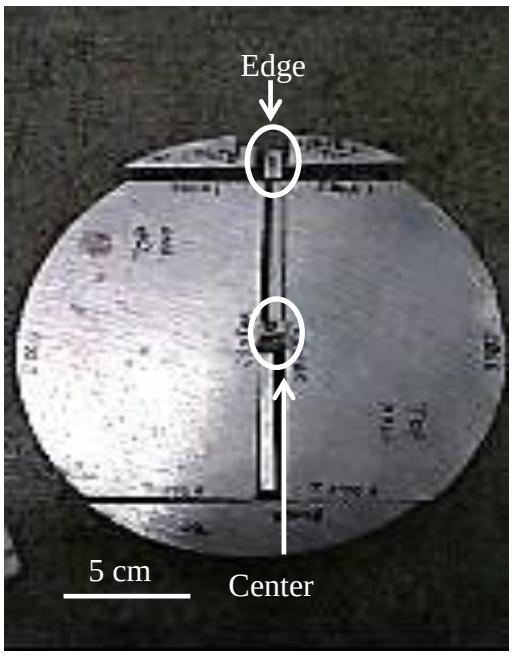

Fig. 4.1 Center and edge sections of a homogenised billet used for analysis

4.1.1 Grain size analysis

Fig. 4.2 shows the grain structure of the center and edge sections of the as-cast billet and homogenised billet. Features such as grain size and dendritic arm spacing (DAS) were measured to study the effect of homogenisation on the grain morphology. About 100 grains per sample were analysed to measure the average grain size and DAS. Table 4.1 gives the summary of the results measured. Homogenisation could have led to an increase in the grain size, as the material is held at high temperature for 5-10 hours which resulted in grain growth. The different solidification conditions like higher cooling rate, different casting speed (in Oxford DC caster) could also result in smaller grain size in as-cast alloy. Also, the center of the billet has a slightly higher average grain size and DAS as compared to the edge for both the alloys. This might be a variation in sampling or spatially in the structure because if the grain boundaries were moving they would create a much smoother grain shape.

4.1.1.1 As-cast billet

The majority of the grains observed in this billet were dendritic in nature. The average grain size at the edge of the billet was measured to be ~10% smaller than the average grain size at the center. The average grain sizes for the center and edge sections were 132±9µm and 110±8µm respectively. There was a very small change in the DAS which was well within experimental error limits. The DAS for center and edge sections were 23±4µm and 19±3µm respectively.

4.1.1.2 Homogenised billet

The majority of the grains observed in this billet were dendritic in nature. The average grain size at the edge of the billet was measured to be ~15% smaller than the average grain size at the center. The average grain sizes for the center and edge sections were 173±8µm and 155±9µm respectively. There was a very small change in the DAS which was well within experimental error limits. The DAS for center and edge sections were 32±4µm and 30±3µm respectively. Ideally, after homogenisation there should be no contrast in the local variation in composition. Homogenisation leads to a 30% increase in the grain size compared to the as-cast counterpart. The observation of dendritic structure in a homogenised alloy shows that the homogenisation process parameters were not chosen to reduce the variation in composition.

Table 4.1 Grain size and DAS for center and edge sections of as-cast and homogenised billet.

Billet / Section	As-cast (center)	As-cast (edge)	Homogenised (center)	Homogenised (edge)
Grain Size	132±9µm	110±8µm	173±8µm	155±9µm
DAS	23±4µm	19±3µm	32±4µm	30±3µm

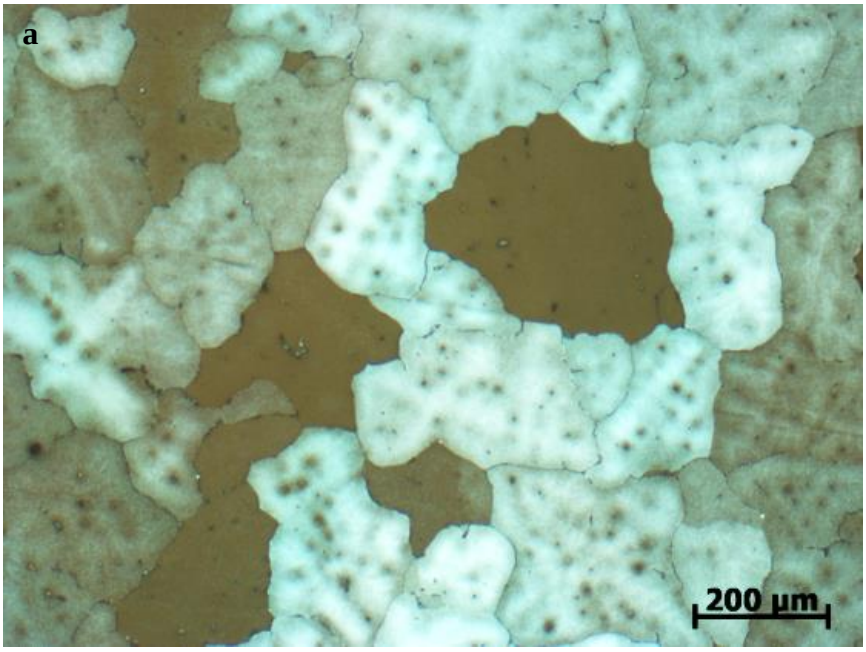

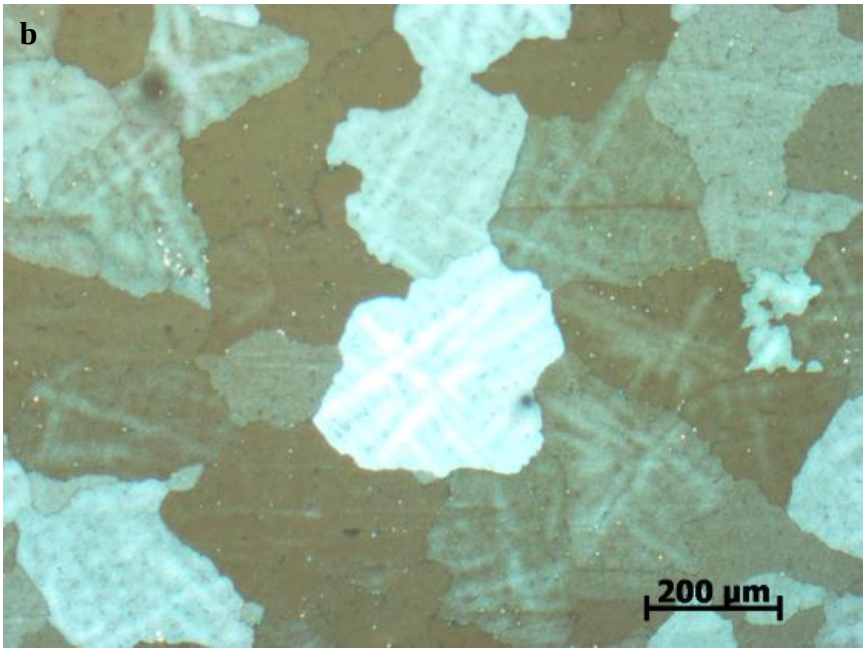

Continued overleaf…

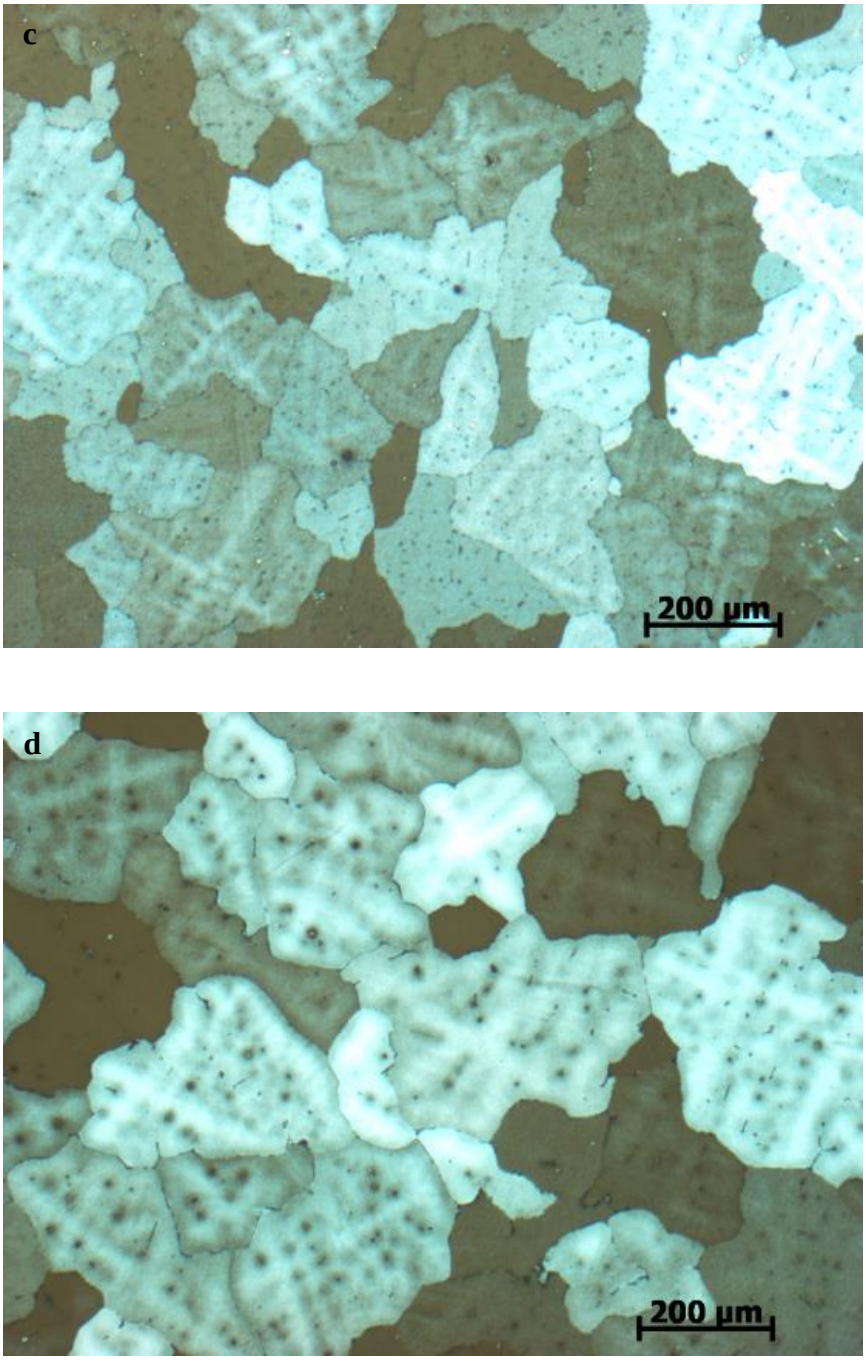

Fig. 4.2 Optical microscopy images showing the anodised grain structure of a) center of as-cast billet, b) center of homogenised billet, c) edge of as-cast billet and d) edge of homogenised billet

4.1.2 Characterisation of the 2D morphology of Fe intermetallics

2D analysis provides us with important information of the microstructure and the intermetallic morphology (Fig 4.3).

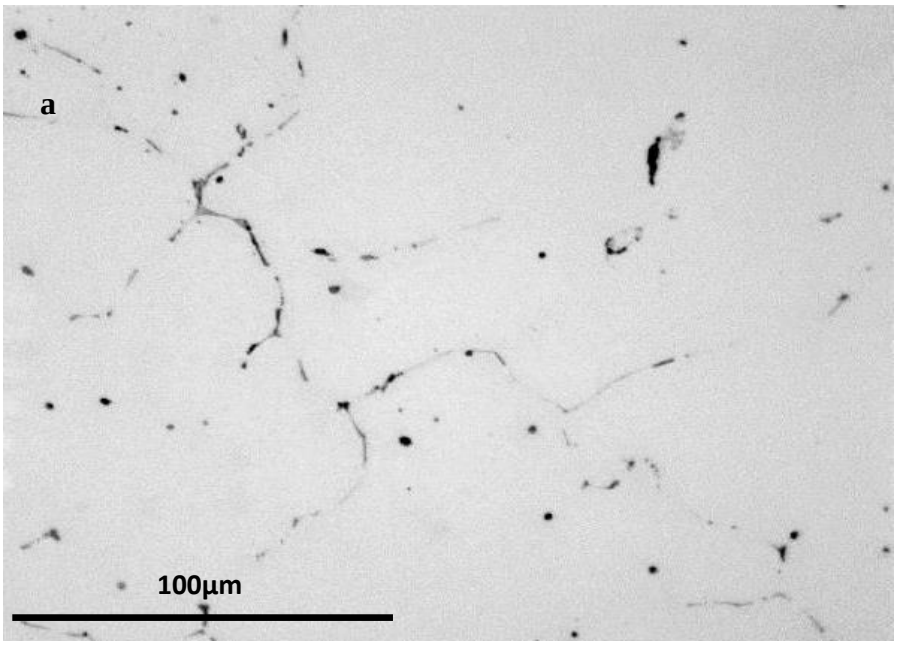

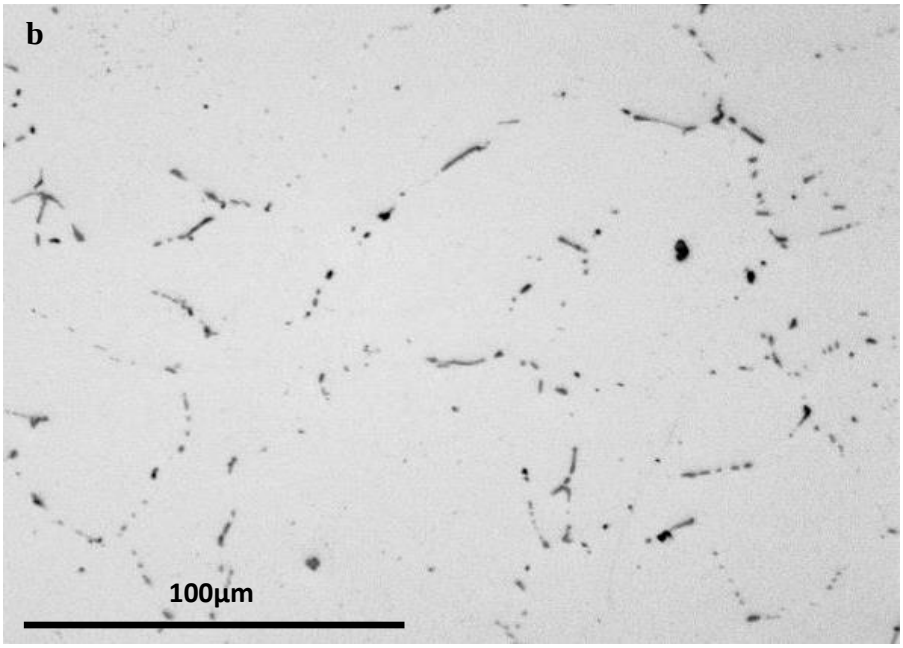

Continued overleaf…

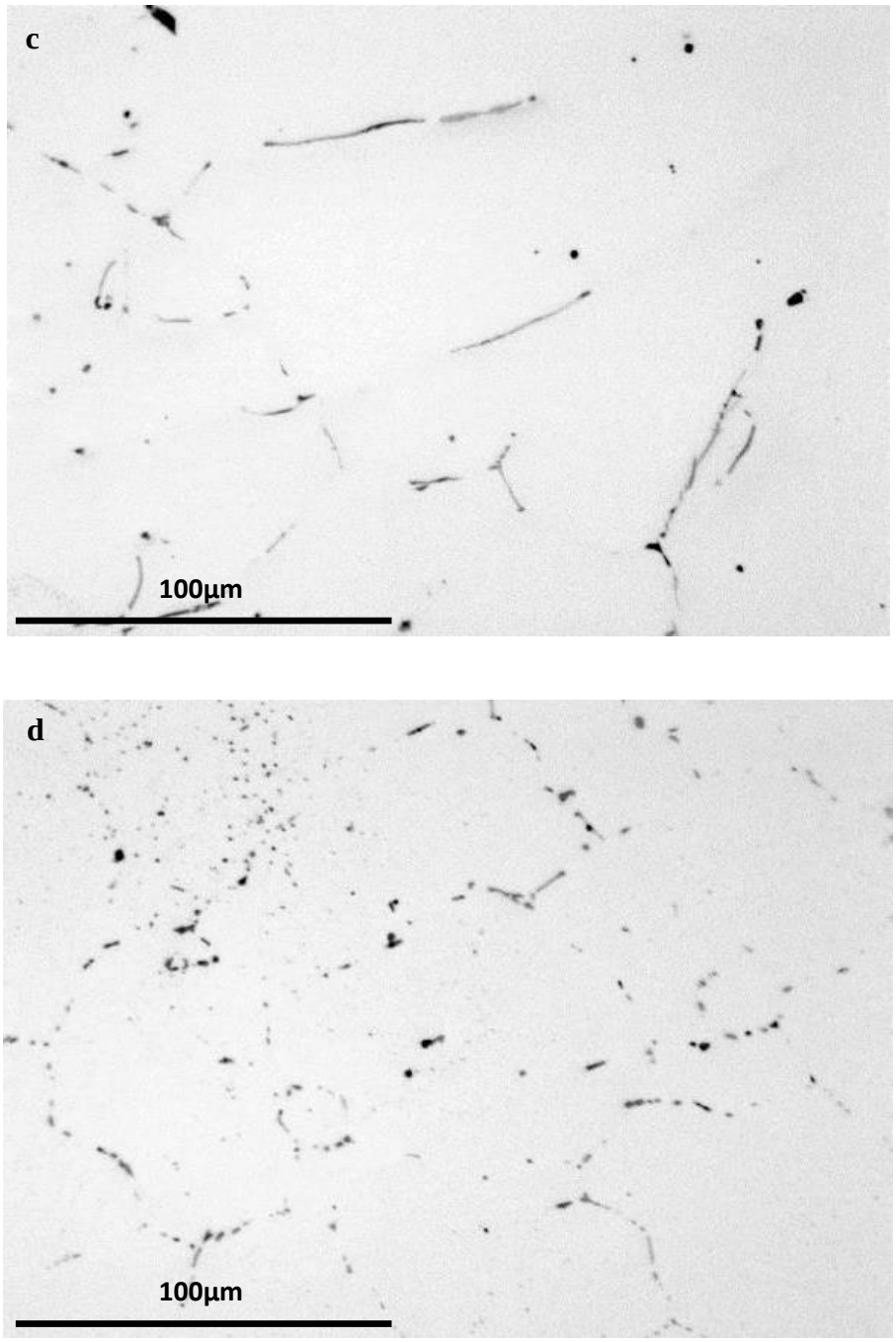

Fig 4.3 Optical microscopy images showing the microstructure of a) center of as-cast billet, b) center of homogenised billet, c) edge of as-cast billet and d) edge of homogenised billet

4.1.2.1 As-cast billet

The majority of intermetallics were observed on cell or grain boundaries. Fig 4.4 shows the intermetallics that were observed in the as-cast billet. Two main types of intermetallics were observed in their regular morphology i.e α-AlFeSi in dendrite-like morphology and β-AlFeSi in needle-like morphology as shown in Fig. 4.4c and 4.4d respectively. The intermetallics appeared to be more interconnected as compared to the homogenised billet see Fig 4.3.

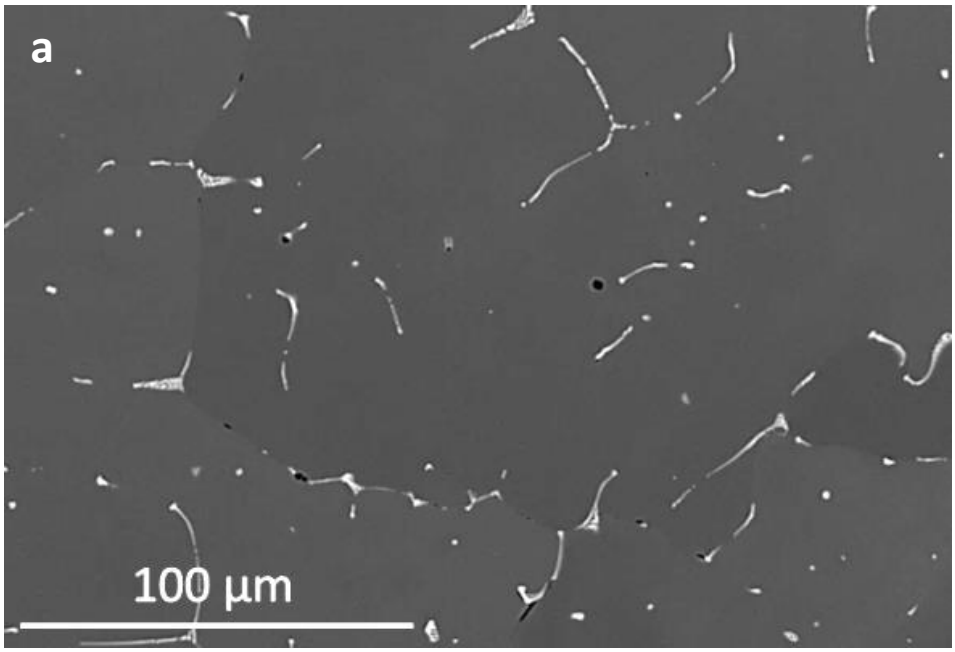

Continued overleaf…

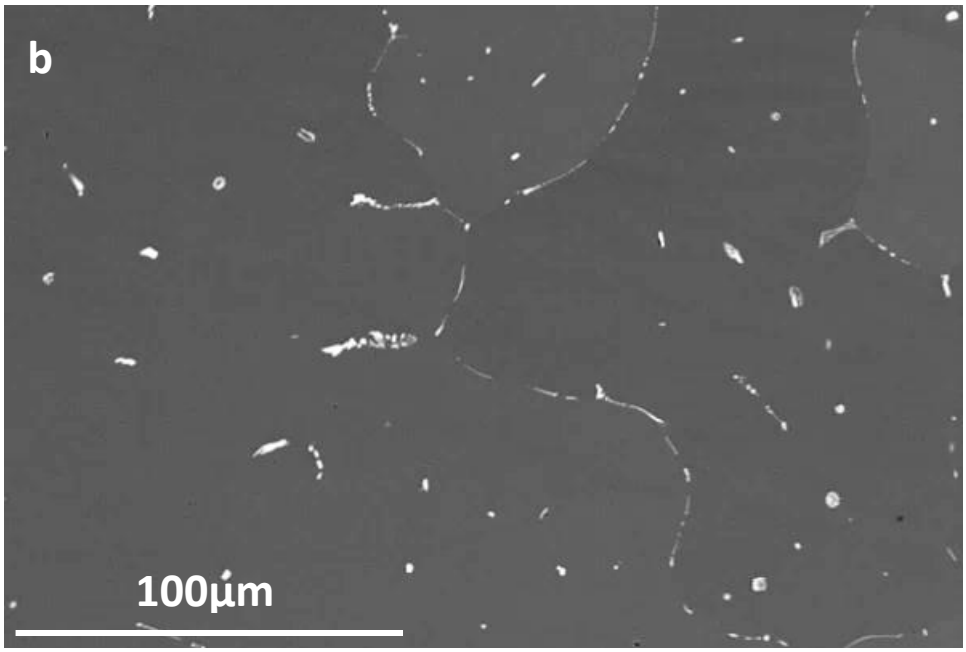

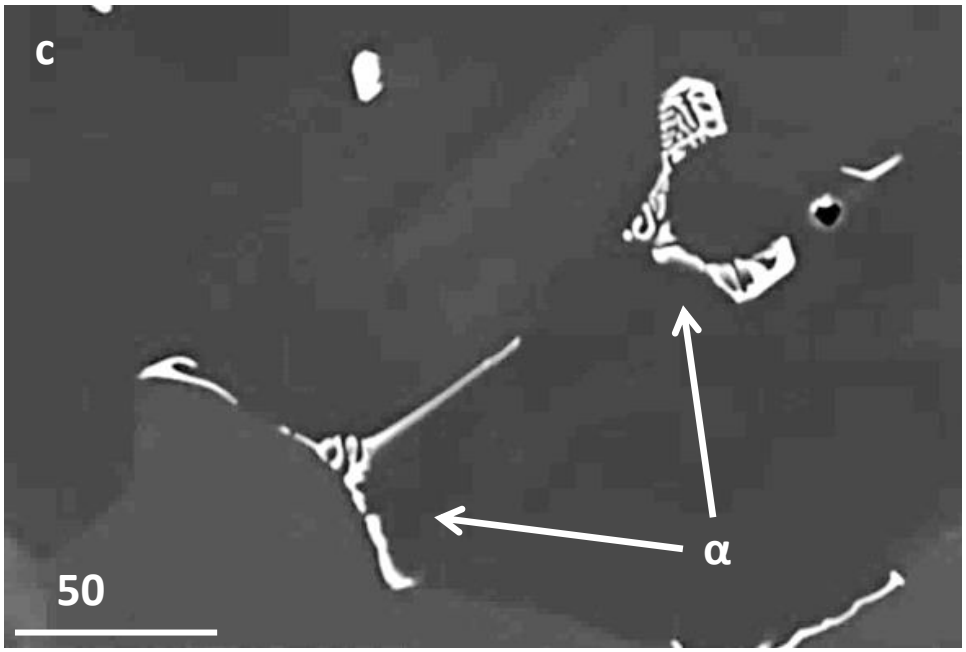

Continued overleaf…

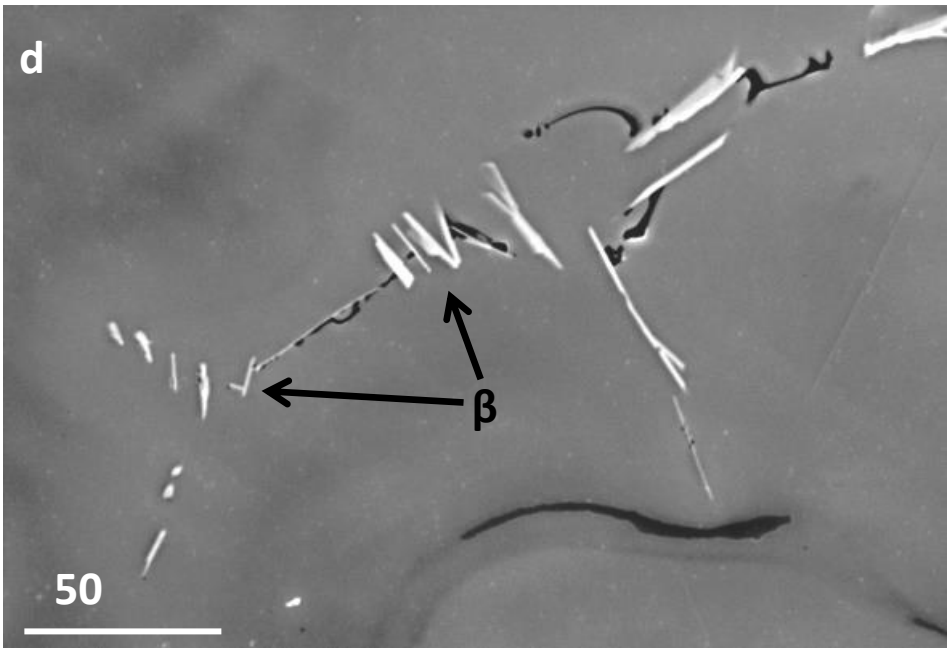

Fig 4.4 BSE micrographs showing intermetallics on grain and cell boundaries of a) center, b) edge of an as-cast sample, c) α-AlFeSi and d) β-AlFeSi.

About 50 measurements per sample were made from the 2D SEM micrographs to calculate the average length of the intermetallics which was determined to be 40±4μm. The intermetallics in the edge section appeared to be more interconnected as compared to the center section. The measured average lengths for center and edge sections were 44±3μm and 37±4μm respectively. The center and edge sections showed slight differences in the density of intermetallics. Grey scale quantification showed the intermetallic percentages to be 2.2% and 2.0% in the center and edge sections respectively.

4.1.2.2 Homogenised billet

The majority of intermetallics were observed on the cell or grain boundaries. Fig 4.5 shows the two main types of intermetallics observed in their regular morphology i.e α-AlFeSi in dendrite-like morphology as shown by black arrows and β-AlFeSi in needle-like morphology as shown by white arrows. The intermetallics appeared to be more broken and less interconnected compared to the as-cast billet. About 50 measurements per sample were made from the 2D SEM micrographs to calculate the average length of the intermetallics which was determined to be 27±5µm. The calculated average length of the intermetallics for homogenised billet was ~40% smaller than in the as-cast billet.

The intermetallics in the edge section appeared to be more broken compared to the center section. The measured lengths for center and edge sections were 29±3µm and 24±4µm respectively. Fig 4.6 shows the intermetallics in the edge and center sections. The center and edge sections showed slight difference in the density of intermetallics. Grey scale quantification showed the intermetallic percentages to be 2.1% and 1.6% in center and edge sections respectively.

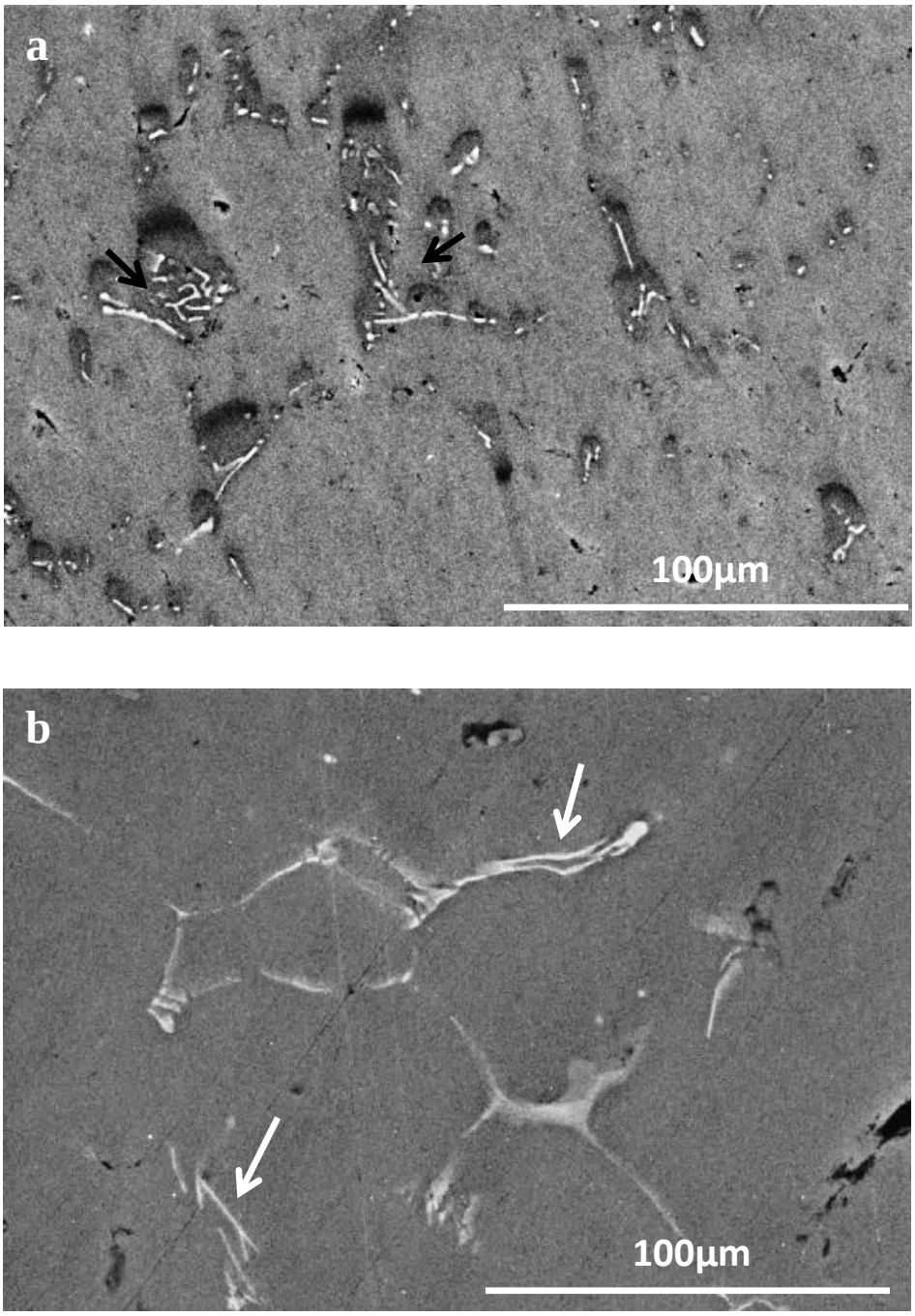

Fig 4.5 SEM micrographs of homogenised billet showing a) SE image of dendrite-like morphology of α-AlFeSi b) BSE image of needle-like morphology of β-AlFeSi

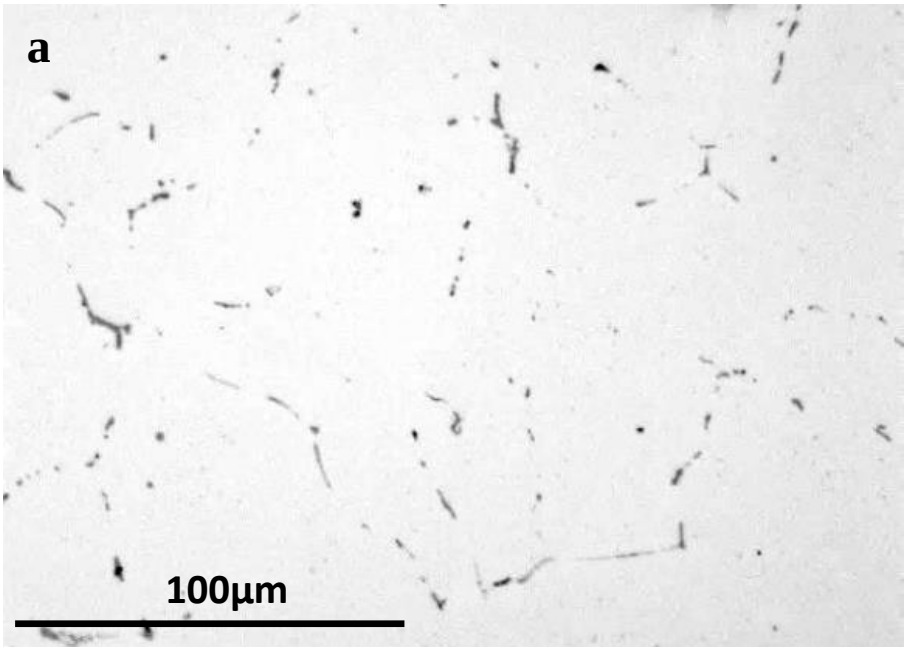

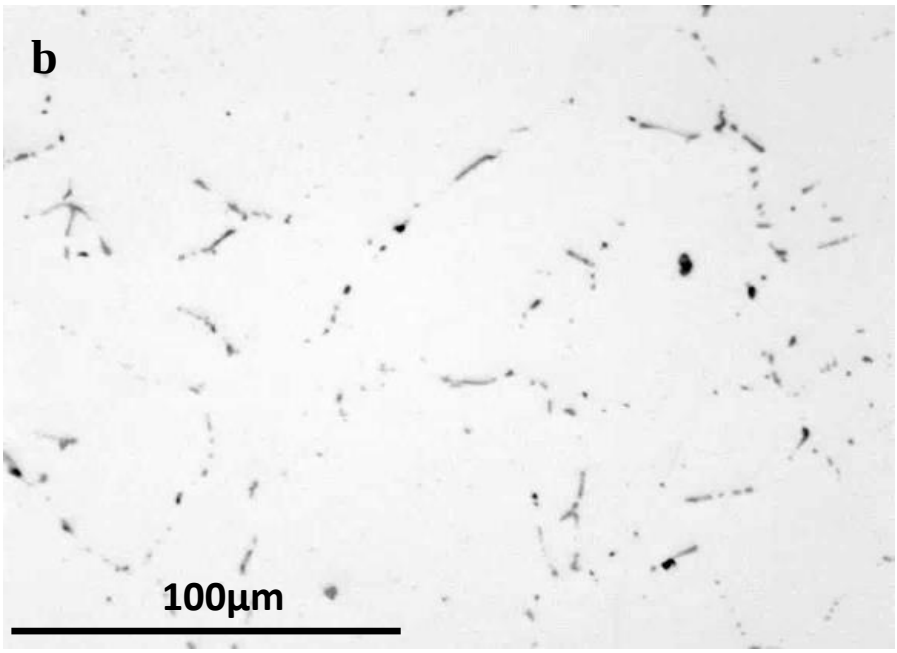

Continued overleaf…

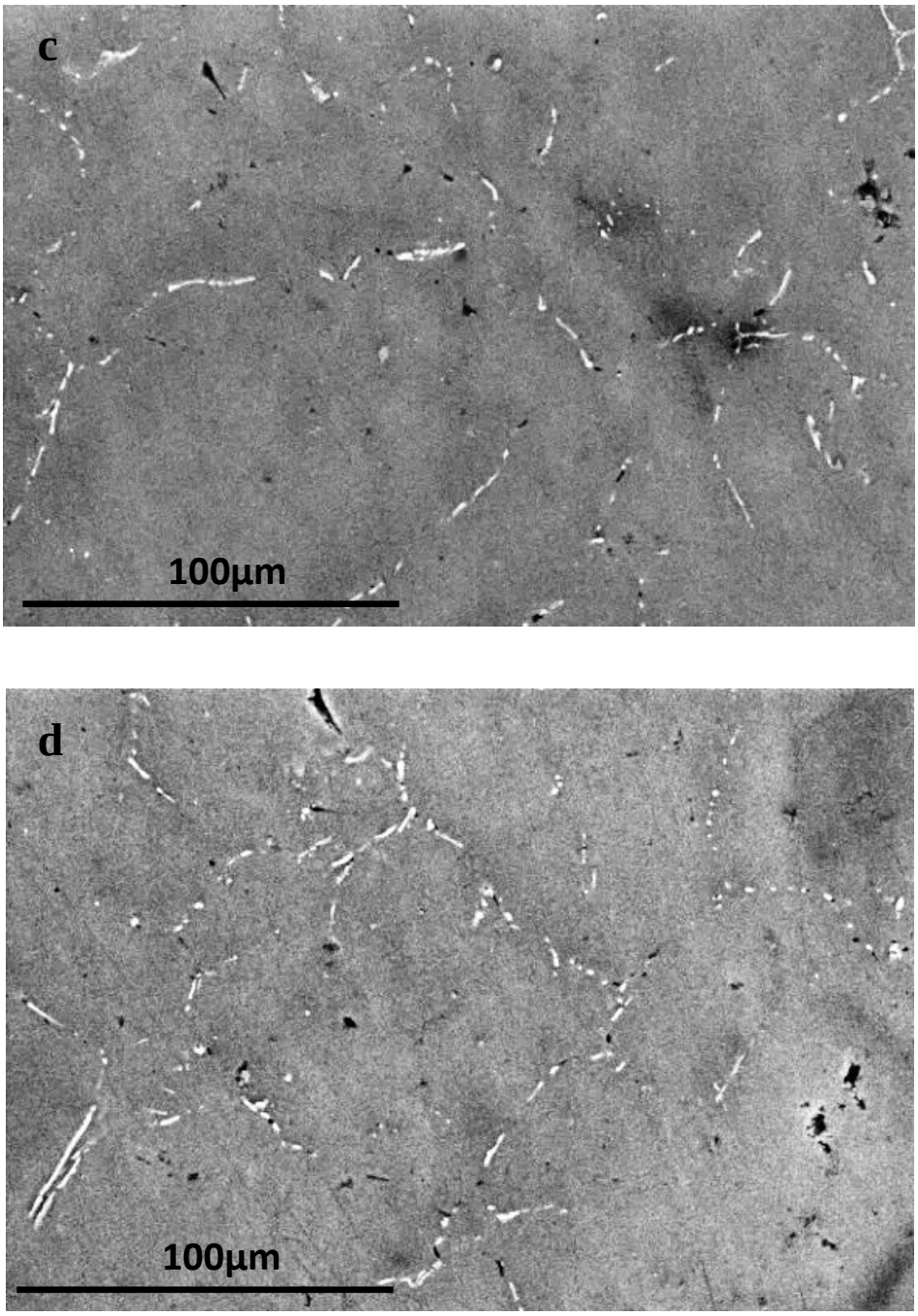

Fig 4.6 Optical micrographs showing broken intermetallics in a) center of homogenised billet, b) edge of homogenised billet, c) SE micrographs showing intermetallics on grain boundaries in c) center of homogenised billet and d) edge of homogenised billet

4.1.3 Characterisation of the 3D morphology of Fe intermetallics

3D analysis provides more complete information on the morphology of the intermetallics and the interconnectivity between them than 2D analysis is able to provide. The 3D morphologies of the intermetallics observed can be correlated very well with their 2D morphologies.

4.1.3.1 As-cast billet

Fig 4.7 shows the intermetallic from the center and edge sections of the as-cast billet. Two main types of intermetallics were observed in their regular morphologies i.e α-AlFeSi in flower-like morphology and β-AlFeSi in platelet/rod-like morphology. Fig 4.8 shows the different features of the α-AlFeSi and β-AlFeSi intermetallics. Features such as folds, ripples and protrusions were frequently noted on AlFeSi intermetallics. Intermetallics in the edge section were possibly more interconnected compared to the center section. About 50 measurements were made to calculate the average interconnectivity and were measured to be 89±5μm and 97±6μm for center and edge sections respectively.

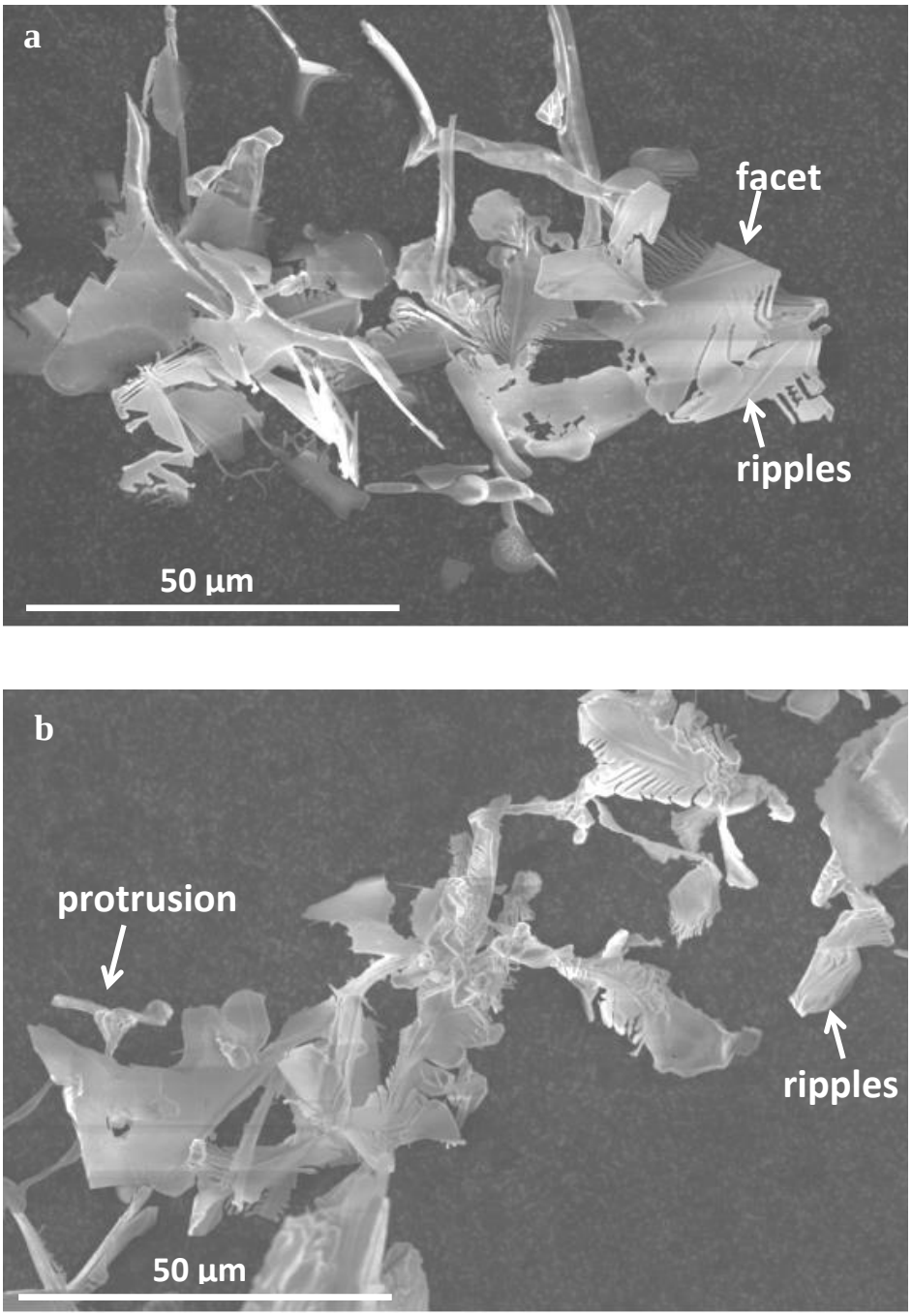

Fig 4.7 SE micrographs showing extracted intermetallics showing a) center of as-cast billet and b) edge of as-cast billet

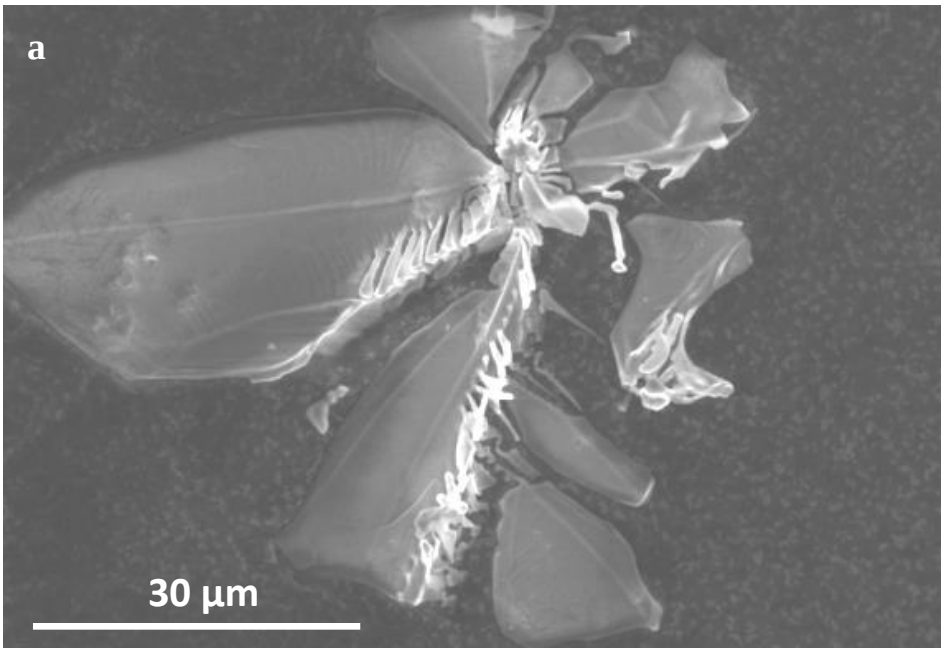

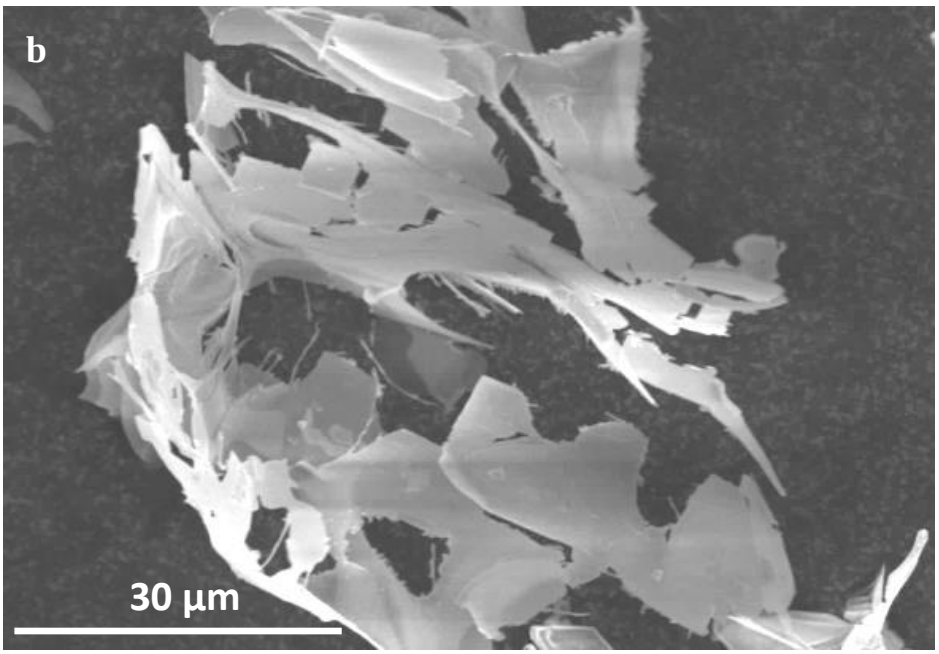

Continued overleaf…

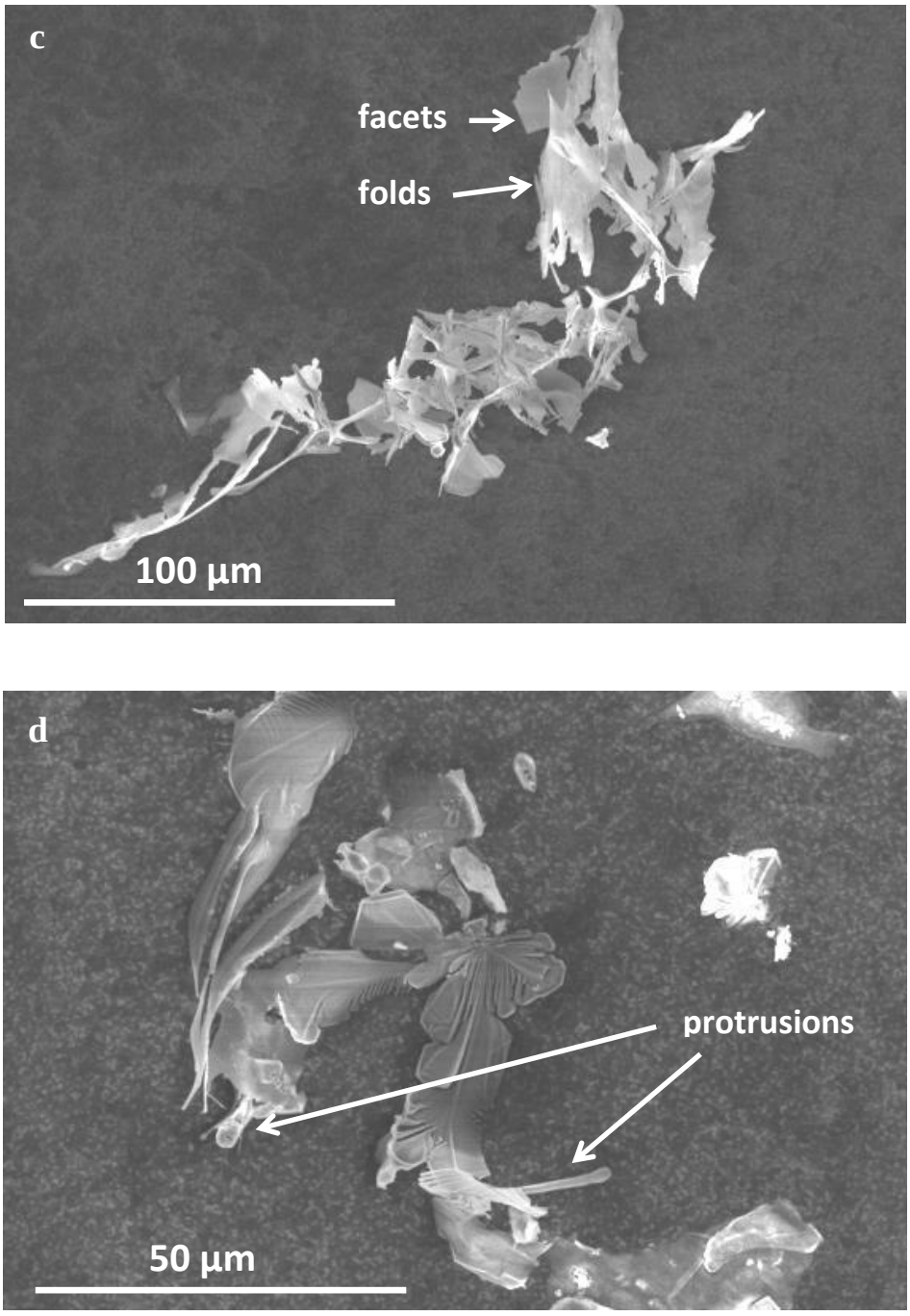

Fig 4.8 SE micrographs showing extracted intermetallics of as-cast billet showing a) α-AlFeSi, b) β-AlFeSi, c) and d) showing the faceted nature of the intermetallics

4.1.3.2 Homogenised billet

Fig 4.9 shows the microstructure of the center and edge sections of the homogenised billet. Again the two main types of intermetallics were observed in their regular morphology i.e α-AlFeSi in flower-like morphology and β-AlFeSi in platelet/rod-like morphology. Fig 4.10 shows the different features of the α-AlFeSi and β-AlFeSi intermetallics. Features such as facets, folds, ripples and protrusions were approximately three times more frequently observed on α-AlFeSi intermetallics of as-cast sample as compared to homogenised sample. Homogenisation resulted in possibly higher interconnectivity between intermetallics in the center compared to the edge section i.e interconnectivity was measured to be 52±5μm and 45±6μm for center and edge sections respectively. It is interesting to note that the facets of the α-AlFeSi intermetallics are smoothed out/dissolve due to homogenisation as shown in Fig 4.10c and Fig 4.10d by red arrows. This is discussed further in section 4.1.5.2. Table 4.2 summarises the effect of homogenisation on the interconnectivity between intermetallics and the area fraction of the intermetallics in the center and edge sections of the billet.

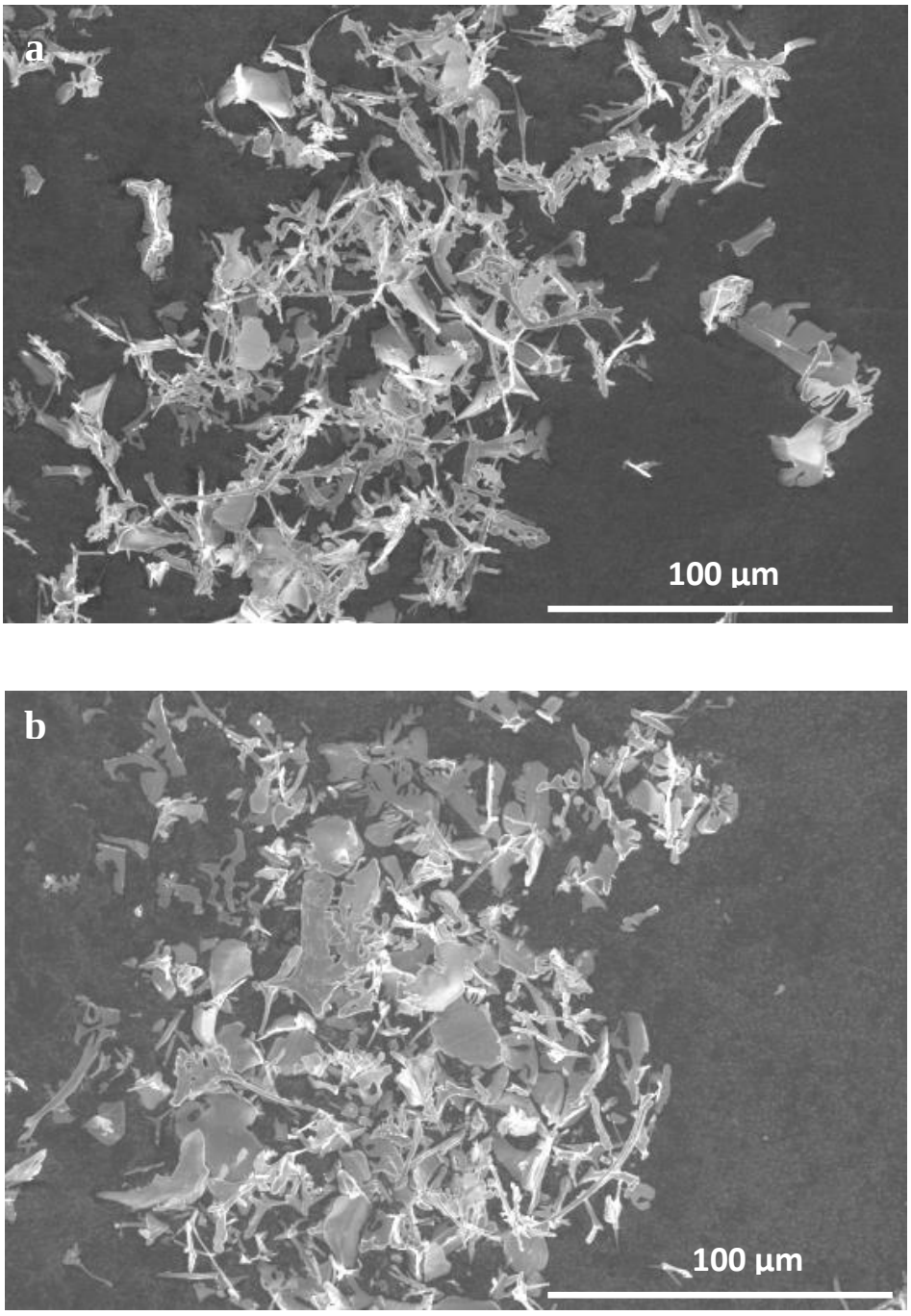

Fig 4.9 SE micrographs showing extracted particles at a) center of homogenised billet and b) edge of homogenised billet

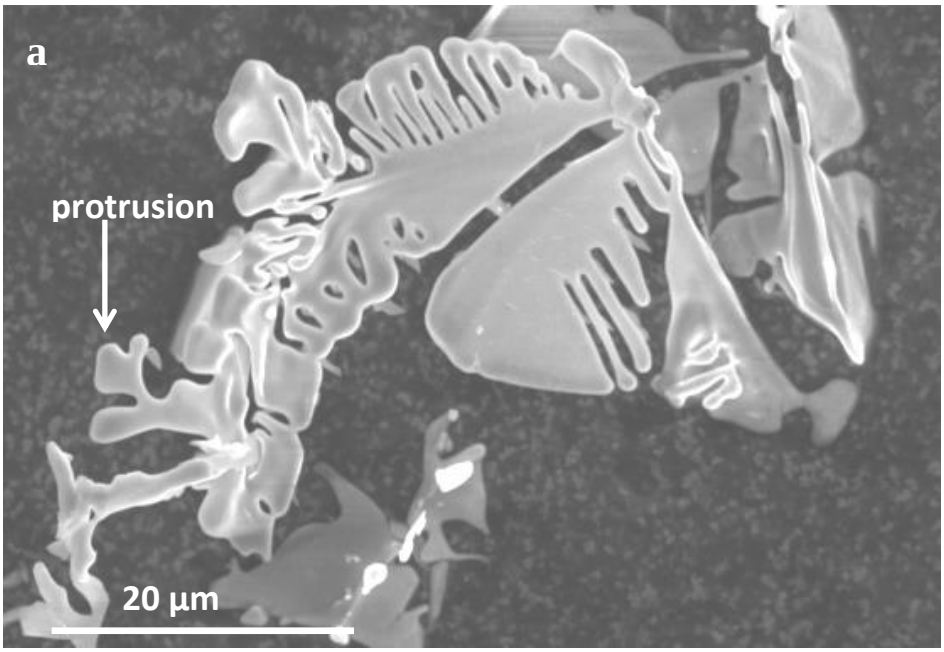

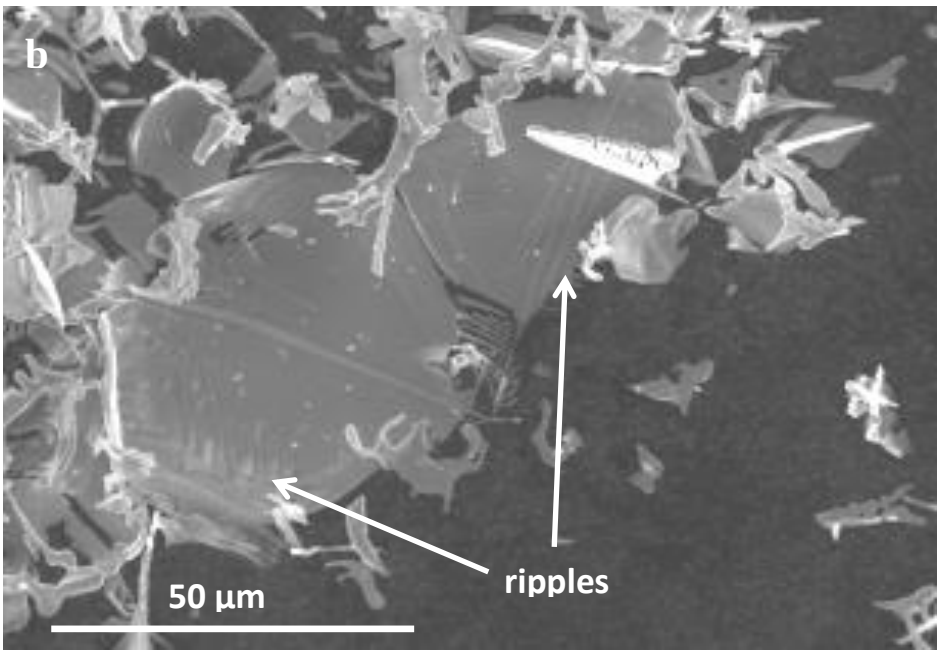

Continued overleaf…

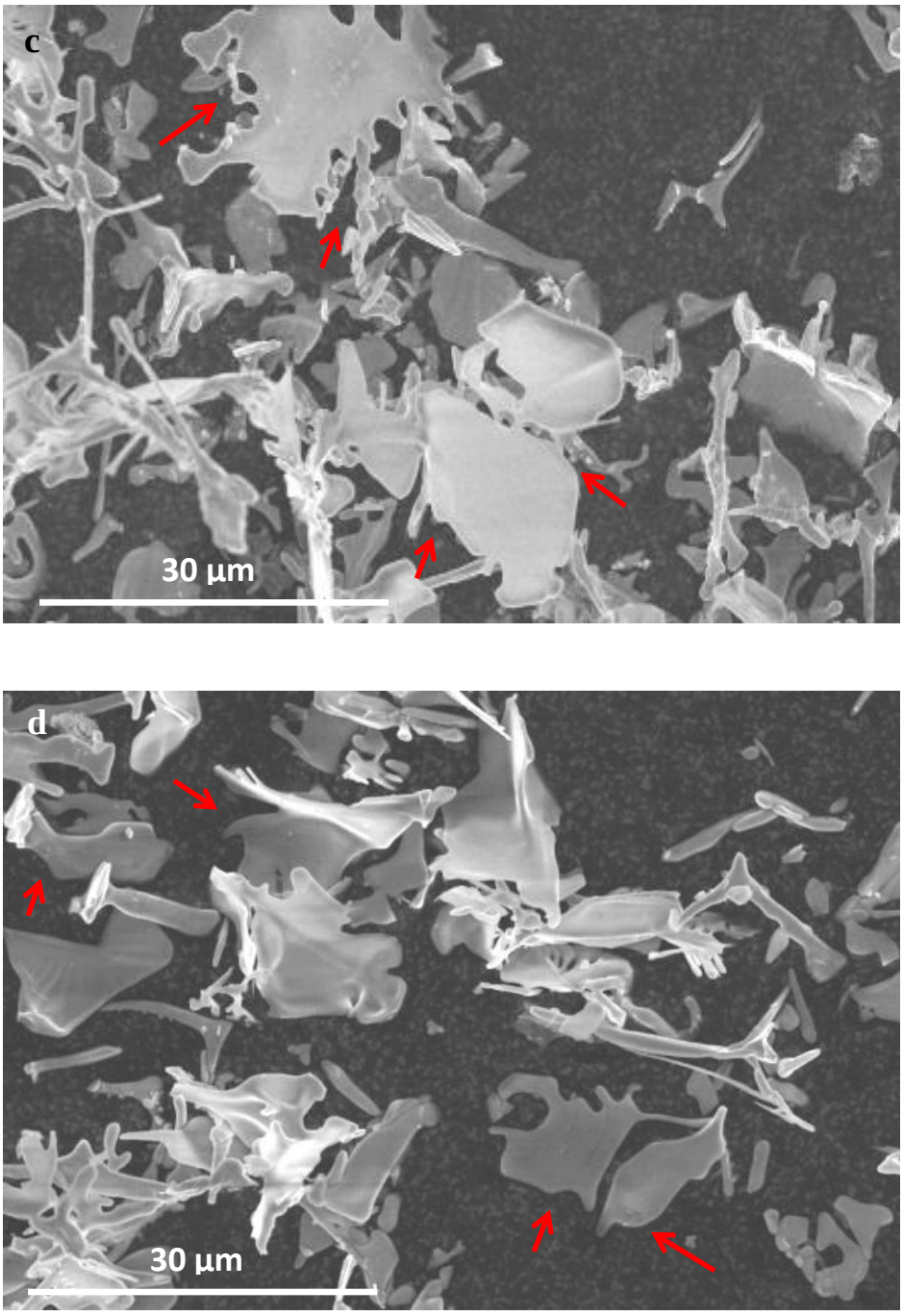

Fig 4.10 SE micrographs showing a) α-AlFeSi, b) β-AlFeSi, c) and d) shows the spheroidising effect of homogenisation on extracted intermetallics

Table 4.2 Summary of the results for the center and edge sections of the as-cast billet and homogenised billet.

Billet / Section	As-cast (center)	As-cast (edge)	Homogenised (center)	Homogenised (edge)
Inter-connectivity (from 3D)	89±5µm	97±6µm	52±5µm	45±6µm
Area fraction of intermetallics (from 2D)	2.2%	2.0%	2.1%	1.6%

4.1.4 X-ray diffraction

XRD analysis provided important quantitative information on the different phases present in the alloy which cannot be obtained from other techniques. Fig 4.11a shows the XRD traces of the extracted intermetallics from as-cast and homogenised samples along with the reference traces for α-AlFeSi, β-AlFeSi and Mg_2Si. Most of the major peaks belonged to AlFeSi-rich intermetallics i.e. α-AlFeSi or β-AlFeSi. Ideally Mg based phases should be dissolved completely during homogenisation **(Dons, 01)**, but some peaks of Mg_2Si phase were still

observed, with relatively low intensity. The small quantity of this phase explains its rare observation during SEM analysis. A magnified trace is shown in Fig. 4.11b for the zone 2θ= 40 - 50 due to the presence of many peaks. Lower Fe/Si ratio in as cast alloy in comparison with homogenised alloy could also contribute to higher amount of β-AlFeSi in as cast alloy (see section 2.2.4).

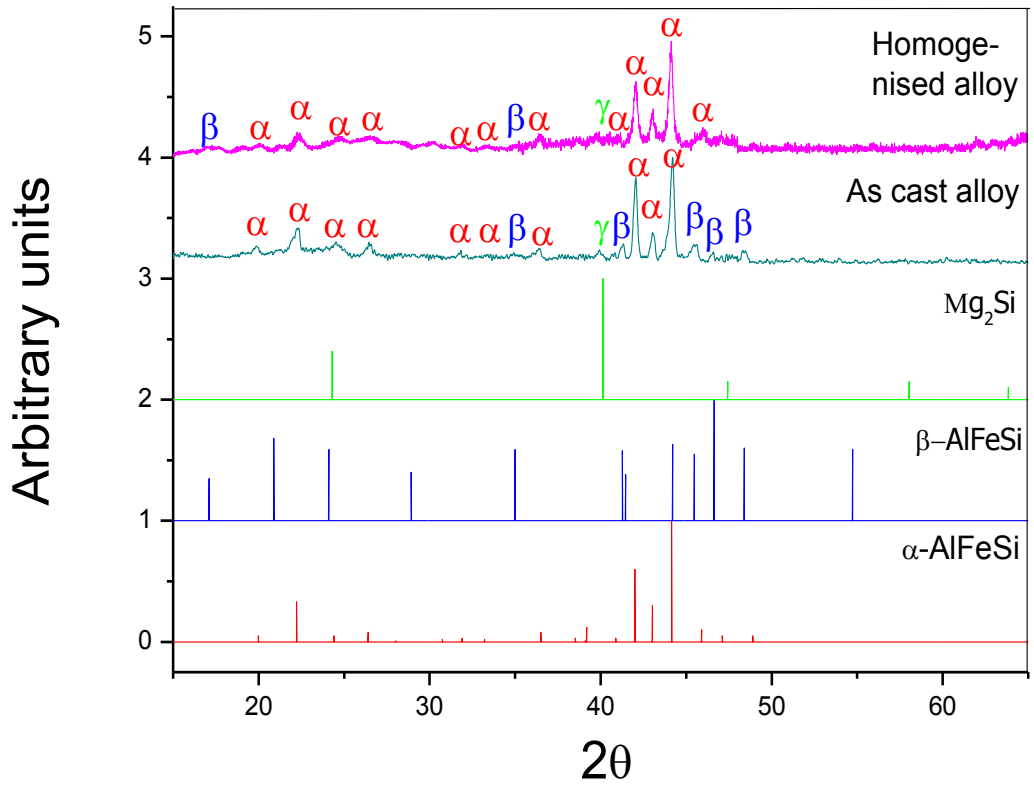

Fig 4.11a XRD plot of extracted intermetallics from homogenised and as-cast billet showing α-AlFeSi and β-AlFeSi peaks (see Appendix I)

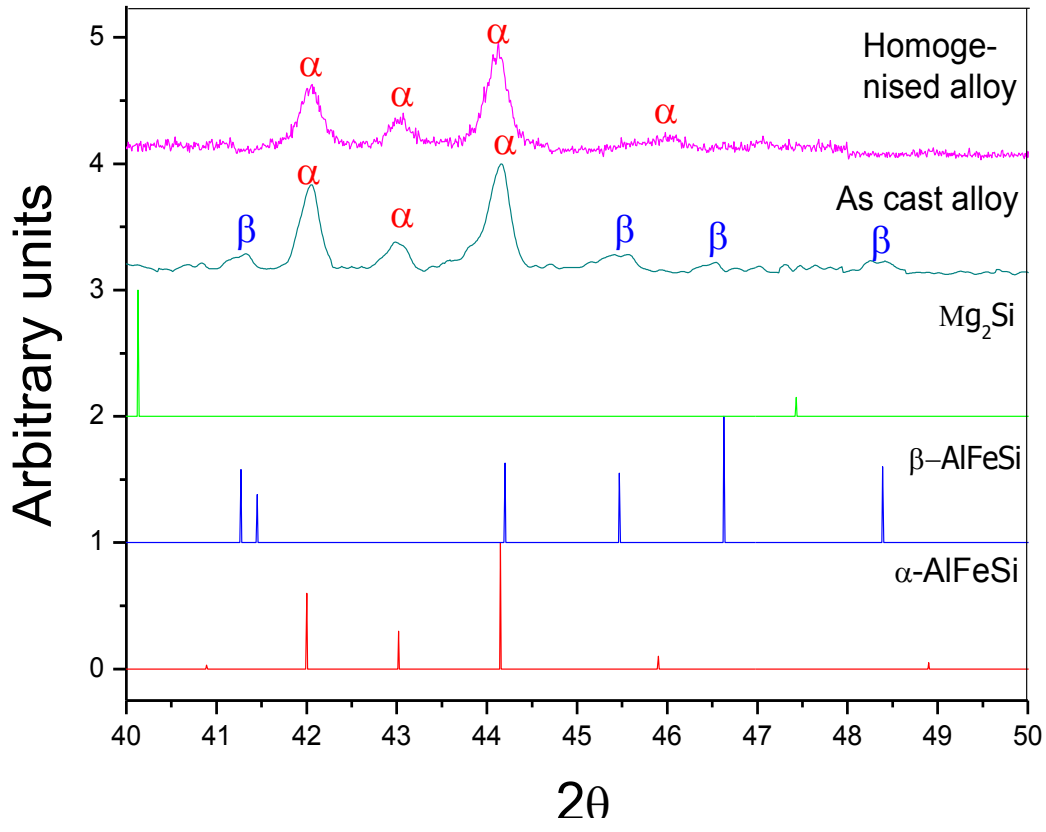

Fig. 4.11b Magnified XRD plot for the region 2θ=40 to 2θ=50 showing the overlapping of the α-AlFeSi and β-AlFeSi (see Appendix I)

4.1.4.1 As-cast billet

The highest peaks belong to α-AlFeSi (44.15°, 42°, 43.01°, 22.22°) or β-AlFeSi (41.27°, 45.47°, 46.63°, 48.39°) which shows that both the phases were present in significant amounts. Another peak with lower intensity was observed at 40.13° which could be attributed to Mg_2Si. Regression analysis confirmed the weight fractions of the phase content. α-AlFeSi was calculated to have 65% weight fraction, whereas β-AlFeSi had 35% (see section 3.6.4 for more details

on calculations). Two other peaks with relatively higher intensities corresponding to β-AlFeSi (41.4^{o} and 35.4^{o}) were also visible.

4.1.4.2 Homogenised billet

All of the highest peaks belong to α-AlFeSi (44.15^{o}, 42^{o}, 43.01^{o}, 22.22^{o}), which shows it's presence as the dominant phase. Two other peaks with relatively low intensities corresponding to β-AlFeSi (17.1^{o} and 34.99^{o}) were also visible. Another peak observed at 40.13^{o} can be attributed to Mg_2Si, was of lower intensity as compared to as-cast sample. Regression analysis confirmed the dominance of α-AlFeSi phase by calculating weight fractions of the phases. α-AlFeSi was calculated to have 80% weight fraction, whereas β-AlFeSi had only 20% (see section 3.6.4 for more details on calculations). This shows the absence/conversion of β-AlFeSi particles due to homogenisation process.

4.1.5 Effect of homogenisation on the Fe intermetallics

The major types of intermetallics present in 6xxx series were described in section 2.4. However, in this section we will mainly discuss the effect of the homogenisation process on the 2D and 3D morphologies of the two most important Fe bearing intermetallics i.e. α-AlFeSi and β-AlFeSi. Both α-AlFeSi and β-AlFeSi were observed in their well-defined morphologies which form eutectically from high Si content liquid **(Merchant et al., 66)**. The dominance of

α-AlFeSi over β-AlFeSi in homogenised alloys is also in accordance with the literature **(Allen et al., 98)** and **(Mondolfo et al., 67)**.

4.1.5.1 Effect of homogenisation on 2D microstructure of Fe intermetallics

The intermetallics were mainly observed at the cell or grain boundaries as shown in Fig. 4.6. As the liquid undergoes non-equillibrium solidification, solute elements such as Fe and Si (in this alloy) segregate at the solid/liquid interface. As a result, there is a high concentration of solute elements in the final liquid which thermodynamically favours the formation of intermetallic. The final liquid takes up the interdendritic spaces between the solidified α-Al leading to the complex dendritic/platelet morphology of the intermetallics due to eutectic reaction (**Kuijpers et al., 04)**. The intermetallics also appeared to be broken in comparison with the as-cast alloy as shown in Fig. 4.3. The reduction in the size of the intermetallics and interconnectivity can be attributed to the phenomena of dissolution and reduction of large intermetallics into smaller ones during the homogenisation process **(Tanihata et al., 99)** and **(Kuijpers et al., 02a)**. This may be due to solute transfer from solute rich regions to solute deprived regions resulting in a more uniform microstructure or transformation of metastable β-AlFeSi phase to equilibrium α-AlFeSi phase **(Zajac et al., 96)**.

The intermetallics in the edge section were measured to be smaller compared to the center of the homogenised alloy. This can be linked with the DC casting process and improper homogenisation process. Cooling rate in the edge section

in DC casting is higher than the centre (see section 2.3). As a result, the center part also showed relatively higher interconnectivity. Also, the existing non-uniformity in composition resulted in different size of the intermetallics. However, nothing can be confirmed until the 3D morphology is verified. The typical Chinese script morphology of the α-AlFeSi was observed because of the slow advancing of the solid/liquid interface which resulted in branched growth process and because it's a eutectic reaction **(Quintero et al., 86)**.

4.1.5.2 Effect of homogenisation on 3D microstructure of Fe intermetallics

Identifying Fe-rich intermetallics (mainly α-AlFeSi and β-AlFeSi) is a very difficult task because of their complex geometry and range of composition. SEM and EDX techniques were used on extracted intermetallics for qualitative analysis of the microstructure. In order to obtain quantitative analysis, XRD proves to be the optimum method. It is the combined information from these three techniques along with the information from 2D analysis that gives a clear picture of the changes in the microstructure. The intermetallics present in the as-cast alloy were very faceted in nature as compared to the homogenised alloy. The dissolution of the faceted sides of the intermetallics in the homogenised alloy is clear as shown in Fig. 4.12 by white arrows.

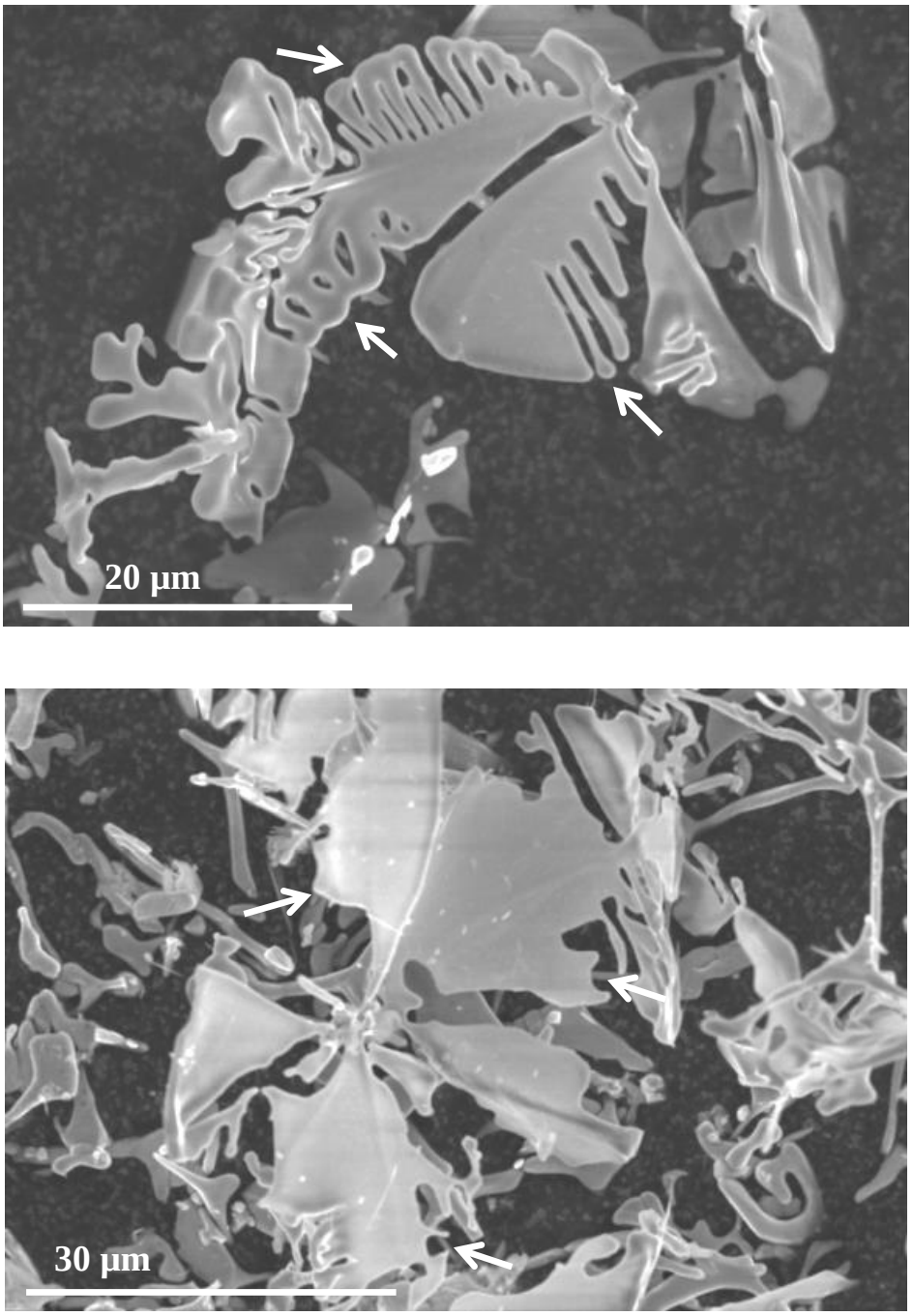

Fig 4.12 SE micrographs of extracted intermetallics showing the spheroidisation effect of the homogenisation process.

During homogenisation, diffusion of solute elements takes place. The faceted/sharp edges of the intermetallics are thermodynamically favourable for diffusion, which causes the spheroidising effect. As a result, time and temperature become the most important factors in determining the quality of homogenisation. Few faceted particles were observed which indicated that the spheroidization of interemetallics occurred partially.

The relative fraction of β-AlFeSi was reduced from 40% in the as-cast alloy to 20% in the homogenised alloy. This can be attributed to the transformation of β-AlFeSi platelets to the more rounded α-AlFeSi phase during homogenisation which is favoured by the presence of small amounts of Mn **(Zajac et al., 93)** and **(Musulin et al., 90)**. Some suggest that the heterogeneous nucleation and growth of α-AlFeSi can occur on β-AlFeSi platelets which results in the rounding-off of the β-AlFeSi intermetallics **(Kuijpers et al., 04)**. However, the other less likely possibility could be the complete dissolution of faceted β-AlFeSi phase in one place and the nucleation of α-AlFeSi phase at another chemically and structurally favourable point. This mechanism will be very slow as diffusion of Fe and Si would be the rate determining step and as a result won't be preferred **(Kuijpers et al., 04)**. Also, XRD analysis still showed the presence of β-AlFeSi intermetallics which confirmed that the homogenisation time and temperature is not fully satisfactory and needs to be optimised in this case.

4.2 Effect of cooling rate on different sections of TP1 test sample

In order to analyse the effect of cooling rate on different sections of the TP1 test sample, four samples at a distance of 12.5mm, 25mm, 38mm and 50mm from the bottom of the mould were analysed. The observations in this study suggest that cooling rate not only influences the Al grain size but also influences the intermetallic phase selection and their size, morphology and interconnectivity. The alloys used for this study are explained in section 3.1.3.1.

4.2.1 Microetching analysis

This study showed the variation in grain structure of different sections of the TP1 mould. The samples for grain structure analysis were anodised using Barker's reagent. Features such as grain size and dendritic arm spacing (DAS) were measured to analyse the effect of cooling rate in the different sections. About 100 grains were analysed to measure the average grain size and DAS using the method described in chapter-3.

Fig 4.13 shows the measured average grain size and DAS. As we move from bottom to top of the TP1 sample, the average grain size and DAS both were observed to increase as the cooling rate decreased. It was interesting to note that the range of the grain sizes measured for all the samples lies between 30 μm to 350 μm with few exceptions. The standard deviation also steadily increased along with the grain sizes as we move from bottom to top of the TP1 sample.

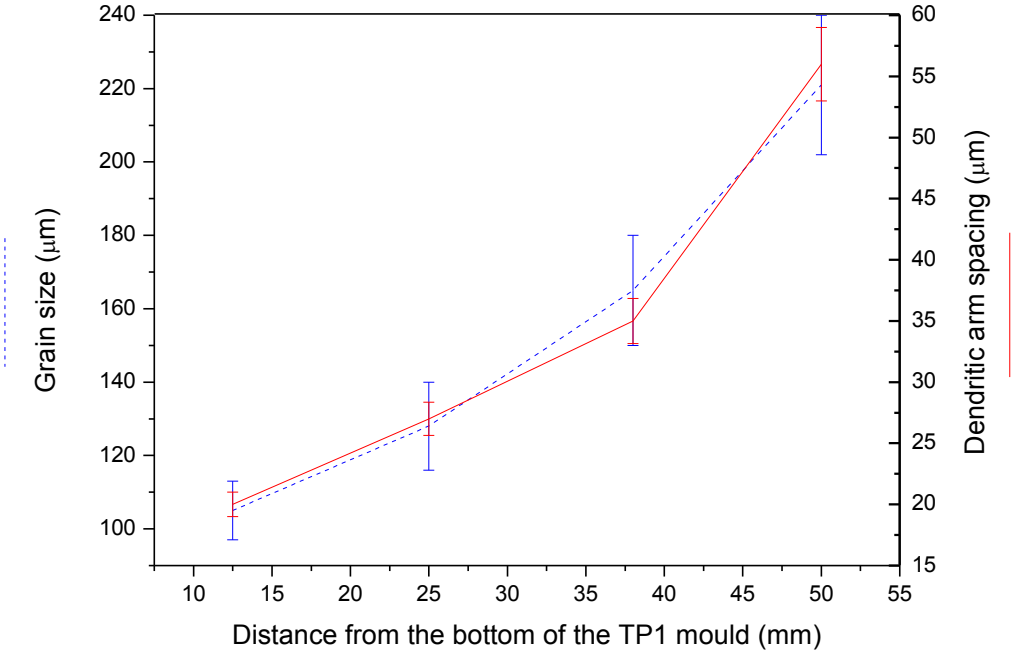

Fig 4.13 Variation of grain size and dendritic arm spacing as a function of the distance from the bottom of the TP1 mould.

The change in DAS suggested that different positions experience different cooling rates. The cooling rates for this system were calculated from the measured DAS using the following empirical equation for Al-Fe-Si alloys (1) **(Westengen et al., 82)** and **(Mulazimoglu et al., 96)**:

$$V = 3.57 \times 10^4 DAS^{-2.56} \quad (1)$$

where V is the cooling rate, Ks^{-1}. The cooling rates calculated with this equation will be compared with the measured cooling rate curve of the TP1 mould **(Tanihata et al., 99)** in a later section. The change in cooling rate at different positions in the TP1 mould was attributed to the heat extraction from the mould by the controlled flowing water (gallon/min) at the bottom. The increase in

cooling rate increases the undercooling temperature and results in the formation of large numbers of fine nuclei in the melt during solidification which leads to fine grains and DAS in the samples close to the bottom of the TP1 mould. The measured grain sizes, DAS and cooling rates for different positions are discussed below.

4.2.1.1 12.5mm

Fig. 4.14a shows the anodized microstructure of the section at 12.5mm. The grains were observed to be dendritic in nature. The grain size and DAS measured for this section were 105±5μm and 20±1μm respectively. The cooling rate calculated using the measured DAS was 16.6 K/s which was in agreement with the measured cooling rate **(Tanihata et al., 99)**.

4.2.1.2 25mm

Fig. 4.14b shows the anodized microstructure of the section at 25mm. The average grain size was slightly larger than the 12.5mm section and was measured to be 128±7μm. The grains observed were dendritic in nature and the DAS measured for this section increased to 27±2μm. The cooling rate calculated using the measured DAS showed a sharp drop compared to the 12.5mm section. The calculated cooling rate for the 25mm section was 7.7 K/s and was in agreement with the measured cooling rate **(Tanihata et al., 99)**.

4.2.1.3 38mm

Fig. 4.14c shows the anodized microstructure of the section at 38mm. The average grain size increased steeply and was measured to be 165±9μm. The grains observed were dendrite in nature and the DAS measured increased further to 35±4μm. The cooling rate calculated using the measured DAS showed a steep drop as compared to the 25mm section. The calculated cooling rate for the 38mm section was 3.9 K/s and was in agreement with the measured cooling rate **(Tanihata et al., 99)**.

4.2.1.3 50mm

Fig. 4.14d shows the anodized microstructure of the section at 50mm. The average grain size increased steeply and was measured to be 221±12μm. The grains observed were dendritic in nature and the DAS measured increased steeply to 54±5μm. The cooling rate calculated using the measured DAS showed a gradual drop as compared to the 38mm section. The calculated cooling rate for 50mm section was 1.1 K/s and was in agreement with the measured cooling rate **(Tanihata et al., 99)**.

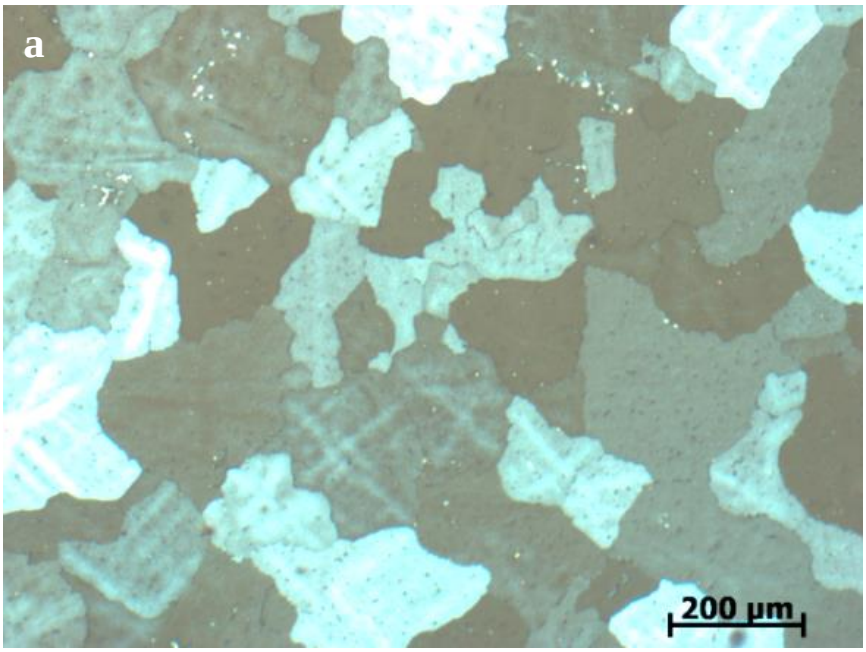

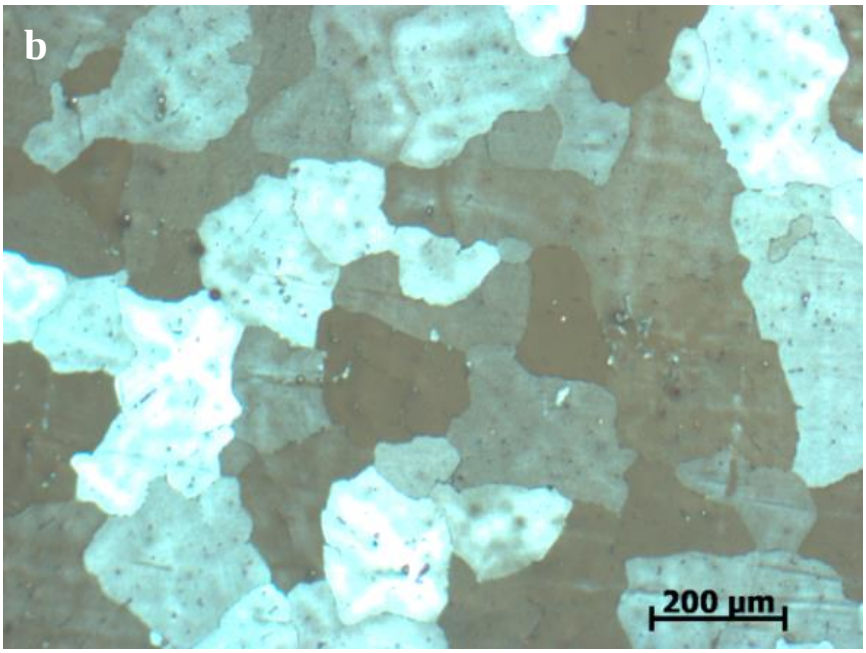

Continued overleaf…

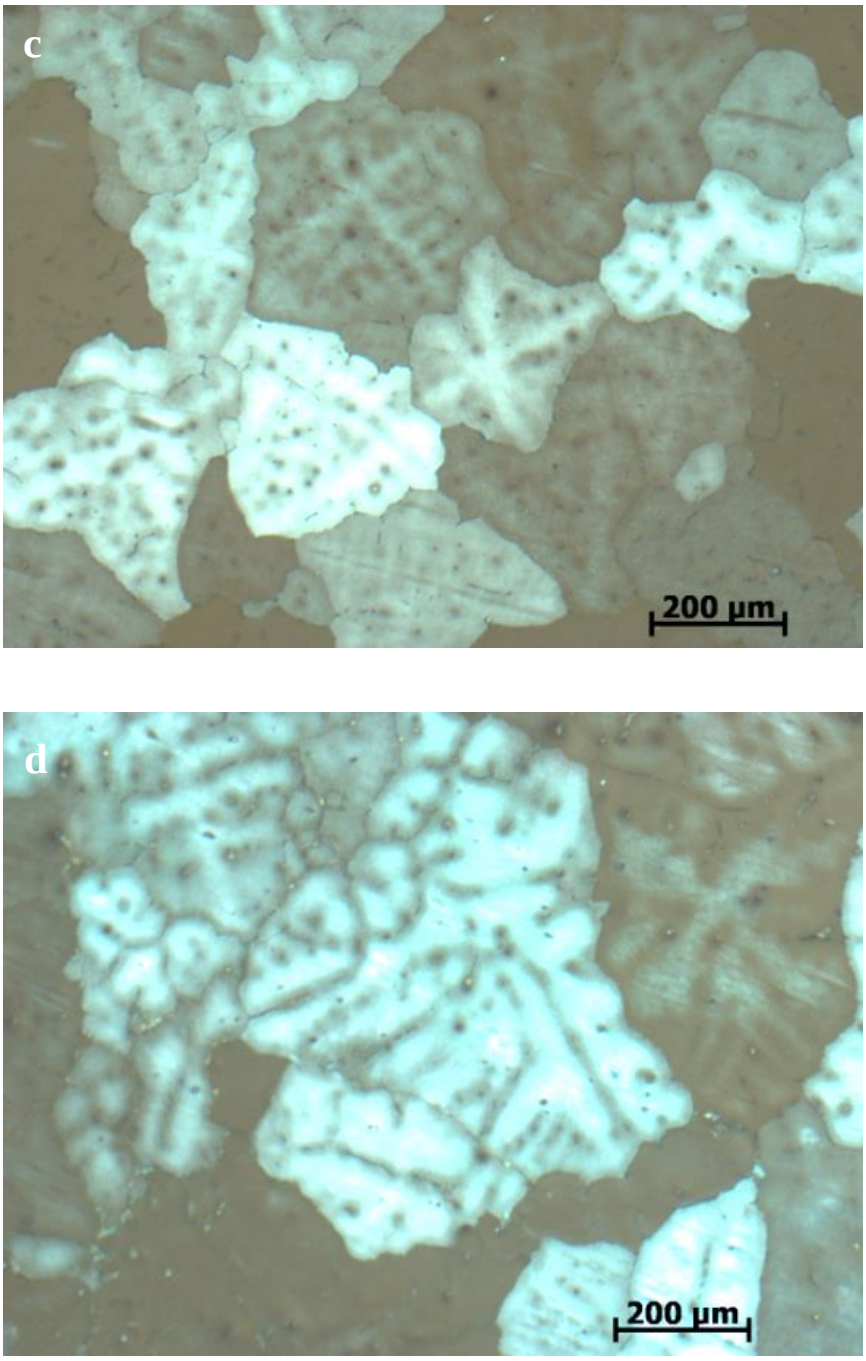

Fig 4.14 Anodised grain structures of a) 12.5mm, b) 25mm, c) 38mm and d) 50mm from the bottom of the TP1 mould

4.2.2 Characterisation of the 2D microstructure

This study showed the variation in morphology of the intermetallics and their interconnectivity in 2D. However, nothing conclusive can be said about the size or interconnectivity based only on the information from 2D analysis, as both these features varies significantly in 3D. Therefore, the size and interconnectivity was measured using 3D analysis. The intermetallics were characterised based on the EDX analysis and previous TEM analysis **(Sha et al., 01)** and **(Hsu et al., 01)**. The α-AlFeSi was mainly observed with a chinese script morphology and the β-AlFeSi mainly existed in a needle-like morphology. About 50 random particles were analysed using EDX to calculate the ratio of α-AlFeSi:β-AlFeSi which is shown in Table 4.3. The Fe-rich intermetallics present at different sections of the TP1 sample were primarily located at cell or grain-boundaries. The grey scale calculations provided the quantitative variation in area fraction of the intermetallics with respect to the cooling rate.

4.2.2.1 12.5mm

Fig. 4.15a shows the 2D morphology of the intermetallics present in the 12.5mm sample. The intermetallics appear to be very small in size and discrete. This can be attributed to the higher cooling rate. α-AlFeSi and β-AlFeSi were the major intermetallics observed with Chinese script and needle-like morphologies respectively. The ratio of α-AlFeSi:β-AlFeSi was observed to be 3:1. The area fraction of the intermetallics measured using the grey scale analysis was 2.6%.

4.2.2.2 25mm

Fig. 4.15b shows the 2D morphology of the intermetallics present in the 25mm sample. The intermetallics were small in size and discrete in nature. However, the intermetallics were slightly larger and more interconnected than the 12.5mm sample. α-AlFeSi and β-AlFeSi were the major intermetallics observed with Chinese script and needle-like morphologies respectively. The ratio α-AlFeSi:β-AlFeSi was observed to decrease slightly to 5:2. The area fraction of the intermetallics measured using the grey scale analysis increased slightly to 2.8%.

4.2.2.3 38mm

Fig. 4.15c shows the 2D morphology of the intermetallics present in the 38mm sample. The intermetallics were bigger in size and the interconnectivity increased significantly compared to the previous two samples. α-AlFeSi and β-AlFeSi were again the major intermetallics observed with Chinese script and needle-like morphologies respectively. The ratio of α-AlFeSi:β-AlFeSi decreased considerably to 3:2. The area fraction of the intermetallics measured using the grey scale analysis increased further to 3.2%.

4.2.2.4 50mm

Fig. 4.15d shows the 2D morphology of the intermetallics present in the 50mm sample. The intermetallics were much bigger in size and the interconnectivity increased greatly compared to the other samples. α-AlFeSi and β-AlFeSi were the major intermetallics observed with Chinese script and needle-like morphologies respectively. The ratio of α-AlFeSi:β-AlFeSi decreased by a large extent to 1:2. The area fraction of the intermetallics measured using the grey scale analysis increased considerably to 3.9%.

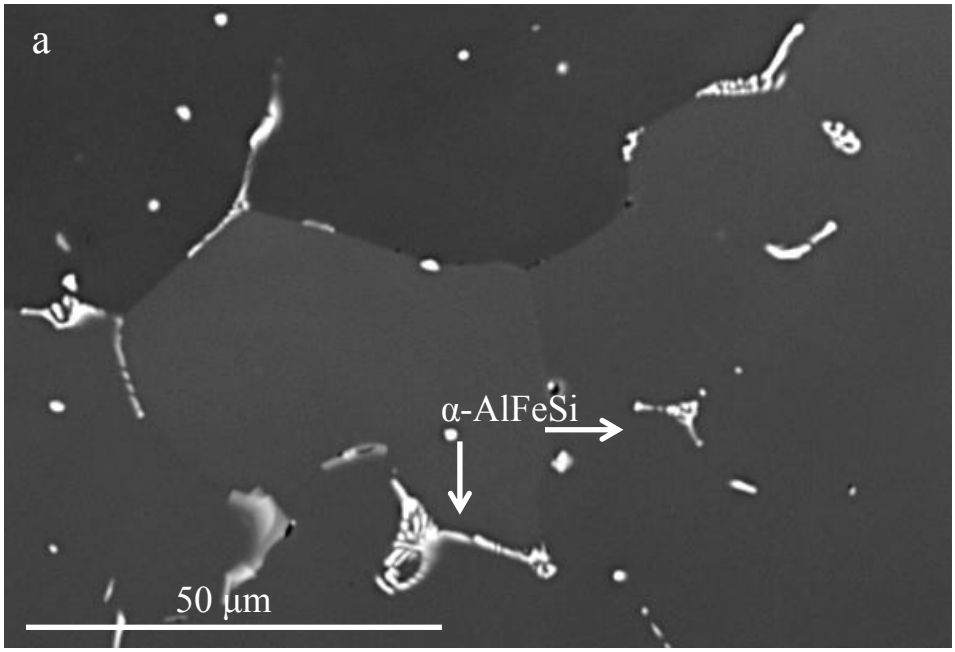

Continued overleaf…

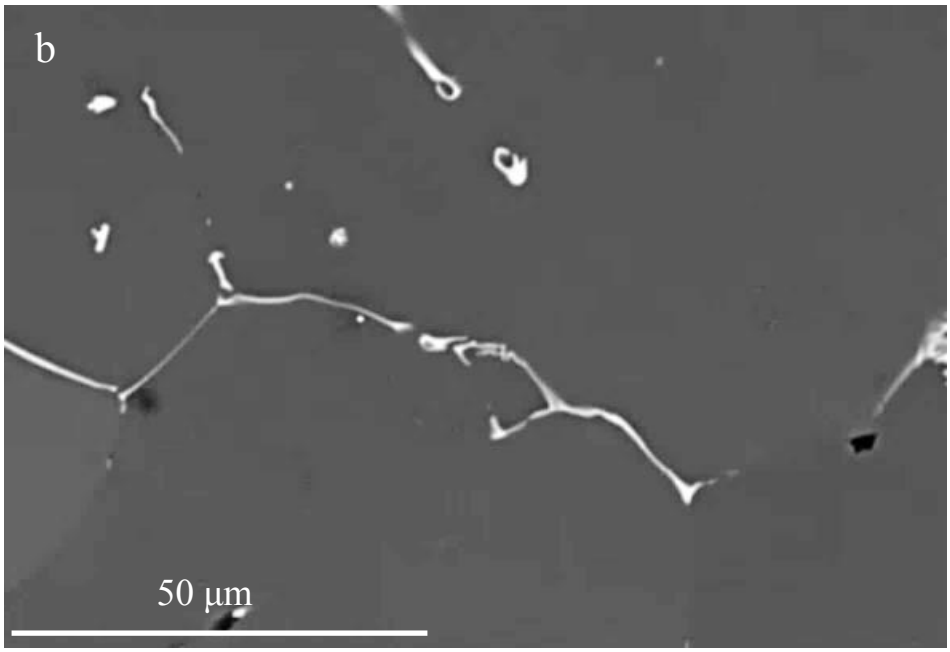

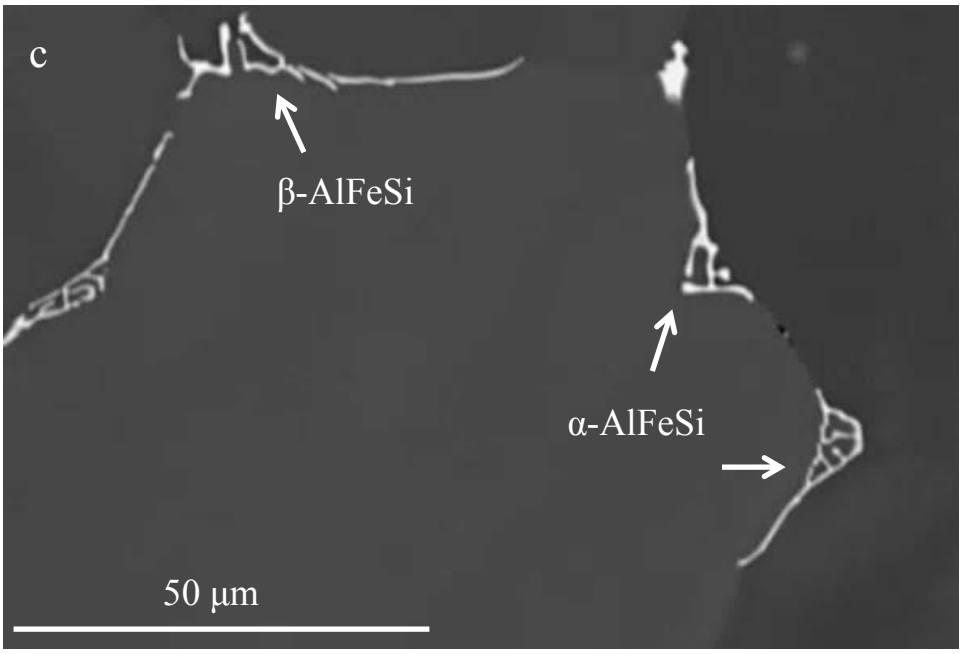

Continued overleaf…

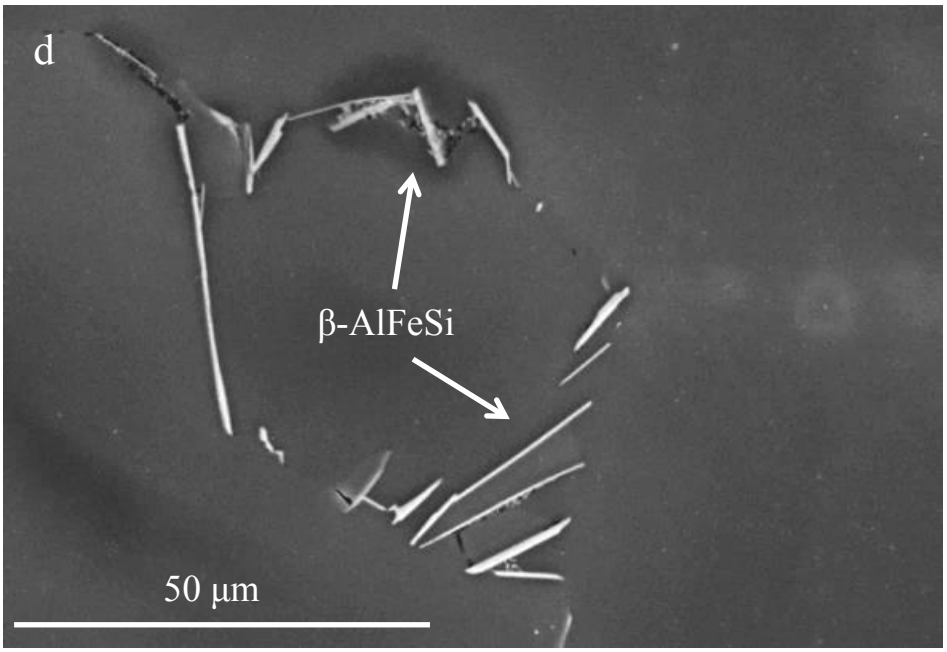

Fig 4.15 Backscattered images showing 2D morphology of intermetallics in sections a) 12.5mm, b) 25mm, c) 38mm and d) 50mm from the bottom of the TP1 mould

Table 4.3 Summary of the 2D analysis results for different sections of TP1

Section of TP1	12.5mm	25mm	38 mm	50 mm
α-AlFeSi:β-AlFeSi	3:1	5:2	3:2	1:2
Area fraction of intermetallics	2.6%	2.8%	3.2%	3.9%

4.2.3 Characterisation of the 3D morphology of intermetallics

Though the 2D metallographic analysis showed fine and discrete intermetallics, the 3D imaging of the extracted particles revealed that they were coarser and well interconnected and varied significantly with position in the TP1 sample. The interconnectivity suggested that these particles grow along the grain/cell boundaries and connect with each other. In order to quantify the size and interconnectivity in this study it was assumed to have no breakage of particles during intermetallic extraction and the sample preparation process. About 50 particles were analysed and the average length of interconnectivity between intermetallics was measured for each section of the TP1 sample.

There were two distant morphologies of particles commonly observed in 3D analysis. α-AlFeSi was observed to have petals or dendrite type morphology in 3D (Fig. 4.16), whereas β-AlFeSi was observed to have platelet/rod-like morphology.

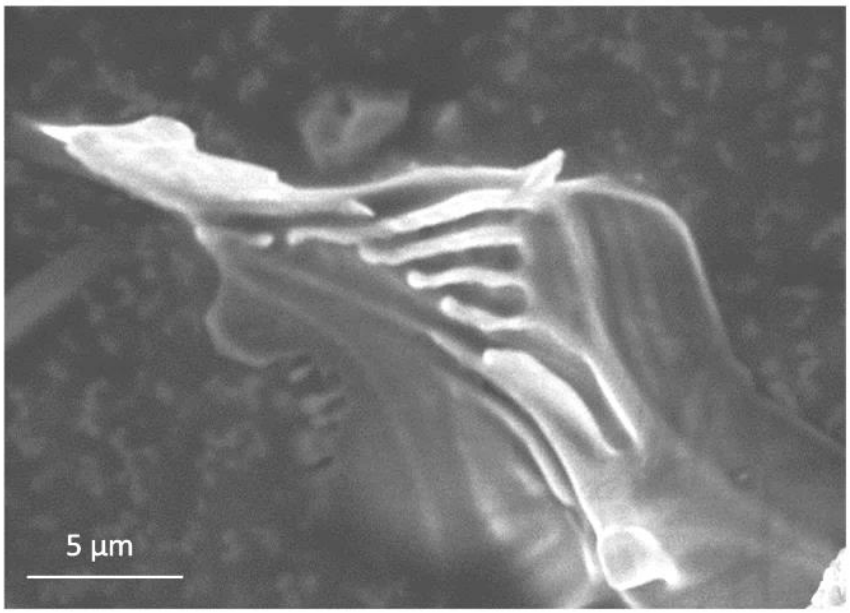

Fig 4.16 SE micrograph of a dendritic type α-AlFeSi intermetallic particle

The approach to measure the average length of the petals in α-AlFeSi and average length of the maximum faceted side in β-AlFeSi has already been described in sections 3.6.1 and 3.6.2 respectively. These measurements provided quantitative analysis of the variation of the size of intermetallics with respect to the variation in cooling rate. The average intermetallic dendrite arm spacing (I-DAS) was also measured as shown in Fig 4.17. It is interesting to note that at low cooling rate the intermetallic particles were highly interconnected with coarse and lengthy particles, whereas at high cooling rates they appear to be less intact with smaller and shorter particles.

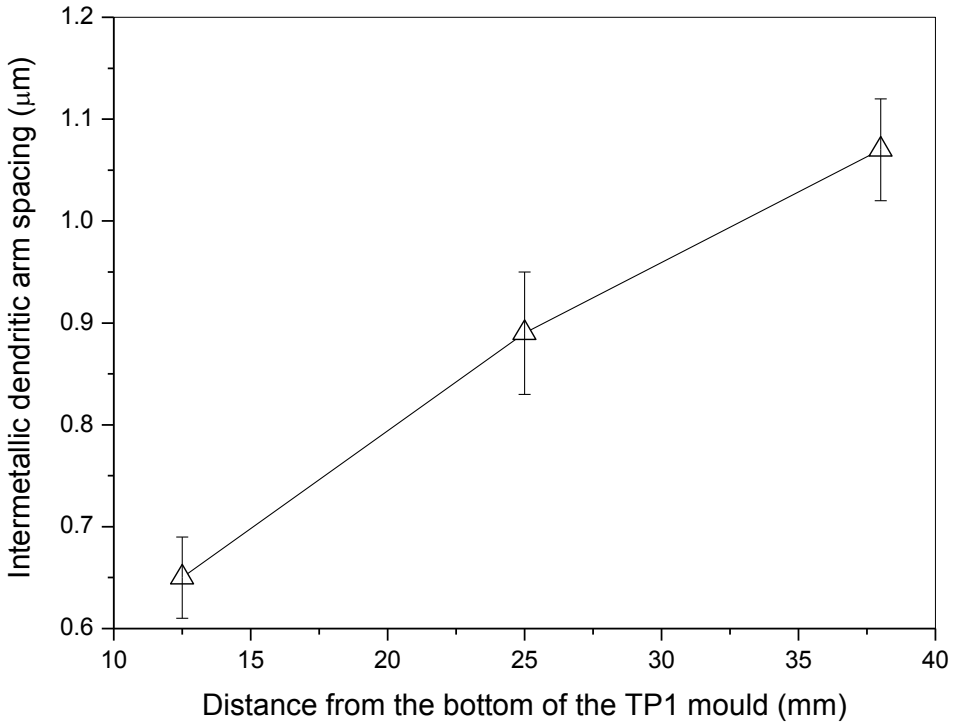

Fig 4.17 The increase in I-DAS on moving towards the top of the TP1

4.2.3.1 12.5mm

Fig. 4.18 shows the 3D features of the extracted intermetallic particles formed at the 12.5mm position. α-AlFeSi was the dominant intermetallic observed in its regular flower-like morphology. The average length of the petals for this sample was 18±3μm, whereas no platelet or rod-like features were noted. The interconnectivity and I-DAS measured for the 12.5mm sample with 16.6 K/s cooling rate were 47±6μm and 0.65μm respectively.

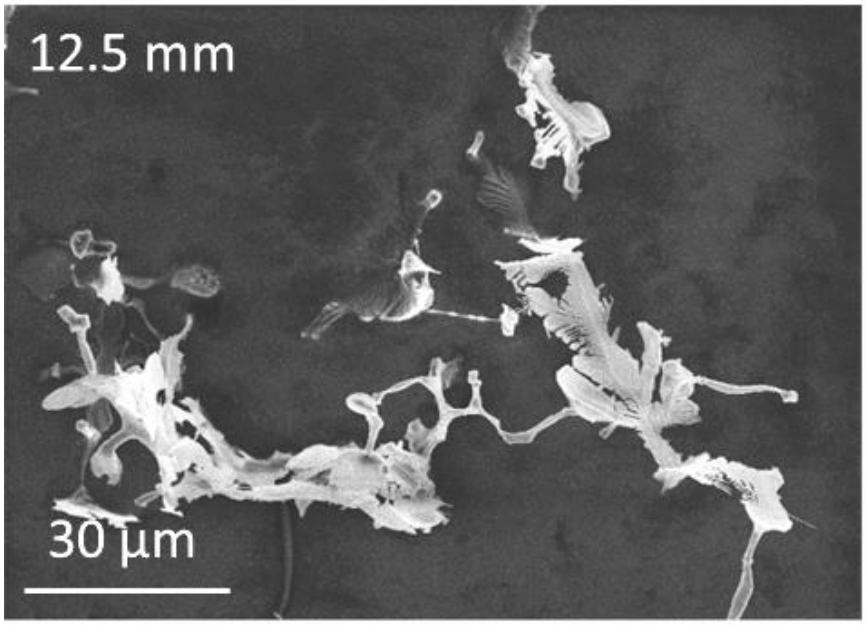

Fig 4.18 SE micrograph of α-AlFeSi intermetallic particles in the 12.5mm section

4.2.3.2 25mm

Fig. 4.19 shows the 3D features of the extracted intermetallic particles formed at the 25mm position. α-AlFeSi and β-AlFeSi were the major intermetallics observed in their regular morphologies i.e. flower-like and platelet/rod-like respectively. α-AlFeSi was the dominant of the two intermetallics. The average length of the α-petals for this sample was 24±3µm, whereas the average length of the maximum faceted side of the β-platelets was 12±2µm. The interconnectivity and I-DAS both increased considerably for the 25mm sample with 7.7 K/s cooling rate and was measured to be 83±8µm and 0.89µm respectively.

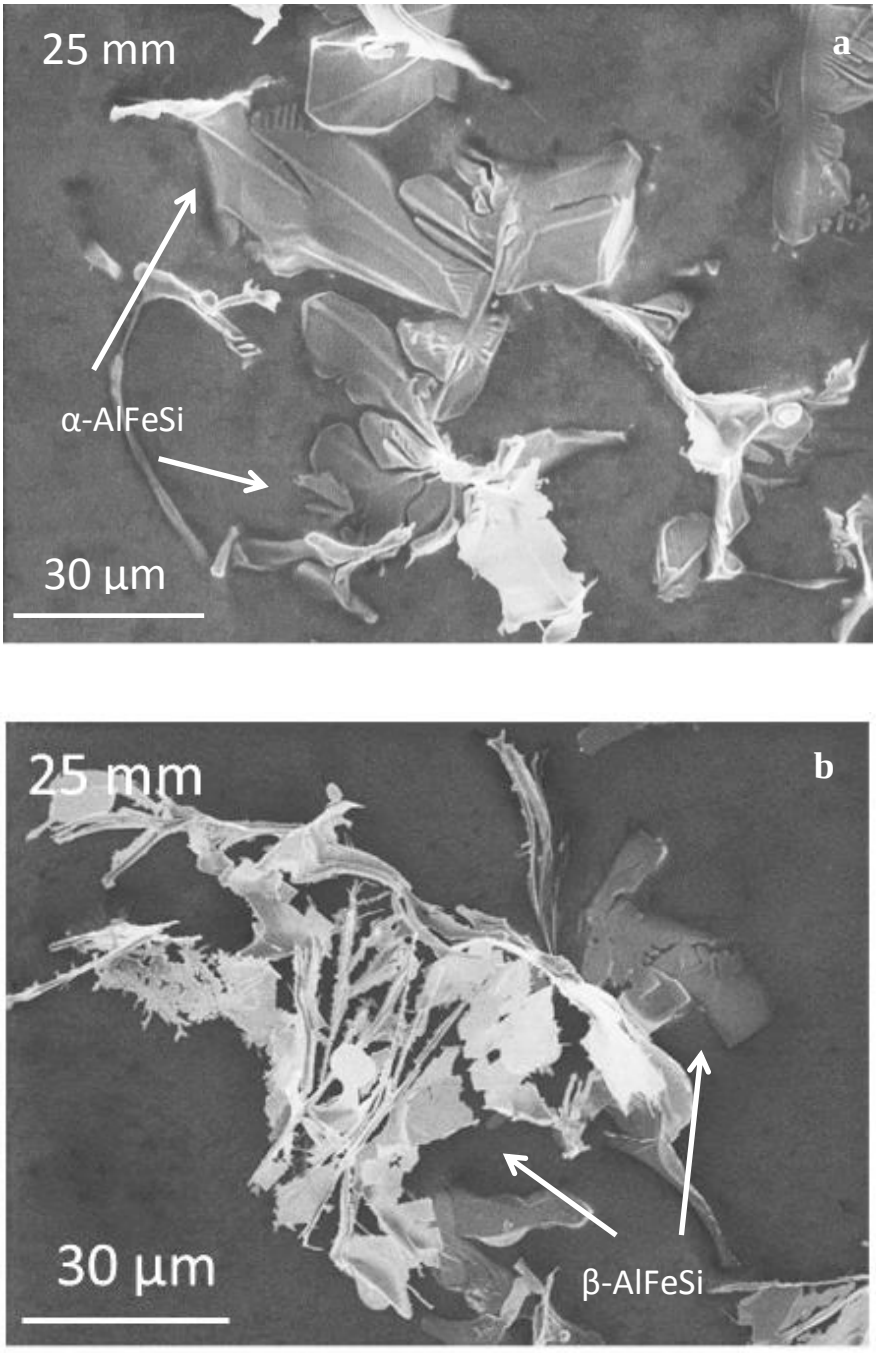

Fig 4.19 SE micrographs of a) α-AlFeSi and b) β-AlFeSi intermetallic particles in the 25mm section

4.2.3.3 38mm

Fig. 4.20 shows the 3D features of the extracted intermetallic particles formed at the 38mm position. α-AlFeSi and β-AlFeSi were the major intermetallics observed in their regular morphologies i.e. flower-like and platelet/rod-like respectively. α-AlFeSi was slightly more dominant of the two intermetallics. The average length of the α-petals and the average length of the maximum faceted side of the β-platelets both increased significantly to 33±4μm and 17±3μm respectively. The interconnectivity and I-DAS also increased considerably for the 38mm sample with 3.9 K/s cooling rate and was measured to be 113±11μm and 1.07μm respectively.

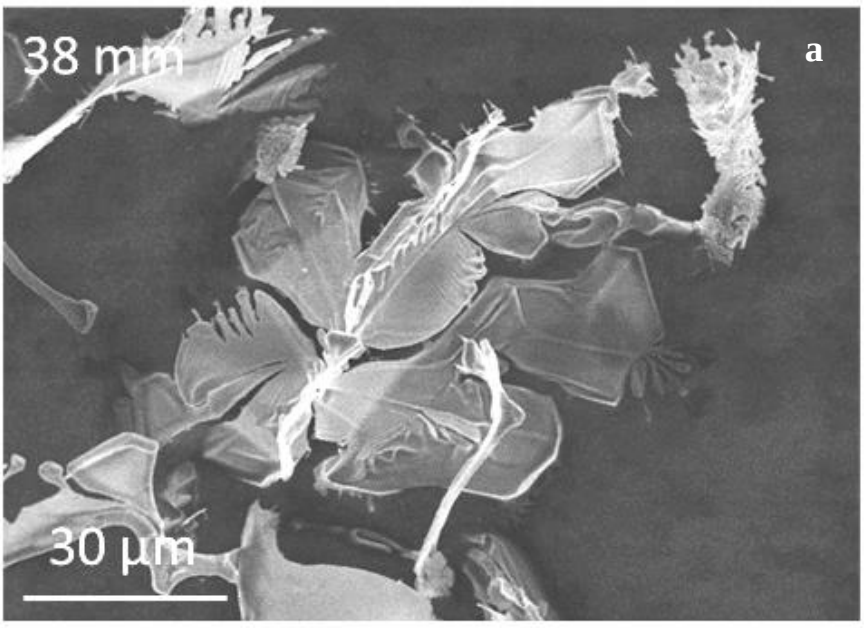

Continued overleaf…

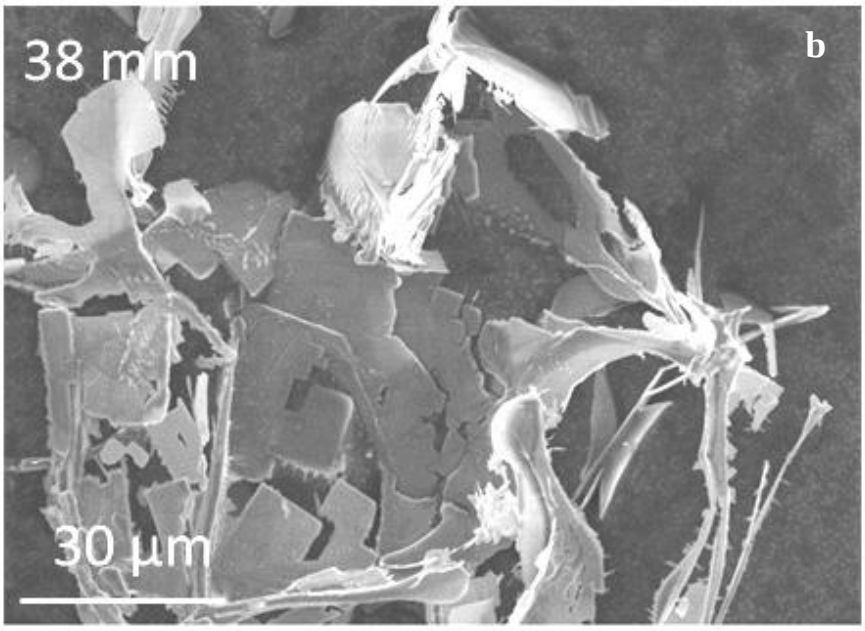

Fig 4.20 SE micrographs showing a) α-AlFeSi and b) β-AlFeSi intermetallic particles in the 38mm section

4.2.3.4 50mm

Fig. 4.21 shows the 3D features of the extracted intermetallic particles formed at the 50mm position.

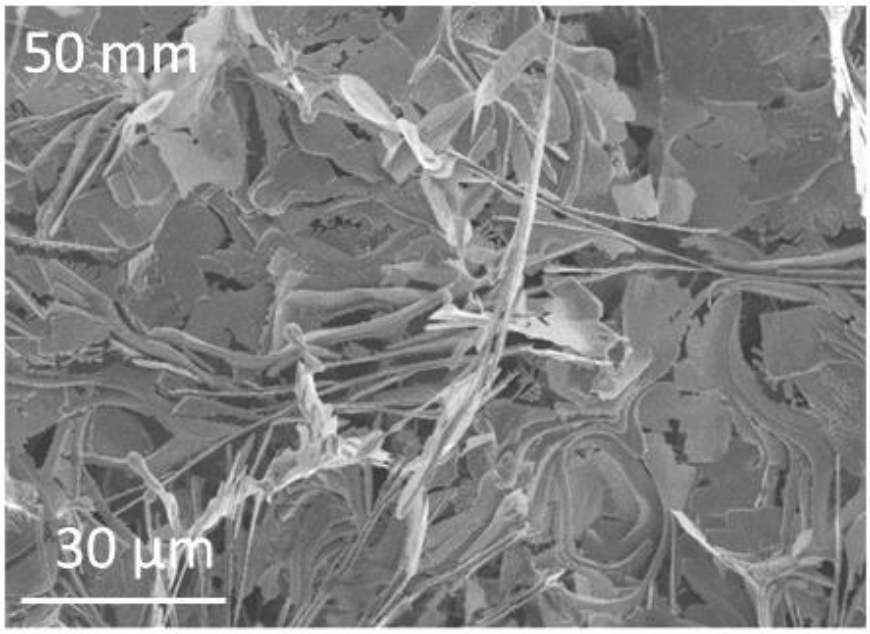

Fig 4.21 SE micrograph of β-AlFeSi intermetallic particles in the 50mm section

β-AlFeSi was the major intermetallic observed in its regular platelet/rod-like morphology. The regular flower-like morphology of α-AlFeSi was absent. As a result, I-DAS was not measured for this sample. The average length of the maximum faceted side of the β-platelets increased significantly to 24±5µm. The extracted sample at 50mm had a highly interconnected and complex network of intermetallics, hence it was not possible to measure the length of interconnectivity using the current approach.

4.2.4 Quantitative analysis of intermetallics using XRD

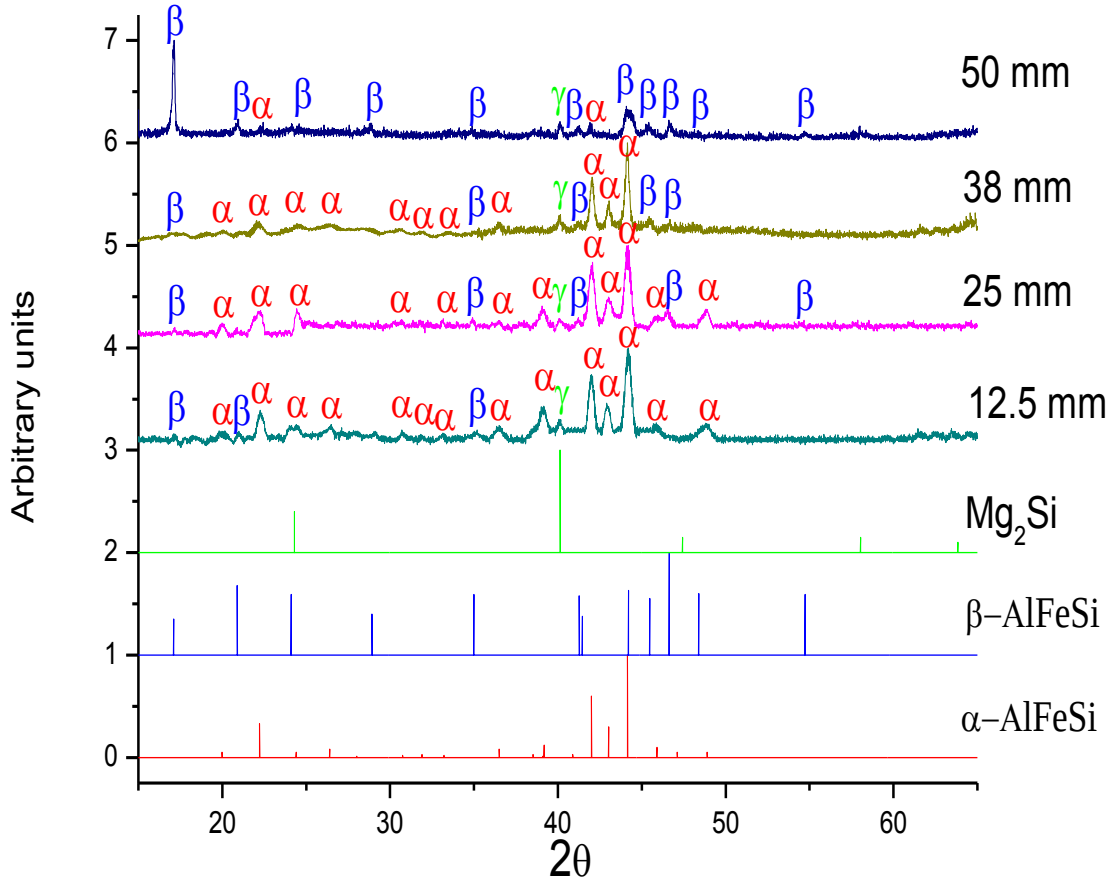

Fig 4.22a XRD traces (normalised) from the extracted intermetallics at different sections of the TP1 sample.

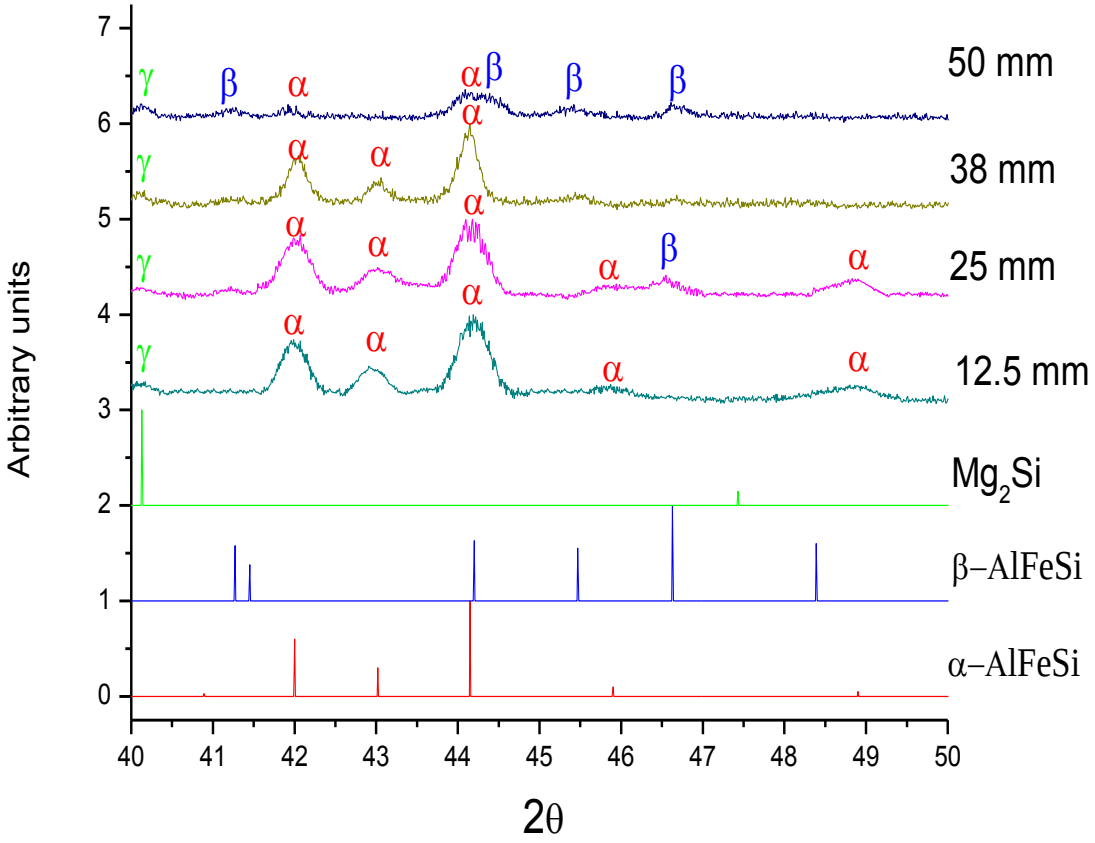

Fig. 4.22b Magnified XRD traces for the region 2θ=40 to 2θ=50 showing the overlapping of the α-AlFeSi and β-AlFeSi peaks.

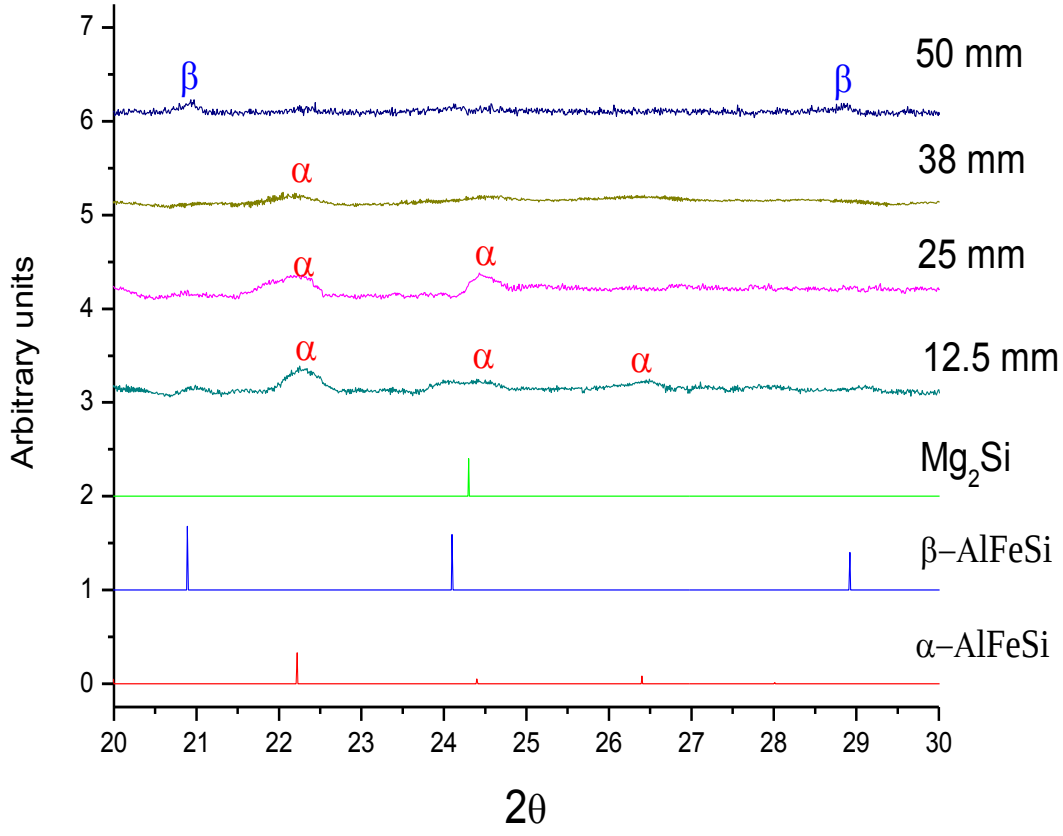

Fig. 4.22c Magnified XRD traces for the region 2θ=20 to 2θ=30 showing the overlapping of the α-AlFeSi and β-AlFeSi peaks.

XRD traces from the extracted intermetallic particles from the samples at different positions are shown in Fig. 4.22a. The peaks were normalised with respect to the highest peak. The majority of the peaks observed belonged to α-AlFeSi (44.15°, 42°, 43.01°, 22.22°, 39.1°, 45.9°, 26.4°, 48.98°) or β-AlFeSi (17.1°, 20.89°, 28.92°, 34.99°, 41.27°, 45.47°, 46.63°). A low intensity peak of another phase namely Mg_2Si (40.13°) explains its rare observation in 3D analysis. Fig. 4.22b and Fig. 4.22c shows the magnified XRD traces to clearly assign the close peaks to the correct phase.

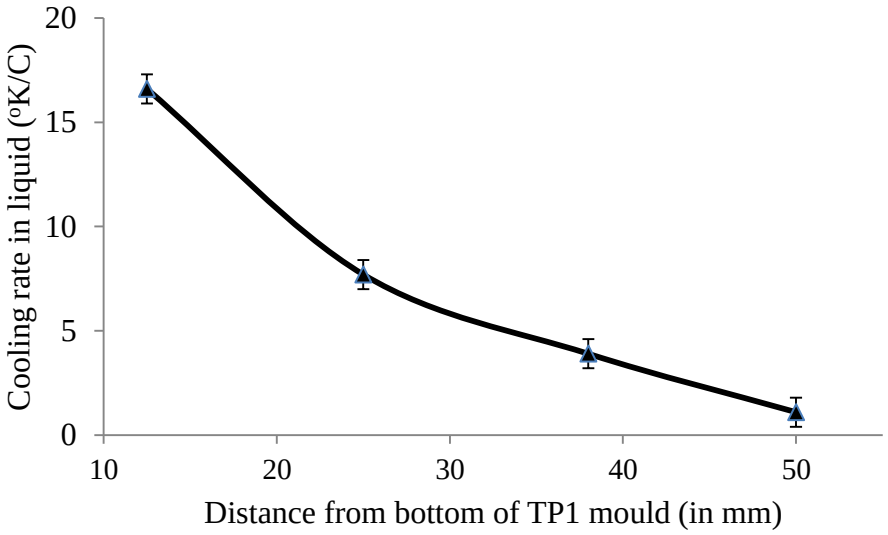

a)

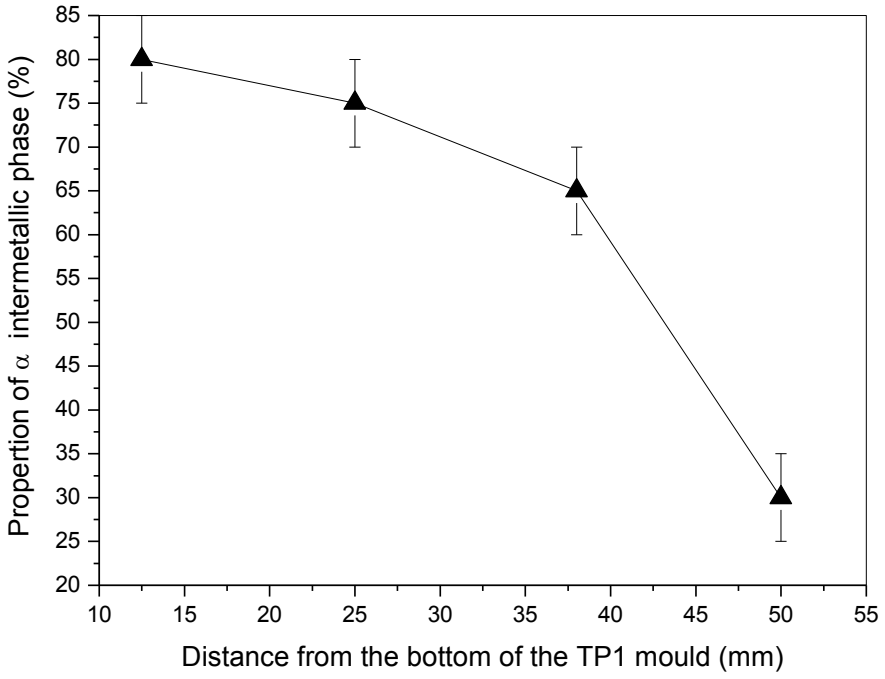

b)

Fig 4.23 a) Variation of the cooling rate and b) amount of α intermetallic phase at different sections of the TP1 sample (section 3.6.4).

The quantitative analysis (see section 3.6.4) shown in Fig. 4.23 suggests that the relative percentage of α-AlFeSi phase decreases and β-AlFeSi phase increases as the cooling rate decreases (~16.6 K/s to 1.1 K/s) which is also in accordance with the theory proposed by Belov et. al. The relative percentage of α-AlFeSi phase calculated for 12.5mm, 25mm, 38mm and 50mm was 80%, 75%, 65% and 30% respectively (see section 3.6.4 for calculation details). The XRD results correlated well with the 2D and 3D SEM results i.e. α-AlFeSi was dominant for the 12.5mm, 25mm and 38mm samples, whereas β-AlFeSi was dominating for the 50mm sample. It can be clearly seen in XRD's that the number and intensity of α-AlFeSi peaks reduced whereas that of β-AlFeSi increased from 12.5mm to 50mm. It is important to note that the highest peak in this study i.e. $\theta=17^0$ is the third highest intensity peak for β-AlFeSi. This observation can attributed to the texture (stress) introduced during sample preparation as described in section 3.6.4. As the relative percentage calculations take into account the peak at 17^o, the very low relative percentage of α-AlFeSi in 50mm could be partially due to the texture introduced. However, it is also important to note the effect of cooling rate on the intermetallic formation i.e. α-AlFeSi was dominant during higher cooling rate, whereas β-AlFeSi was dominant for lower cooling rate.

4.2.5 Phase selection

In general, during the solidification of Al alloys solute elements such as Fe and Si segregate to the inter-dendritic regions or grain/cell boundaries. The composition of segregated liquid increases and results in various variant/ invariant reactions as the temperature drops. Previous investigations of

6xxx series Al alloys showed the possibility of various equilibrium and non-equilibrium eutectic, peritectic and quasi-peritectic reactions **(Hsu et al., 01)** and **(Sha et al., 03)**. It is likely that in this Al-Mg-Si (AA6063) system, α-Al is the primary phase to form first followed by other secondary constituent phases. This will be discussed further in chapter-5 on the basis of theoretical calculations using MTDATA. Based on the XRD analysis, α-AlFeSi and β-AlFeSi are the constituent phases in this system. Previous experimental analysis of similar alloys suggests α-AlFeSi forms first followed by β-AlFeSi **(Backerud et al., 86)**.

The present observation of α-AlFeSi dominating at high cooling rate supports the argument that α-AlFeSi forms through eutectic reactions rather than peritectic reactions during solidification. Also at higher cooling rates the peritectic reaction (3) would be incomplete, resulting in more retained α-AlFeSi. β-AlFeSi dominating at low cooling rate supports the argument that β-AlFeSi can form through either/both eutectic or quasi-peritectic solidification reactions. At slow cooling rate there is time for solid state diffusion, which is one of the growth controlling factors for a peritectic reaction. Previous investigations also suggest that the metastable β-AlFeSi quasi-peritectic reaction is more favorable at low growth velocities **(Sha et al., 03)**. Thus these Al-Mg-Si alloys solidified with slow cooling rates and low growth velocities favor the formation of β-AlFeSi.

The elemental composition at different cross-sectional positions is given in Table 4.4. There is a slight variation in the Si content. Such an increase in Si near the top of the mould might also push the solidification reaction a little to form β-AlFeSi. The level of solute segregation also depends on the cooling rate as the diffusion co-efficient of solute elements vary **(Dutta et al., 02)**. It is important to note that though the relative percentages of the two AlFeSi phases varies with cooling rate, there is no other phase identified. This can be attributed to the displacement of other possible equilibrium reactions under the investigated cooling rates. Below are the suggestions for possible reactions occurring during solidification i.e. (1), (2), (3) and (4). However, reaction (4) might be suppressed to some extent as (3) is favoured for high Si content and low cooling rate.

$L \rightarrow (Al) + Al_{13}Fe_4$…..…….…….(1)

$L + Al_{13}Fe_4 \rightarrow (Al) + \alpha$-AlFeSi..……...(2)

$L + \alpha$-AlFeSi $\rightarrow$ (Al) + β-AlFeSi…….……...(3)

$L + \alpha$-AlFeSi $\rightarrow$ (Al) + β-AlFeSi + Mg_2Si……..…(4)

It is also possible that at higher cooling rate, reaction (1) may not complete and result in retained $Al_{13}Fe_4$. However as α-AlFeSi is more stable phase than $Al_{13}Fe_4$, the amount of retained $Al_{13}Fe_4$ will be much less. As a result no $Al_{13}Fe_4$ was observed during SEM and no peak was detected by the XRD.

Table 4.4 Elemental composition measured at different positions using OES (see section 3.6.5)

Distance	Si	Fe	Mn	Mg	Ti	Al
12.5 mm	0.53	0.20	0.05	0.55	0.01	98.60
25 mm	0.52	0.20	0.06	0.56	0.01	98.61
38 mm	0.55	0.21	0.06	0.56	0.01	98.58
50 mm	0.57	0.21	0.06	0.55	0.01	98.59

4.2.6 Intermetallic interconnectivity

Most of these Fe bearing constituent particles which form at the primary Al grain or cell boundaries were interconnected. Interconnectivity depends on the grain size. At slow cooling rate the grains are larger so the grain boundary area per unit volume is smaller. Hence the liquid should remain interconnected to lower volume fraction of liquid and as a result coarse, lengthy and well interconnected intermetallics form. Such interconnected intermetallics were also observed in a DC billet **(Kuijpers et al., 02)**. At high cooling rates the grain boundary area per unit volume is larger; therefore a volume fraction of solute rich liquid will now split into a larger number of channels. As a result fine, short and less interconnected intermetallics will form. It is also possible that such fine and short interconnected intermetallics might break-up during the extraction process. It is the interconnectivity that makes the as-cast billet/strip difficult for further downstream processing. Therefore it is essential to develop a casting process that can result in less interconnected constituent particles.

4.2.7 Intermetallic size and morphology

There were two distinct morphologies of Fe bearing intermetallic particles observed. Petals or dendrite type morphology particles which are associated with cubic α-AlFeSi phase. In 2D metallographic analysis these particles are described as having Chinese script type morphology. A closer look at these petal-like particles shows that one side edge is often faceted whereas others are dendritic. This is because the α-AlFeSi particles have blended interface with primary Al, as a result they can take different shapes **(Sha, 01)**. As the cooling rate decreases, these particles start to grow larger. In addition, the increase in spacing between the dendrite arms of the α-AlFeSi with a decrease in cooling rate also suggests that there are variations in the local liquid solidification conditions.

The monoclinic β-AlFeSi phase typically has faceted plate type morphology. In 2D analysis these particles resembled needles. A closer look at the faceted edges of these extracted platelets shows steps. This suggests that step growth is the major growth mechanism for these β-AlFeSi platelets under these solidification conditions. In-addition, it has been observed that these particles have fine twin planes aligned parallel to the facet interface **(Sha, 01)**. It has been proposed that the growth of this phase is also possible by a re-entrant edge mechanism and that bending of the plates during growth is not possible **(Mulazimoglu et al., 96)**. But later during in-situ real time observation it was observed that this platelet type β-AlFeSi has the capability to bend to accommodate other phases during solidification **(Terzi et al., 10)**. As the cooling rate decreases the particles grow larger along the preferred orientations.

4.3 Comparison of the microstructures formed in the DC cast alloy and TP1 sample

In order to control the solidified microstructure it is very important to understand the formation and behavior of Fe intermetallic phases. For this purpose the TP-1 test could prove to be very convenient and economical. This test is designed to predict the grain size and it was not developed to investigate the intermetallics formation. The test provides a sample (38mm from the bottom of the TP-1 mould) which duplicates the cooling rate of the center of a 180 mm DC cast billet **(TP1, 90)**. However, no conclusive results on the effect of TP-1 test on the intermetallic particles can be found in the literature. Hence a detailed comparative study of the intermetallic particles present in DC cast material (similar to the one in section 4.2) and TP-1 should give a proper picture about the effectiveness of TP-1 test for simulating DC casting with respect to intermetallics. The details of the alloys used for this study can be found in section 3.1.3.1.

4.3.1 Grain Size

The DC cast billet containing 0.015% grain refiner was remelted to cast TP-1 samples. The microstructure of the TP-1 cast sample was more dendritic than of the DC billet and the measured average grain size (Fig. 4.24) was 1.5 times larger. Though both samples would have had similar amounts of grain refiner, the grain refiner was not so effective after re-melting. One possible reason could

be the potent substrates (TiB_2) might have formed clusters during re-melting and so reduce the ability to nucleate α-Al **(Sha, 01)**.

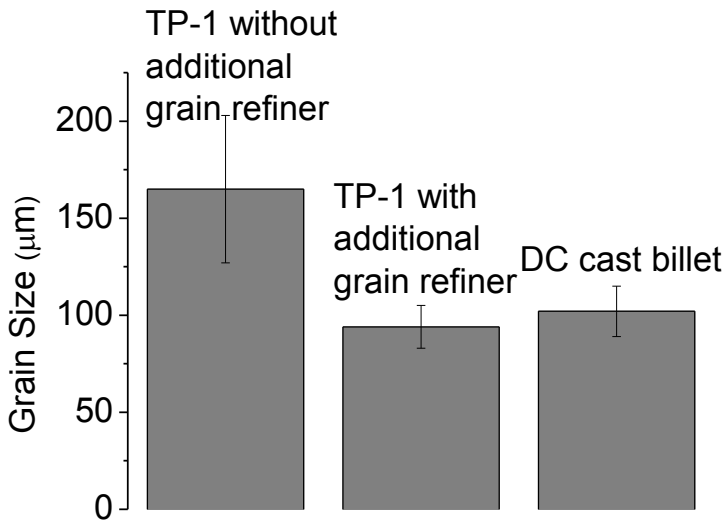

Fig 4.24 Graph showing the average grain sizes measured for different samples.

Hence, further 0.015% TiB_2 was added during re-melting of DC cast alloy to make the TP-1 alloy grain size similar to that of the DC billet (Fig. 4.24). This is because the addition of fresh grain refiner introduces more active potent substrates to the melt which nucleate and refine α-Al. Due to the similarity in grain sizes, the following results will focus only on the DC cast billet sample and TP-1 sample with additional grain refiner (GR).

4.3.2 Morphology of Fe Bearing Intermetallics

Two-dimensional (2D) views of the intermetallic particles in the metallographic samples shows that the intermetallics were mainly located at cell or grain-boundaries as shown in Fig. 4.25. This is because the final liquid between two

solid surfaces is rich in solute elements and thermodynamically favours the formation of intermetallics.

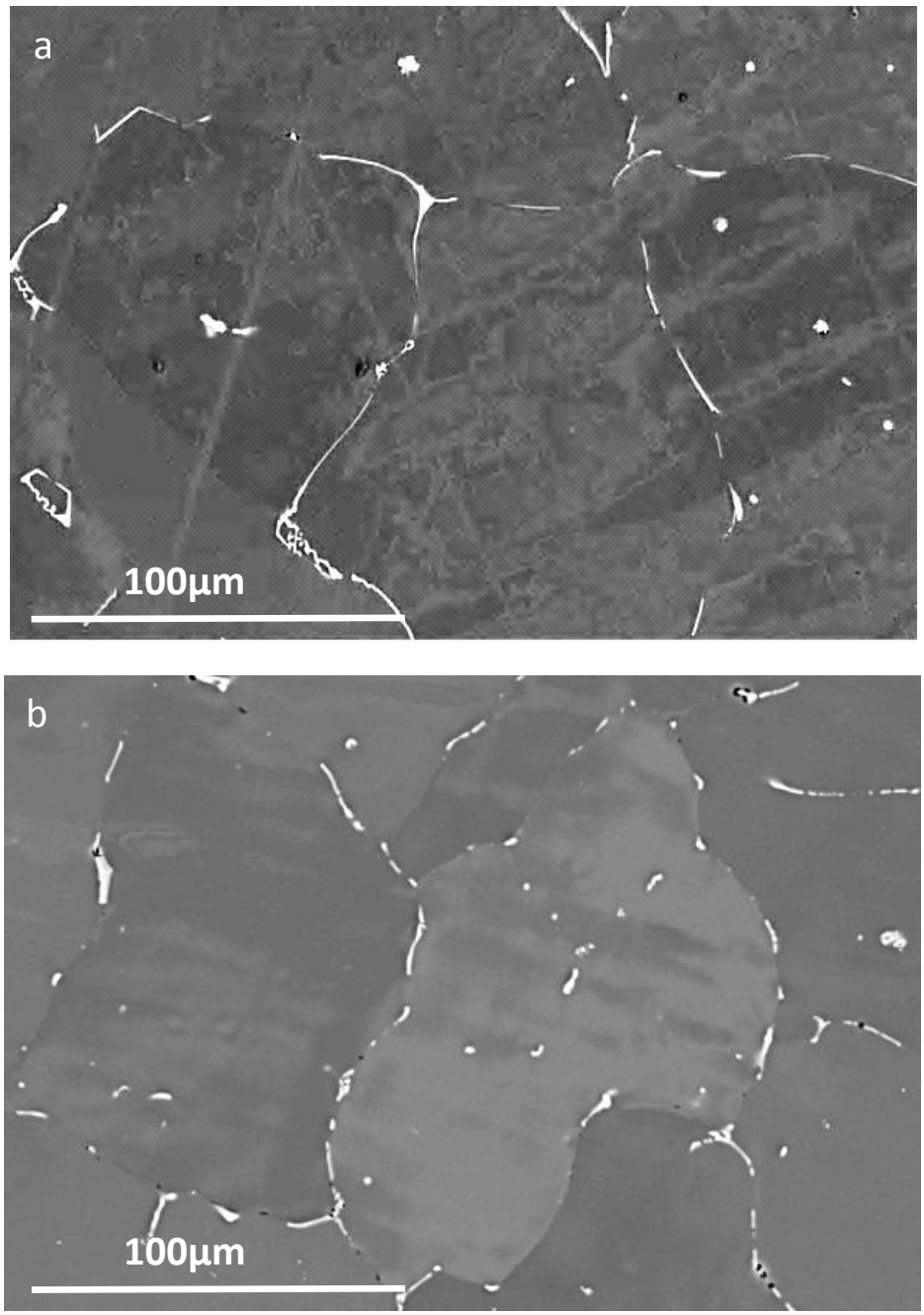

Fig 4.25 SE micrographs showing 2D microstructures of a) TP-1 with additional GR and b) DC billet.

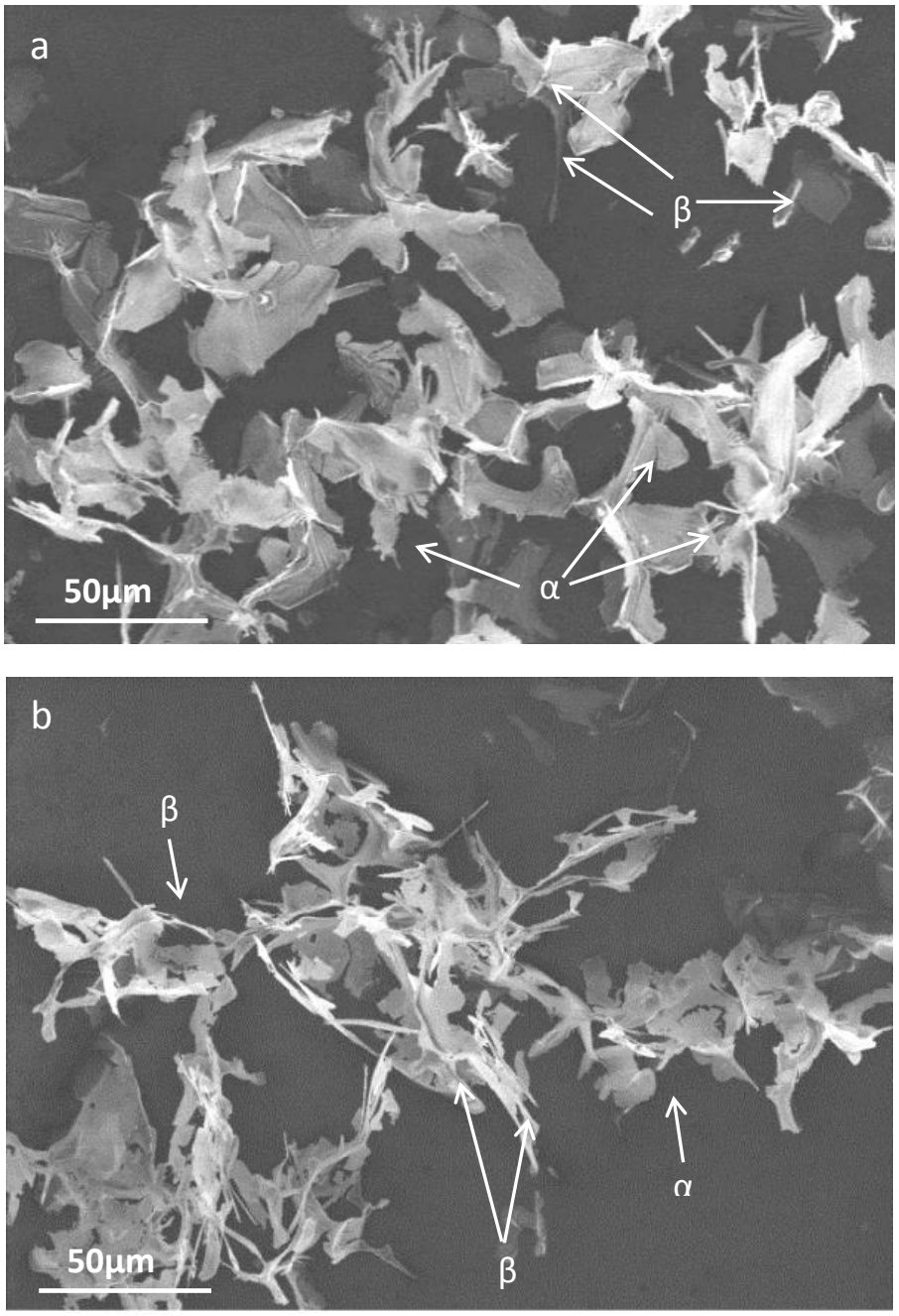

Figure 4.26 SE micrographs of extracted intermetallics in a) TP-1 with additional GR and b) DC billet.

The 2D morphology of the intermetallic particles in the TP-1 sample was more connected and less broken (Fig. 4.25a) with average length of the particles being 29±4μm, whereas in DC cast billet (Fig. 4.25b) the average length of a particle was about 16±3μm. However, the area fraction of intermetallics in the DC cast billet was almost the same when compared with TP-1. The three dimensional (3D) extracted intermetallic particles can be seen in Fig. 4.26. Though the 2D image of metallographic samples showed fine and broken intermetallics, the 3D image of the extracted particles reveals that they were coarse and well interconnected. The 3D morphology of the intermetallics in the DC billet were found to be more interconnected i.e. the average length in the DC billet was 350 μm as compared to the average length of 180 μm in TP-1 with additional grain refiner. The DC cast billet particles were also observed to be thin and more fibrous. The interconnectivity suggests these particles grow along the direction of the α-Al.

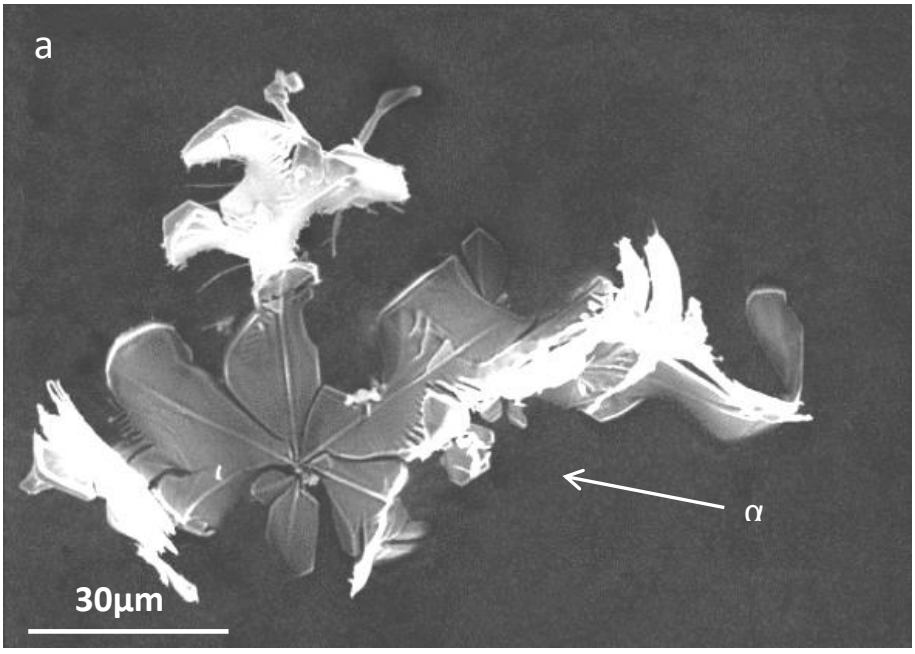

Continued overleaf…

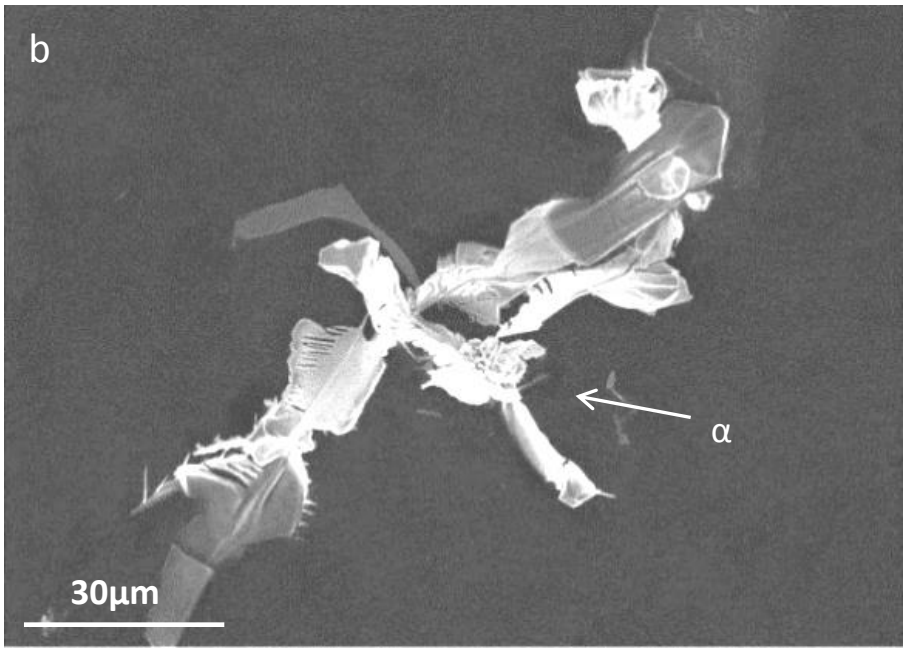

Fig 4.27 SE micrographs of α-AlFeSi intermetallic particles in a) TP-1 with additional GR and b) DC billet.

In 3D imaging α-AlFeSi was mainly observed to have a petal-like morphology as shown in Fig. 4.27. The full flower type morphology of the α-AlFeSi is more frequently observed in the TP-1 sample (Fig. 4.27a). The average length of the petals in the TP-1 sample was 41±4µm whereas for DC billet it was 23±3µm.

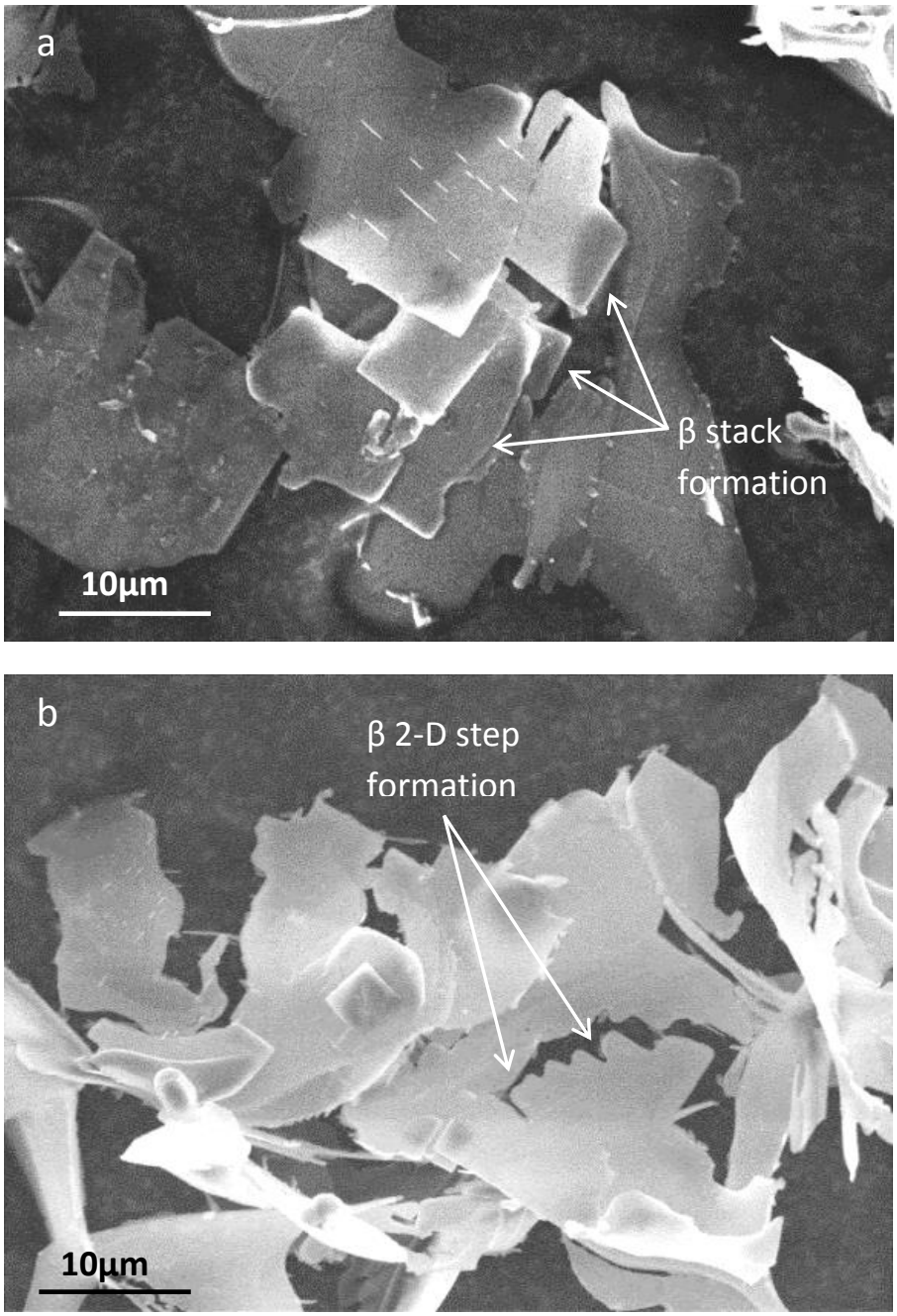

Fig 4.28 SE micrographs of β-AlFeSi intermetallic particles in a) TP-1 with additional GR and b) DC billet.

Similarly in 3D imaging the β-AlFeSi was observed to have a plate-like morphology. The β-AlFeSi particles in the TP-1 sample were mostly observed to grow in stack formation as shown in Fig. 4.28a, whereas the ones in DC billet were mostly forming 2-D steps (Fig 4.28b). The average interdendritic arm spacing for intermetallics in the TP-1 sample was 0.9±0.1μm whereas for DC billet it was 0.6±0.1μm. Also, the average length of the greatest faceted side of the β-AlFeSi particles in the TP-1 sample was 11.8±3μm in comparison to 7.6±2μm in the DC billet. The lateral growth of the monoclinic β-AlFeSi platelets is quite rapid along preferred orientations. When there is any physical obstruction in the growth front, these platelets must jog and once they have overcome the obstacle they grow in the preferred orientation parallel to the parent plate. Such types of jogs and connected platelets produce the stack formation observed in 3D imaging as shown in Fig. 4.28a. The platelets observed in the DC cast billet (Fig. 4.28b) suggest that they are also able to branch. It is shown that the morphology of the intermetallic particles can take the shape of the interdendritic space **(Meredith et al., 97)**.

4.3.3 Phase Identification

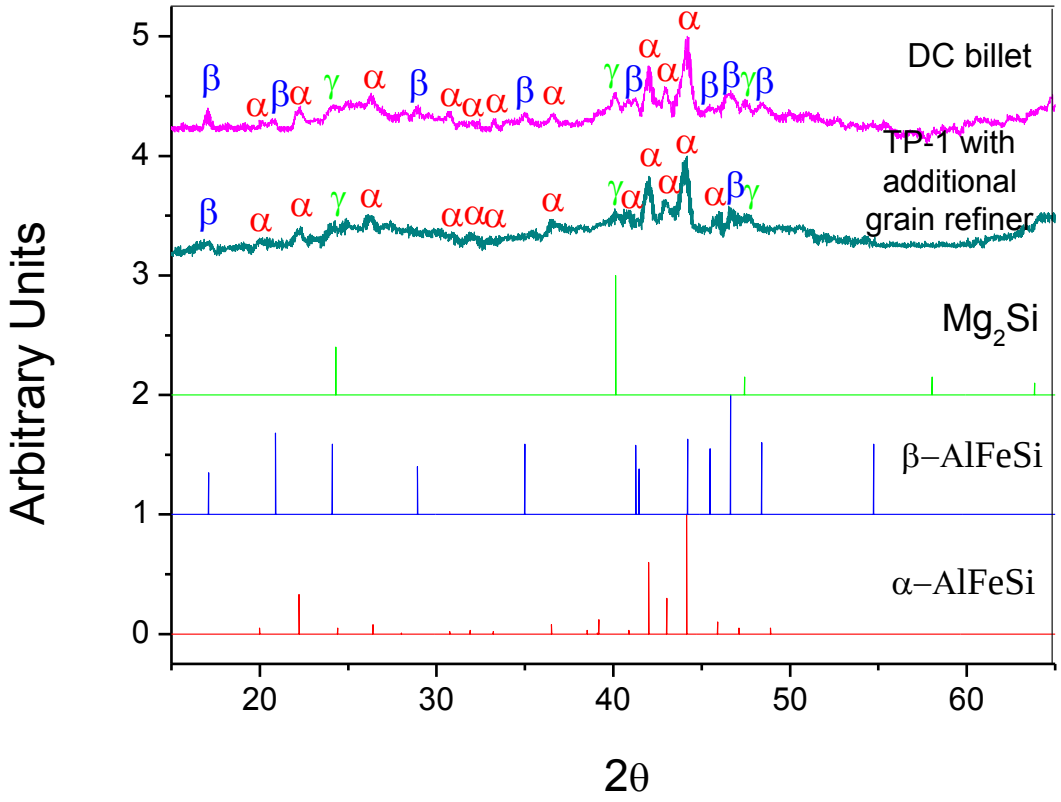

Fig 4.29a XRD spectra from the TP-1 with additional grain refiner and DC billet showing α-AlFeSi and β-AlFeSi peaks.

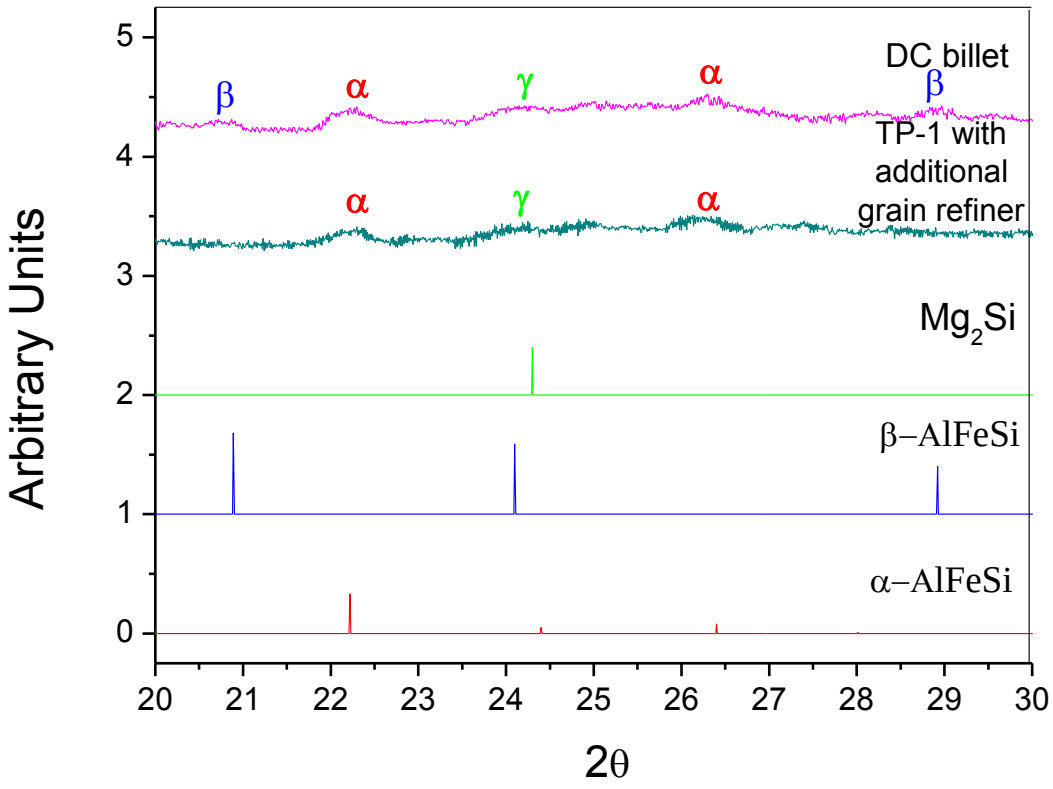

Fig. 4.29b Magnified XRD traces for the region 2θ=20 to 2θ=30 showing the overlapping of the α-AlFeSi and β-AlFeSi peaks.

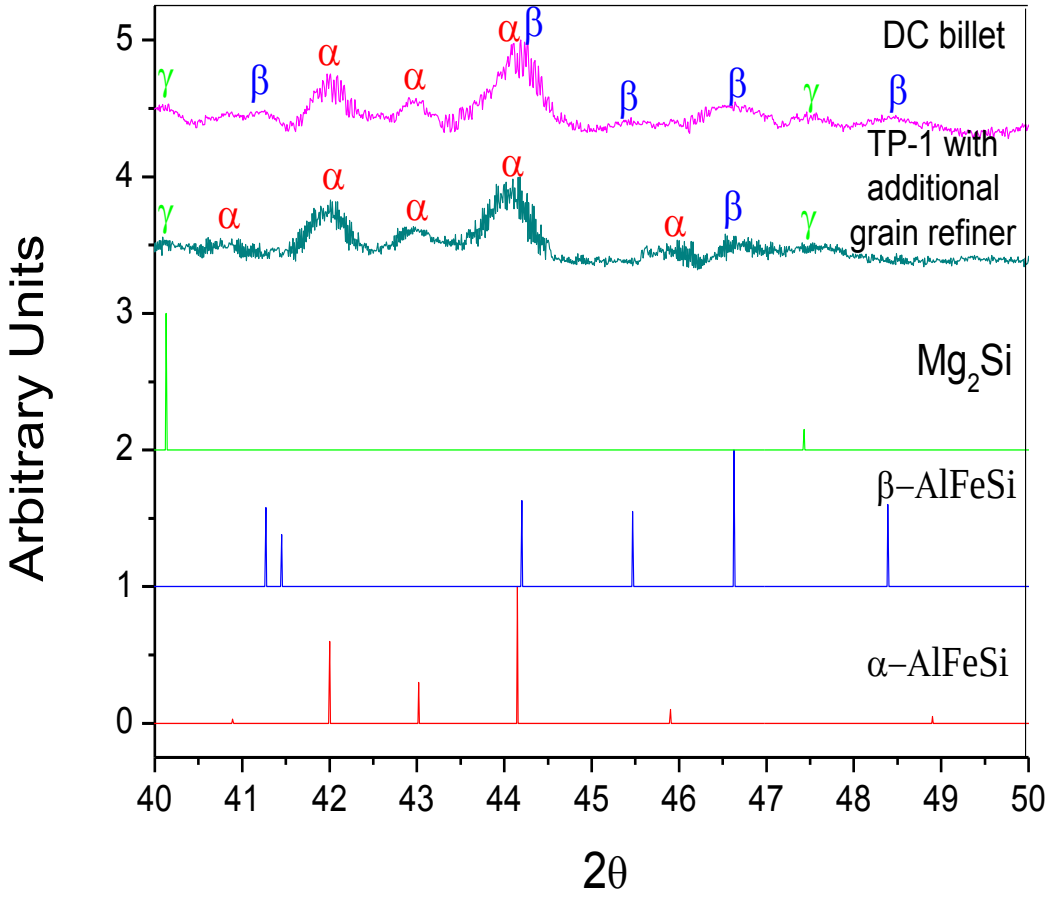

Fig. 4.29c Magnified XRD traces for the region 2θ=40 to 2θ=50 showing the overlapping of the α-AlFeSi and β-AlFeSi peaks.

XRD traces showed peaks from three intermetallic phases, namely α-AlFeSi, β-AlFeSi and Mg_2Si as shown in Fig. 4.29a. Fig. 4.29b and Fig. 4.29c shows the magnified XRD traces to clearly mark the peaks close to each other. Higher α-AlFeSi (44.15°, 42°, 43.01°, 22.22°, 36.5°, 45.9°, 26.4°) and β-AlFeSi (17.1°, 20.89°, 24.1°, 28.92°, 34.99°, 41.27°, 45.47°, 46.63°, 48.39°) peaks indicate that they were the dominant intermetallic phases in the alloy. Lower intensity peaks of the other phase, namely Mg_2Si (40.13°, 24.3°, 47.43°), explains its rare

observation in 3D analysis. The strong β-AlFeSi peak from the DC billet (17.03^{o}) resulted in slightly higher value of the relative fractions of β-AlFeSi intermetallics in the DC billet than the TP-1 with additional GR i.e 40% β-AlFeSi in DC billet and 35% β-AlFeSi in TP-1 with additional GR. However it is important to note that these calculations have an error of ±10% and so both the samples might have similar amount of α-AlFeSi. The similar grain sizes of the TP-1 with additional GR and the DC billet suggested similar cooling conditions, however the different sizes and morphologies of the intermetallic phases point toward different solidification conditions.

In addition to the cooling rate there are other factors governing the intermetallic phase selection, which include growth velocity, growth temperature and local solute distribution **(Allen et al., 98)**. DC casting is a complex solidification process **(Eskin, 08)**. It has been shown that the solidification velocity changes with solid volume fraction **(Allen et al., 98).** Since all of these intermetallic phases form during the last stages of solidification, after 90% of the sample has formed solid α-Al, the local solidification conditions play a significant role in the type of phase forming in addition to the shape of the primary Al. Kinetic undercooling plays an important role in the mechanism of growth rate affecting the phase selection **(Burden et al., 74)**. Therefore prediction of intermetallic phase formation may be completely unreliable based only on the cooling rate.

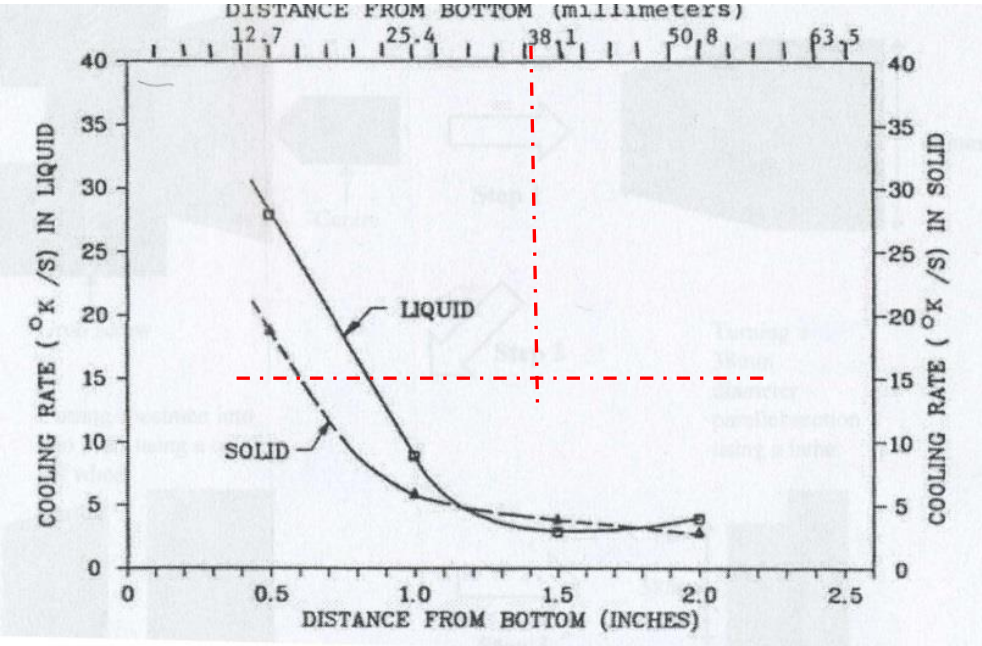

Fig. 4.30 Variation of cooling rate with the distance from the bottom of the TP1 mould **(Tanihata, 99)**.

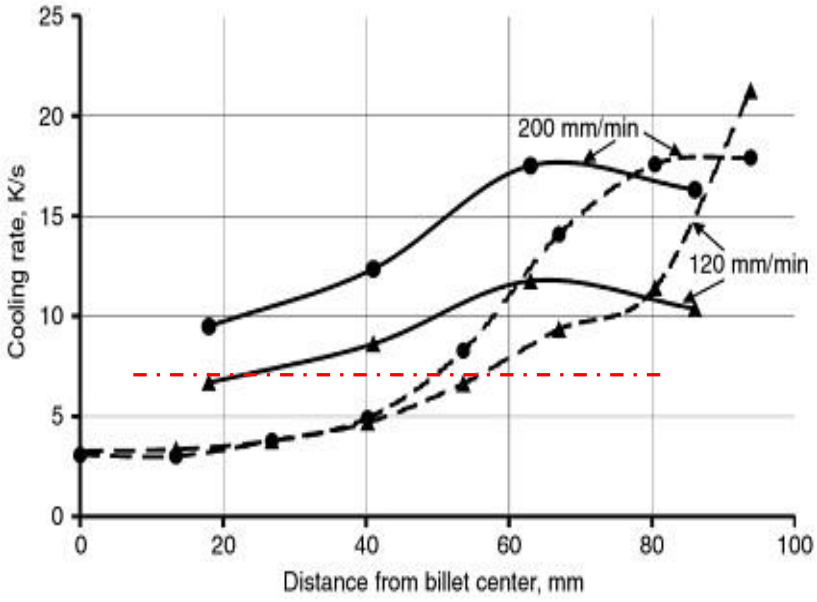

Fig. 4.31 Cooling curve for DC casting along the billet radius at different casting speeds estimated using dendritic arm spacing (solid lines) and the distance between liquidus and solidus (dashed lines) **(Eskin, 04)**.

Fig 4.30 shows the cooling curve for TP1 **(Tanihata, 99)**. Fig 4.31 shows the cooling curve for a 8" DC cast billet at different casting speeds (200mm/min and 120mm/min) using dendritic arm spacing (solid lines) and distance between liquidus and solidus (dashed lines) **(Eskin, 04)**. The red lines in both the figures shows the region where the TP1 sample replicates the cooling rate of 7" DC cast billet. It can be concluded that the cooling rate for a 8" DC cast billet (~0-20mm from the center of the billet) calculated on the basis of the distance between liquidus and solidus (dashed lines) and the TP1 sample at 38mm from the bottom of the mould have similar cooling rates.

TP1 provided promising results when it comes to the quantity of intermetallic phases, however TP1 was not good in representing the morphology of the intermetallics formed in DC casting. Hence, TP1 was only partially neat DC casting simulating technique.

Other techniques like DTA and DSC cannot be used for simulating DC casting conditions as these techniques are designed for small sample volume so they can be less accurate and hence were not considered. Other known techniques like Bridgeman growth and DC simulator were not considered.

5. Theoretical calculations

The effect of composition variation on phase formation was studied using MTDATA software tool (refer to section 3.1.3.2 for more details). MTDATA was used to gain an understanding about the phases to expect for a range of alloy compositions through lever rule calculations using validated NPL Aluminium Database-Ver. 6.10. This data was helpful in analysing the phases observed in the next set of alloys, i.e. prefil alloys (section 3.1.3.3) and TP1 alloys (section 3.1.3.4), which will be discussed in chapter-6.

While performing the lever rule calculations, only frequently observed phases like α-Al, α-AlFeSi, β-AlFeSi, $Al_{13}Fe_4$ and Mg_2Si were allowed to form and other phases like Si, γ-AlFeSi, δ-AlFeSi, $\pi(Al_8FeMg_3Si_6)$ were suppressed as they were less likely to form and were rarely observed during past research. Theoretical calculations were conducted on a range of compositions. Table 5.1 shows the range of compositions for different elements used in this study. The composition ranges for Fe and Si in this study were chosen within the 6xxx series and close to the values used for earlier experiments (3.1.2 and 3.1.3.1). The thinking behind adding high amount of Mg i.e. beyond 6xxx series in prefil and TP1 alloys, was to generate more in-situ Mg oxides and to study their effect on intermetallic formation. However, Mg will also affect the phase formation behaviour and hence MTDATA will help us to develop an understanding of the phases preferred with different Mg levels, while keeping the other elements constant. MTDATA cannot predict the

nucleation effect and hence was not used to study the effect of Mg oxides on intermetallic formation.

Due to various limitations, the phases predicted by MTDATA are unlikely to mirror exactly the real cast structure.. For example, MTDATA takes into account the average solidification rate and predict the phase according to that undercooling. However, in reality, the solidification rate/undercooling could be much higher. MTDATA uses the composition value for lever rule calculations, which could fluctuate significantly under real conditions from location to location. Also, it is important to note that the real solidification conditions lie somewhere between lever rule (complete diffusion in solid) and scheil (no diffusion in solid) conditions. Hence either of the two extreme scenarios will provide us only with an approximate picture. The real solidification conditions might result in the formation of other preferred phase than predicted by MTDATA. Hence it is important to only use the MTDATA calculations as a guide.

Table 5.1 shows the composition ranges of elements used for MTDATA analysis

Element	Fe	Si	Mg
Composition range	0.1-0.4 wt%	0.3-0.6 wt%	0-5.1 wt%

It is important to note that the variation in the Fe and Si composition (as mentioned in the Table 5.1) did not affect the MTDATA plots significantly (except for very minor changes in mass fraction and temperature values). Hence, only the MTDATA plots (calculated using lever rule) for the alloys Al-0.2Fe-0.4Si-X(0-5%)Mg will be discussed from this point. Fig. 5.1 shows the MTDATA graphs plotted using lever rule calculations for different Mg levels. The dotted lines with S and L abbreviations in Fig. 5.1 denote solid and liquid respectively, i.e. everything at temperatures beyond liquid (L) line is 100% liquid and everything below solid line (S) is 100% solid. The region between L and S is the semi solid/semi liquid region. The reason why L and S lines are vertical and does not have any gradient is because they are actually representing one point on the liquidus and solidus lines in Al-Mg-Fe-Si phase diagram.

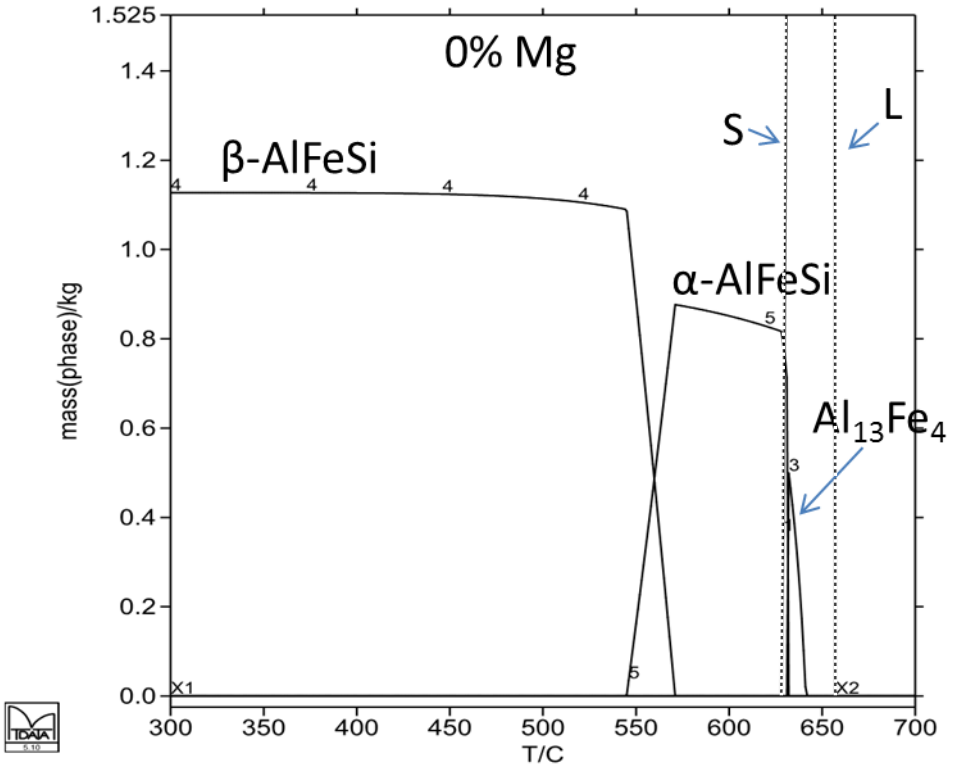

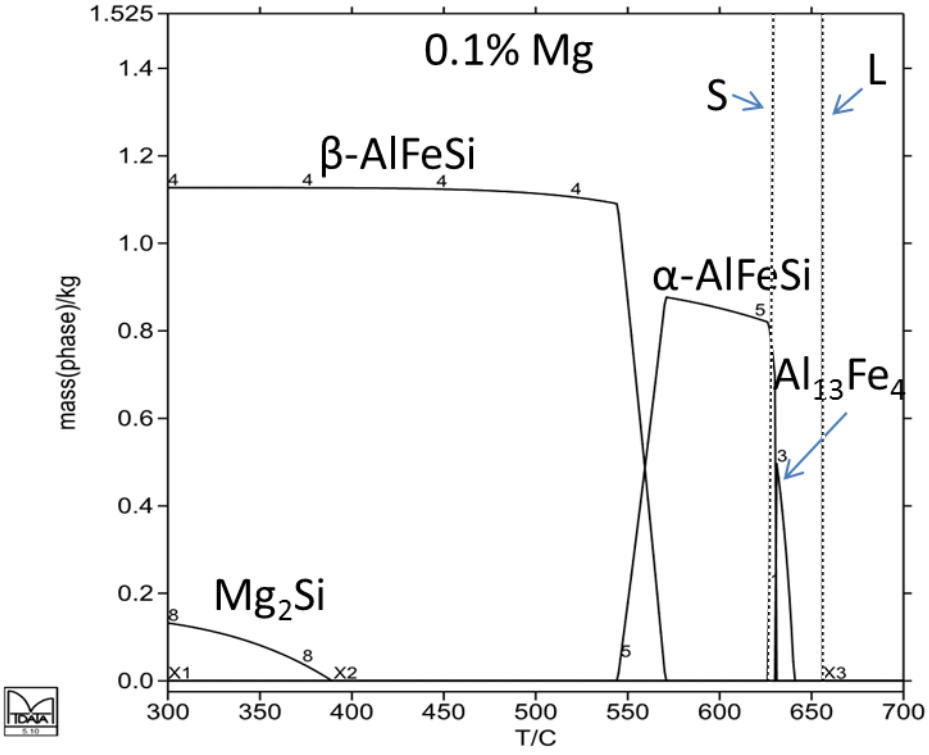

Continued overleaf…

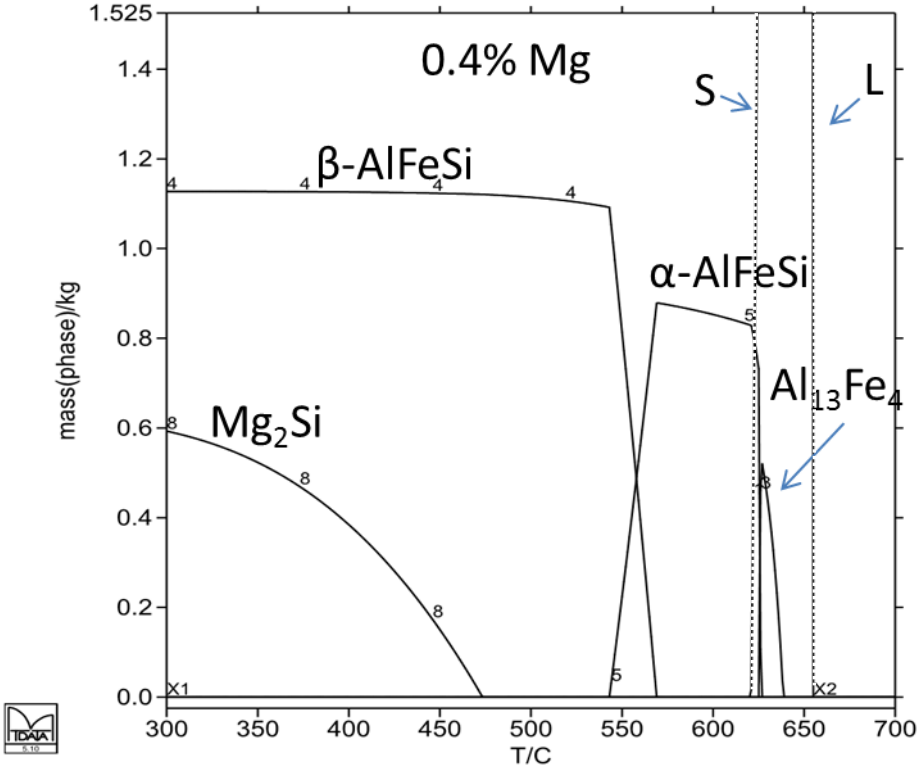

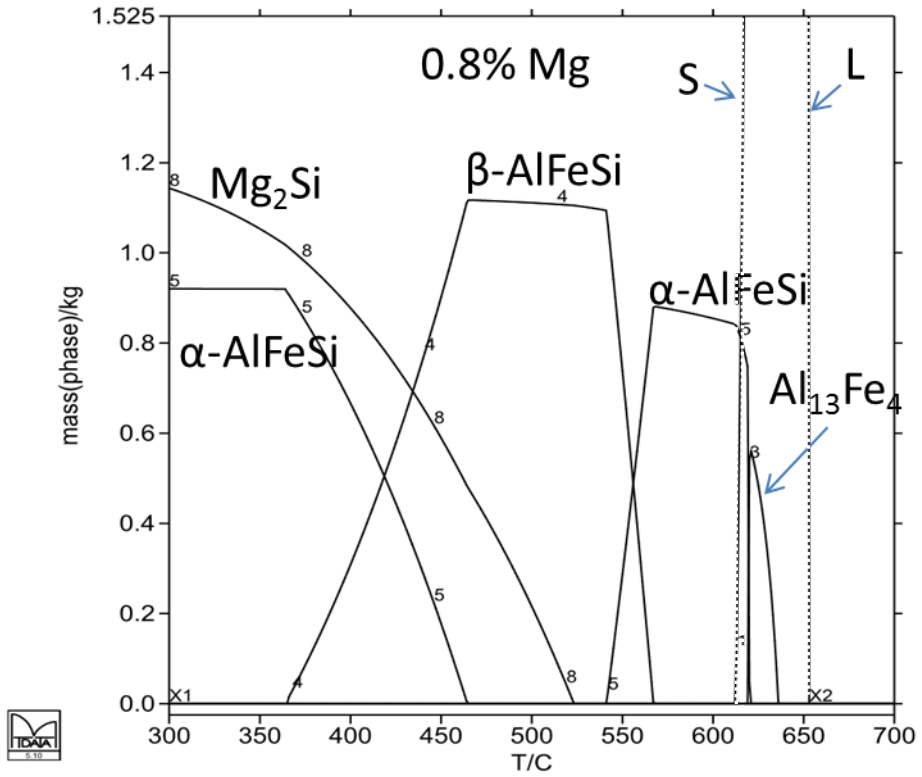

Continued overleaf…

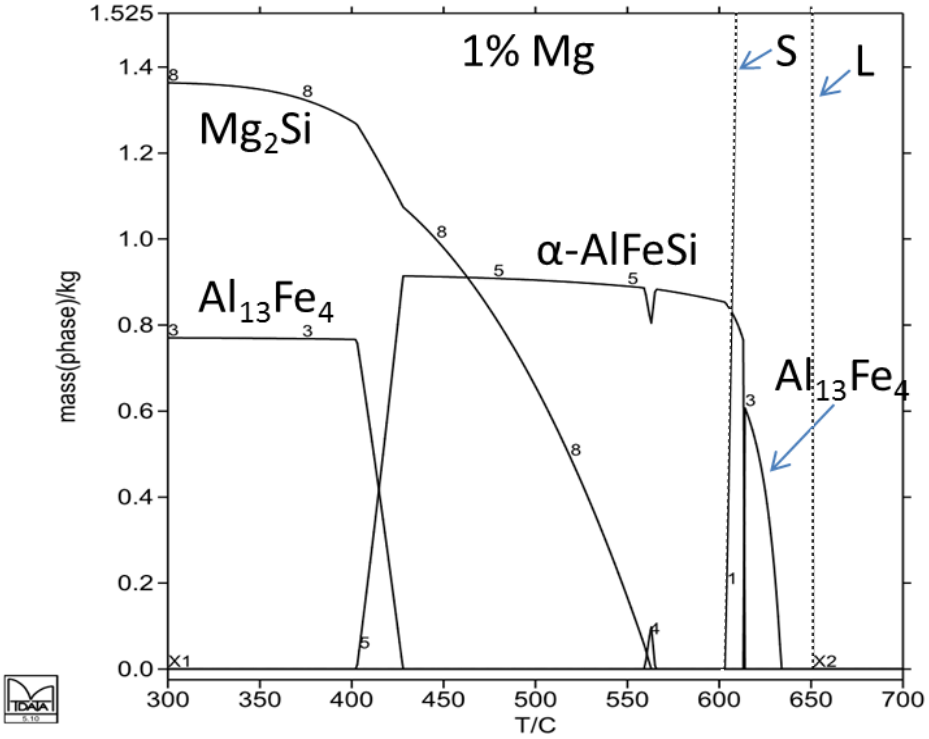

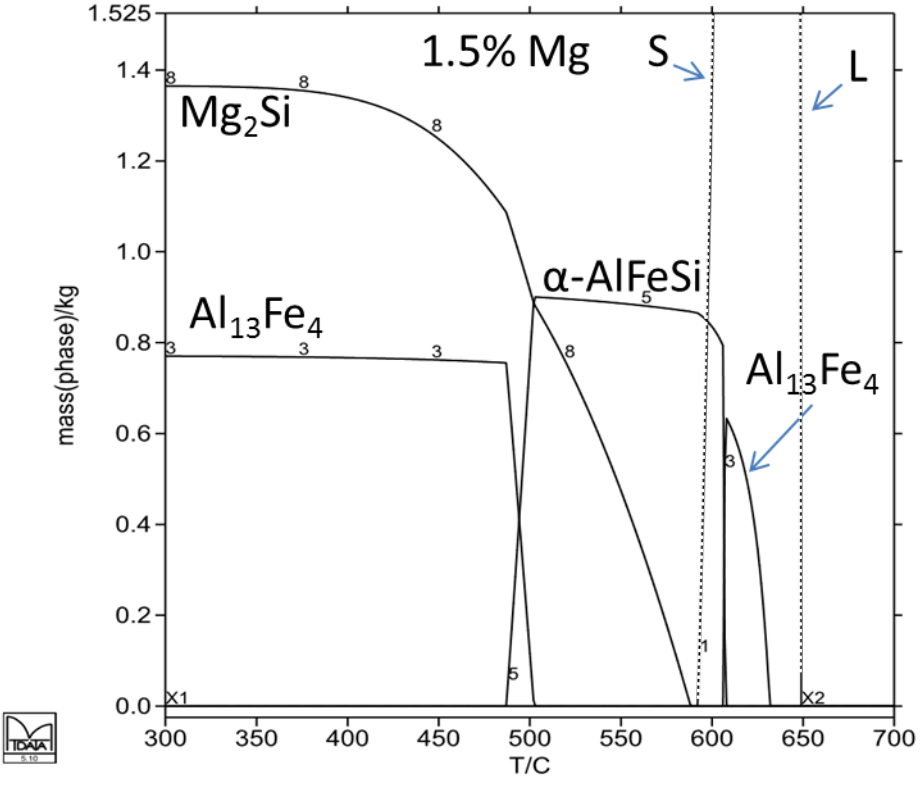

Continued overleaf…

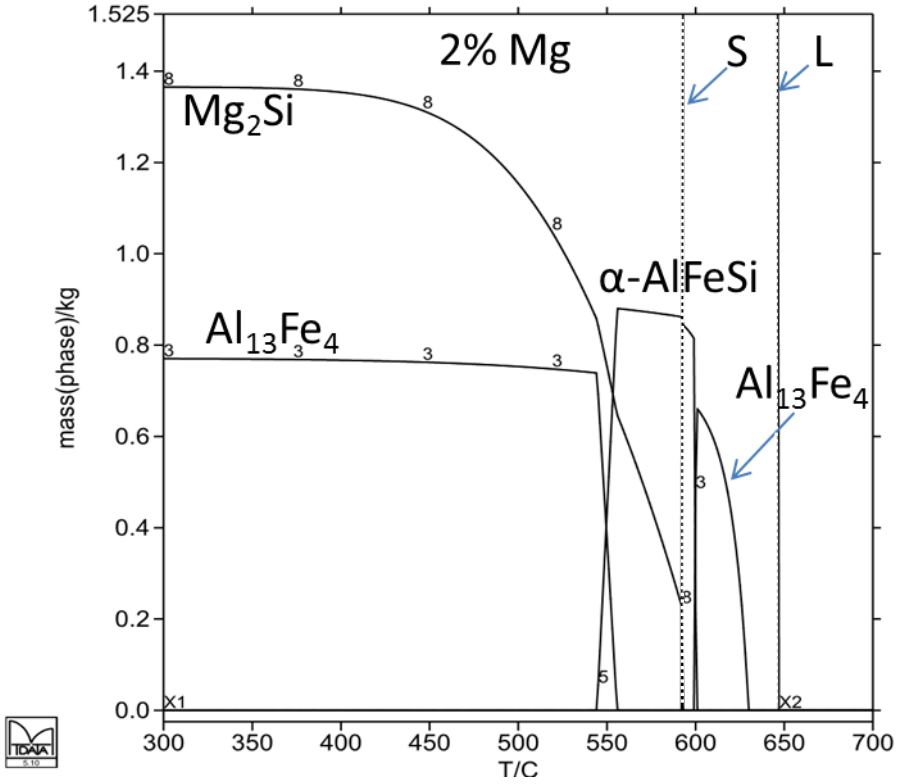

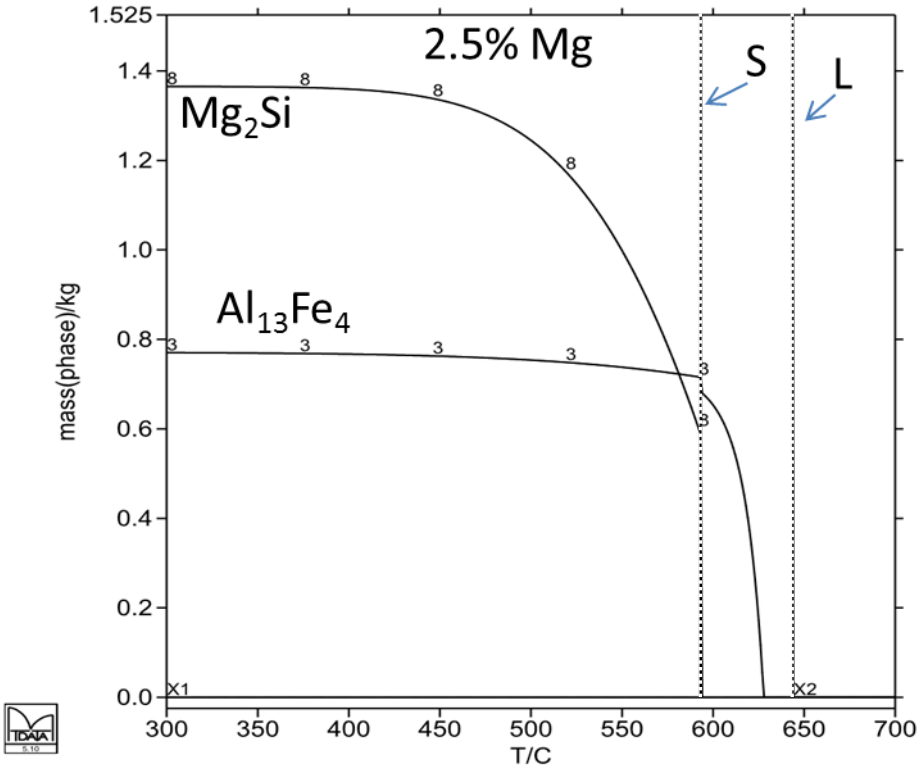

Continued overleaf…

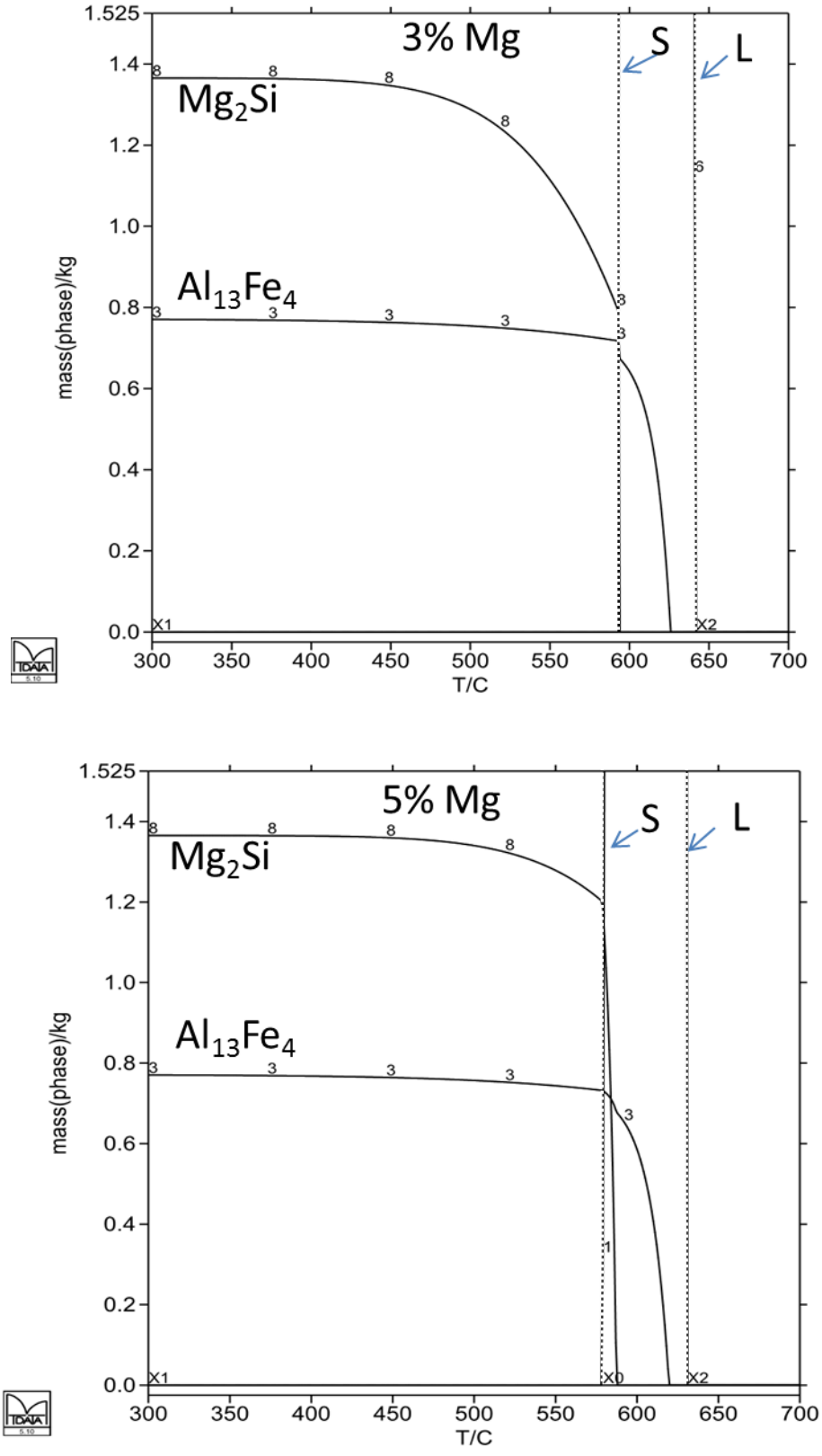

Fig 5.1 shows the MTDATA plots (mass(kg) vs T(^{o}C)) for different Mg content

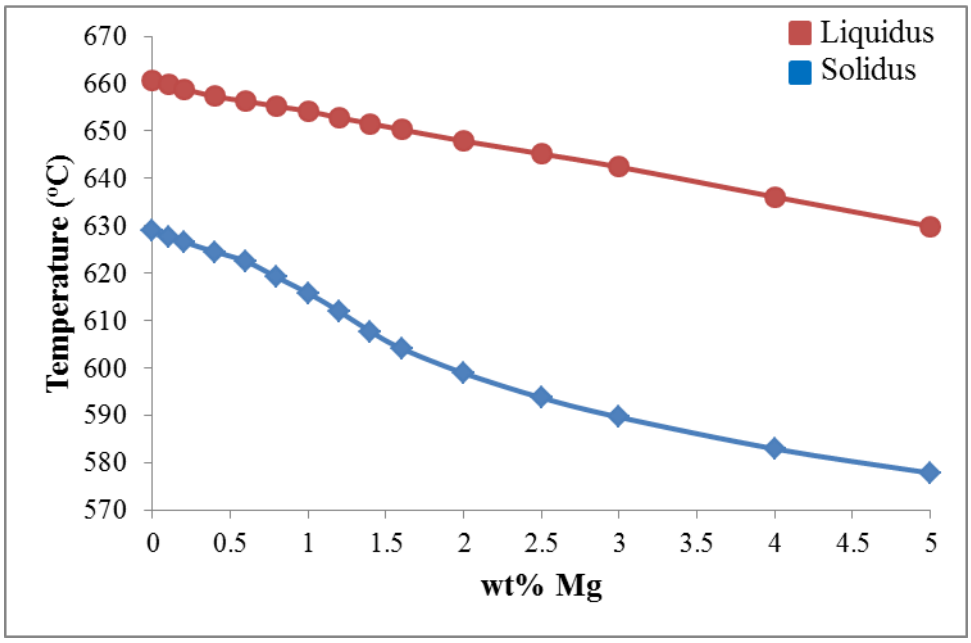

Fig 5.2 shows the solidus and the liquidus temperatures as a function of Mg content.

As the Mg content was increased, it was interesting to note the drop in both the liquidus and solidus temperatures from 660°C (0 wt%) to 630°C (5 wt%) and 630°C (0 wt%) to 580°C (5 wt%) respectively. Also, the region between liquidus and solidus widens (Fig. 5.2) with the increase in Mg content, which might allow further nucleation and growth of the intermetallics.

Phase fraction vs temperature plots (Fig. 5.1) for various Mg content provided valuable information on different phases to be expected. For eg. in 0.4 wt% Mg plot, the first solid (primary Al) formed at 658°C (liquidus temperature). As the temperature dropped, the fraction of primary Al increased and at 640°C $Al_{13}Fe_4$ forms from the remaining liquid. As the temperature dropped further, the fraction of both primary Al and $Al_{13}Fe_4$ increased. At 630°C, α-AlFeSi start to form from the remaining liquid while the fraction of $Al_{13}Fe_4$ steeply decreased to

zero. On the other hand the fraction of primary Al kept increasing. As the temperature further dropped, the fraction of α-AlFeSi and primary Al increased. At 620^{o}C (solidus temperature) there was no liquid left in the system. Any phases that nucleate or grow below this temperature were formed from Al solid solution via solid state reactions (β-AlFeSi in case of 0.4 wt% alloy). The reactions in region between L and S temperatures are solidification reactions and below S temperature are solid state transformations.

For all the compositions, $Al_{13}Fe_4$ was the first phase to form from the liquid i.e.

L → Al + $Al_{13}Fe_4$ (~620 (5 wt%) - 645^{o}C (0 wt%))...…….....(1)

It is interesting to note that the mass fraction of $Al_{13}Fe_4$ increased until α-AlFeSi starts to form in the liquid and then decreases as α-AlFeSi continues to form (for Mg≤2%) which can be explained by the following reaction:

L+ $Al_{13}Fe_4$ → Al + α-AlFeSi (~600-630^{o}C).....…….(2)

The alloy was fully solidified in the temperature range of 580^{o}C (5 wt%) - 630^{o}C (0wt%) as shown in Fig. 5.2. Mg_2Si andβ-AlFeSi were more stable than α-AlFeSi for Mg≤0.5%, whereas α-AlFeSi was the stable phase for 0.5%<Mg<1%. It is important to note that β-AlFeSi forms from solid solution for Mg<0.8 wt%, as seen in the MTDATA plots. However, Sha et al., showed that β-AlFeSi can form from liquid via the peritectic reaction (3) under equilibrium conditions when α-AlFeSi phase was suppressed **(Sha et al., 03)**.

L + $Al_{13}Fe_4$ → Al + β-AlFeSi.....…….(3)

For Mg≤0.5% alloys, it is interesting to note that the amount of β-AlFeSi formed was fixed, whereas the amount of Mg_2Si increased with Mg content. This is because some Si in the liquid is absorbed by β-AlFeSi, which formed before Mg_2Si. However, the fraction of β-AlFeSi phase was limited (and constant) due to the fixed Fe content in the alloy and not due to the Si content. Whereas, the amount of Mg_2Si formed was limited due to the Mg content (for low Mg alloys) and not due to the residual Si (after β-AlFeSi formation). Therefore, the fraction of Mg_2Si phase increased with the increase in Mg content for Mg ≤0.5% (See Fig. 5.1).

For 0.5%<Mg<1% alloys, although α-AlFeSi was formed before Mg_2Si via solidification reaction. The final fraction of α-AlFeSi phase formed through solid state transformation was limited, as the decomposition of β-AlFeSi provided the Fe and Si in the solute for α-AlFeSi. However, Mg was also combining with Si to form Mg_2Si, which resulted in low Si availability and effectively high Fe:Si ratio favouring α-AlFeSi formation. It is also interesting to note that the fraction of Mg_2Si phase increased further with the Mg content and achieved the maximum value at Mg=1wt% and the fraction of α-AlFeSi decreased as less Si was available (see Fig 5.1).

For 1%≤Mg<2.5%, neither α-AlFeSi nor β-AlFeSi were stable but $Al_{13}Fe_4$ and Mg_2Si were the most stable phases, whereas for Mg≥ 2.5%, $Al_{13}Fe_4$ and Mg_2Si forms directly from the liquid.

$L \rightarrow Al + Al_{13}Fe_4 + Mg_2Si$ (~590^{o}C(2.5 wt%)-630^{o}C (1wt%))……..(4)

The fraction of Mg_2Si phase increased with the increase in Mg content and reached maximum value for 1% Mg. This can be attributed to the limited amount of Si content (0.4%) in the alloy. Since Mg reduces the solubility of Si in the solid Al, further increase in Mg above 1wt% will not promote AlFeSi intermetallic because there will be no Si available to react with Fe to form AlFeSi intermetallics. As a result, $Al_{13}Fe_4$ was the other stable phase formed for Mg ≥1%.

For Si=0.4%, it was interesting to note that at a low Si:Mg ratio (≤1:2), all the Fe was absorbed by the $Al_{13}Fe_4$ phase, whereas for high Si:Mg ratio (>1:1), all the Fe was absorbed by the β-AlFeSi phase. For all the other Si:Mg ratios between 1:2 and 1:1, α-AlFeSi was more stable than β-AlFeSi.

Isothermal plots by Belov et. al at 450^{o}C (Fig. 5.3) are also in agreement with the MTDATA calculation. Please note that in Fig. 5.3, 'F'' denotes $Al_{13}Fe_4$ andthe dotted red line denotes the Si content (0.4%) in the alloys (in this study). The dotted rectangular box in Fig. 5.3 denotes the composition range for 6003 alloys used by Belov et al. for their experimental purpose and is not relevant for this study. As the Mg content was increased in the isothermal plot at 450^{o}C (Fig. 5.3), it showed the stability moving from β-AlFeSi, to β-AlFeSi + Mg_2Si, to α-AlFeSi + β-AlFeSi + Mg_2Si, to α-AlFeSi + Mg_2Si and finally to $Al_{13}Fe_4$ + Mg_2Si.

From the MTDATA calculations it can be concluded that α-AlFeSi and β-AlFeSi were the stable phases for low Mg alloys. A phase shift was observed with the increase in Mg content, i.e Mg_2Si and $Al_{13}Fe_4$ being the more stable phases than AlFeSi intermetallics. The summary from the MTDATA calculations is presented

in Table 5.2 which shows the phases predicted for a given Mg content. Given the results predicted by the MTDATA calculation, it was decided that a broad range of Mg content (0 wt% -5 wt%) would be examined in the actual experiments, which will be discussed in Chapter 6.

Table 5.2 shows the summary of the phases to be expected for different Mg content during the next set of experiments i.e. prefil and TP1.

Alloy composition	α-AlFeSi	β-AlFeSi	$Al_{13}Fe_4$	Mg_2Si
Mg≤0.5%	No	Yes	No	Yes
0.5%≤Mg<1%	Yes	No	No	Yes
Mg ≥1%	No	No	Yes	Yes

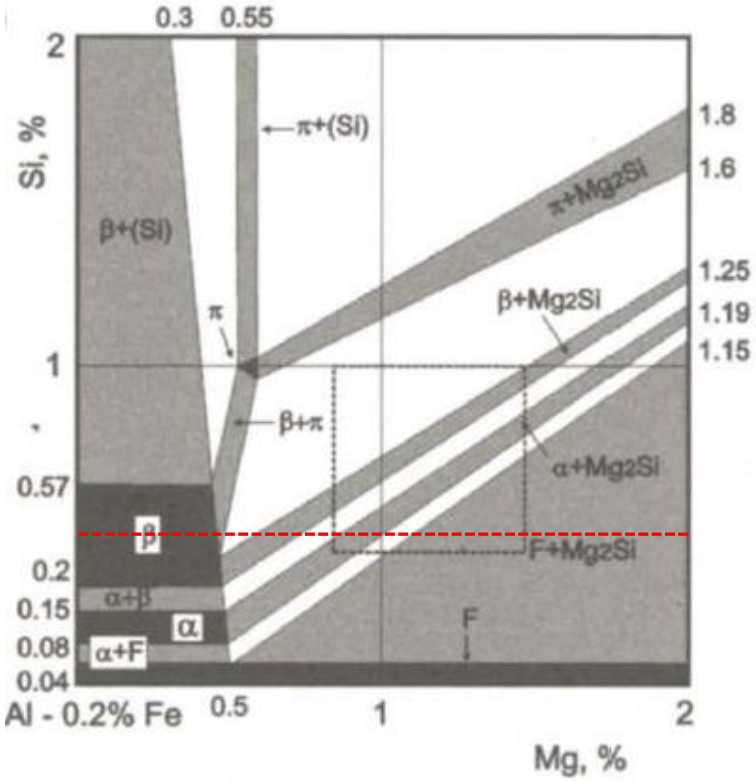

Fig. 5.3 shows the isothermal plot for Al-0.2%Fe at 450^{o}C **(Belov, 05)**

6. Results and Discussion II

6.1 Study of inclusions present in Al-0.3Fe-0.5Si-X Mg alloys using prefil technique

The main aim of this study was to concentrate and analyse the microstructure of the inclusions present and their effect on the intermetallic formation. For this purpose four alloys were prepared with a wide range of Mg content (0.1 wt%, 0.5 wt%, 1.3 wt% and 5.1 wt%) using the base alloy system of Al-0.3Fe-0.5Si (see section 3.1.3.3 for more details on alloy preparation). The qualitative analysis of the microstructures of these alloys was carried out using a wide range of techniques including optical microscopy, SEM and XRD. The 2D and 3D morphologies of the inclusions were studied in depth and are described in sections 6.1.1 and 6.1.2 respectively. The identification of different inclusions and Fe-intermetallics was conducted with the help of XRD (section 6.1.3). While using EDX for identification of inclusions, the information from previous research was utilised for example if the Mg/O ratio is less than 0.4, the oxide is highly likely to be $MgAl_2O_4$-rich oxide, if the Mg/O ratio is more than 1, the oxide consists of a high percentage of pure MgO **(Bakhtiarani et al., 11).** For example in Fig. 6.1b the Mg/O is ~0.5 which indicates a mixture of MgO and spinel.

6.1.1 Characterisation of the 2D morphology of inclusions

Fig 6.1 shows the 2D morphologies of the different types of inclusions namely Al_2O_3, TiB_2, Mg-oxide, typically present in the alloys with different Mg

contents. These inclusions were identified using EDX analysis and AlFeSi intermetallics were identified using the ratio of Fe to Si from EDX analysis and the morphologies described in existing literature **(Cooper, 67)** and **(Allen et al., 99)**. Techniques such as SE and BSE were used on the same area to characterise further details in the microstructure.

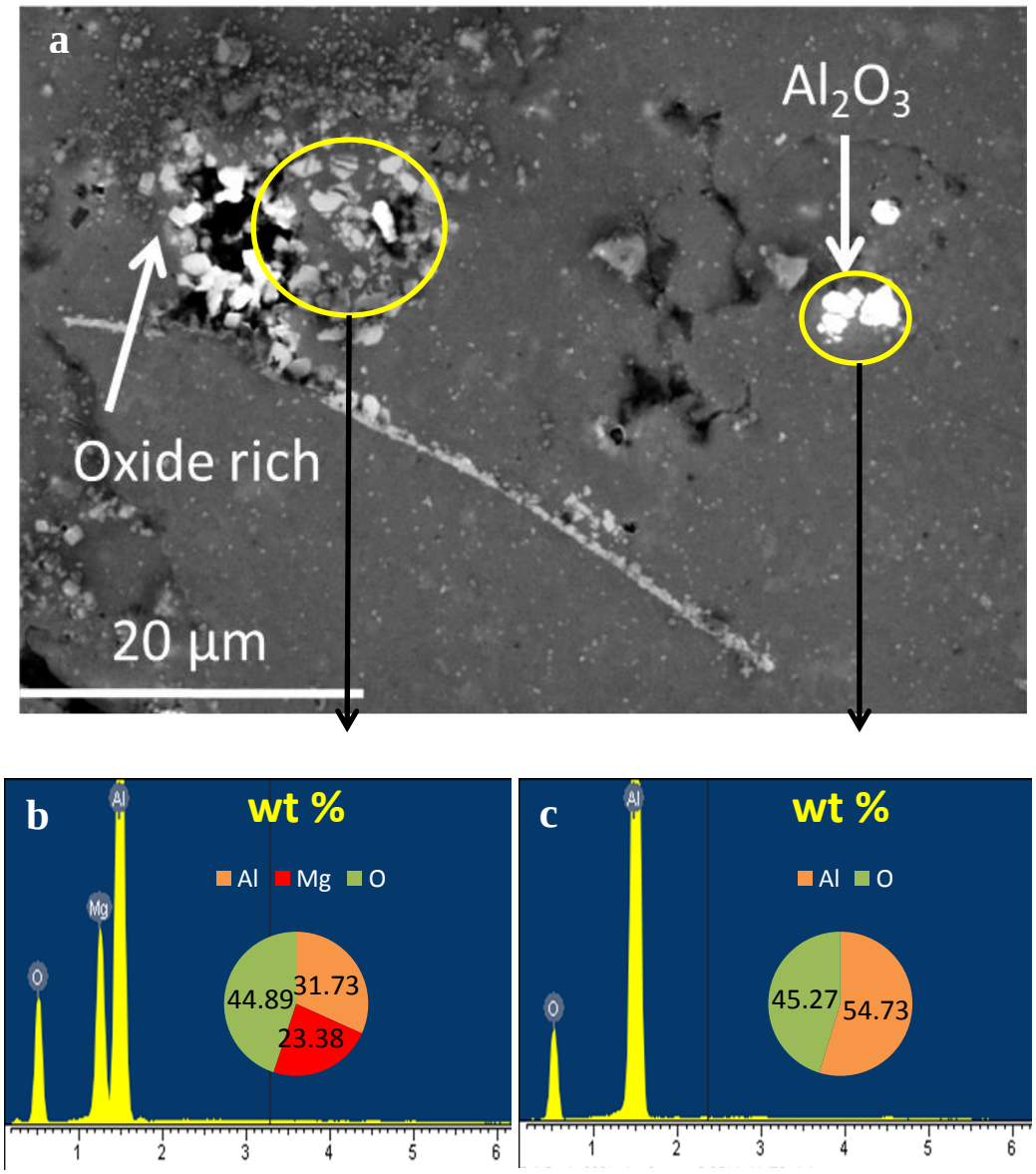

Continued overleaf…

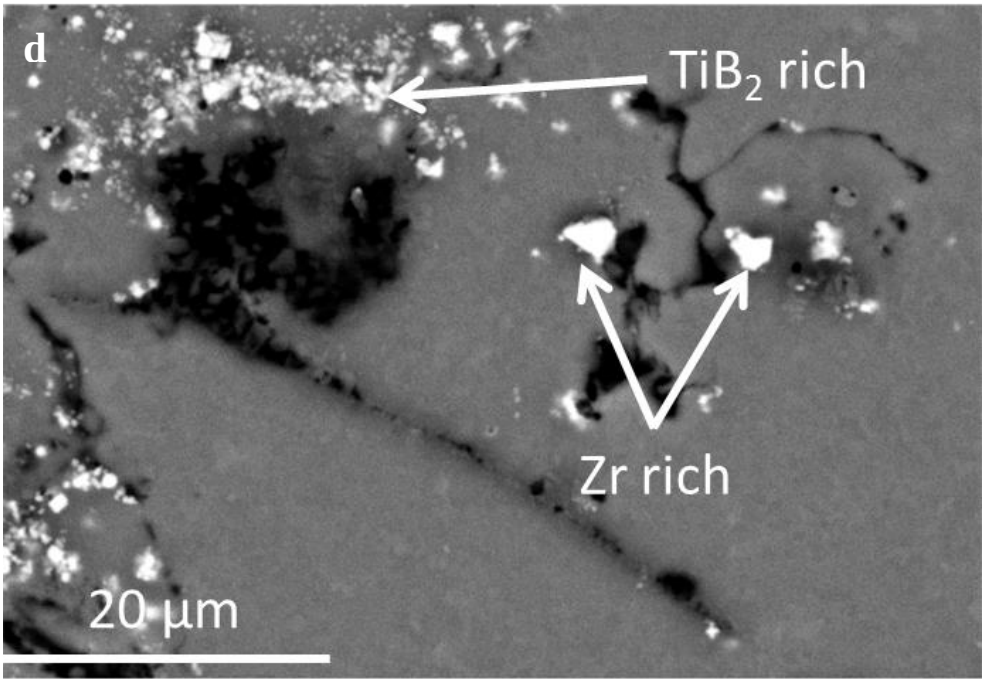

Fig 6.1 Prefil alloys showing a) SE image showing oxide cluster and Al_2O_3 particles, b) EDX spectra of oxide cluster (MgO and spinel), c) EDX spectrum of the Al_2O_3 and d) BSE image of the same area showing clusters of TiB_2 rich particles and Zr rich particles.

6.1.1.1 Prefil alloy with 0.1 wt% Mg

A wide range of inclusions were observed in this alloy. Clusters of inclusions including TiB_2 rich, Spinel ($MgAl_2O_4$), MgO and Al_2O_3 rich were frequently observed. Crack-like features were also spotted frequently across the microstructure and the majority (90%) of them were in association with the AlFeSi-intermetallics. These cracks were identified as oxide bi-films with the help of EDX analysis (Fig. 6.2b). However, as 2D analysis provides only partial information further details of the oxide bi-film will be discussed on the basis of

3D morphology. Fig. 6.2a shows the association of AlFeSi-intermetallics around the oxide bi-film and Fig. 6.2c is a backscattered image showing the presence of AlFeSi-intermetallic underneath the oxide bi-film. The oxide formation behaviour of Mg will be discussed later in section 6.3.1 and section 6.3.2. Mg_2Si was also observed on rare occasions.

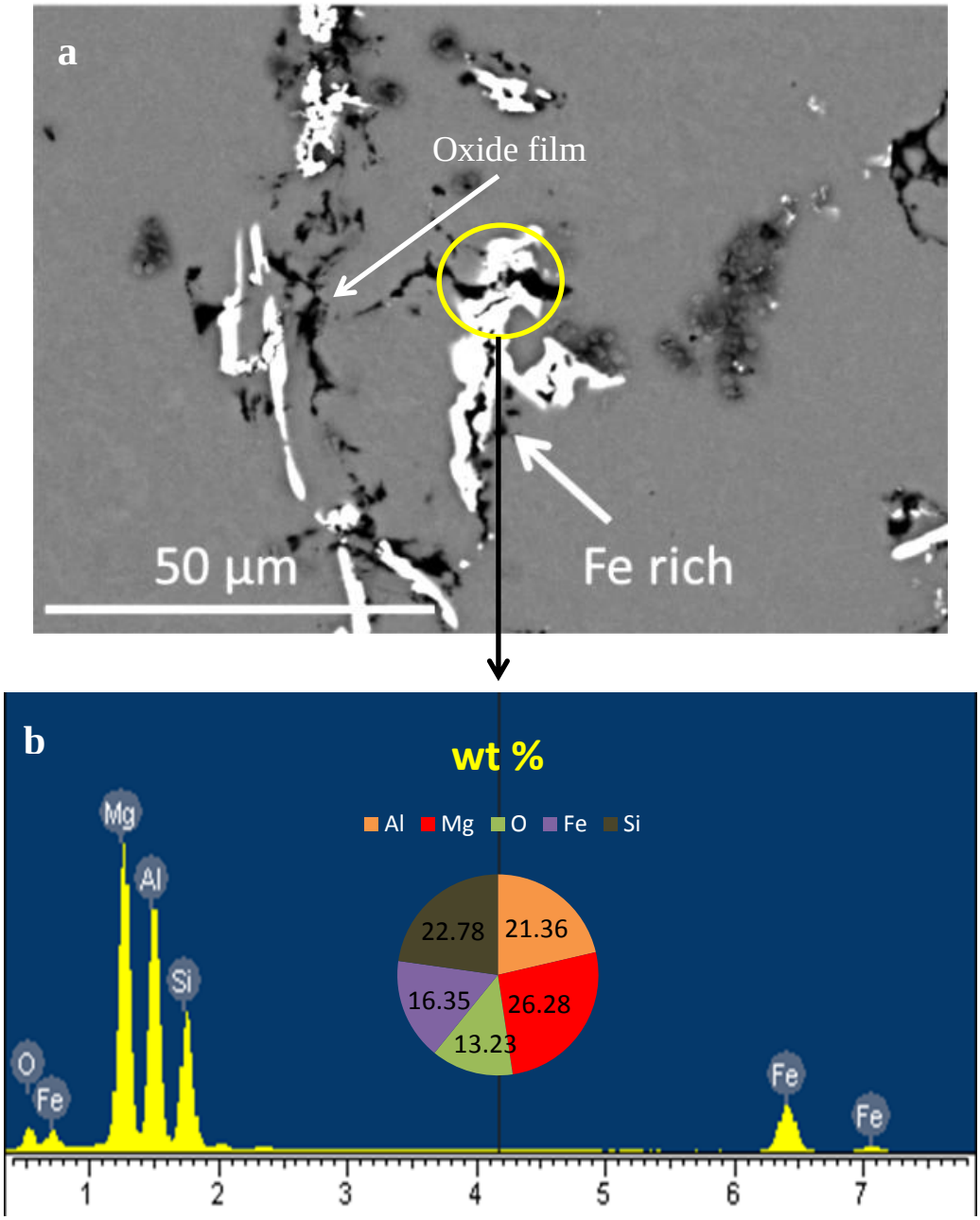

Continued overleaf…

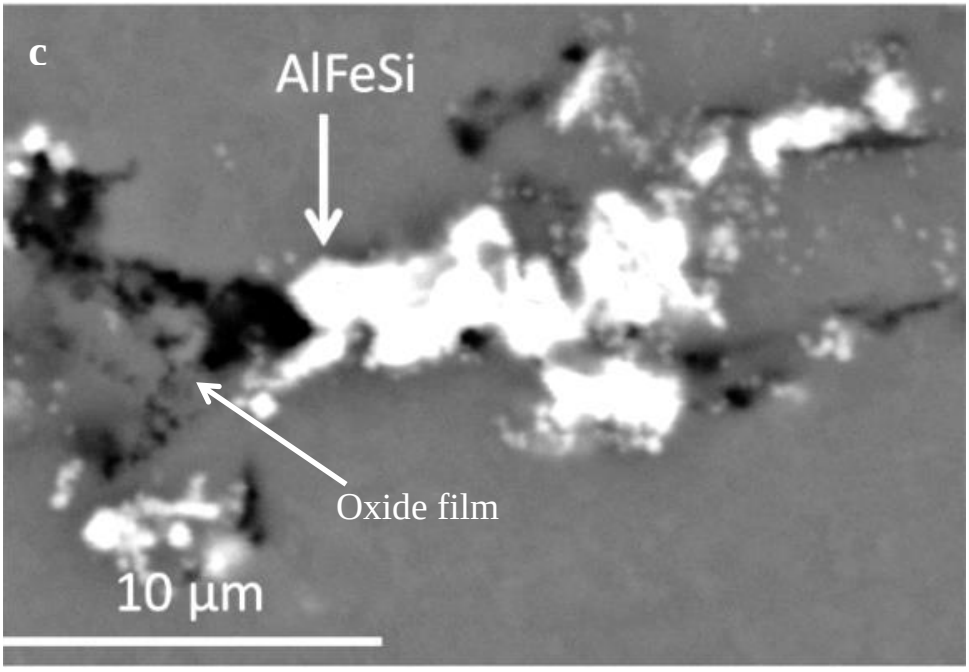

Fig 6.2 BSE micrographs of prefil alloy with 0.1 wt% Mg showing a) intermetallics formed around the oxide bi-films, b) EDX spectrum showing the presence of oxide bi-films along with the AlFeSi intermetallics and c) AlFeSi intermetallic (probably α-AlFeSi) observed under the oxide layer.

6.1.1.2 Prefil alloy with 0.5 wt% Mg

Clusters of inclusions such as Spinel ($MgAl_2O_4$), MgO and TiB_2 were frequently observed in this alloy. However, Al_2O_3 was observed on rare occasions. Crack-like (oxide bi-films) features similar to those in the 0.1 wt% Mg alloy were observed in association with the AlFeSi-intermetallics. The EDX spectra in

Fig. 6.3 b also shows the Mg/O value close to 0.5 which means that spinel is more dominating than MgO.

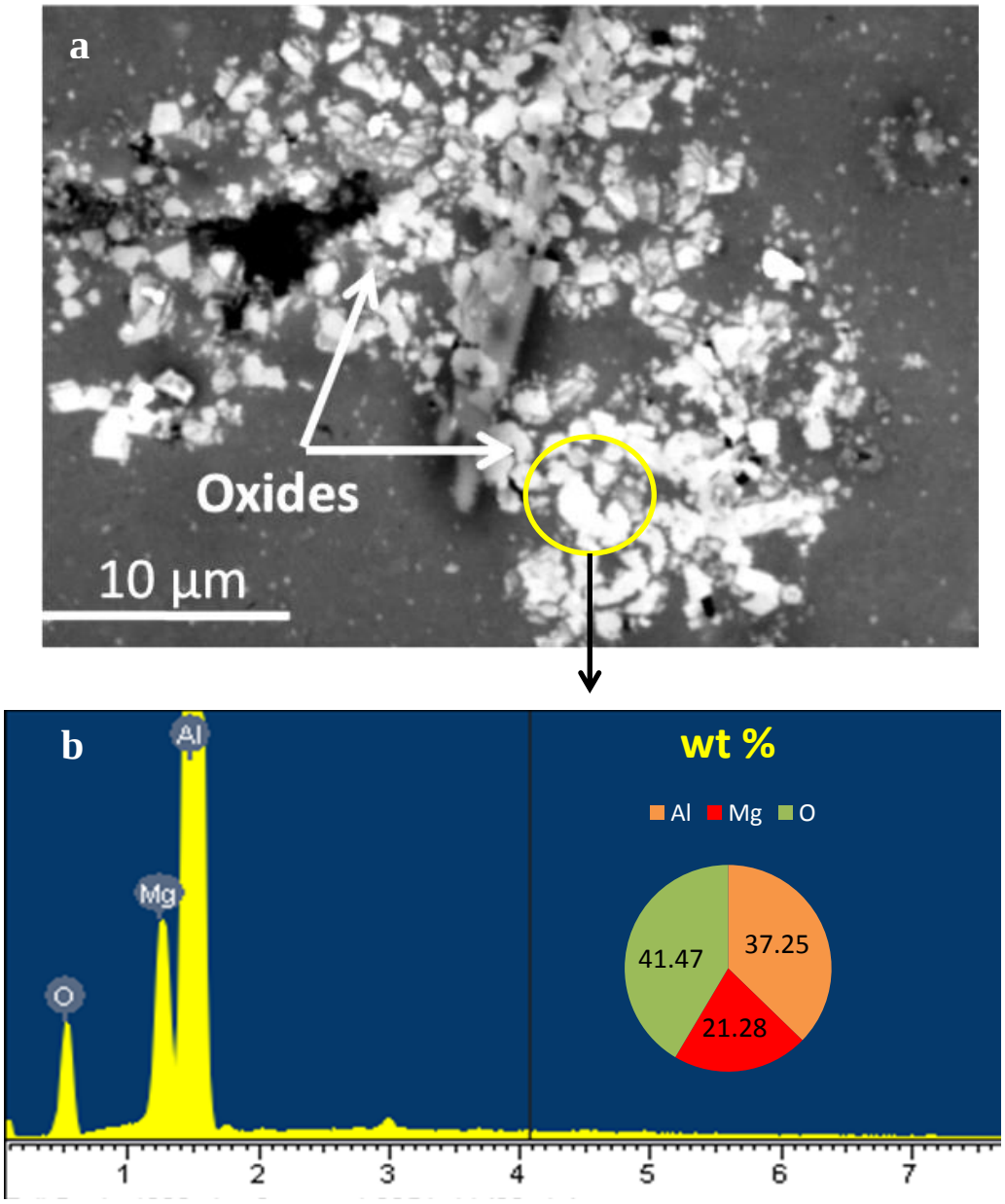

Continued overleaf…

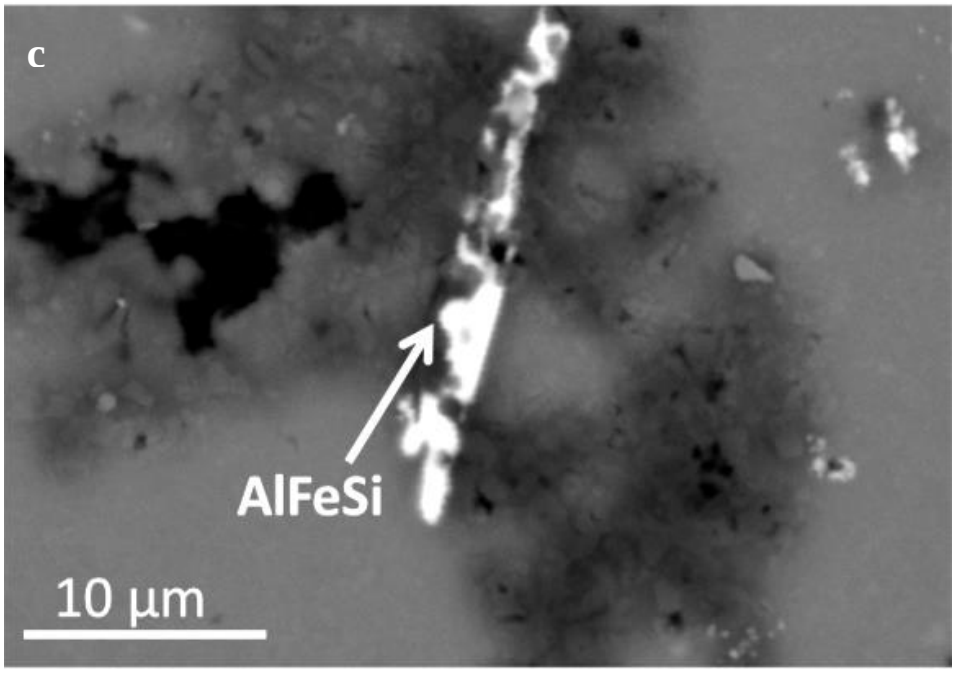

Fig 6.3 Micrographs of 0.5 wt% Mg prefil alloy showing a) SE image displaying clusters of spinel along with the oxide bi-film, b) EDX spectrum showing the composition of the spinel detected and c) BSE image of the same area displaying the bright AlFeSi intermetallic underneath the layer of oxide.

Fig 6.3 shows the SE and BSE images of the same sample area. Fig. 6.3a is the SE image and clearly displays the presence of clusters of spinel (~50µm in size), whereas Fig. 6.3b is the BSE image showing the presence of an AlFeSi-intermetallic underneath the layer of spinel particles. These clusters were commonly observed across the sample and 80% of them had one or two AlFeSi-intermetallics underneath them. Mg_2Si was also observed but not frequently.

6.1.1.3 Prefil alloy with 1.3 wt% Mg

As the Mg content was increased from 0.5 wt% Mg to 1.3 wt% Mg, the number of clusters of oxides increased by approximately 30%. It was also interesting to note that the number of oxide bi-films (crack-like features) increased significantly. Fig 6.4 shows the SE and BSE images of the same sample area. Fig. 6.4a shows the SE image displaying the presence of clusters of mixed MgO and spinel, whereas Fig. 6.4b shows the BSE image displaying the presence of Fe-intermetallic underneath the layer of spinel particles. Fig. 6.4c shows the EDX which confirms the presence of both MgO (Mg/O ratio>1) and spinel (Mg/O ratio ~0.5). Clusters of TiB_2 were also observed in this alloy. However, Al_2O_3 was not observed. Mg_2Si was observed frequently in Chinese script morphologies and mainly in association with the $Al_{13}Fe_4$ intermetallics. Only about 15% of the Mg_2Si observed was not associated with $Al_{13}Fe_4$ intermetallic. AlFeSi intermetallics were also observed however occasionally.

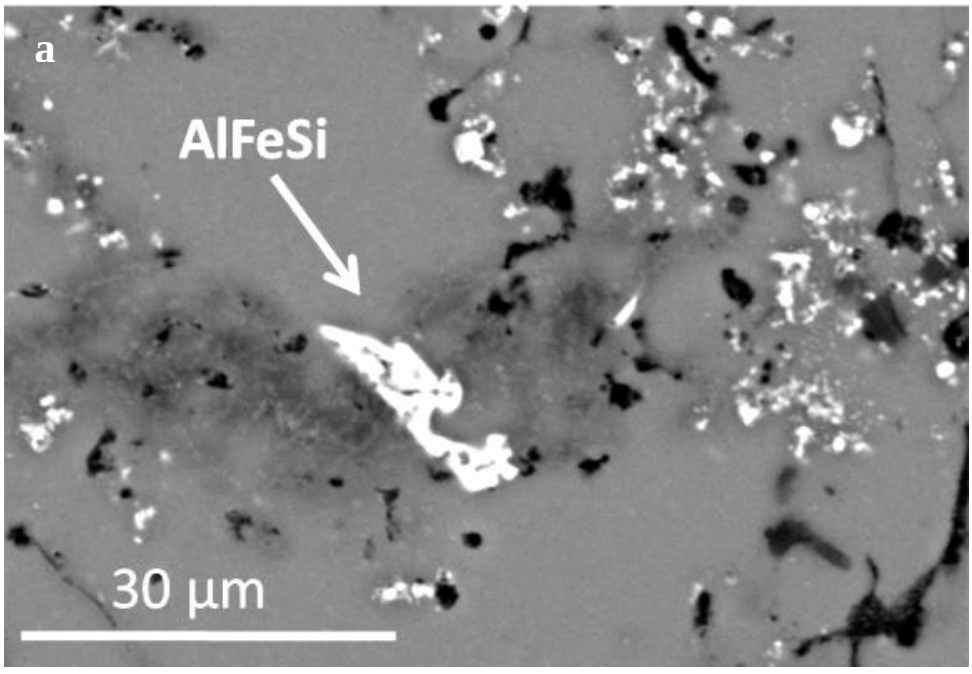

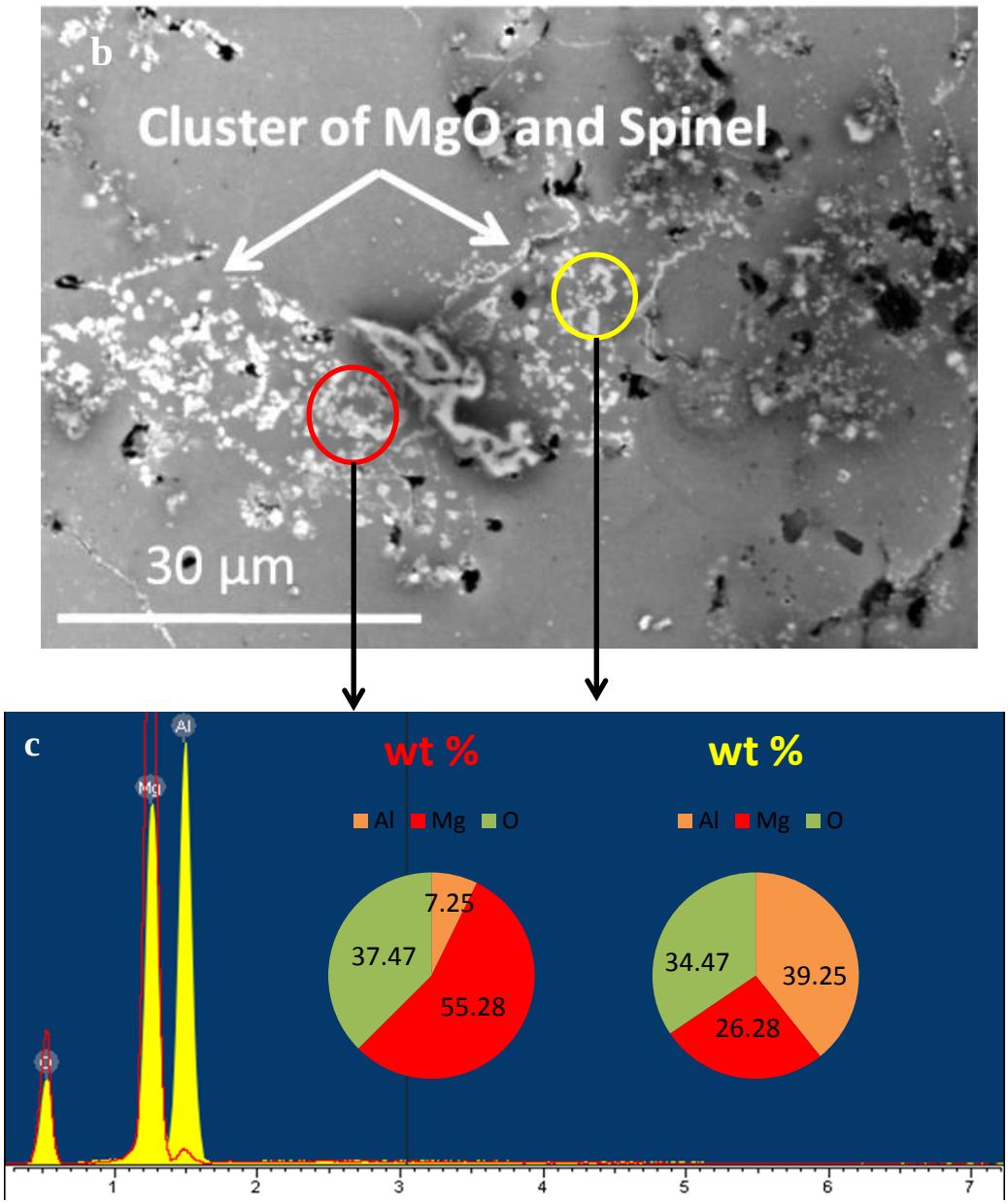

Continued overleaf…

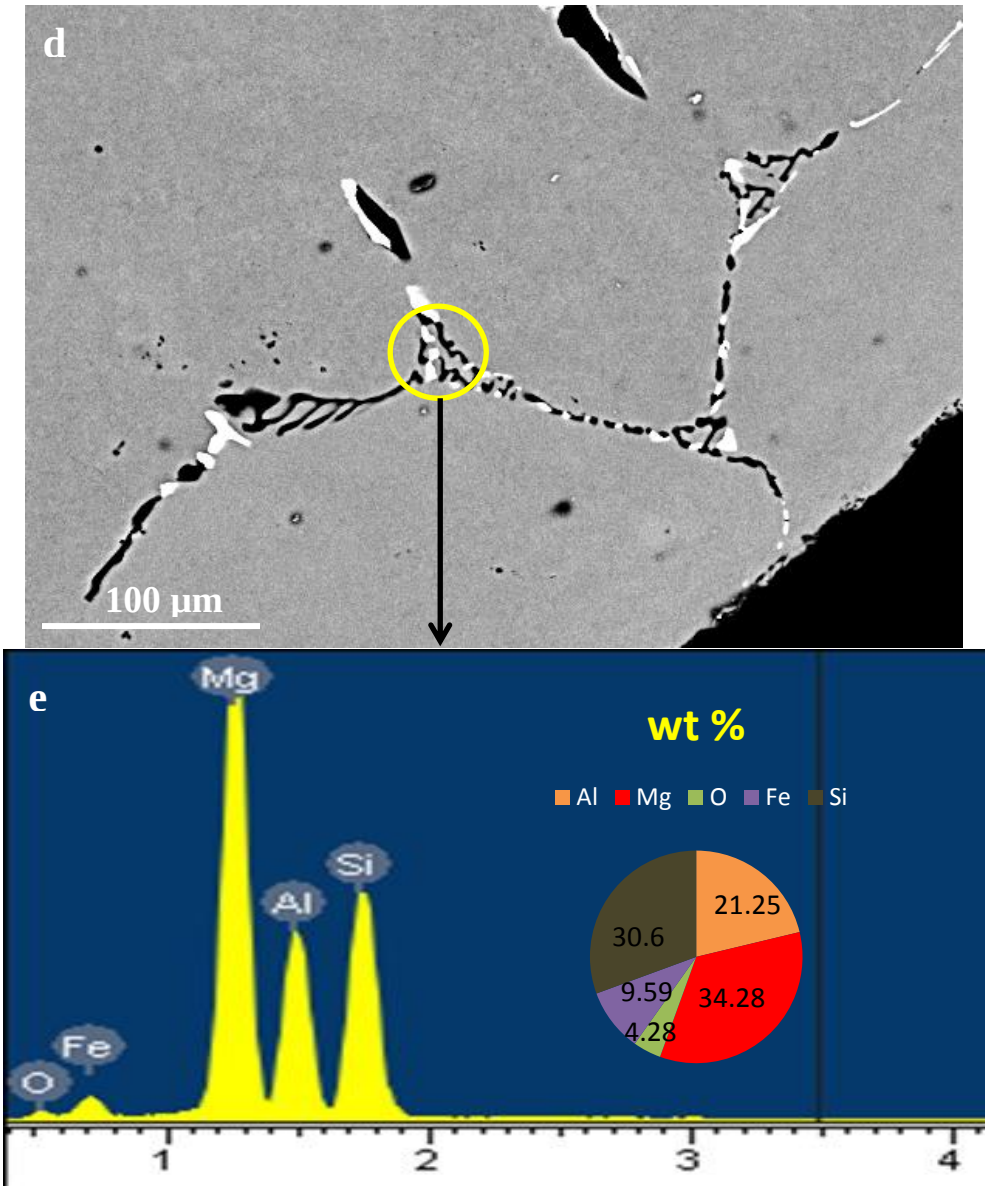

Fig 6.4 Micrographs of 1.3 wt% Mg prefil alloy showing a) BSE image displaying an AlFeSi intermetallic underneath the layer of oxide, b) SE image of the same area displaying clusters of MgO and spinel along with oxide bi-films, c) EDX confirming the presence of MgO and spinel, d) BSE image displaying the Chinese script morphology of Mg_2Si and its association with the $Al_{13}Fe_4$ intermetallic and e) EDX confirming the presence of Mg_2Si and $Al_{13}Fe_4$ intermetallic.

6.1.1.4 Prefil alloy with 5.1 wt% Mg

As the Mg content was increased significantly, the clusters of oxides also increased considerably. Also, MgO was the only oxide observed and no spinel was detected. The clusters of MgO were observed to have lather-like morphology (see Fig. 6.5a) and were found mainly to be associated with oxide bi-films. The number of oxide bi-films (crack-like features) also increased by many folds.

Fig. 6.5 shows the SE and BSE images of the same sample area. Fig. 6.5a shows the SE image displaying the presence of clusters of MgO (bright contrast areas), whereas Fig. 6.5b shows the BSE image clearly marking the association of oxide bi-films with the clusters. It is important to note that the typical AlFeSi intermetallics (α-AlFeSi and β-AlFeSi) were rarely observed. Instead, $Al_{13}Fe_4$ was observed more frequently (see chapter–5 and section 6.4.3 for more details on phase shift). Mg_2Si was spotted very frequently and was mainly observed in Chinese script morphologies and in association with the $Al_{13}Fe_4$ intermetallics. Fig. 6.5c shows the typical Chinese script morphologies of Mg_2Si (in yellow circles). About 45% of the Mg_2Si observed was not associated with any Fe-intermetallic. Clusters of TiB_2 inclusions were also observed in this alloy, however Al_2O_3 was not observed. The phase transformation from AlFeSi intermetallics to Mg_2Si and $Al_{13}Fe_4$ will be discussed later in section 6.4.2.

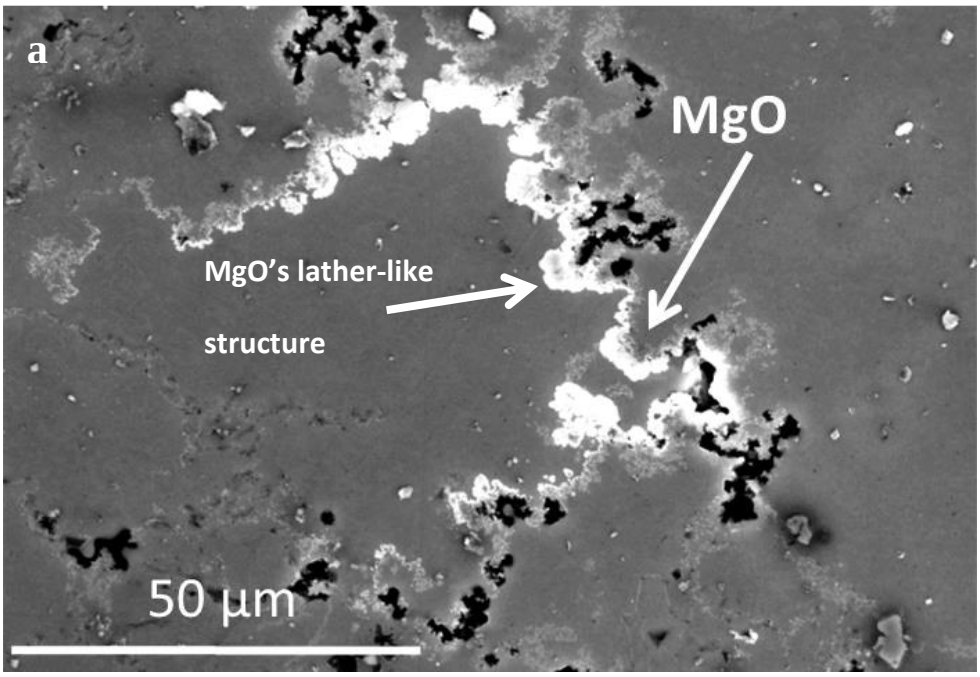

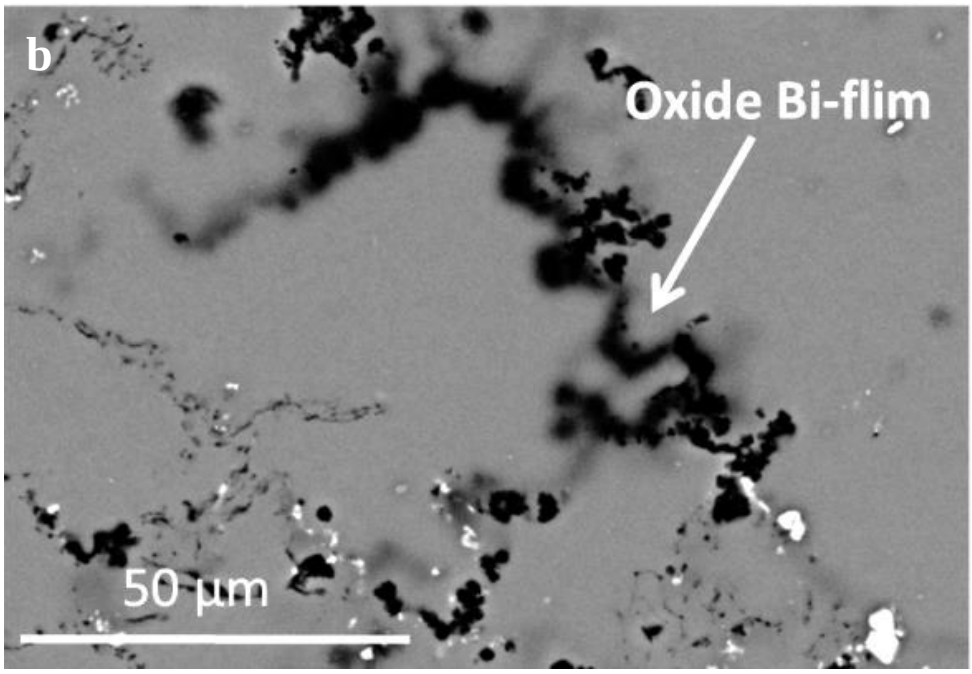

Continued overleaf…

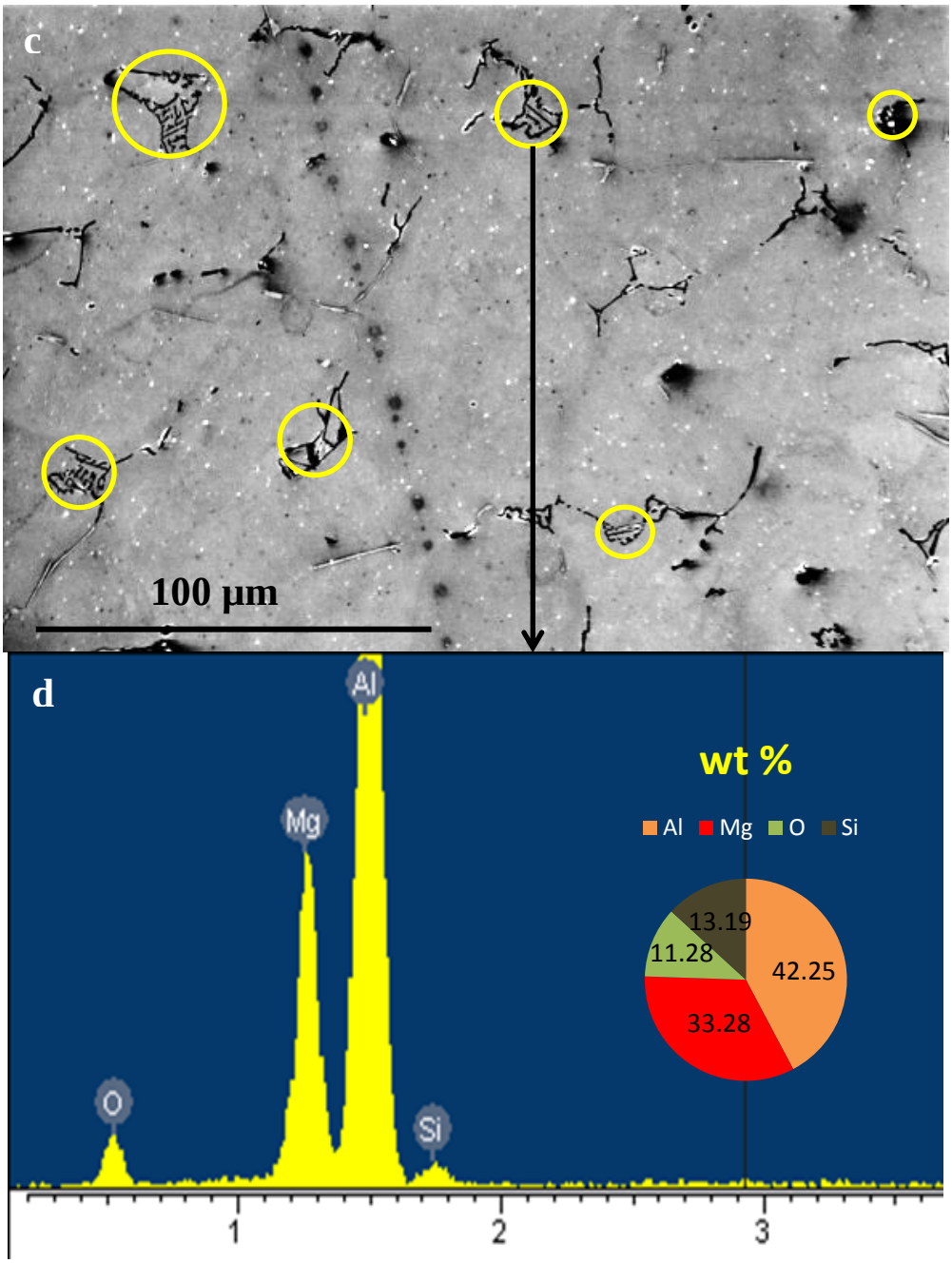

Fig 6.5 Micrographs of 5.1 wt% Mg prefil alloy showing a) SE image displaying a cluster of MgO, b) BSE image of the same area displaying the oxide bi-films, c) SE image showing the Chinese script morphologies of Mg_2Si not in association with AlFeSi intermetallics and d) EDX confirming the presence of Mg_2Si

6.1.2 Characterisation of 3D morphology of inclusions

A number of different inclusions and intermetallics were observed in the alloys with different Mg contents. Fig. 6.6 shows the 3D morphology of TiB_2 (hexagonal) and Al_2O_3 (elongated rod-like) inclusions. These inclusions and intermetallics were extracted by dissolving the aluminium matrix using IEA (refer to section 3.4). For this purpose the section at the top of the ceramic filter was used because of the highest density of inclusions. The inclusions were identified using EDX analysis and intermetallics were identified using the ratio of Fe to Si from EDX analysis and the morphology in existing literature **(Cooper, 67) & (Allen et al., 99)**.

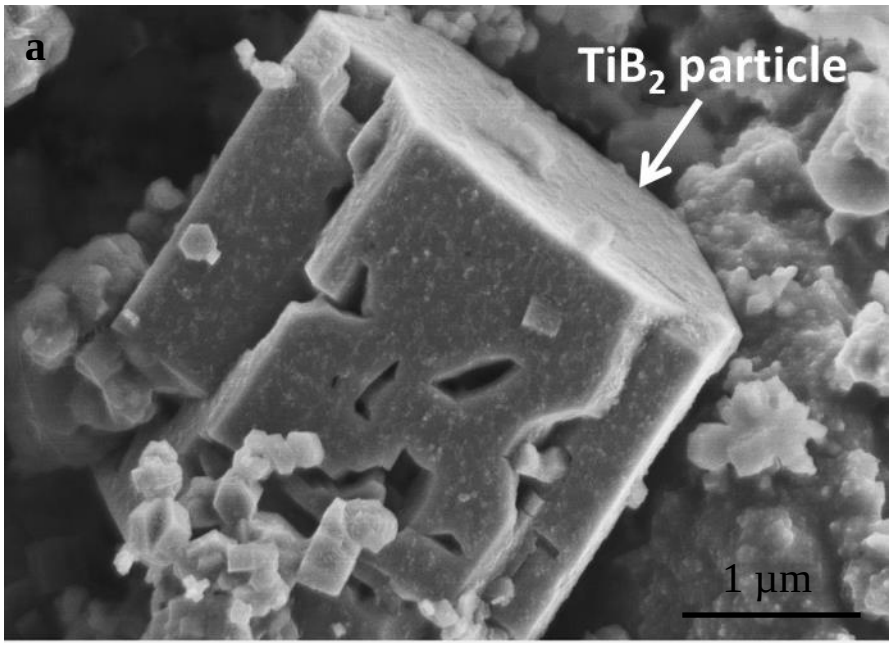

Continued overlead…

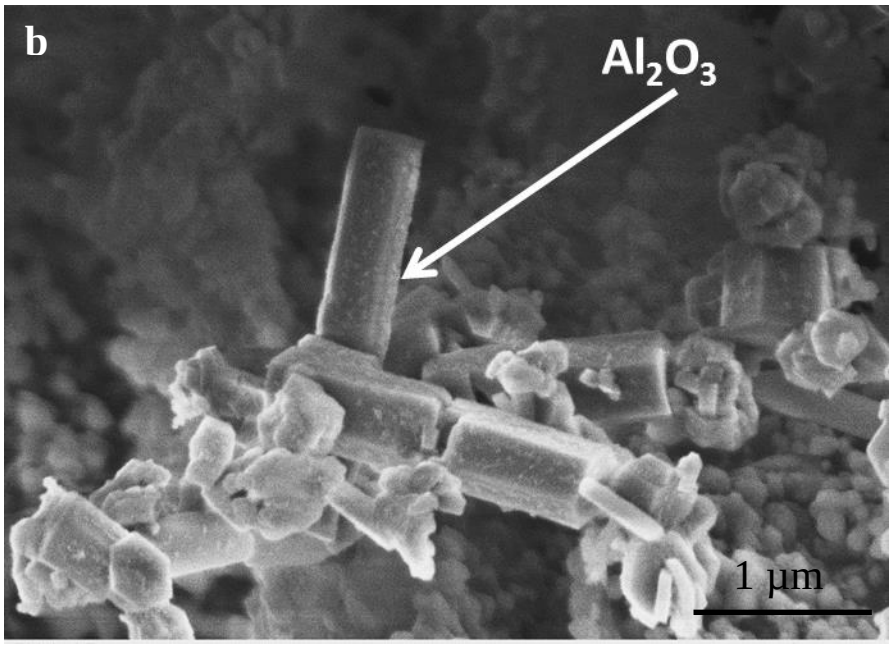

Fig 6.6 3D SE micrographs of extracted prefil alloys showing hexagonal morphology of a) Ti particle and b) Al_2O_3 particle

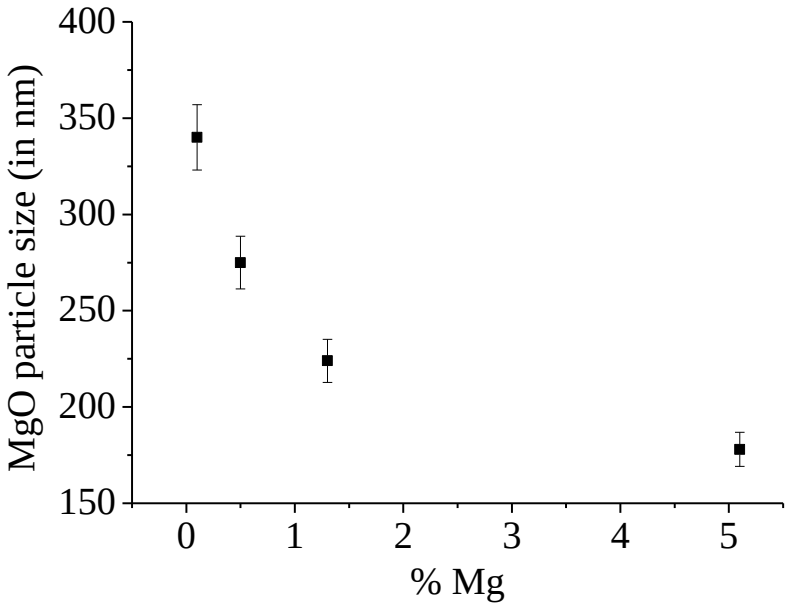

Fig 6.7 Variation of average particle size of MgO as a function of Mg wt%

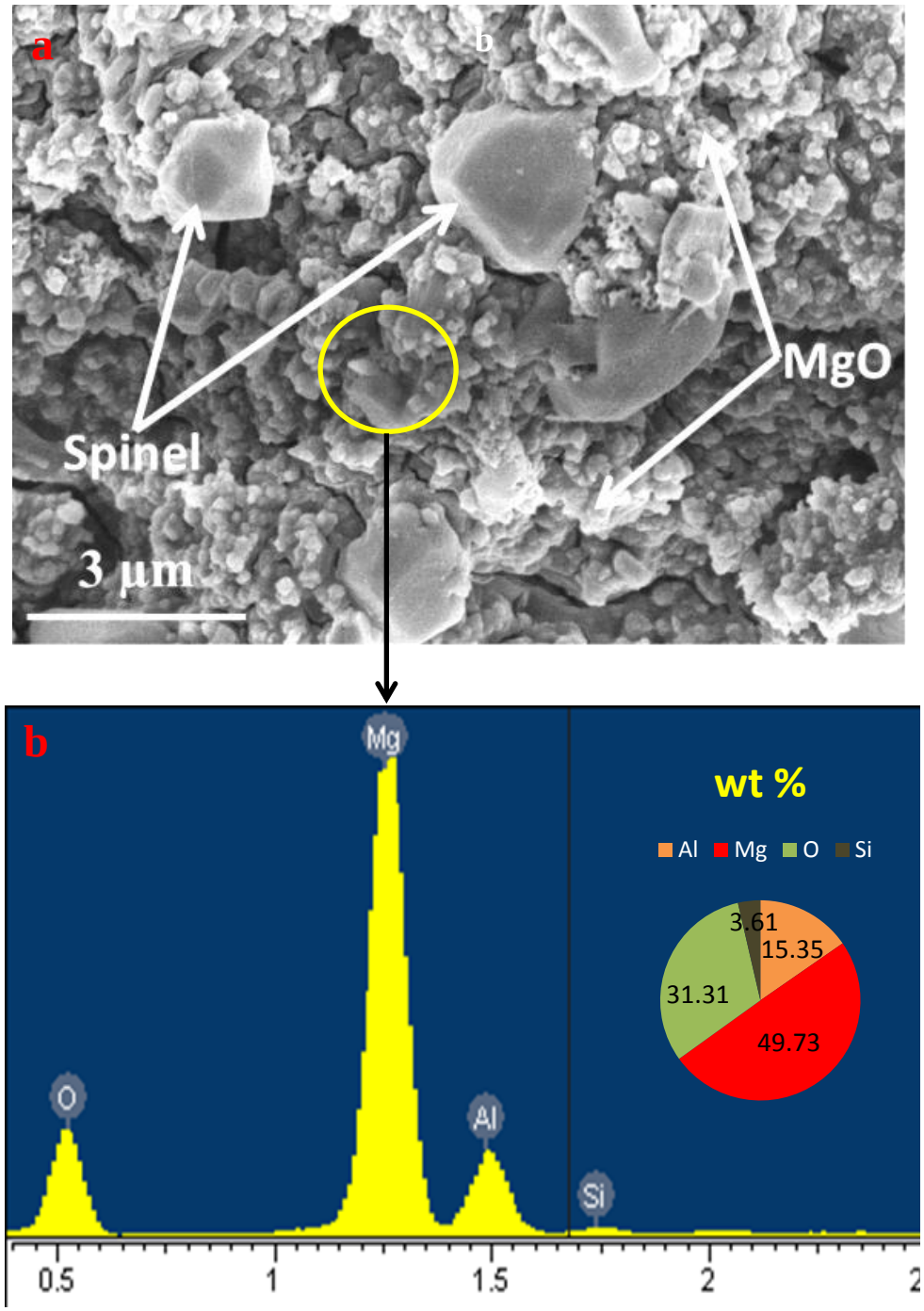

Fig 6.8 a) 3D SE micrograph of extracted inclusions from a prefil alloy showing the octahedral morphology of spinel and spherical morphology of MgO particles and b) EDX spectrum confirming the dominance of MgO (Mg/O ~1.6).

Fig. 6.7 shows the change in MgO average particle size with increasing Mg content (refer to section 3.1.3.3 for exact composition of the alloys). The data in Fig. 6.7 was obtained using the SEM images from different sections of the sample and image analysis software to measure the diameter of the MgO particles. Two types of Mg rich oxides were mainly observed in this alloy i.e. MgO and spinel ($MgAl_2O_4$). Spinel was observed to have faceted or octahedron morphologies, whereas MgO particles had spherical morphology as shown in Fig. 6.8. Fig. 6.8b also demonstrates the Mg/O>1, which confirms the dominance of MgO over spinel.

A change in the nature of the oxide with Mg content is also noted. Crack-like features were frequently observed during 2D analysis and can be correlated with the oxide bi-films observed in 3D analysis. Table 6.2 at the end of the section provides a summary of the 2D and 3D morphology of oxides and oxide bi-films observed in this study. Clusters of inclusions including TiB_2 and Al_2O_3 were observed which can be correlated with the 2D SEM observations. Fig. 6.6a and Fig. 6.6b show the hexagonal morphologies of TiB_2 and Al_2O_3 particles respectively. It is interesting to note that Al_2O_3 particles were more elongated compared to TiB_2 particles. After analysing about 50 particles with the help of EDX analysis and measuring the aspect ratio (length/width), it can be concluded that when the aspect ratio was greater than 1.8 then the particle is likely to be Al_2O_3 or if it was smaller than 1.8 then it is TiB_2.

The approximate area of the clusters of MgO and spinel in an alloy was calculated on the basis of the EDX analysis and their respective morphologies. This was used to calculate the ratio of spinel:MgO for prefil alloys.

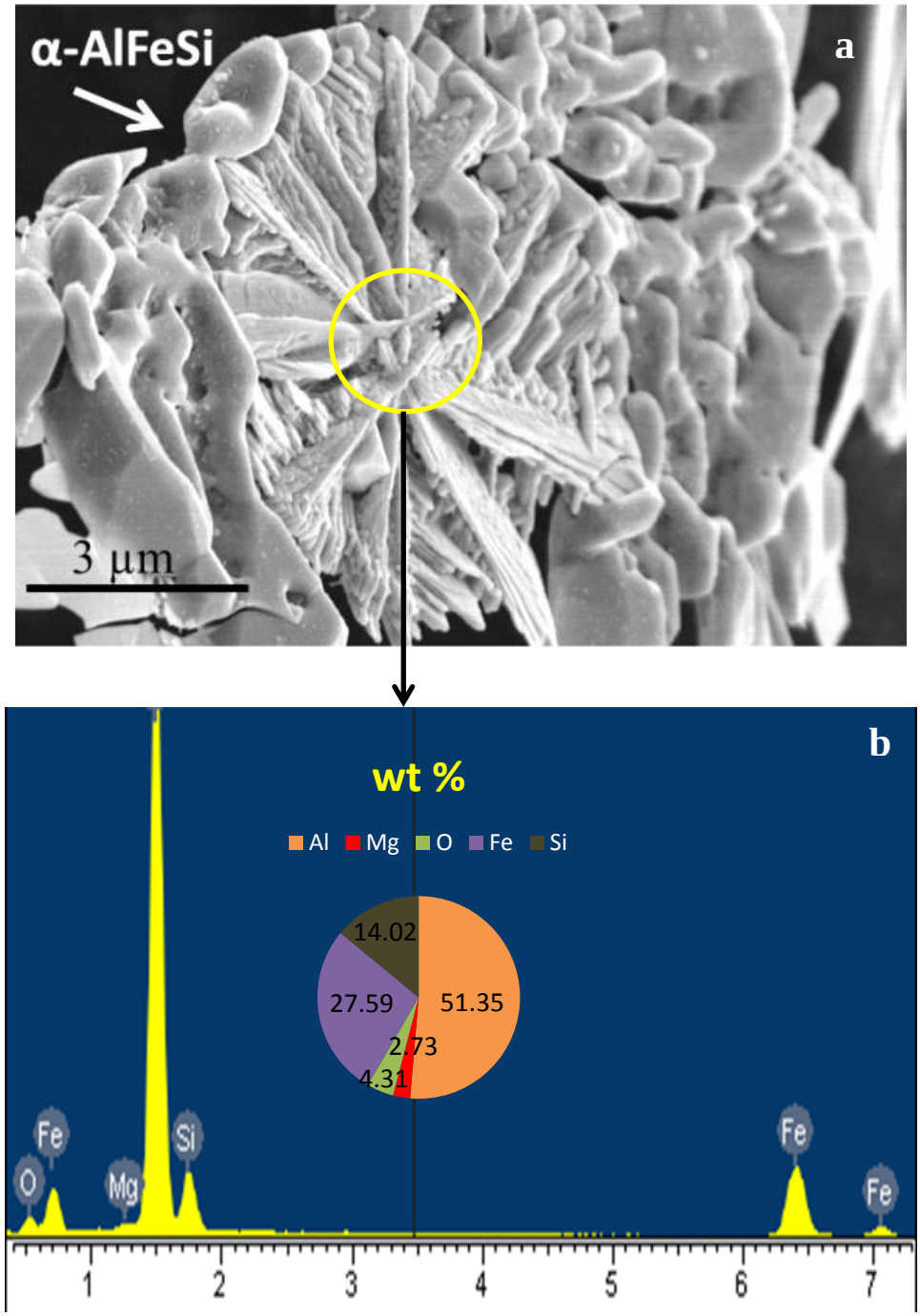

Continued overleaf…

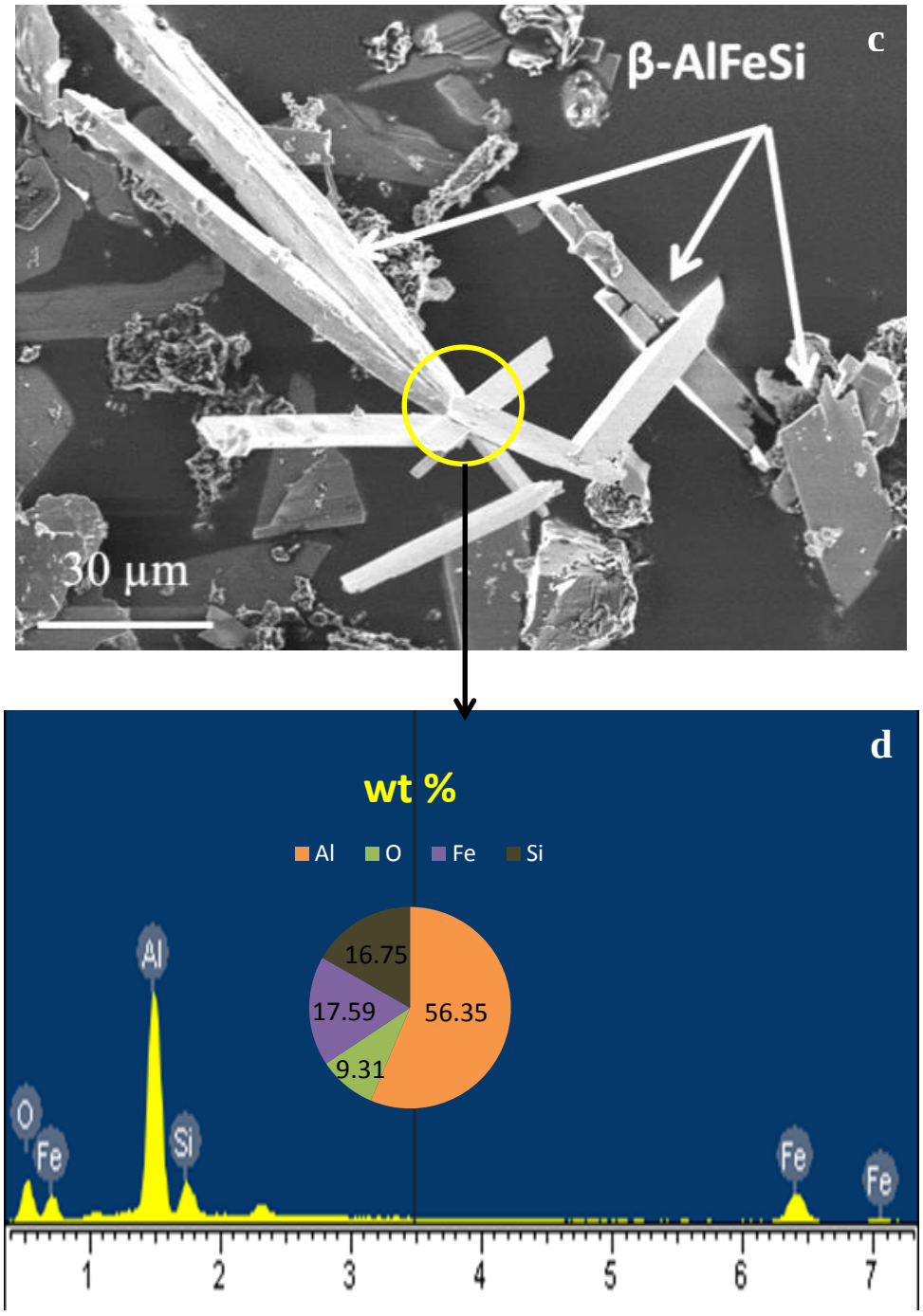

Fig 6.9 3D SE micrographs of extracted intermetallics from 0.1 wt% Mg a) & c) showing the flower-like morphology of α-AlFeSi and platelet/rod-like morphology of β-AlFeSi respectively and b) & d) showing the EDX spectra confirming the compositions of α-AlFeSi and β-AlFeSi respectively.

Two types of AlFeSi intermetallics were mainly observed during this study i.e. α-AlFeSi was observed in flower-like morphology and β-AlFeSi was observed in platelet/rod-like morphology as shown in Fig. 6.9a and Fig. 6.9c respectively. This was also confirmed by the high and low Fe/Si ratio obtained using the EDX analysis as shown in Fig. 6.9b (Fe/Si ~2) and Fig. 6.9d (Fe/Si ~1) respectively.

6.1.2.1 Prefil alloy with 0.1 wt% Mg

Fig 6.10a shows the dry and wet surfaces of the oxide bi-film. It is interesting to note that the dry surface is very smooth whereas the wet surface is very rough. Fig. 6.10b shows the particles attached to the wet surface of the oxide bi-film. After careful EDX analysis, these particles were found to be spinel. In this alloy, MgO was present in very small quantities and spinel was the dominant oxide. The ratio of spinel:MgO was measured to be 7:2 (section 6.1.2). Fig. 6.10c shows one of the few MgO clusters observed. It is important to note that spinel was mainly observed on the wet surface of the oxide bi-film and not as a separate cluster. On the other hand, MgO was observed mainly as separate clusters and not on the oxide bi-film (see Fig. 6.10c).

The size of about 100 MgO particles was measured and Fig. 6.11 shows the particles size distribution for this alloy. The average measured size of the MgO particles was 340±17nm. The other interesting feature to note was the presence of ripples and cracks on the dry surface of the oxide bi-film as shown in Fig. 6.10d. This will be discussed in detail later in section 6.3.3.

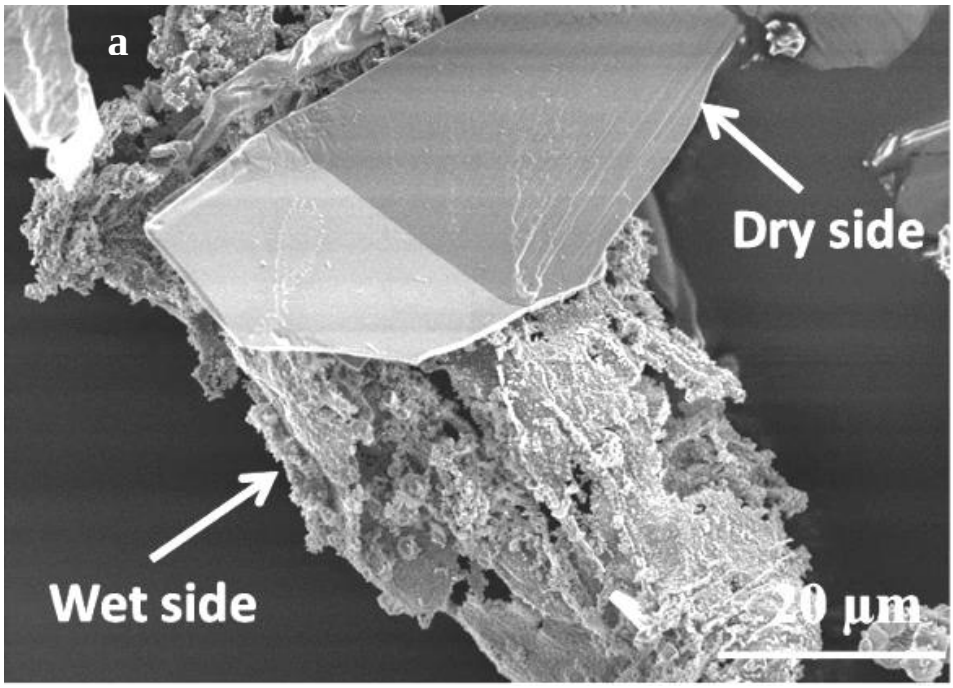

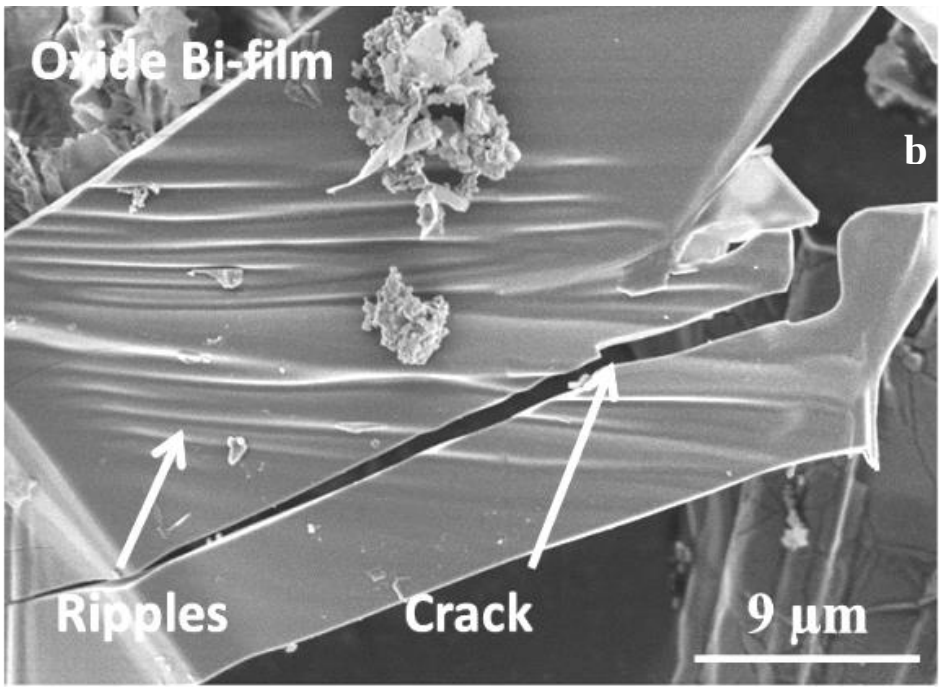

Continued overleaf…

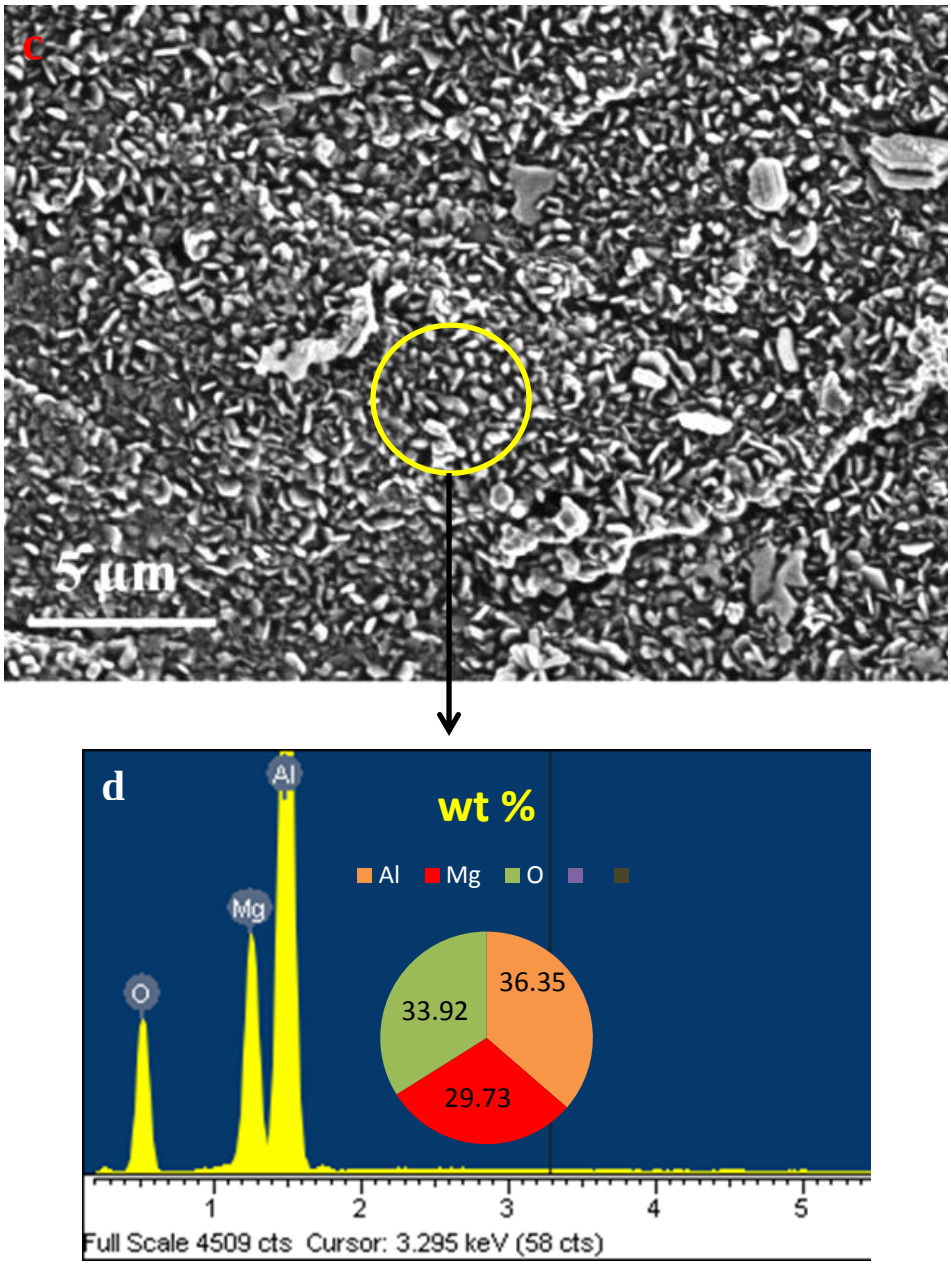

Continued overleaf…

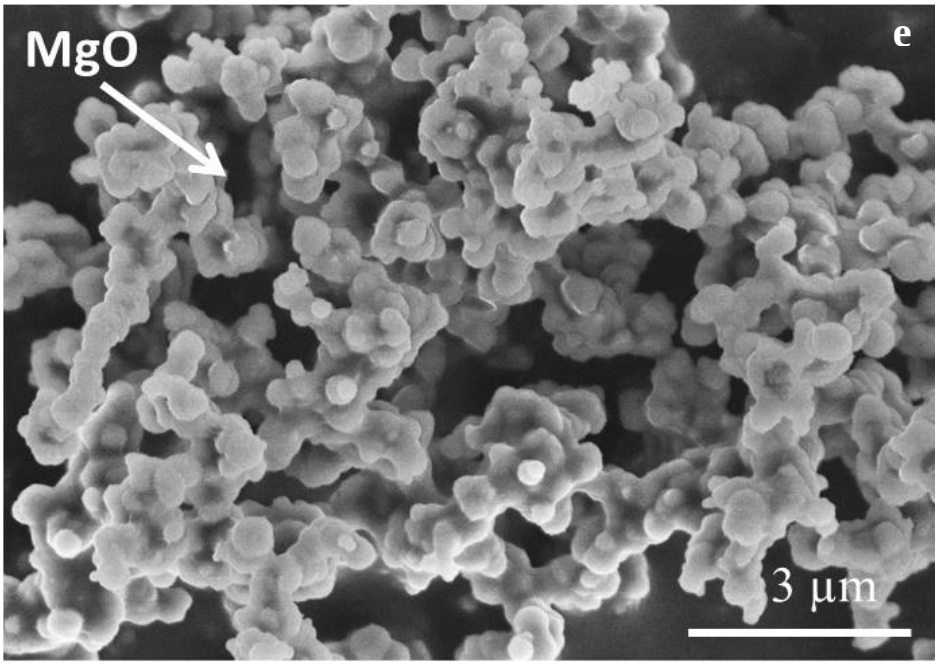

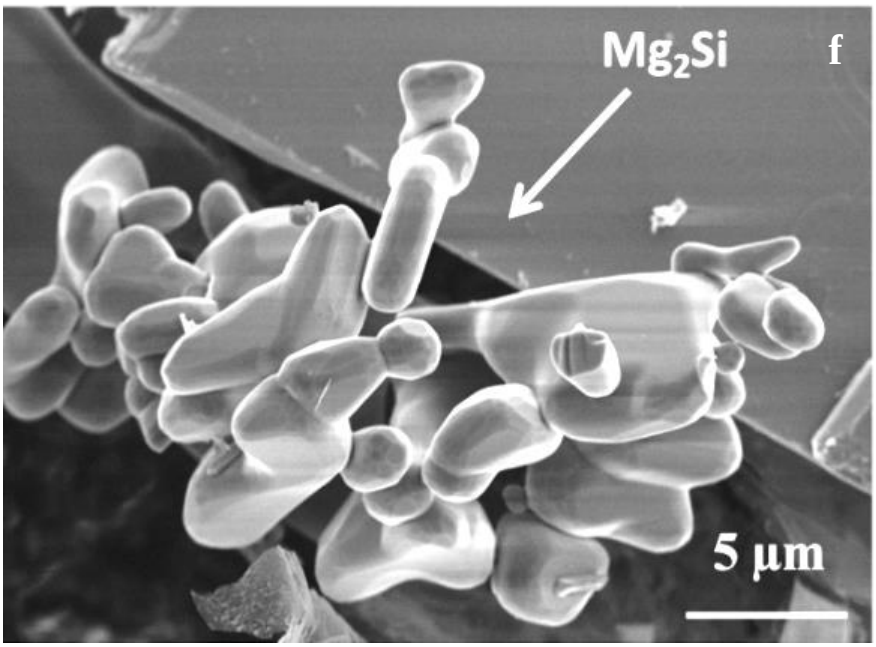

Continued overleaf…

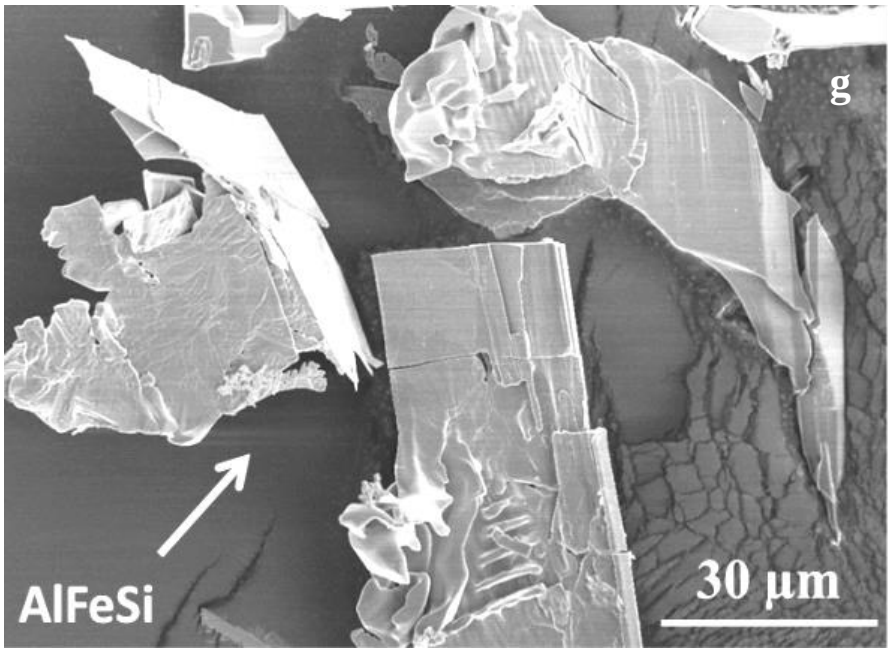

Fig 6.10 3D SE micrographs of the 0.1 wt% Mg prefil alloy showing a) dry and wet surfaces of the oxide bi-films, b) cracks and ripples on the oxide bi-film dry surface c) magnified image of the oxide particles attached to the wet surface of the oxide bi-film, d) EDX confirming the presence of spinel at the wet surface of bi-film, e) MgO cluster, f) capsule-like morphology of Mg_2Si and g) AlFeSi intermetallics.

Typical flower-like morphology of α-AlFeSi and rod-like morphology of β-AlFeSi were observed in this alloy. Mg_2Si was observed on very rare occasions and was observed to have capsule-like morphology as shown in Fig. 6.10e.

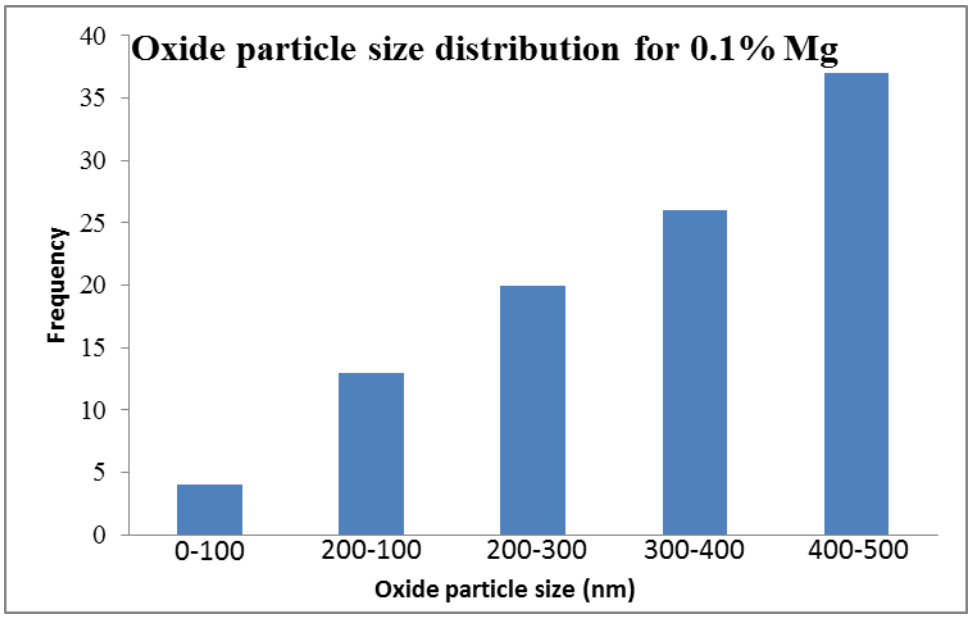

Fig 6.11 MgO particle size distribution in the 0.1 wt% Mg prefil alloy

6.1.2.2 Prefil alloy with 0.5 wt% Mg

Fig. 6.12a shows the particles attached to the wet surface of the oxide bi-film. After analysing these particles using EDX analysis at different sections of Fig. 6.12c, they were found to be a mixture of spinel and MgO (0.5<Mg/O<1.5). Similar to the 0.1 wt% Mg alloy, this alloy also had spinel as dominant oxide and the ratio of spinel:MgO was measured to be 11:8 (smaller than 7:2 in 0.1 wt% Mg). It is important to note that spinel was again observed on the wet surface of the oxide bi-film only and not as separate clusters (Fig. 6.12a & 6.12c), whereas MgO was observed both as separate clusters and partly on the oxide bi-film.

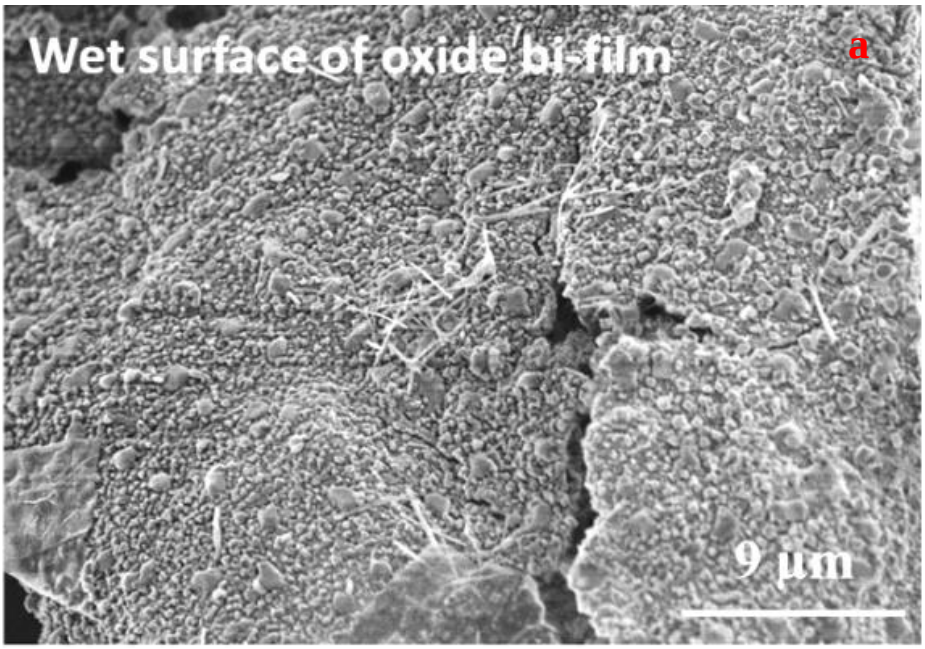

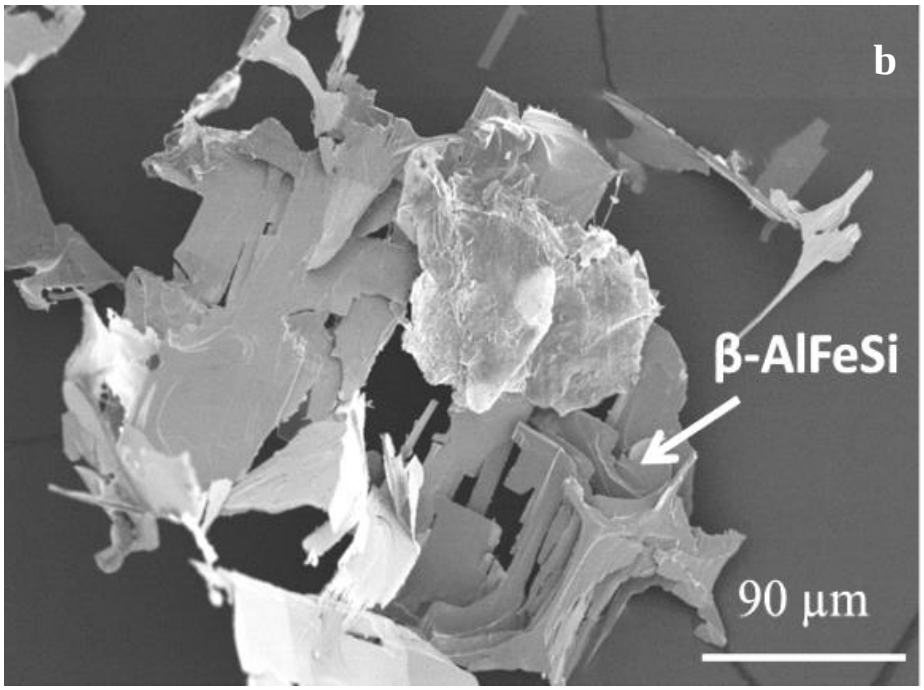

Continued overleaf…

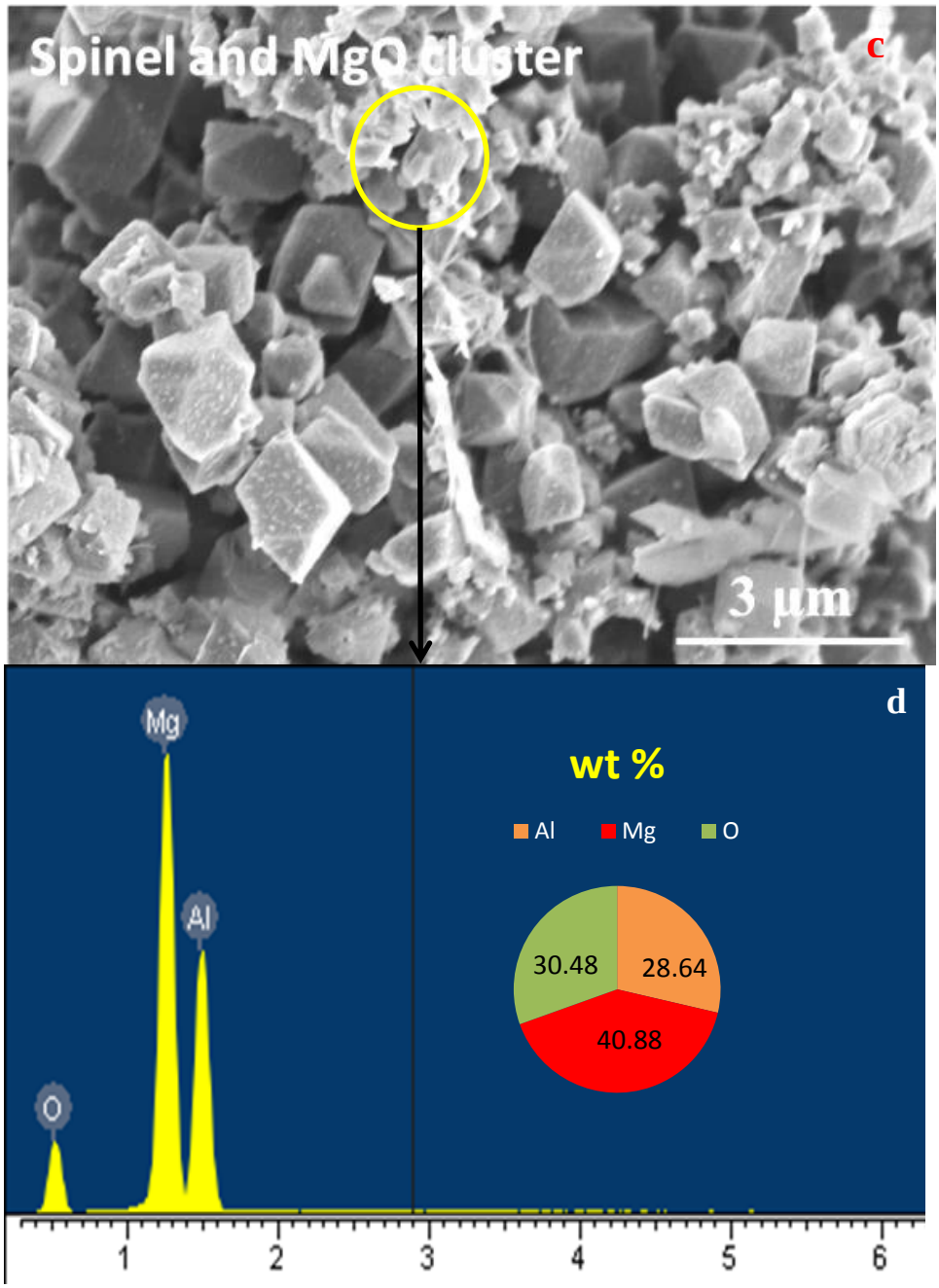

Fig 6.12 3D SE micrographs of the 0.5 wt% Mg prefil alloy showing a) wet surface of the oxide bi-films, b) layered structure of β-AlFeSi, c) magnified image of the MgO and spinel oxide particles attached to the wet surface of the oxide bi-film and d) EDX spectrum confirming the composition as a combination of both MgO (small spherical particles) and spinel (large octahedral particles).

Fig. 6.13 shows the particle size distribution for this alloy. The average measured size of the MgO particles was 275±14nm, which was a little smaller than for the 0.1 wt% Mg alloy. Ripples and cracks on the surface of the oxide bi-film were found similar to the 0.1 wt% Mg alloy. α-AlFeSi and β-AlFeSi were observed with their conventional morphologies. However, β-AlFeSi was observed to have grown in a layered structure as shown in Fig. 6.12b. Mg_2Si and $Al_{13}Fe_4$ were observed on rare occasions and were observed to have capsule-like morphology and platelet morphology respectively. Fig. 6.12c shows the cluster of MgO and spinel which is confirmed by the EDX as shown in Fig. 6.12d (Fe/Si ~1.3).

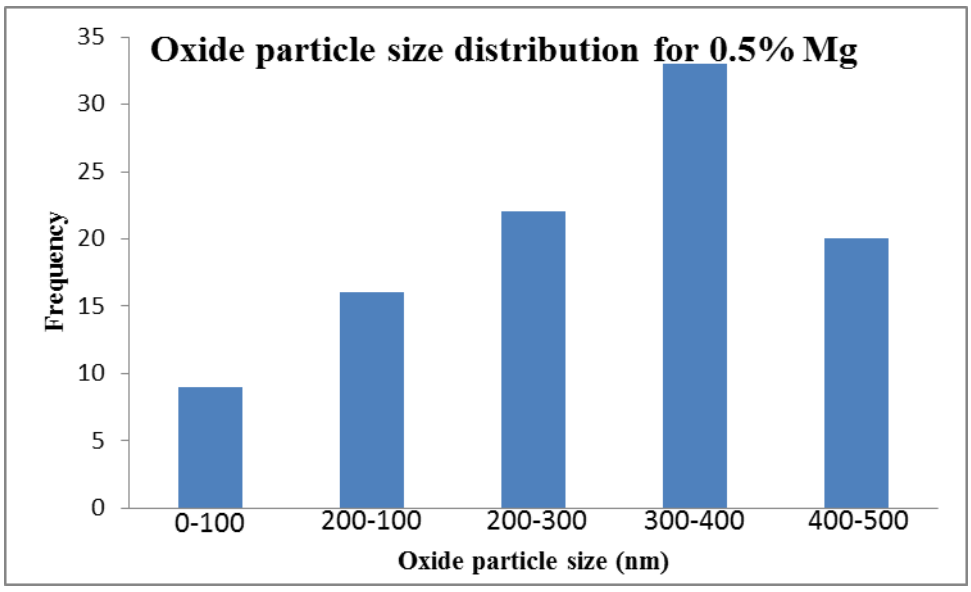

Fig 6.13 MgO particle size distribution in 0.5 wt% Mg prefil alloy

6.1.2.3 Prefil alloy with 1.3 wt% Mg

The nature of the oxides changed dramatically as the Mg content was increased to 1.3 wt%. Contrary to the high number of oxide bi-films observed during 2D analysis of 1.3 wt% sample, no oxide bi-films were observed during 3D analysis. However, it is interesting to note that the intermetallic particles were covered extensively with an oxide layer as shown in Fig. 6.14. This observation will be discussed later in section 6.1.2.5. The oxide layer consisted of only MgO particles and no spinel particles were observed. These MgO particles appeared to be attached to the surface of the intermetallic particles very firmly and were on the scale of few nanometers. Fig 6.15 shows the overall MgO particles size distribution for this alloy. The average measured size of the MgO particle was 224±11nm, which was significantly smaller than 0.5 wt% Mg alloy. Mg_2Si and $Al_{13}Fe_4$ were the major phases in this alloy and only a few particles of α-AlFeSi were observed. However, no β-AlFeSi was found.

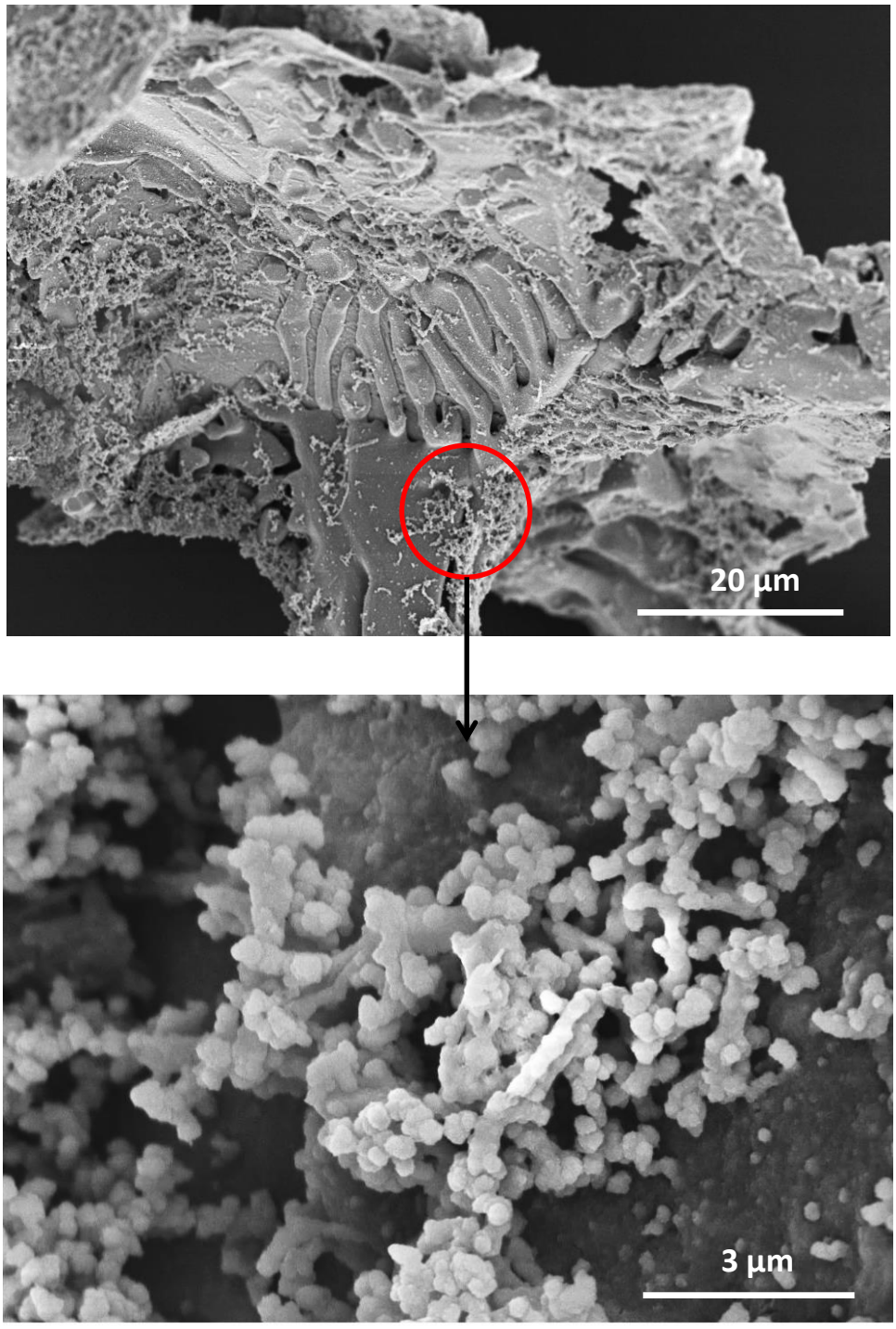

Continued overleaf…

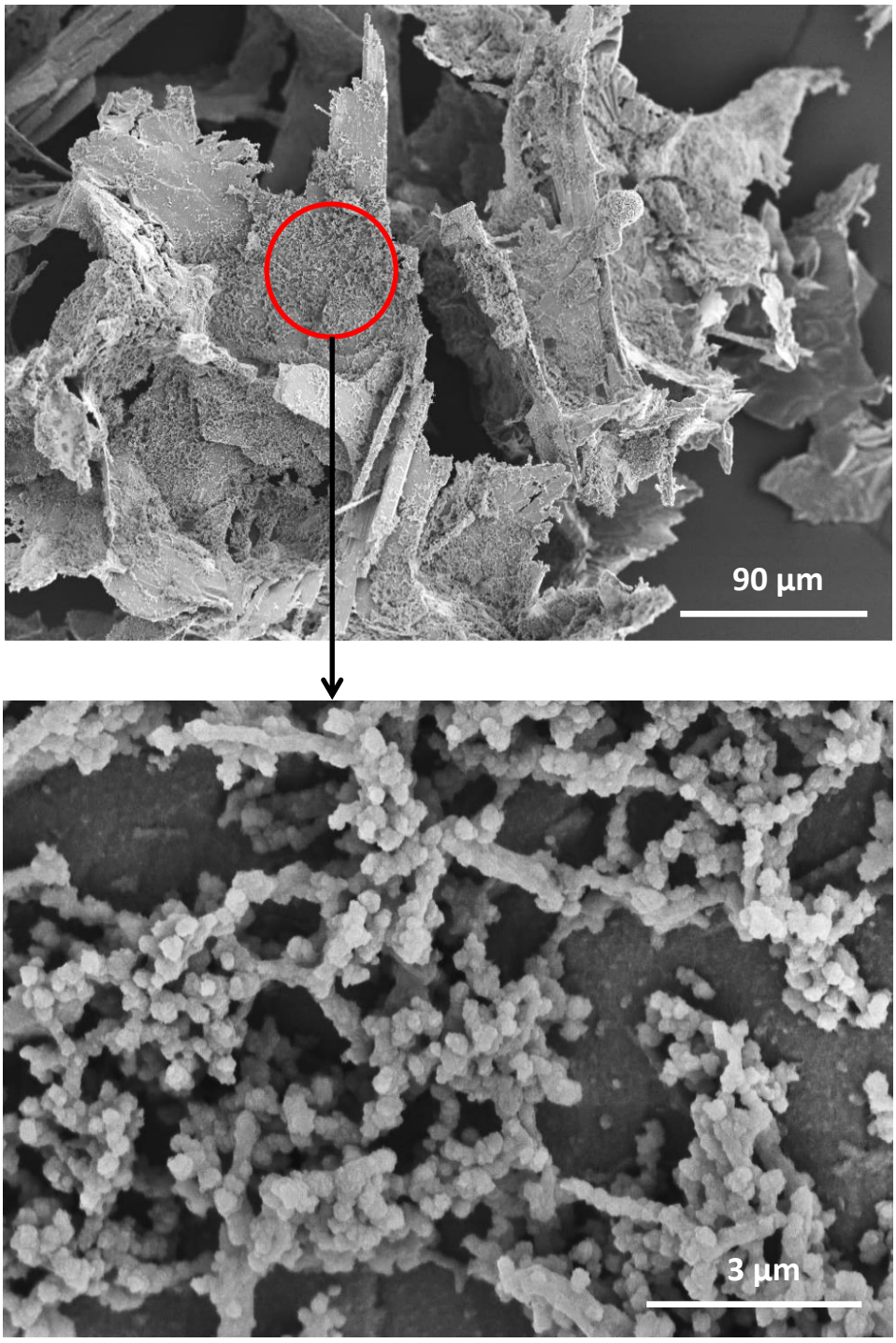

Fig 6.14 3D SE micrographs of the 1.3 wt% Mg prefil alloy showing the layer of oxide particles on the intermetallics.

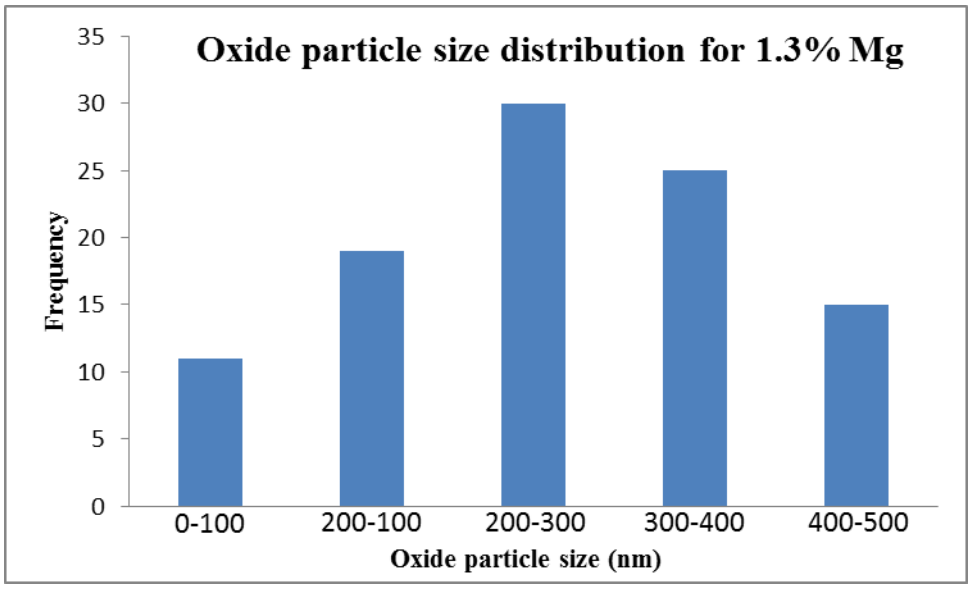

Fig 6.15 MgO particle size distribution in the 1.3 wt% Mg prefil alloy

6.1.2.4 Prefil alloy with 5.1 wt% Mg

The nature of oxides remained quite similar to the 1.3 wt% Mg alloy. Contrary to the high number of oxide bi-films observed during 2D analysis of 5.1 wt% sample, no oxide bi-films were observed with 3D analysis. However, it is interesting to note that the intermetallic particles were covered even more extensively with an oxide layer as shown in Fig. 6.16. This phenomenon is discussed further in section 6.1.2.5. The more extensive coverage of intermetallics by oxide particles could be attributed to the enhanced formation of MgO due to the increase in Mg content. The oxide layer consisted of only MgO particles and no spinel particles were observed in this alloy.

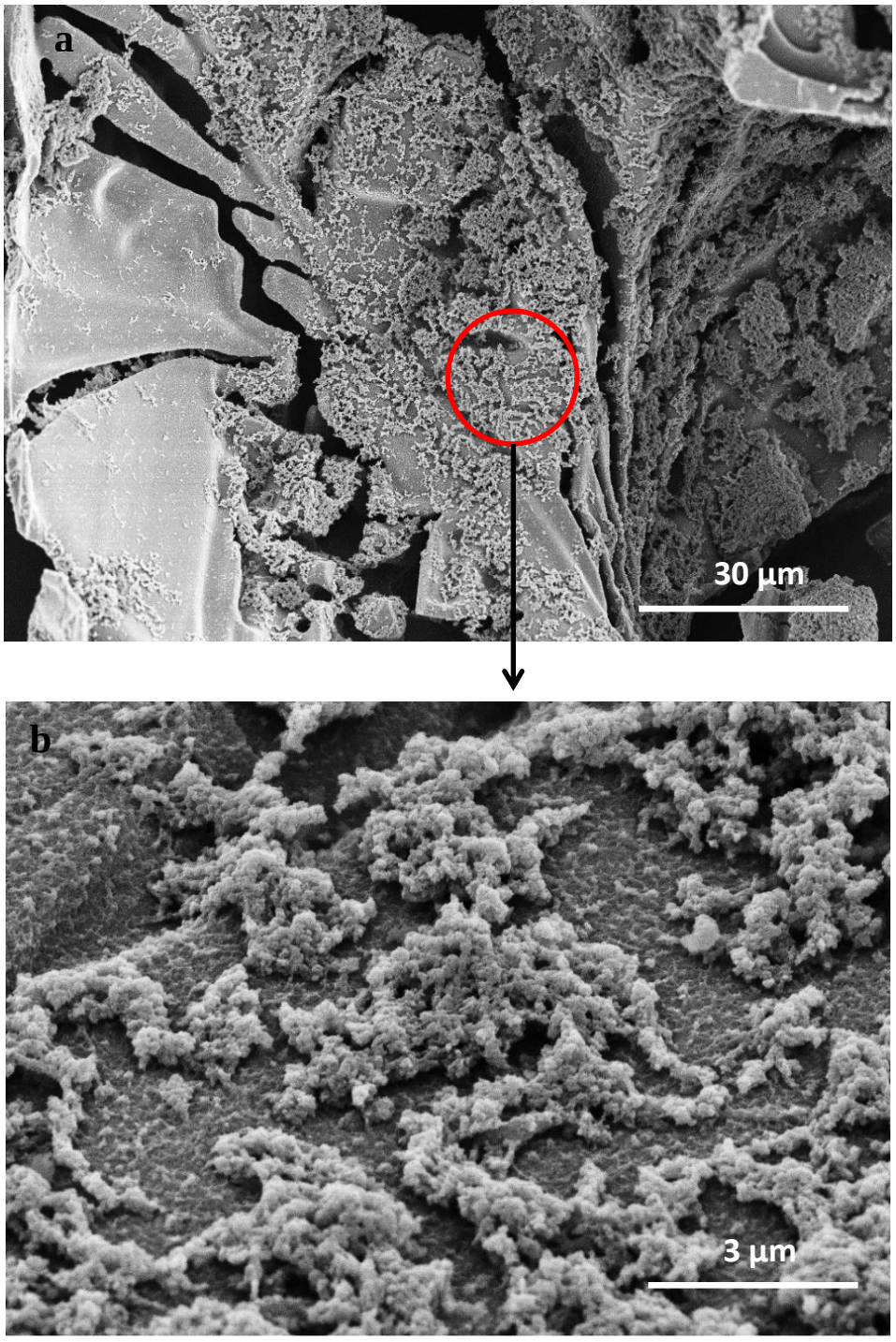

Continued overleaf…

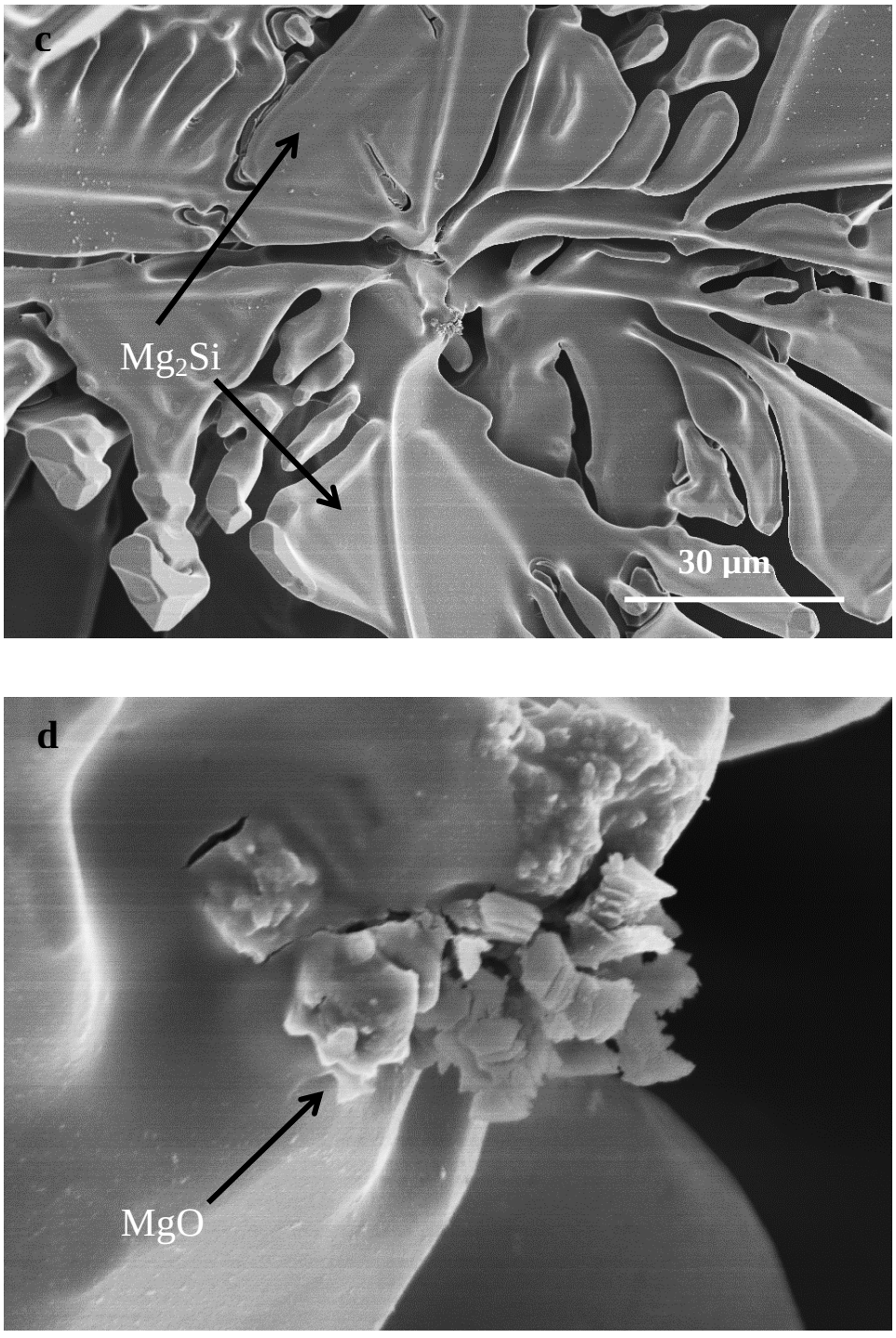

Fig 6.16 3D SE micrographs of the 5.1 wt% Mg prefil alloy showing a) and b) the layer of oxide particles on Mg_2Si, c) flower-like morphology of Mg_2Si phase and d) MgO at the most probable nucleation point of Mg_2Si (see Fig. 6.40 for EDX and composition)

The MgO particles appeared to be attached to the surface of the intermetallic particles very firmly and were on the scale of a few nanometers as can be seen in Fig. 6.16. Mg_2Si was mainly observed with a flower-like morphology in this alloy as shown in Fig. 6.16c. MgO particles were also observed at locations which appeared to be the nucleating point for the Mg_2Si flower-like structure (see Fig. 6.16d). Approximately 20% of the Mg_2Si flowers were observed with this feature suggesting that MgO is a good nucleating substrate for Mg_2Si. This will be discussed in detail in section 6.4.2.2.

MgO clusters were also observed very frequently as shown in Fig. 6.17. EDX spectra also confirms the presence of MgO (Mg/O>1.5). Fig. 6.18 shows the overall particle size distribution for this alloy. The overall average measured size of MgO particles was 178±9nm, which was the smallest of all of the prefil alloys.

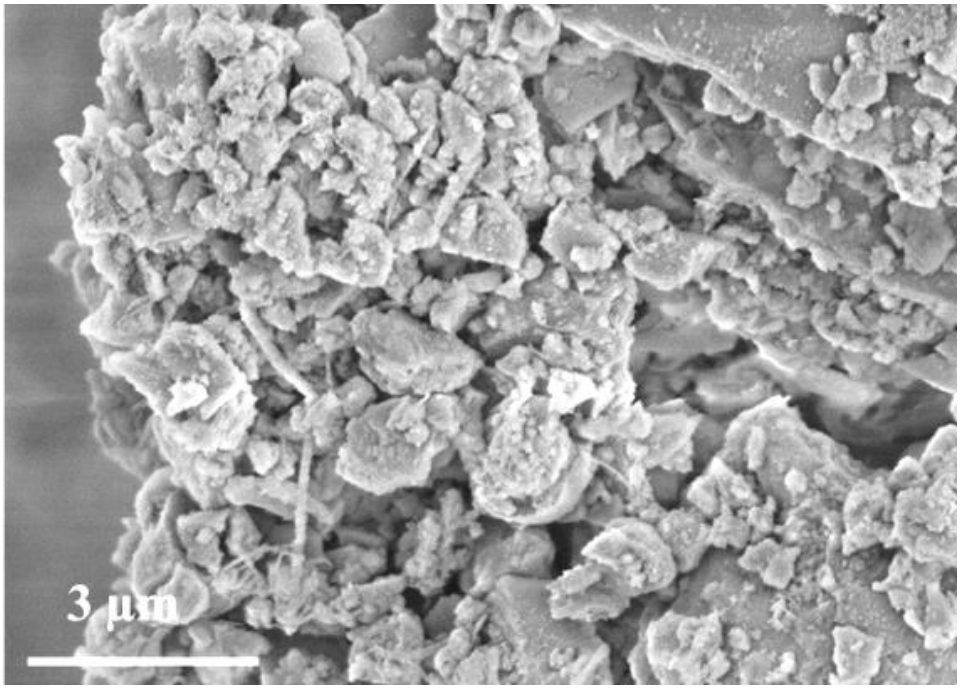

Continued overleaf…

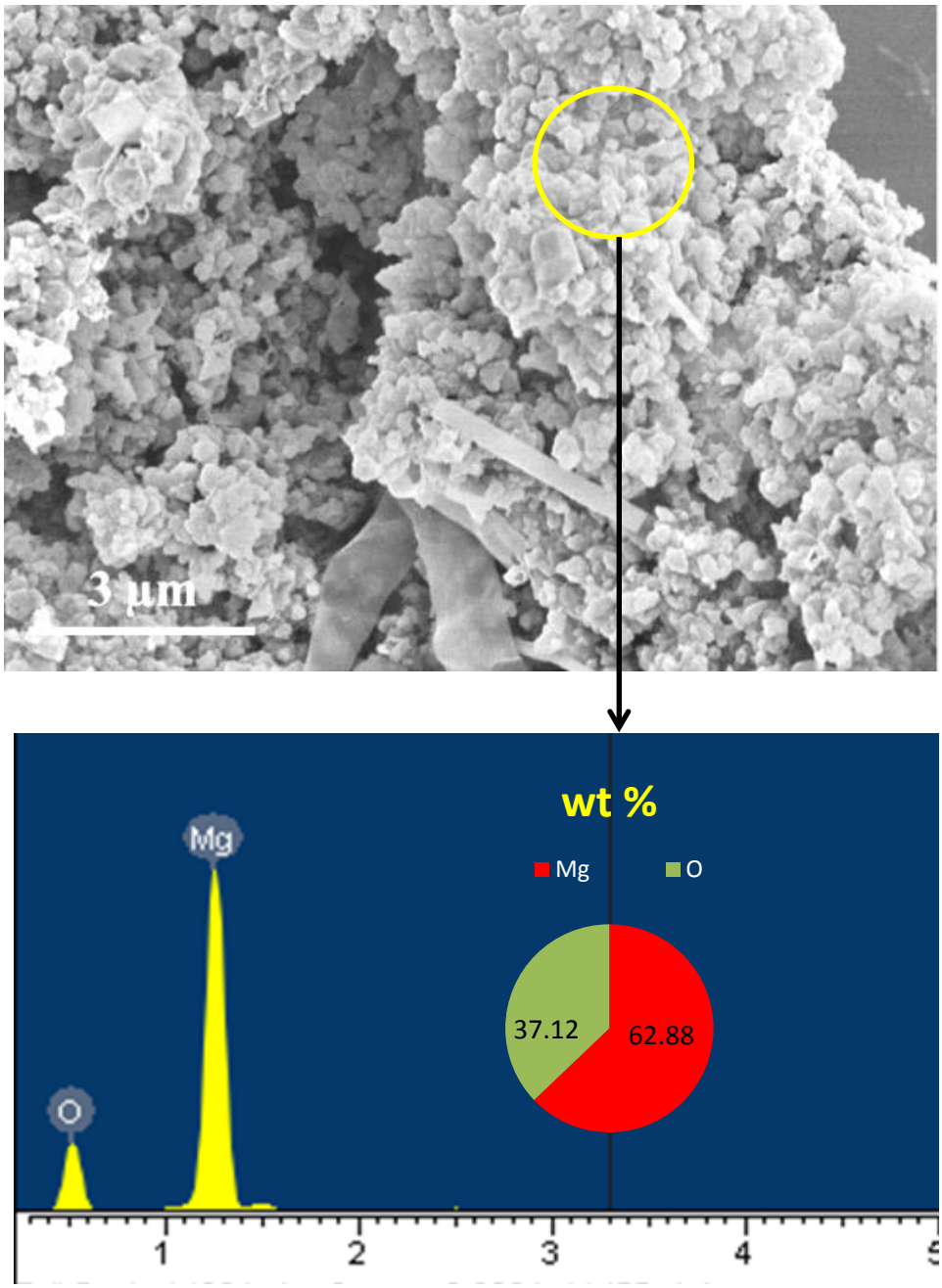

Fig. 6.17 3D SE micrographs showing the clusters of oxides formed in the 5.1 wt% Mg prefil alloy and EDX spectrum confirming the composition of MgO clusters.

It is important to note that Mg_2Si and $Al_{13}Fe_4$ were the major phases in this alloy α-AlFeSi and β-AlFeSi were observed very rarely. This shift of phases from AlFeSi intermetallics to other phases is discussed in detail later in section 6.4.2.

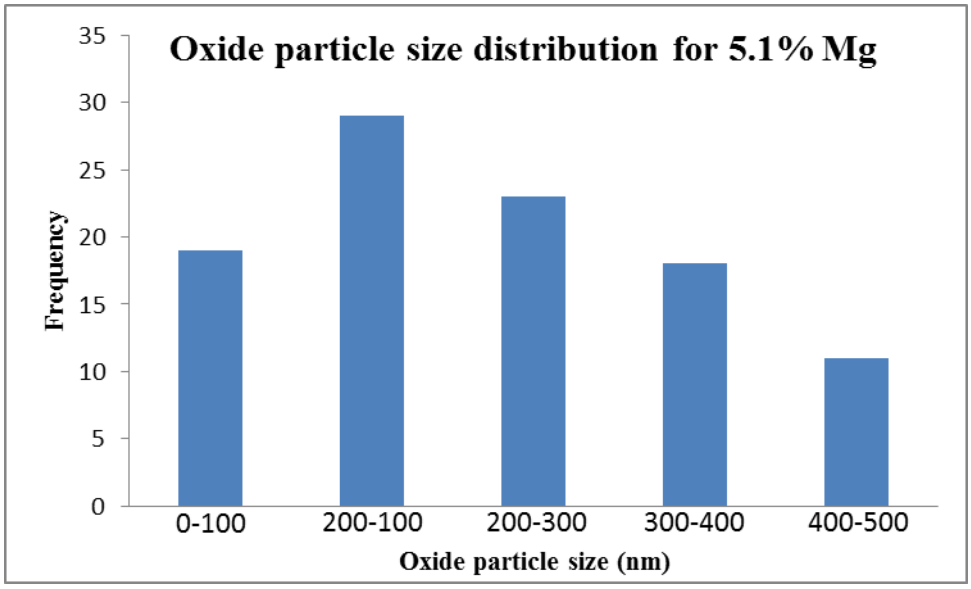

Fig 6.18 MgO particle size distribution in the 5.1 wt% Mg prefil alloy

6.1.2.5 Oxide coating on the intermetallics

Oxide coating of the intermetallics could be either during the prefil experiment or could be an artefact of extraction process i.e. oxide particles could have deposited over intermetallics sitting on the filter in the prefil machine or extraction apparatus. Also, some intermetallic particles were observed without any coating on them which further cast questions on the mechanism of coating.

However, it is interesting to note that there were many oxide bi-films observed during 2D analysis of high Mg prefil alloys which disappeared after extraction (as evidenced by 3D SEM analysis). Also, these oxide films were much larger in size and strained as compared to the ones in low Mg alloys and so relatively easier to break during the turbulent extraction process. Hence it is possible that oxide particles settle on top of the intermetallics when the Al matrix is dissolved during extraction process (section 3.5).

On the other hand, the oxide particles observed during 3D SEM appears to be bonded with the intermetallics on their surface rather than just sitting (artefact of extraction). This could have happened only during the high temperature which is not achieved during extraction process. Hence it is possible that the intermetallics formed in high density inclusion liquid were stopped by the filter during the prefil experiment and then the oxides stuck on their surface while the melt was flowing through the filter (section 3.1.3.3). Also, the oxide films act as a substrate for Fe-intermetallics or Mg_2Si (that forms from the last liquid) to grow along their surface. Oxide films support the formation of the intermetallics rather than physically obstructing their growth.

6.1.3 X-Ray Diffraction

Fig. 6.19a shows the XRD patterns of the extracted particles from the prefil alloys with different Mg contents along with the reference patterns for major phases and inclusions. The peaks observed belonged to α-AlFeSi, β-AlFeSi,

Mg_2Si, $Al_{13}Fe_4$, $MgAl_2O_4$, MgO, Al_2O_3 and TiB_2. It is interesting to note the transition from spinel to MgO as the Mg content was increased. Al_2O_3 and TiB_2 were present in small amounts as observed during the SEM analysis. The highest intensity peak of TiB_2 overlapped with the α-AlFeSi peak. Some of the α-AlFeSi, β-AlFeSi, Mg_2Si and $Al_{13}Fe_4$ peaks also overlapped or were very close to each other, as a result a separate zoom in XRD was plotted as can be seen in Fig. 6.19b. The highest peak of MgO also overlapped with the highest peak of $Al_{13}Fe_4$, which make it harder to observe the change in MgO with Mg content. Small peaks of Mg oxides indicated that the fraction of oxide formed was very low.

It is also important to note the shift in phase change from α-AlFeSi and β-AlFeSi to Mg_2Si and $Al_{13}Fe_4$. This shift in phase formation and associated thermodynamic calculations using MTDATA is discussed in detail later in section 6.4. Regression analysis was used to calculate the relative weight fractions of α-AlFeSi and β-AlFeSi (100 - α-AlFeSi weight fraction) **(Lui, 05)**. The approximate relative fraction of other phases and oxides observed in all the prefil alloys were calculated using SEM and EDX analysis and is shown in Table 6.1.

6.1.3.1 Prefil alloy with 0.1 wt% Mg

The presence of high α-AlFeSi (44.15°, 42°, 43.01°, 22.22°, 36.5°, 45.9°, 26.4°, 48.98°) and few β-AlFeSi (24.1°, 46.63°) peaks indicate that α-AlFeSi was the

dominant AlFeSi intermetallic phase present, which correlates with SEM analysis. For the 0.1 wt% Mg alloy, spinel peaks observed (36.85^o, 44.83^o) fits well with their frequent observation during SEM analysis. Small peaks from MgO (42.92^o), TiB_2 (34.13^o, 61.1^o) and Al_2O_3 (35.15^o) were also detected. Negligible peaks were detected for Mg_2Si and $Al_{13}Fe_4$. The relative weight fraction of α-AlFeSi calculated for 0.1 wt% Mg was 60%.

6.1.3.2 Prefil alloy with 0.5 wt% Mg

Similar to the 0.1 wt% Mg alloy, the presence of high α-AlFeSi (44.15^o, 42^o, 43.01^o, 22.22^o, 36.5^o, 45.9^o, 26.4^o, 48.98^o) and one β-AlFeSi peak (46.63^o) in this alloy indicated that that α-AlFeSi was the dominant AlFeSi intermetallic phase present. However, the intensities of the peaks reduced with the increase in Mg content in comparison with 0.1 wt% Mg alloy. For 0.5 wt% Mg, both spinel (36.85^o, 44.83^o) and MgO (42.92^o) peaks were observed, which correlates with SEM analysis. $Al_{13}Fe_4$ peaks showed no change from the 0.1 wt% Mg alloy. Small peaks for Mg_2Si (40.13^o, 24.3^o), Al_2O_3 (35.15^o) and TiB_2 (34.13^o, 61.1^o) were also detected. The relative weight fraction of α-AlFeSi calculated for 0.5 wt% Mg was 70%.

6.1.3.3 Prefil alloy with 1.3 wt% Mg

Contrary to the other Mg alloys, this alloy had the presence of relatively small peaks of α-AlFeSi (44.15^o, 42^o, 43.01^o, 22.22^o, 36.5^o, 45.9^o, 26.4^o), no β-AlFeSi

peaks and high intensity peaks for Mg_2Si (40.13^o, 24.3^o, 47.43^o, 58.04^o, 63.83^o) and $Al_{13}Fe_4$ (27.26^o, 43.15^o, 44.81^o) which indicated a shift in phase formation with the increase in Mg content. $Al_{13}Fe_4$ and Mg_2Si peaks were dominant in this alloy. MgO peaks (42.92^o, 62.3^o) were observed which explain their frequent observation during SEM analysis. Negligible spinel peak (44.83^o) was detected as MgO was the more stable oxide. Relatively smaller peaks of Al_2O_3 (35.15^o) and TiB_2 (34.13^o, 61.1^o) were observed. The relative weight fraction of α-AlFeSi calculated for 1.3 wt% Mg was 80%.

6.1.3.4 Prefil alloy with 5.1 wt% Mg

High intensity peaks for Mg_2Si (40.13^o, 24.3^o, 47.43^o, 58.04^o, 63.83^o) and $Al_{13}Fe_4$ (27.26^o, 43.15^o) were observed. No peaks were noted for α-AlFeSi and β-AlFeSi intermetallics which indicated the complete shift in phase formation as the Mg content was increased further. This observation correlates well with the presence of only Mg_2Si and $Al_{13}Fe_4$ particles during SEM analysis. The presence of MgO peaks (42.92^o, 62.3^o) and absence of spinel peaks correlates well with the SEM observation. Small peaks of Al_2O_3 (35.15^o, 57.49^o) and TiB_2 (34.13^o, 61.1^o) peaks were also observed. The relative weight fraction of α-AlFeSi calculated for 5.1 wt% Mg was 70%.

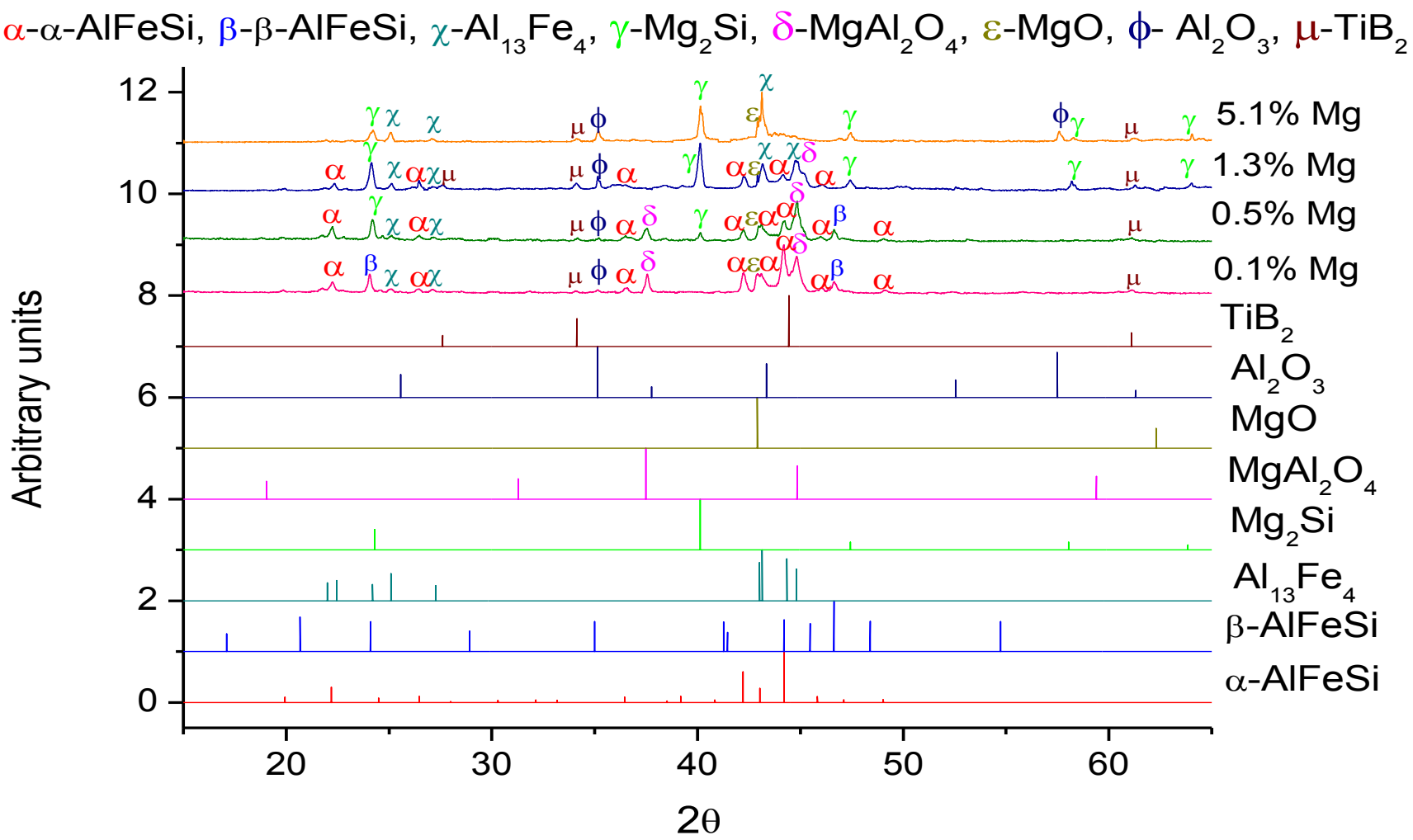

Fig 6.19a XRD patterns of the prefil alloys along with reference patterns (Appendix I) for major phases and inclusions. Cont..

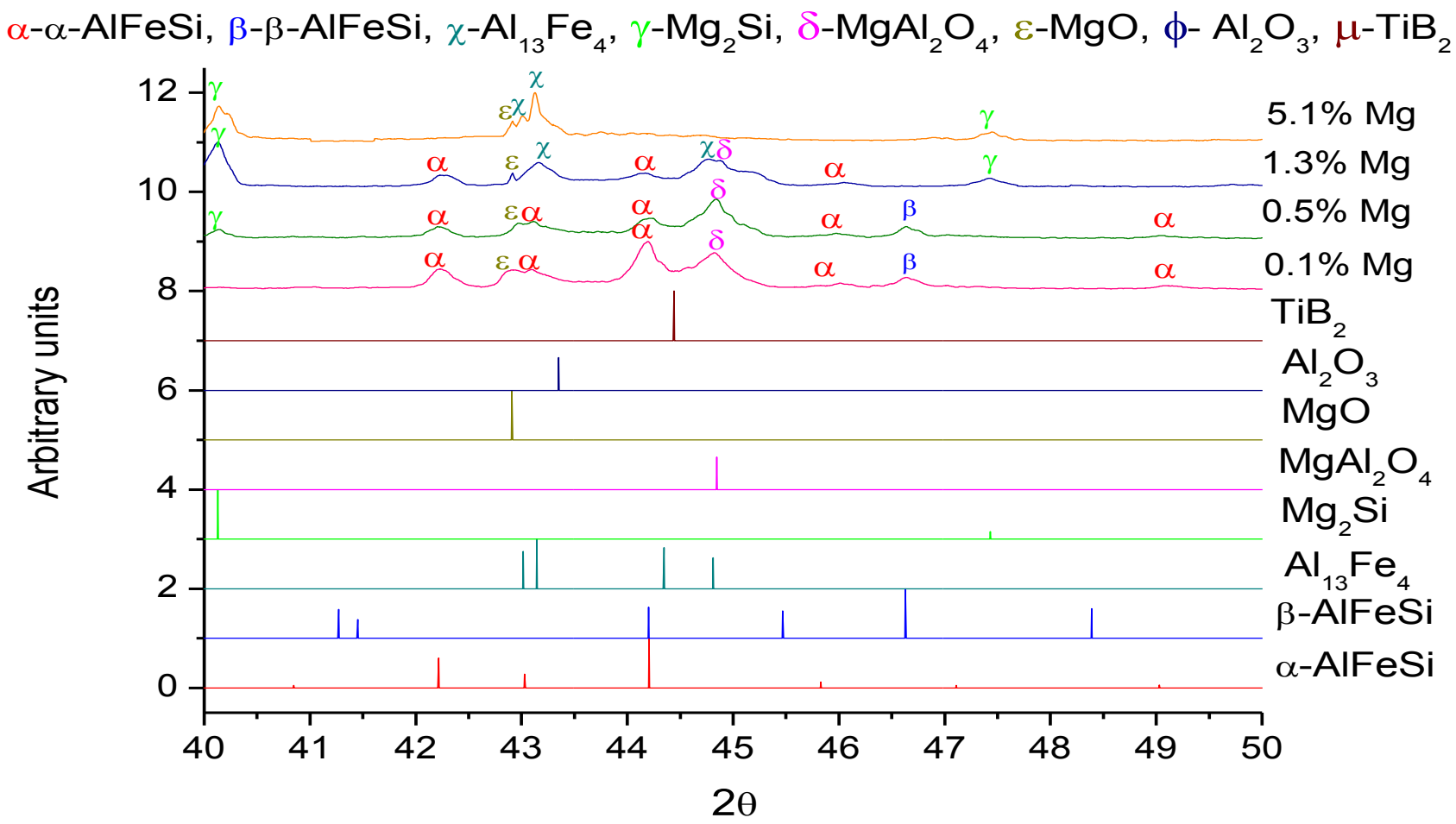

Fig 6.19b Zoom in XRD patterns of the prefil alloys along with reference patterns for 2θ=40 to 2θ=50.

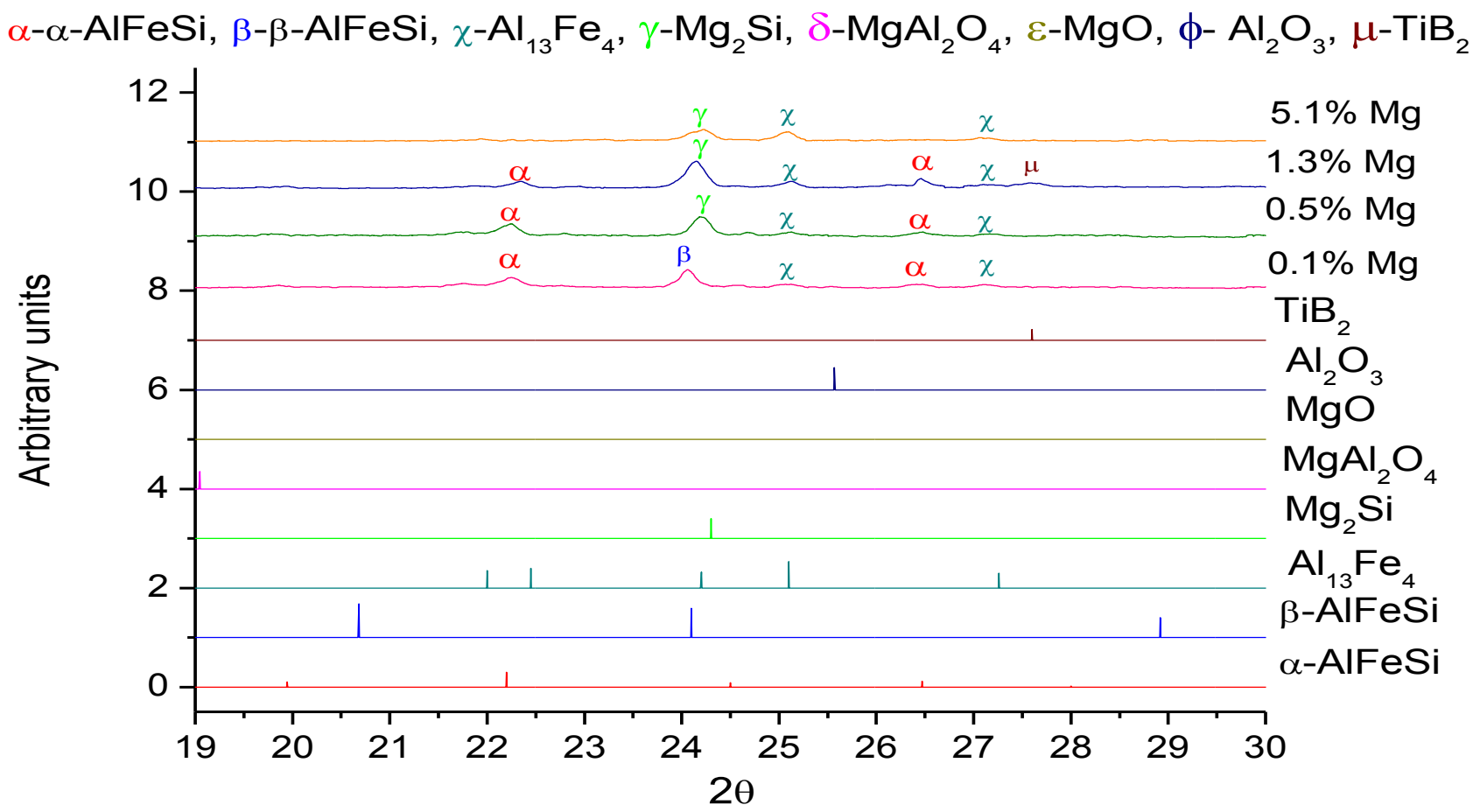

Fig 6.19c Zoom in XRD patterns of the prefil alloys along with reference patterns for 2θ=20 to 2θ=30.

Table 6.1 Approximate relative fraction of phases and oxides observed in prefill alloys with various Mg content.

		Rel. fraction of phases				Rel. fraction of oxides		
Mg%	Oxide Bi-films	$Al_{13}Fe_4$	β-AlFeSi	α-AlFeSi	Mg_2Si	Γ-Al_2O_3	MgO	Spinel
0.1	Yes (2D & 3D)	3%	30%	65%	2%	10%	20%	70%
0.5	Yes (2D & 3D)	15%	15%	55%	15%	5%	40%	55%
1.3	Yes (2D only)	20%	5%	20%	55%	2%	83%	15%
5.1	Yes (2D only)	30%	Absent	Absent	70%	2%	95%	3%

Table 6.2 Summary of the 2D and 3D morphology of oxides and oxide bi-film observed

Inclusion	2D morphology	3D morphology
MgO	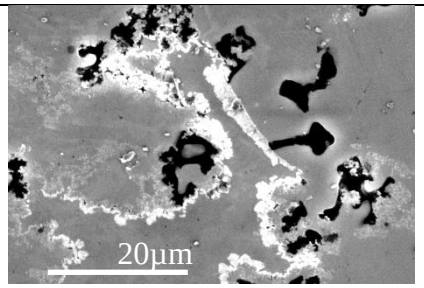	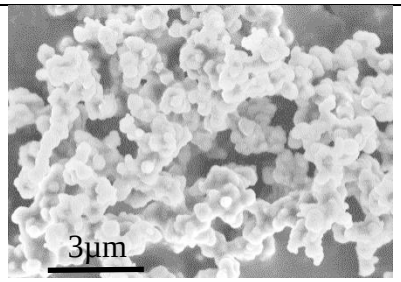
Spinel	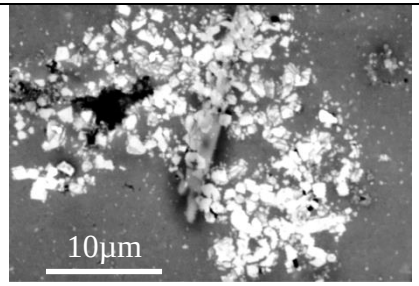	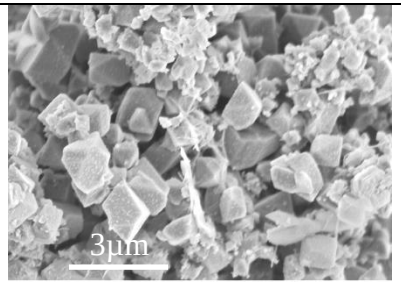
Oxide bi-film	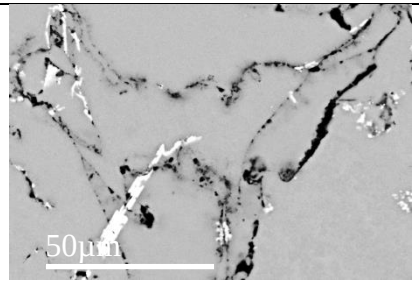	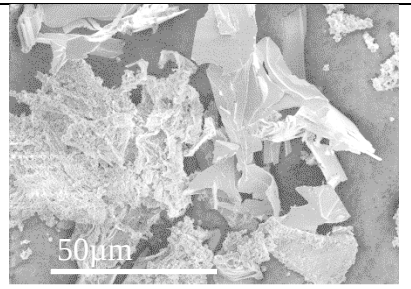

6.2 Analysis of Al-0.2Fe-0.4Si-X Mg using TP1 test

After becoming familiar with the inclusions and the phases present in the chosen alloy system from the analysis of the prefil alloys, it was important to check for them in conditions relatively closer to the commercial casting. The data about morphologies of the inclusions (mainly Mg oxides) from prefil analysis would be utilised in this study to identify the inclusions as they will be scarce. For this study a much wider range of Mg alloys were prepared to analyse the effect of inclusions (Mg oxides) on AlFeSi intermetallic formation. For this purpose, Mg was added to the master alloy Al-0.2Fe-0.4Si (made from high purity Al, Al-80Fe and Al-50Si) in order to obtain the compositions of 0.4 wt%, 0.8 wt%, 1.2 wt%, 1.6 wt%, 2 wt%, 2.5 wt%, 3.0 wt% and 5.0 wt%. All these alloys were cast using TP1 test. The compositions of different alloys were given previously in Table 3.3. The microstructures of these alloys were analysed using a wide range of techniques. Section 6.2.1 and 6.2.2 describes the grain structure of the alloys at both macro and micro level respectively. The 2D and 3D morphologies of the phases were studied in depth and reported in sections 6.2.3 and 6.2.4 respectively. The quantitative analysis of the AlFeSi intermetallics and other phases was conducted with the help of XRD and is discussed in section 6.2.5.

6.2.1 Macrostructure

Fig. 6.20 shows the macroetched images of all the alloys with different Mg contents. A reduction in grain size can be clearly observed as the Mg content was increased. This might be due to availability of more nucleation sites and

growth restriction due to excess solute and is discussed in detail in section 6.4.1. Also, there was a gradual change in the grain nature from columnar to equiaxed.

In order to make the understanding of the analysis easier, the alloys were divided into three categories i.e. low Mg content alloys (0 wt%, 0.4 wt% and 0.8 wt%), intermediate Mg content alloys (1.2 wt%, 1.6 wt% and 2 wt%) and high Mg content alloys (2.5 wt%, 3.0 wt% and 5.0 wt%).

6.2.1.1 Low Mg content alloys

In the low Mg content alloys columnar grains were observed to be dominant over equiaxed grains. However, the area fraction of equiaxed grains was observed to increase with the increase in Mg content i.e.15% in 0 wt% Mg, 28% in 0.4 wt% Mg and 32% in 0.8 wt% Mg. As observed in the grain size analysis from anodised microstructures (see Fig. 6.21), the size of the grains reduced from 0 wt% Mg to 0.4 wt% Mg and then increased for 0.8 wt% Mg. However, this reduction was within the error limit as shown in Fig.6.22.

6.2.1.2 Intermediate Mg content alloys

The grain size and nature changed significantly in 1.2 wt% Mg with respect to the 0.8 wt% Mg sample. No columnar grains were observed in these alloys and the grain structure was completely dominated by equiaxed grains. The grain size was observed to decrease with an increase in Mg content, however not significantly as shown in Fig. 6.22.

6.2.1.3 High Mg content alloys

The grain size reduced significantly in these alloys compared to other Mg content alloys and decreased further with an increase in Mg content. However, the grain structure remained dominated by equiaxed grains and showed no change when the Mg content was increased above 3.0 wt% Mg to 5.0 wt% Mg. It is important to note that the general grain structure for high Mg content alloys is similar to the alloys with grain refiner. This will be discussed in detail, later in section 6.4.1.

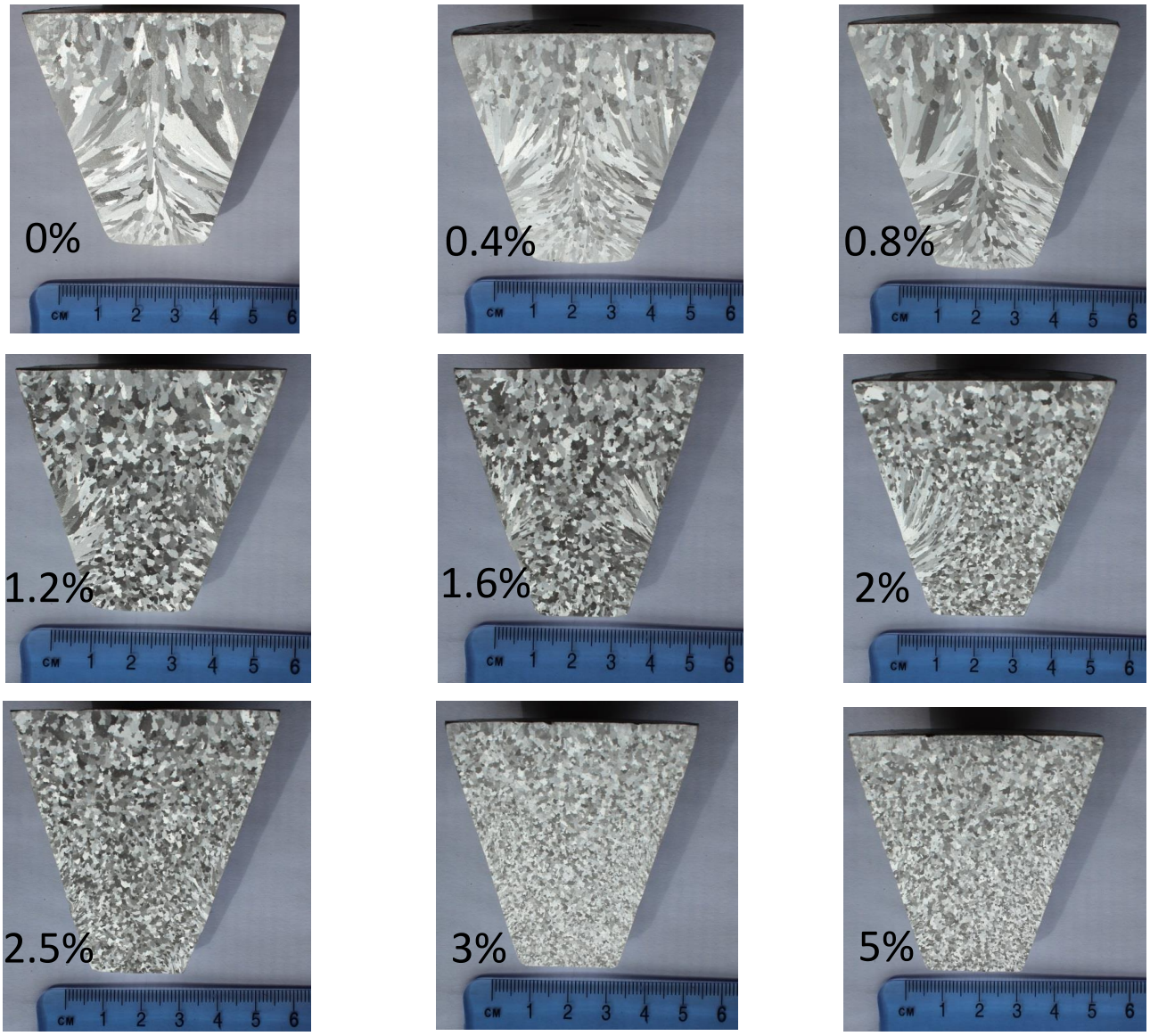

Fig. 6.20 Macoetched images showing grain structure in TP1 samples containing different Mg wt%

6.2.2 Grain Morphology

Grain size and SDAS are the two important factors that describe the grain morphology of the alloy. Fig. 6.21 shows the anodized microstructure of the samples with different Mg contents. It can be noted that the difference between the grain size and dendritic arm spacing is large as shown in Fig. 6.22. In such cases the grains are dendritic in nature.

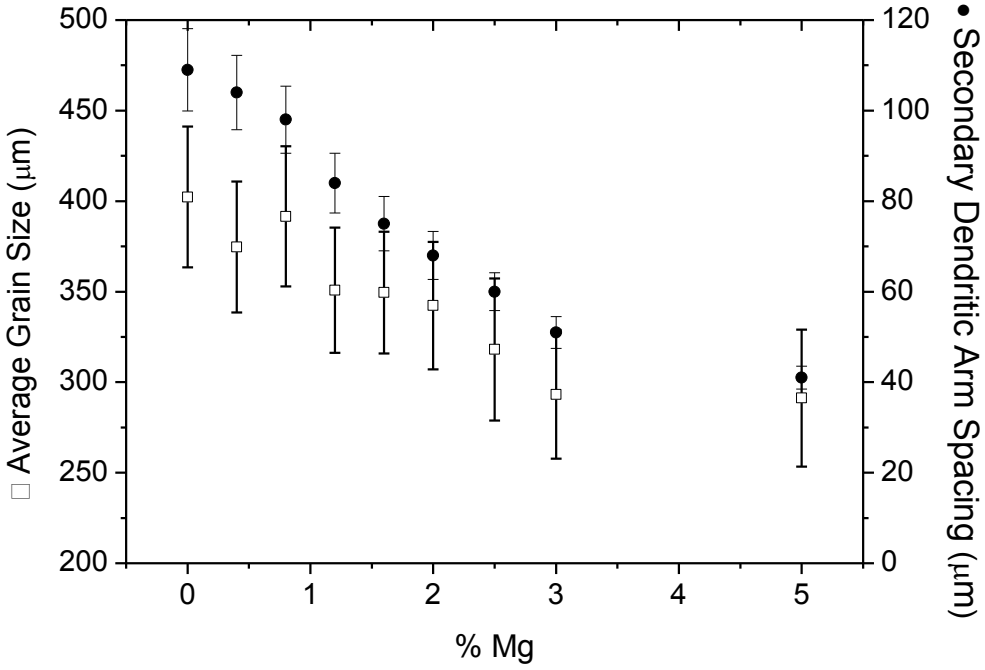

Fig 6.22 Variation of grain size and dendritic arm spacing in TP1 samples with different Mg wt%.

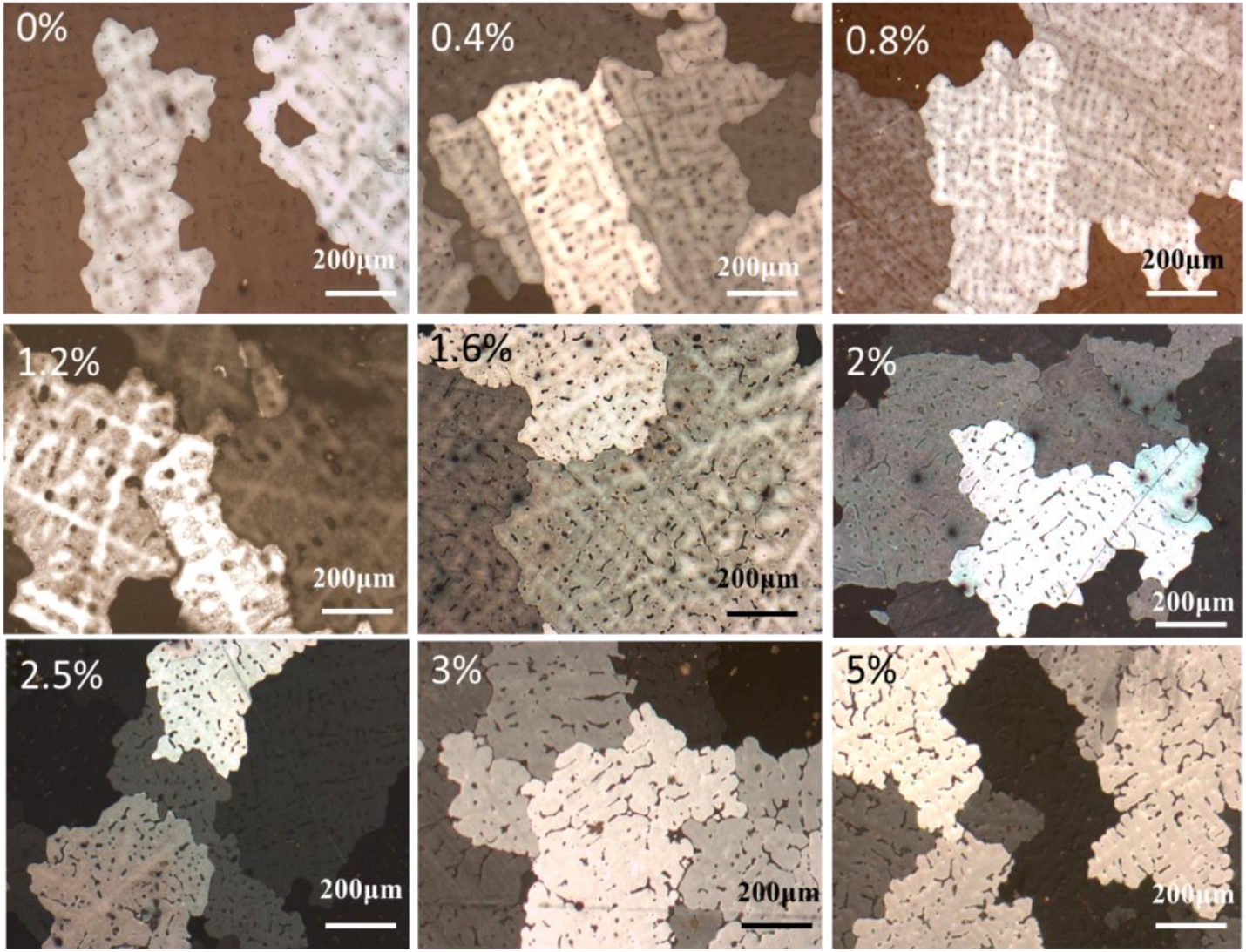

Fig 6.21 Optical micrographs showing the grains of anodised TP1 samples with different Mg wt%.

It is interesting to observe that the grain morphology varied significantly with Mg content. Fig. 6.22 shows the measured average grain size and secondary dendrite arm spacing (SDAS) of the samples with different Mg content. The grain size and SDAS were observed to be directly proportional to each other. The changes observed during the grain size analysis were also verified by macroetching.

6.2.2.1 Low Mg content alloy

The average grain size in the base alloy (0 wt% Mg) was measured to be 402±39μm, which reduces to 375±36μm in the 0.4 wt% Mg alloy. However, the grain size increased to 392±39μm in the 0.8 wt% Mg alloy. Thus, in general there is no significant variation in grain size in low Mg content alloys as all three samples were well within the standard deviation. On the other hand, the secondary dendritic arm spacing (SDAS) decreased gradually from 109±9μm in the 0 wt% Mg alloy to 104±8μm in the 0.4 wt% Mg alloy and 98±7μm in the 0.8 wt% Mg alloy.

6.2.2.2 Intermediate Mg content alloys

There was a significant drop in the grain size of intermediate Mg content alloys when compared with low Mg content alloys. However, there was negligible variation in grain size within the intermediate Mg content alloys. The grain size measured in these alloys decreased slightly with Mg content. The average grain

sizes measured were 351±35µm, 350±34µm and 342±35µm in the 1.2 wt% Mg, 1.6 wt% Mg and 2.0 wt% Mg alloys respectively. Similar to the low Mg content alloys, the SDAS decreased further from 84±7µm in the 1.2 wt% Mg alloy to 75±6µm in the 1.6 wt% Mg alloy and 68±5µm in the 2.0 wt% Mg alloy. However, it is to be noted that the standard deviation in SDAS was also decreasing with Mg content.

6.2.2.3 High Mg content alloys

Another significant drop in grain size was measured between intermediate Mg content alloys and high Mg content alloys. The average grain size reduced from 318±39µm in the 2.5 wt% Mg alloy to 293±36µm in the 3.0 wt% Mg alloy. However, the grain size did not vary on a further increase of Mg content as can be noted from the grain size of 291±38µm in the 5.0 wt% Mg alloy. The SDAS decreased gradually from 60±4µm to 51±4µm and to 45±3µm in in the 2.5 wt%, 3.0 wt% and 5.0 wt% Mg alloys respectively. It is interesting to note that though the grain size was constant for high Mg content alloys, the SDAS still decreased as did the standard deviation.

6.2.3 2D Characterisation of intermetallics

Fig. 6.23 shows the general 2D morphology of the intermetallics present in the alloys with different Mg contents. These intermetallics were identified using the ratio of Fe to Si with the help of EDX and the morphologies reported in existing

literature **(Cooper, 67) & (Allen et al., 99).** In general If the Fe:Si>2 than it implies the intermetallic to be α-AlFeSi and if Fe:Si ≤ 1 than β-AlFeSi. However, in many cases the intermetallics have complex geometry with 1<Fe:Si<2. In such instances one should not rely completely on the Fe:Si ratio only as it can provide misleading information. It is interesting to note that the intermetallics were observed mainly on cell or grain boundaries. However, with the increase in Mg content, the tendency of AlFeSi intermetallics and Mg compounds to form within the cell or grain boundaries increased.

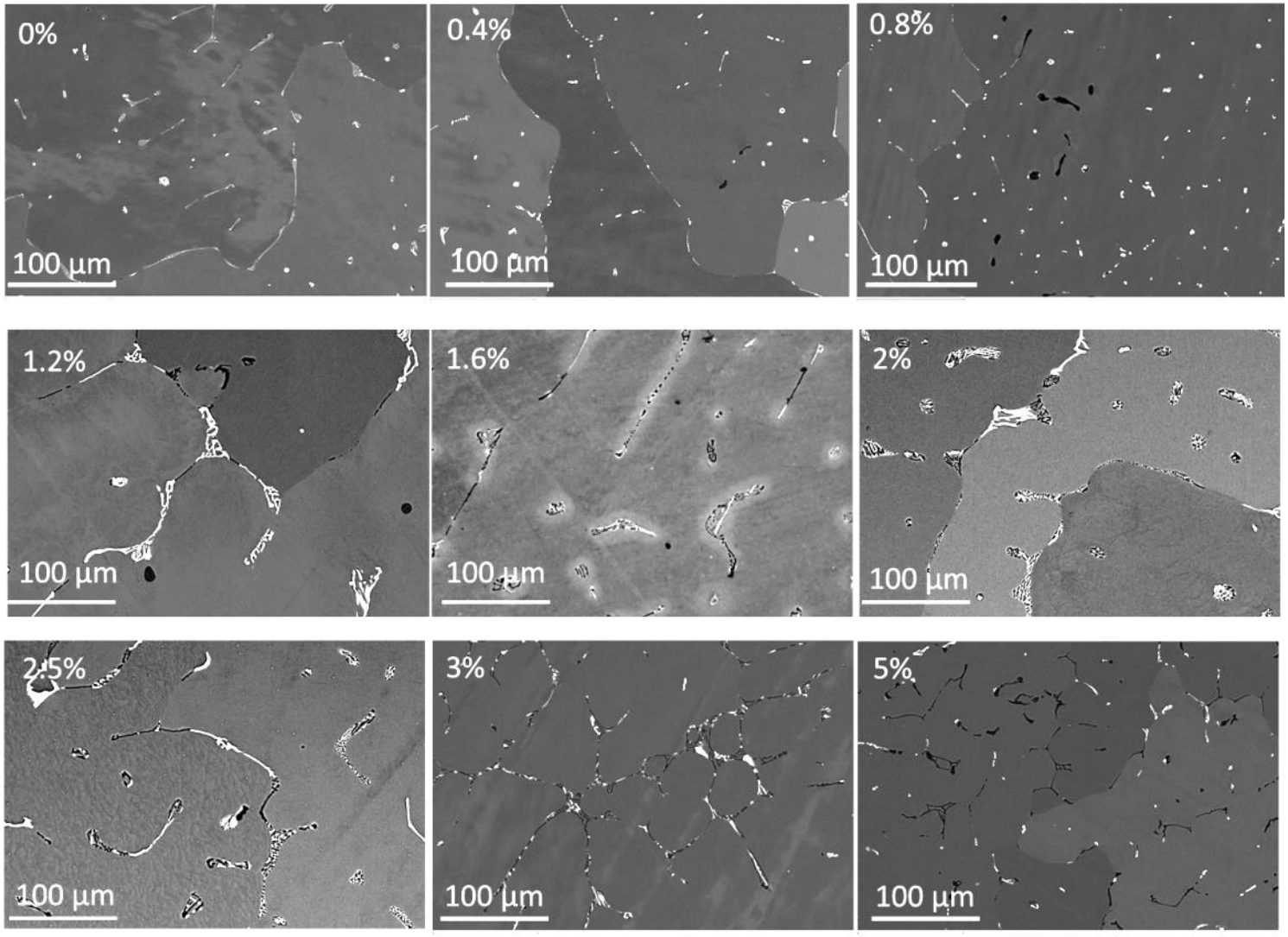

Fig 6.23 2D SE micrographs of TP1 samples showing the formation of intermetallics on grain/cell boundaries

6.2.3.1 Low Mg content alloys

AlFeSi intermetallics i.e. α-AlFeSi and β-AlFeSi were the commonly observed intermetallics in these alloys. α-AlFeSi was mainly observed with a Chinese script morphology, whereas β-AlFeSi was found as needles. Also, the intermetallics in these alloys were observed mainly on cell or grain boundaries as shown in Fig. 6.24. Fig. 6.24 shows the Chinese script morphology of α-AlFeSi particle which is confirmed using EDX spectra (Fe:Si>2). However, Mg_2Si phase was also observed as isolated phases of random morphology within cell boundaries for Mg ≤ 0.8 wt%.

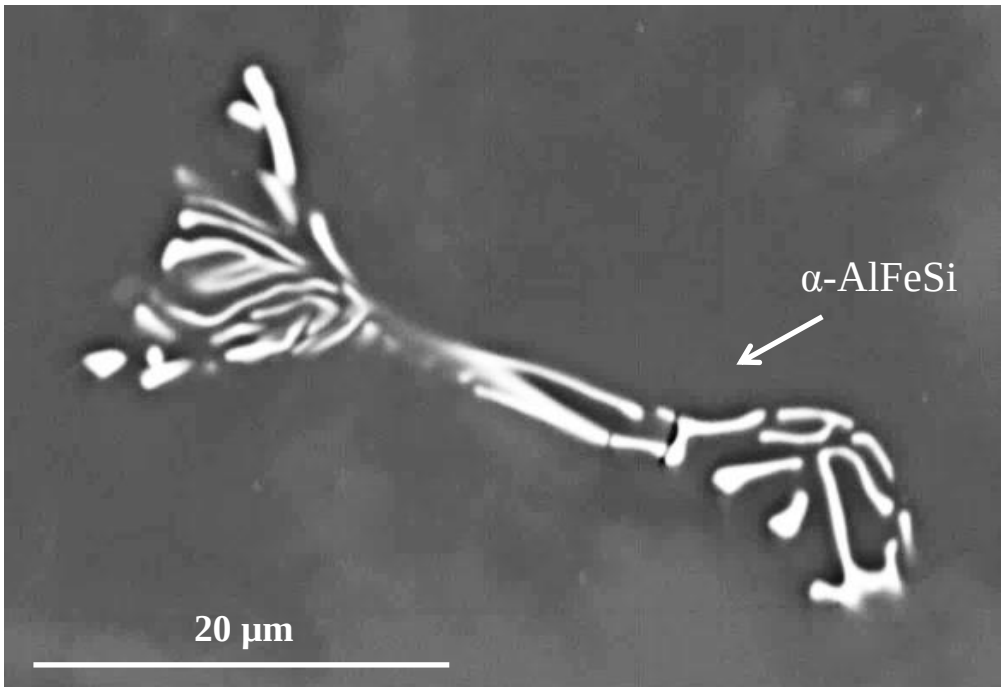

Continued overleaf…

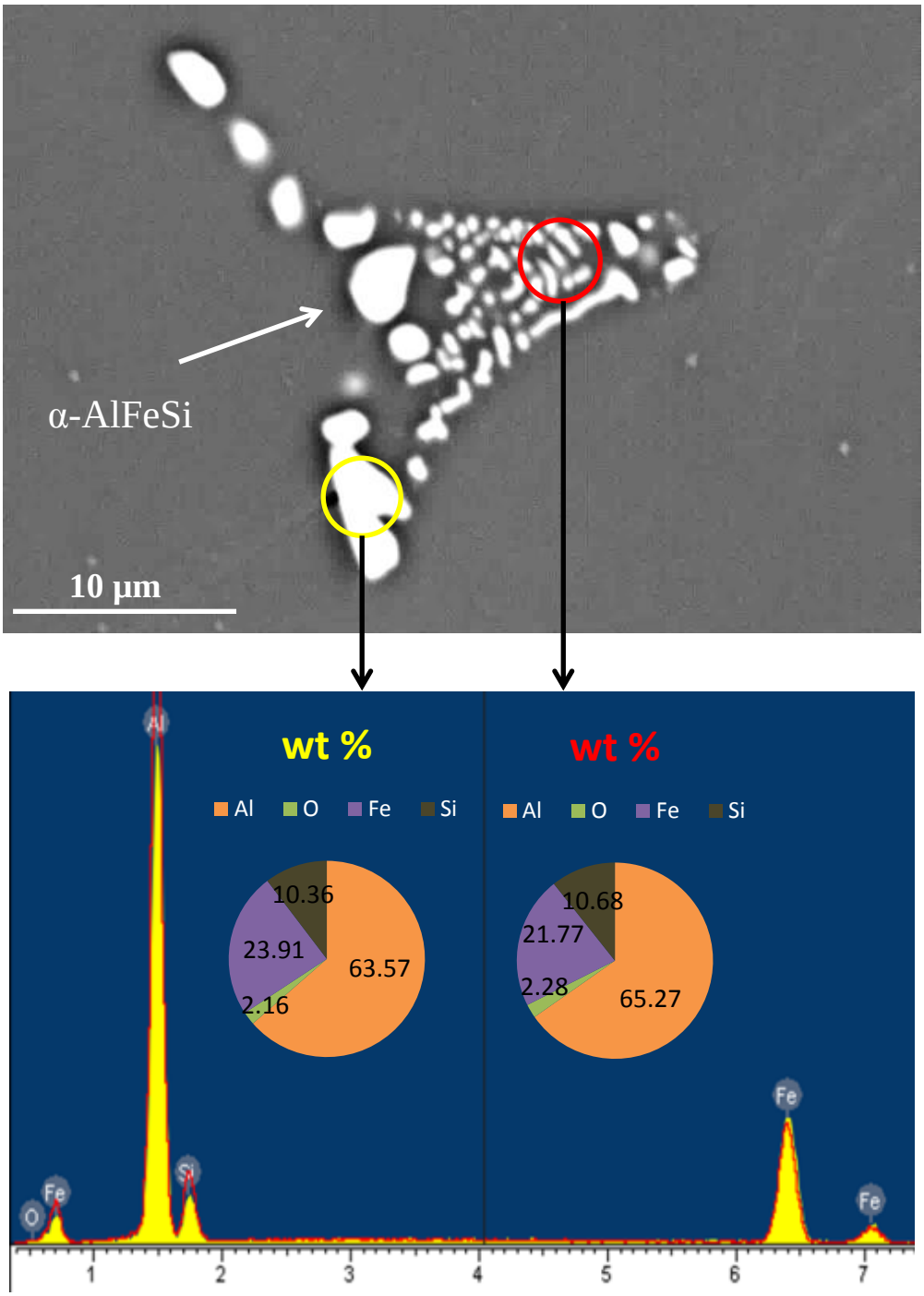

Continued overleaf…

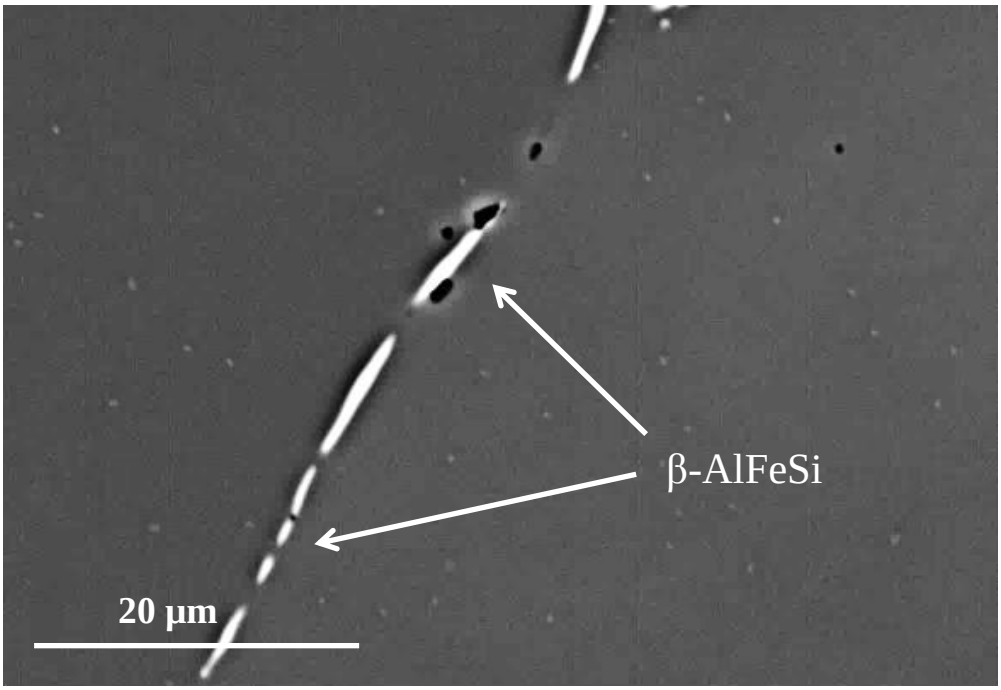

Fig. 6.24 2D BSE micrographs of low Mg content alloys showing the Chinese script and needle morphologies of α-AlFeSi and β-AlFeSi respectively.

6.2.3.2 Intermediate Mg content alloys

Fig. 6.25 shows the Fe-rich intermetallics (mainly $Al_{13}Fe_4$) and Mg_2Si phase observed for these alloys. α-AlFeSi and β-AlFeSi were rarely observed in these alloys. For 0.8 wt% < Mg ≤ 1.2 wt% α-AlFeSi intermetallic dominated over β-AlFeSi (both less than $Al_{13}Fe_4$), whereas for Mg > 1.2 wt%, neither α-AlFeSi nor β-AlFeSi were observed. For Mg contents 1.2 wt% to 2 wt%, Mg_2Si was not observed as an isolated phase and was found to be associated with $Al_{13}Fe_4$ in both Chinese script and needle-like morphologies. Also in these alloys, SEM and EDX analysis provides inconclusive results due to complex interconnected

morphologies. Therefore, it is hard to differentiate between α-AlFeSi, β-AlFeSi and $Al_{13}Fe_4$.

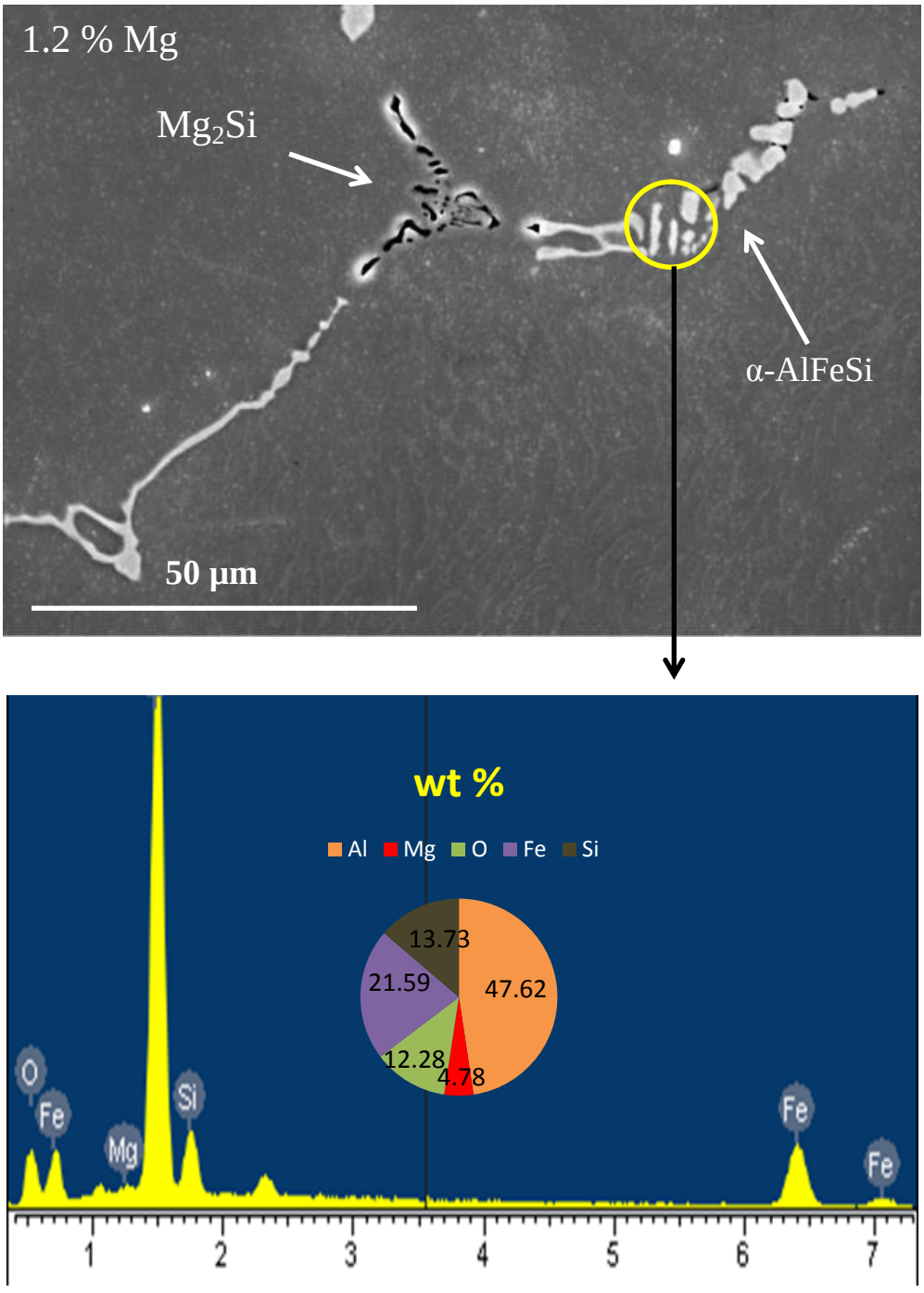

Continued overleaf…

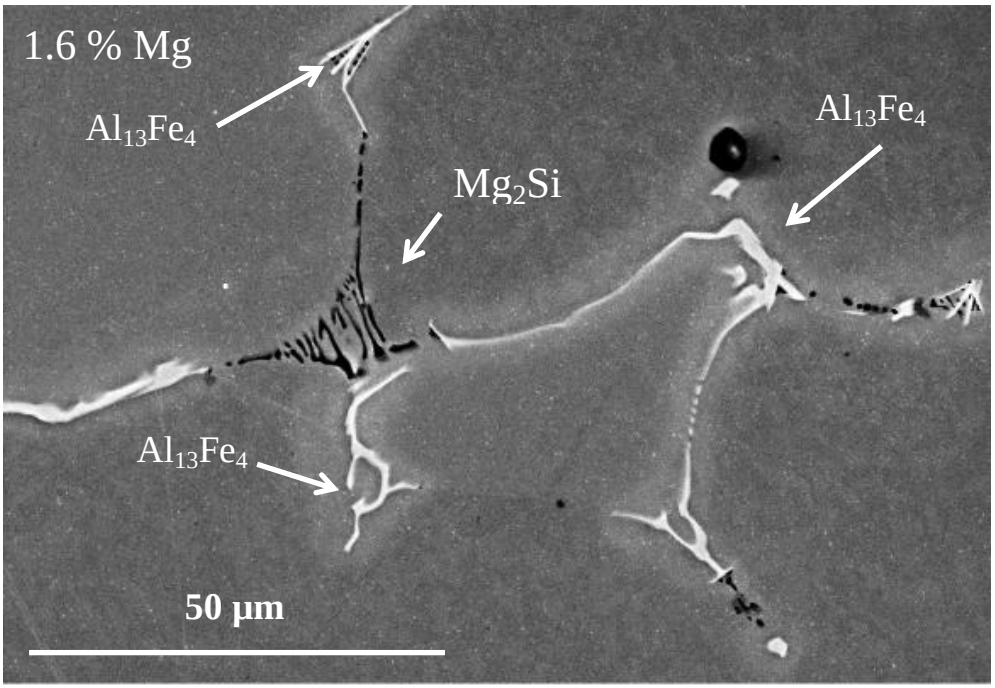

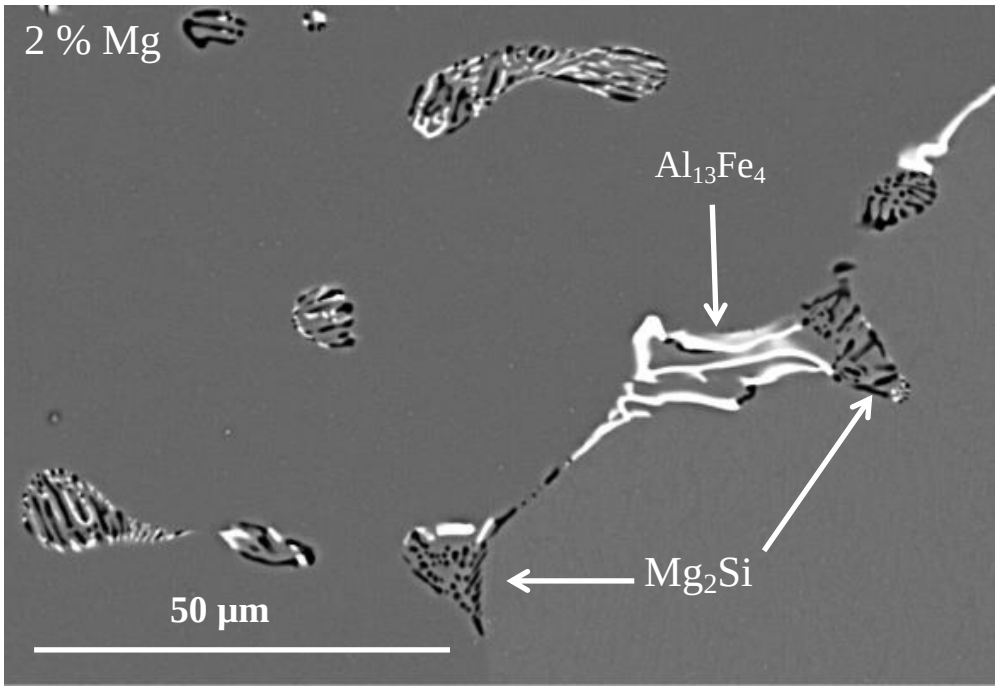

Fig. 6.25 2D SE and BSE micrographs of intermediate Mg content alloys showing the morphologies of α-AlFeSi, $Al_{13}Fe_4$ and Mg_2Si.

6.2.3.3 High Mg content alloys

Fig. 6.26 shows the Fe-rich intermetallics (only $Al_{13}Fe_4$) and Mg_2Si phase observed for these alloys. In the higher Mg content alloys, the major Fe-rich intermetallic phase was $Al_{13}Fe_4$ and α-AlFeSi and β-AlFeSi were not observed. Also, MTDATA calculations showed $Al_{13}Fe_4$ and Mg_2Si as the dominant phases over α-AlFeSi and β-AlFeSi for high Mg content alloys (see chapter-5 for more details). The other interesting feature of the microstructures was the distribution of Mg_2Si phase. For 2.5 wt% Mg and 3.0 wt% Mg, Mg_2Si and $Al_{13}Fe_4$ were found to be associated with each other in Chinese-script morphology only. For high Mg content i.e. 5.0 wt%, Mg_2Si was the major phase and was frequently observed as an isolated phase within cell boundaries and mainly in the Chinese-script morphology.

The area fraction of Mg_2Si and Fe-rich intermetallics (α-AlFeSi, β-AlFeSi and $Al_{13}Fe_4$) is plotted with respect to Mg content (Fig. 6.27) using grey scale quantification. For this plot, Fe-rich intermetallics was considered more suitable than α-AlFeSi or β-AlFeSi as there was a phase shift from AlFeSi intermetallics in low Mg alloys (Mg<1.2 wt%) to $Al_{13}Fe_4$ in high Mg alloys (Mg>1.2 wt%). Also due to complex interconnectivity of intermetallics, it is not always possible to differentiate between them. Grey scale quantification on 2D micrographs confirmed that Mg_2Si was one of the major phases for Mg ≥ 2.0 wt%. The EDX spectra in Fig. 6.26 also confirmed the presence of Mg_2Si (black) and $Al_{13}Fe_4$ (white).

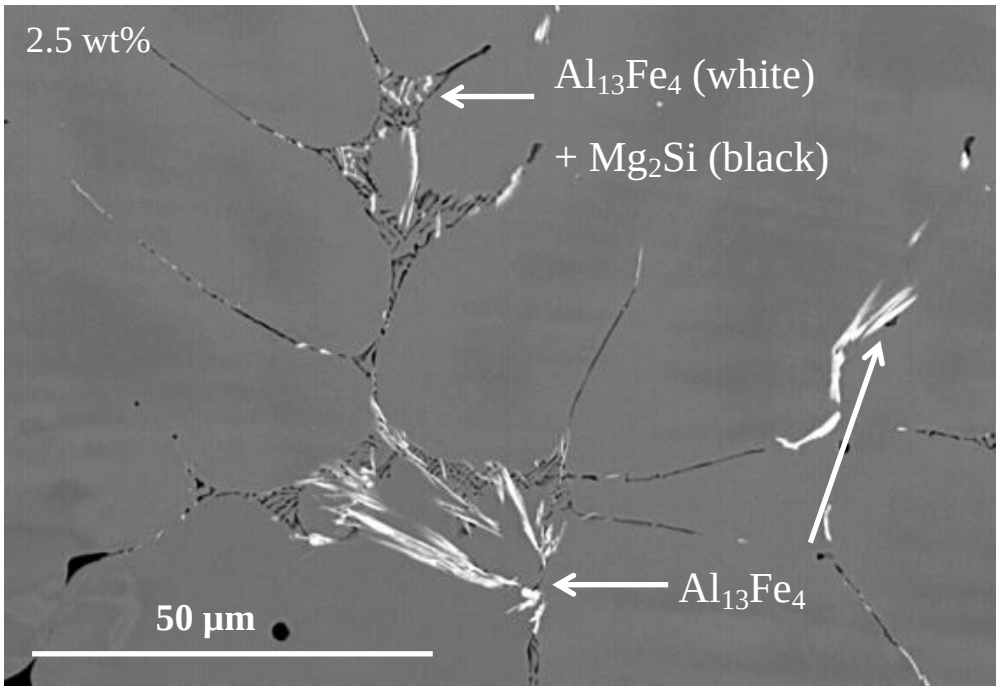

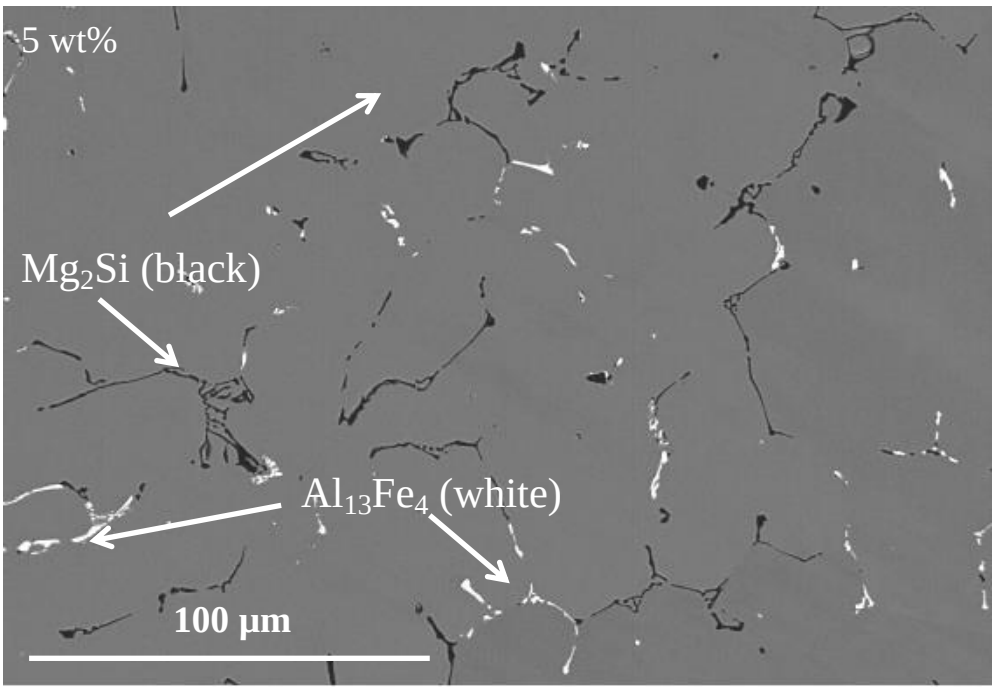

Continued overleaf…

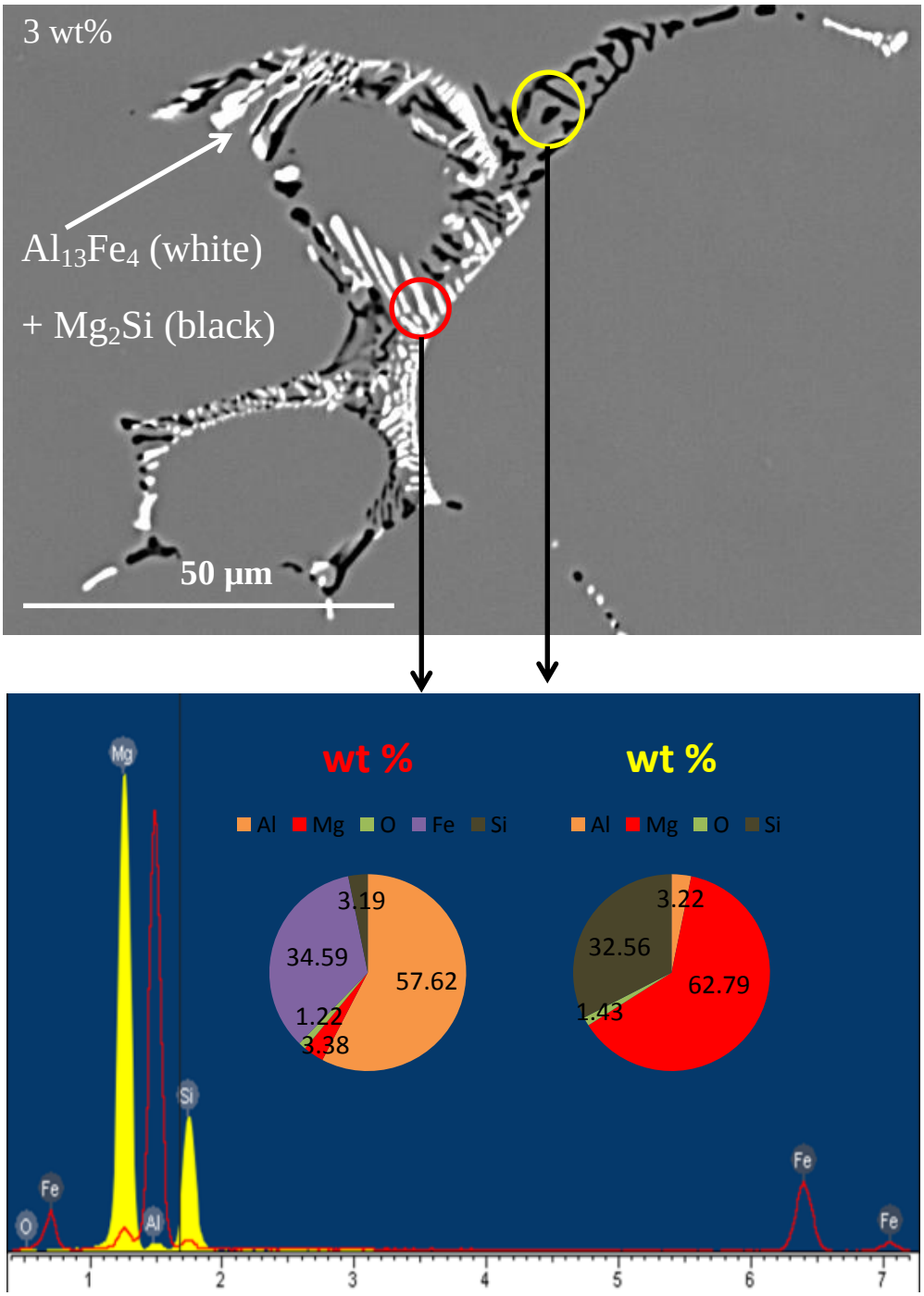

Fig. 6.26 2D BSE micrographs of high Mg content alloys showing the interconnected morphologies of Mg_2Si and $Al_{13}Fe_4$ in 2.5wt% and 3wt%, and isolated Chinese script morphology of Mg_2Si in 5wt%.

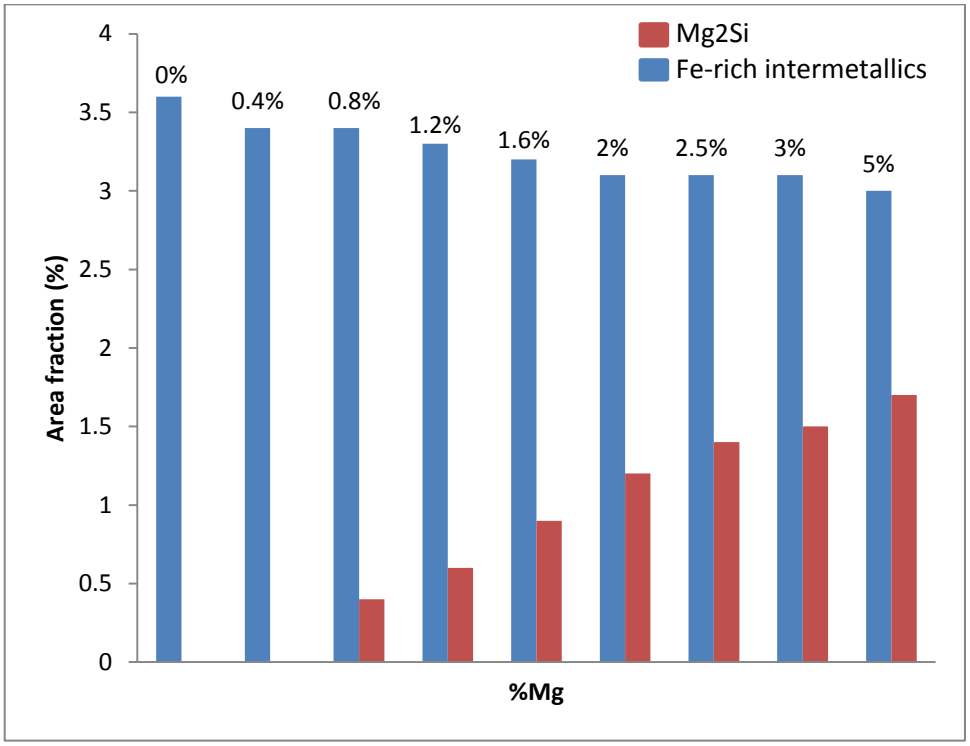

Fig 6.27 Grey scale measurement showing the variation in area fraction of Fe-rich intermetallics (α-AlFeSi, β-AlFeSi and $Al_{13}Fe_4$ combined) and Mg_2Si phase with change in Mg wt%.

6.2.3.4 2D morphology of oxide bi-films

Crack-like features were also observed in the 2D characterisation of samples with different Mg contents. Similar cracks have been reported previously **(Cao et al., 00) & (Cao et al., 03)**. These crack widths can be associated with the distance between two dry surfaces of the oxide bi-films, which were confirmed to be oxide using EDX.

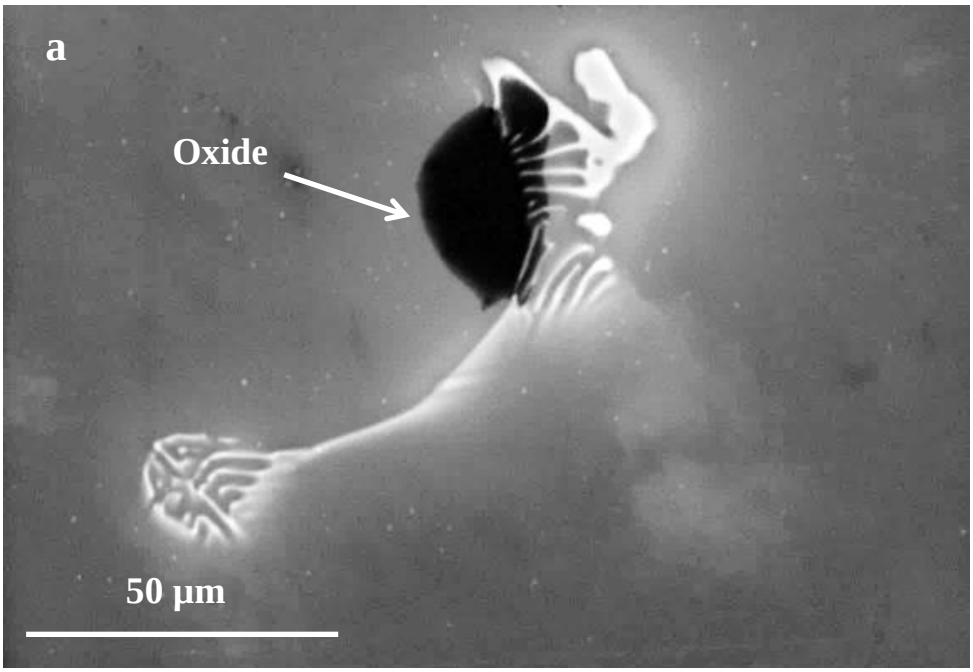

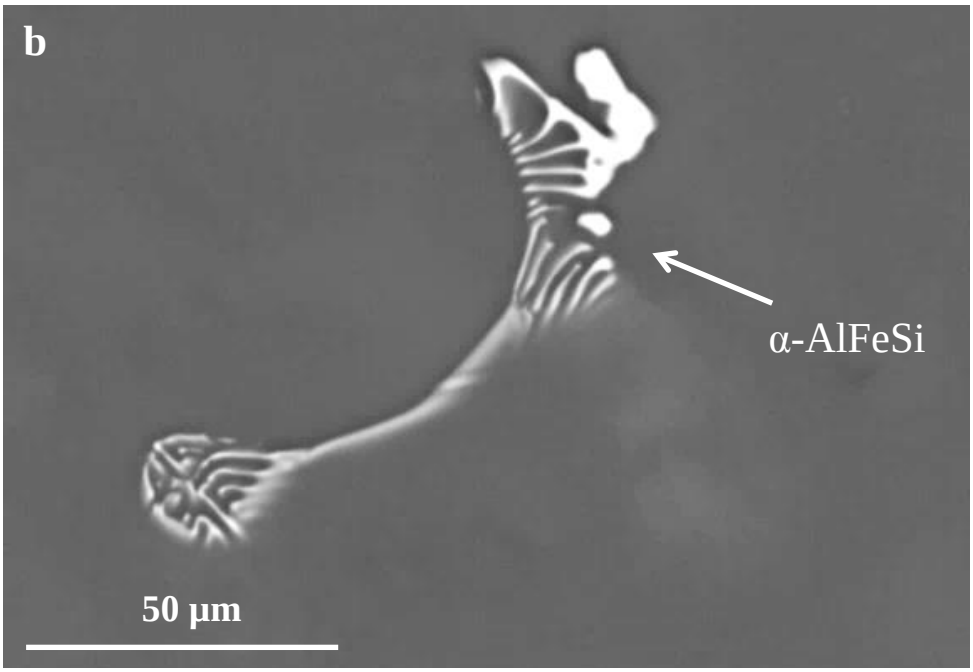

Continued overleaf…

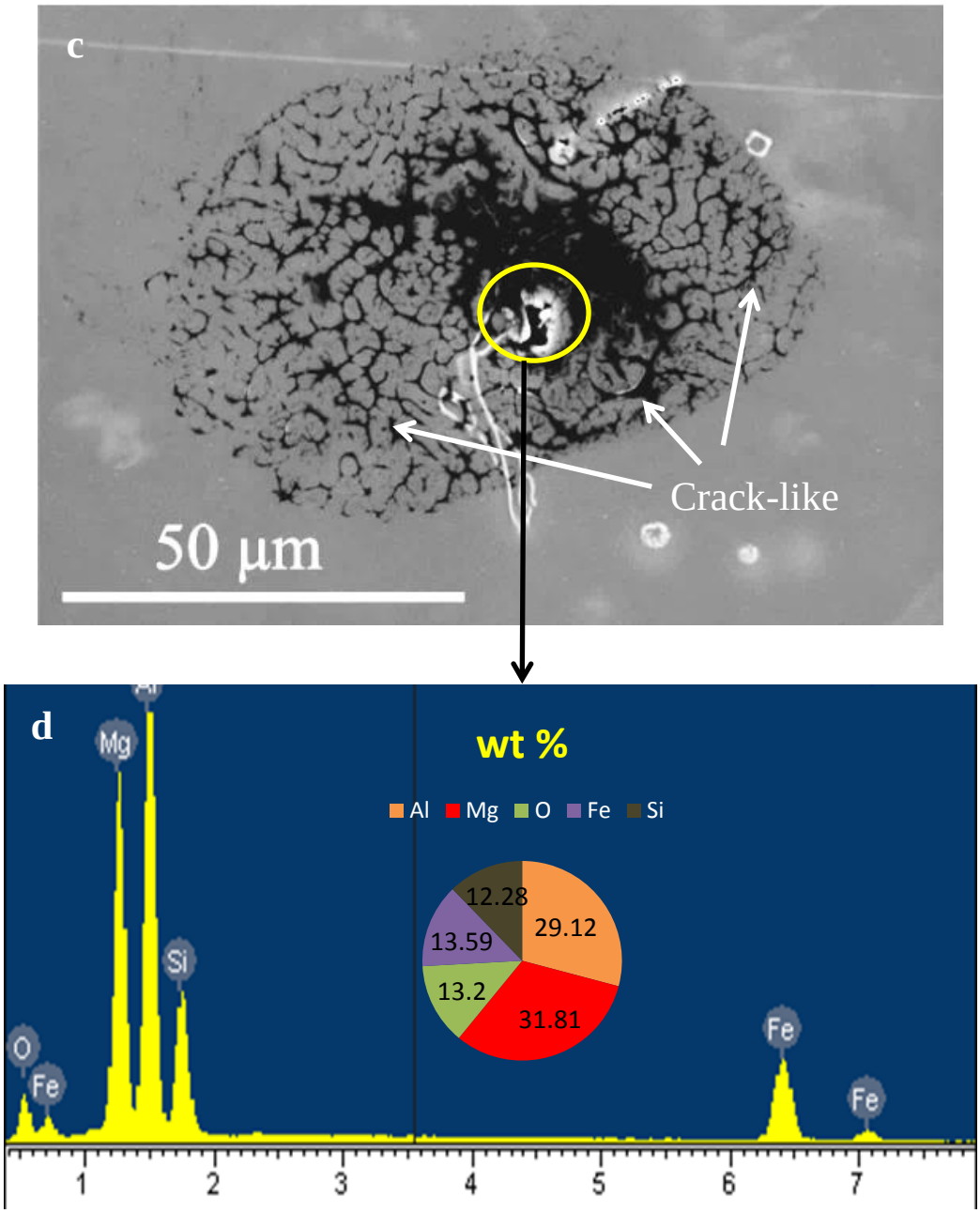

Continued overleaf…

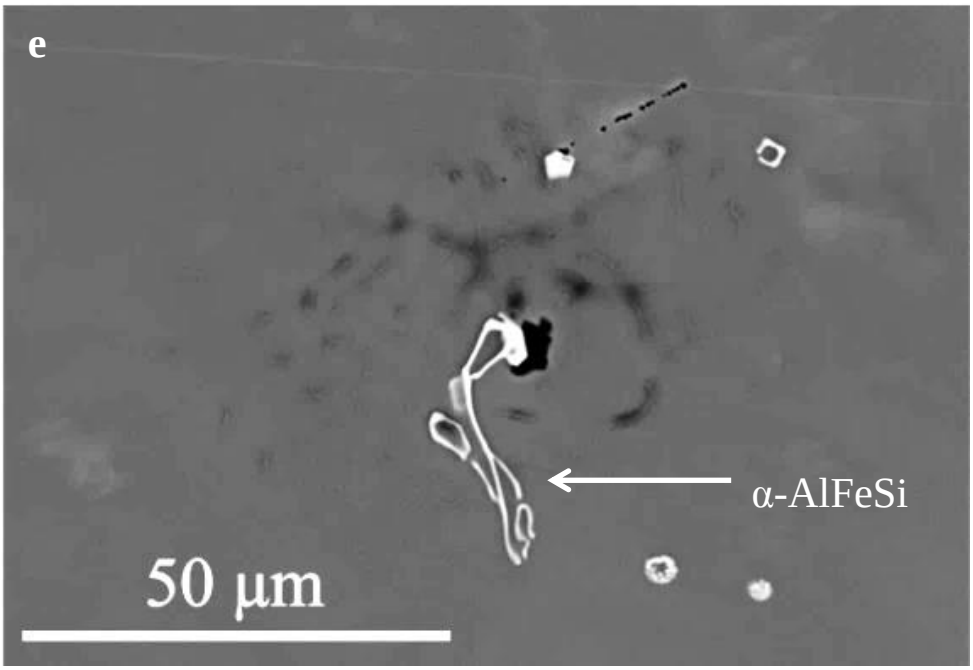

Fig 6.28 a) & c) SE images showing the oxide bi-films and α-AlFeSi, b) & e) BSE images of the same areas showing the intermetallics underneath the layer of oxide bi-film and d) EDX spectrum confirming the presence of both oxide bi-film and AlFeSi intermetallic.

A number of AlFeSi intermetallics were observed to be associated with the oxide bi-films. These intermetallics were observed using the backscattered signal where they appeared to be originating from the wet surface of the oxide bi-films as shown in Fig. 6.28. However, EDX proved to be inconclusive to identify the type of the AlFeSi intermetallic particles as low Fe:Si with Chinese script morphology of α-AlFeSi provides contradictory result. The association of oxides with the intermetallics will be discussed later in section 6.4.2. Add explanation for phase observation or mention that it will be explained in next section.

6.2.4 Characterisation of the 3D morphologies of intermetallics

α-AlFeSi, β-AlFeSi, $Al_{13}Fe_4$ and Mg_2Si were the major phases observed. They were mainly identified on the basis of their regular morphology and EDX analysis. The approach to measure the interconnectivity and length of the intermetallic particles was discussed in section 3.7. It was assumed that little/no breakage occurred during the extraction or sample preparation process. Due to limitations associated with the SEM and EDX, it is not possible to distinguish between α-AlFeSi and β-AlFeSi intermetallics in complex interconnected microstructure. Hence Fig. 6.29 and Fig. 6.30 measures Al-Fe-Si phases in general and not as α-AlFeSi and β-AlFeSi intermetallics. About 50 particles for each sample were measured and the interconnectivity, I-DAS, maximum length of the petals of α-AlFeSi and maximum size of β-AlFeSi platelets are shown in Fig. 6.29, Fig. 6.30, Fig. 6.31 and Fig. 6.32 respectively. Though the 2D micrographs showed intermetallics as broken and isolated, they were observed to be significantly coarser and much more interconnected in 3D micrographs. Hence, it is important to have a three dimensional view of intermetallics to obtain complete information. Table 6.3 at the end of the section provides the summary of the 2D and 3D morphologies of different major phases observed in TP1 cast samples.

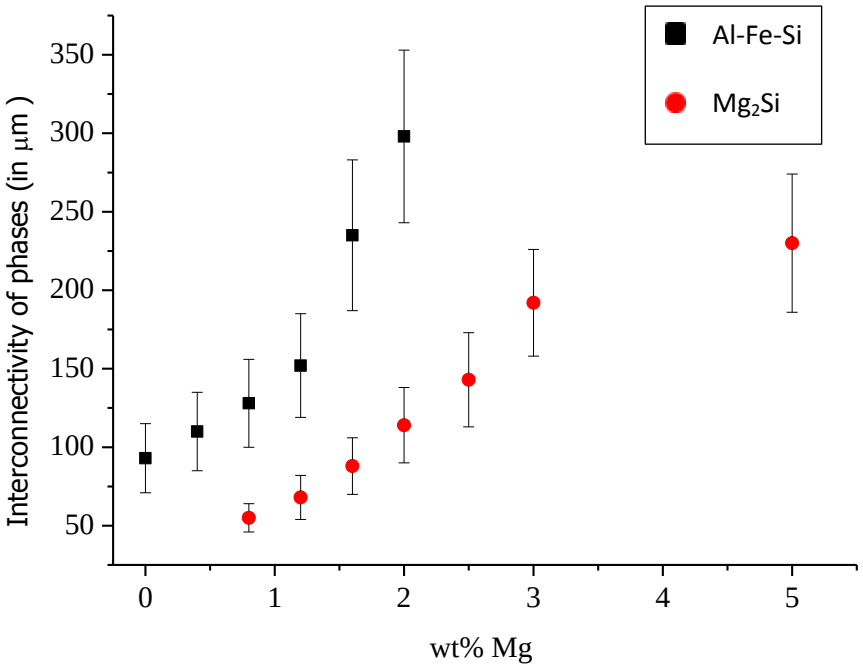

Fig 6.29 Variation of interconnectivity between AlFeSi phases and Mg_2Si with the increase in Mg wt%.

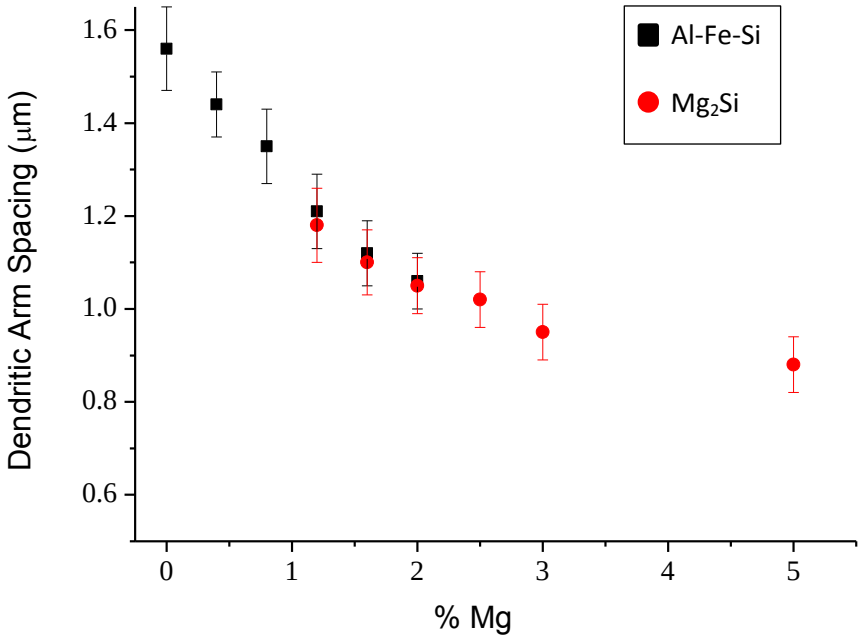

Fig 6.30 Variation of I-DAS with the increase in Mg wt%.

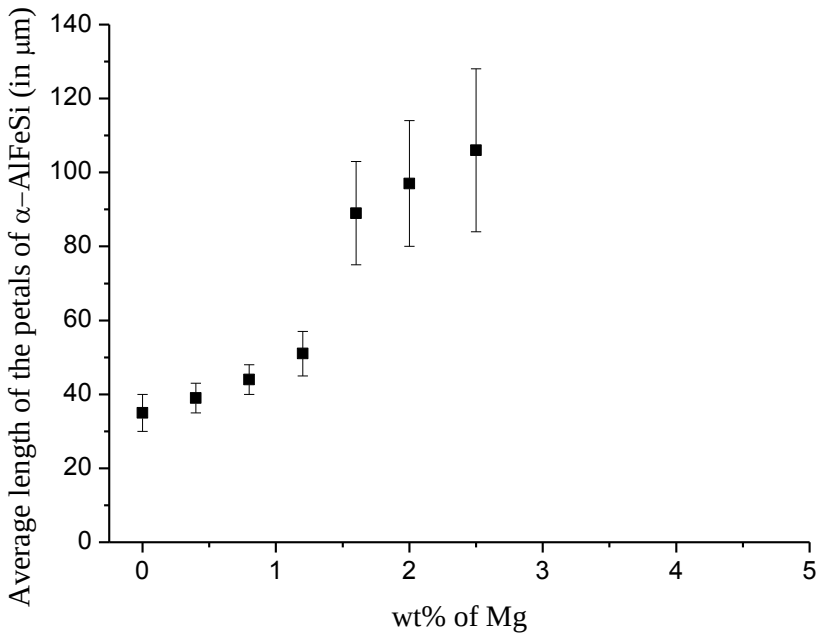

Fig. 6.31 Variation of the average length of the petals of α-AlFeSi with the Mg wt%. No α-AlFeSi was observed for 3.0 wt% and 5.0 wt% Mg.

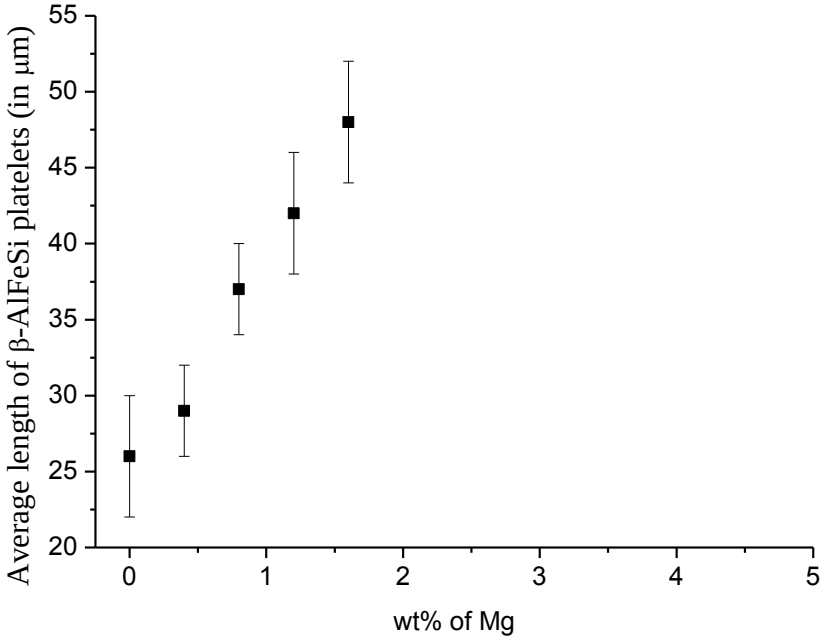

Fig. 6.32 Variation of the maximum size of the β-AlFeSi platelets with the Mg wt%. No β-AlFeSi was observed for alloys with Mg > 1.6 wt%.

6.2.4.1 Low Mg content alloys

For low Mg content alloys, the extracted particles mainly consisted of Fe-rich intermetallics i.e. α-AlFeSi and β-AlFeSi. Fig. 6.33 shows the different features observed in these alloys.

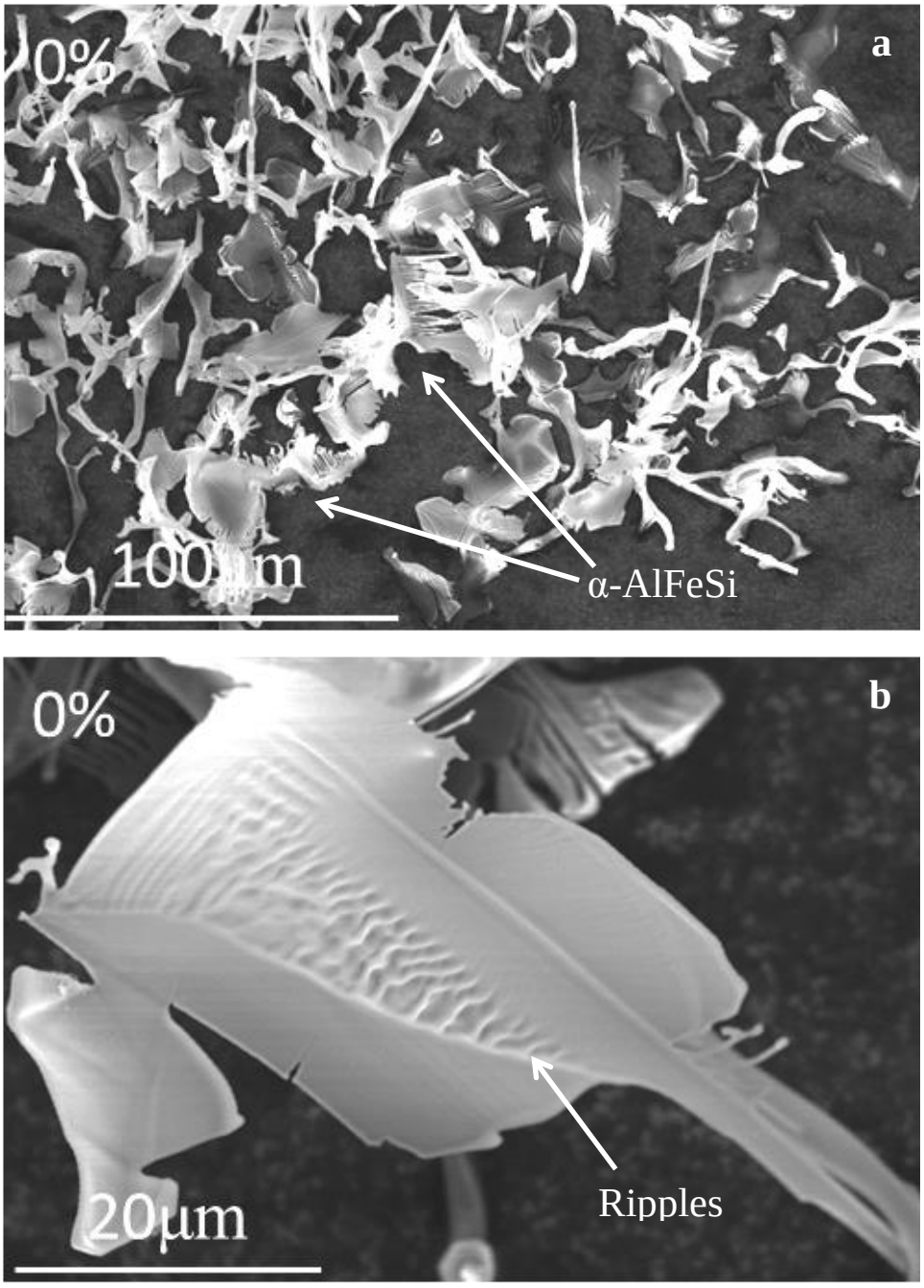

Continued overleaf…

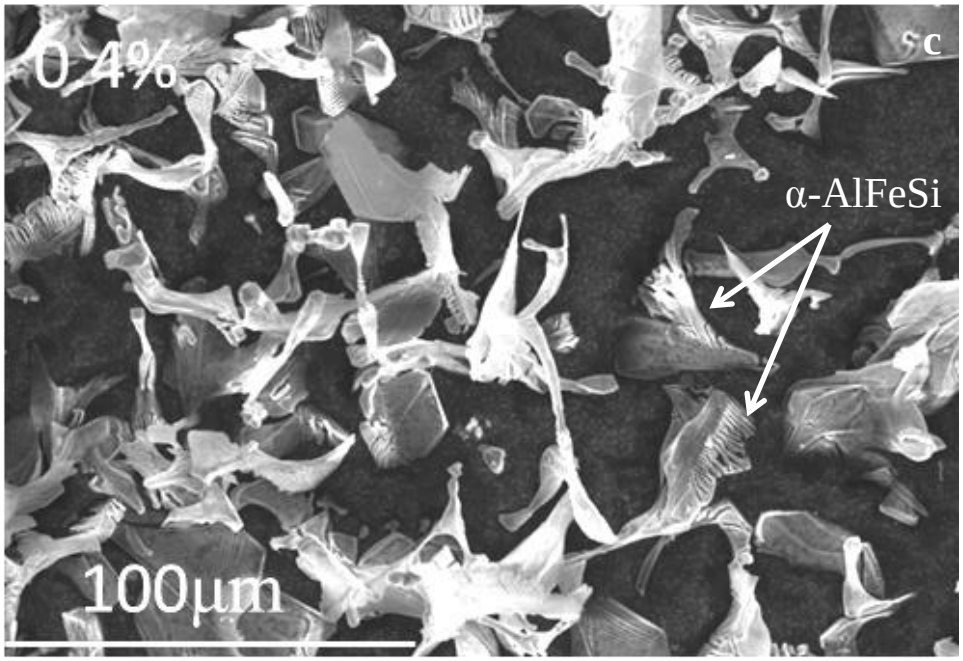

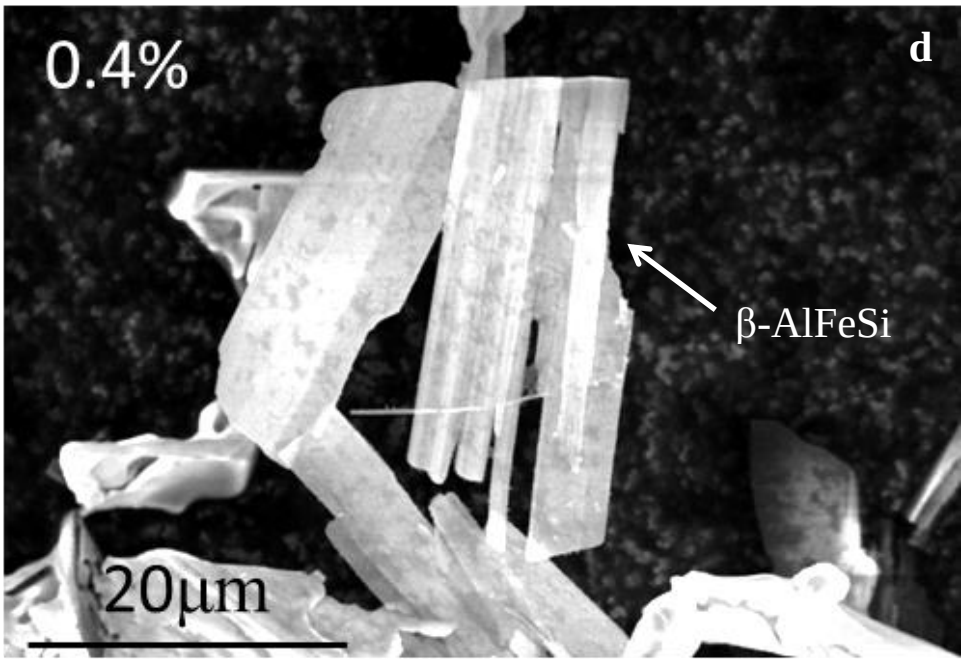

Continued overleaf…

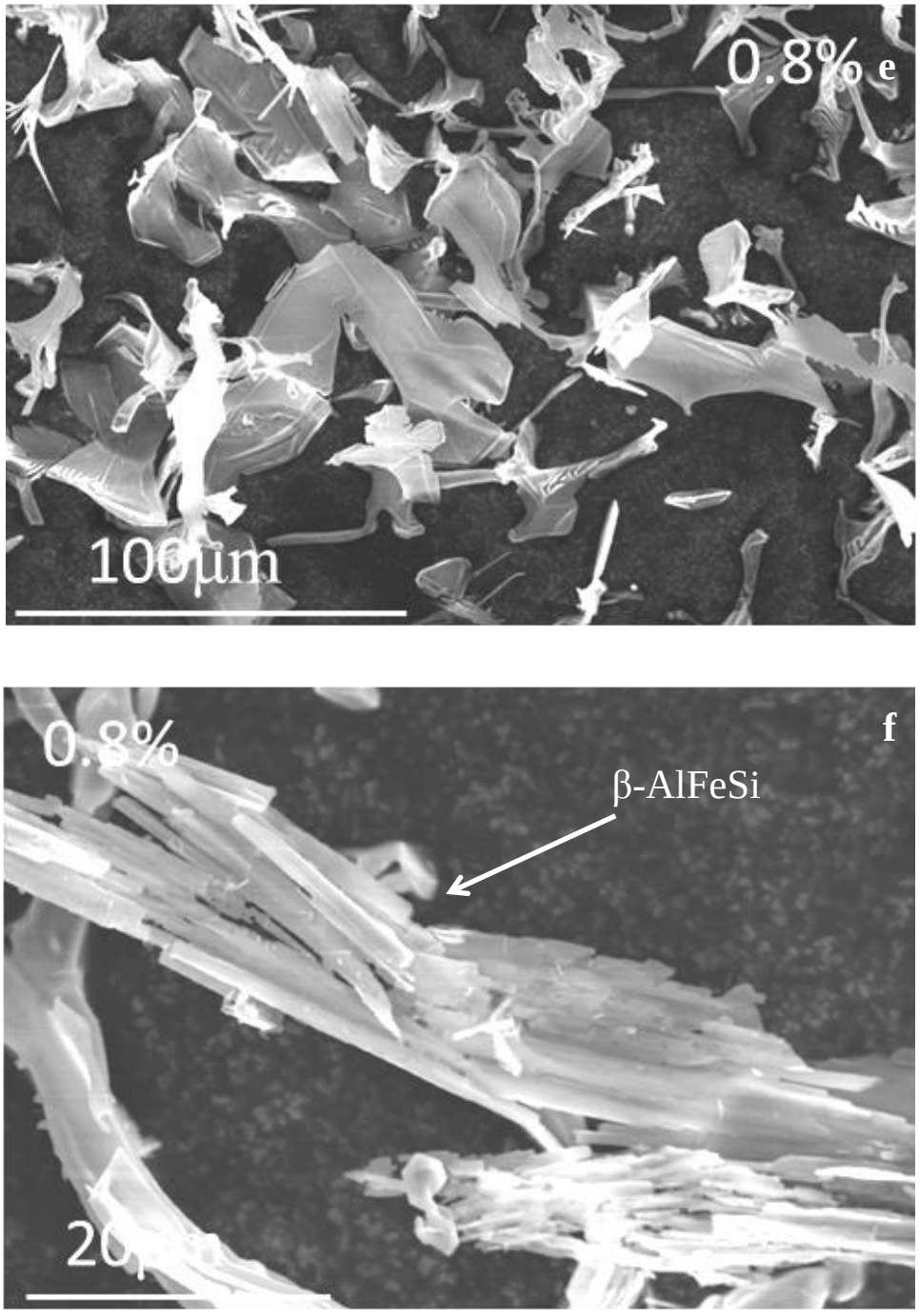

Fig. 6.33 SE micrographs showing the extracted intermetallics of a) & b) 0 wt% Mg, c) & d) 0.4 wt% Mg and e) & f) 0.8 wt% Mg.

α-AlFeSi was generally dendritic and this increased in nature with the Mg content. α-AlFeSi was commonly observed with a flower-like morphology which correlated well to the Chinese script morphology in 2D. β-AlFeSi was commonly observed as platelets/rods which can be correlated to the needle morphology in 2D as shown in Fig. 6.33d and Fig. 6.33f. $Al_{13}Fe_4$ was completely absent in these alloys but Mg_2Si was present in very small fractions in the 0.4 wt% and 0.8 wt% Mg alloys. Also, the intermetallic dendrite arm spacing (I-DAS) decreased from 1.6±0.1µm to 1.4±0.1µm as the Mg content was increased from 0 wt% to 0.8 wt%. The length of the α-AlFeSi petals increased from 35±5µm to 44±4µm and the size of the β-AlFeSi platelets increased from 26±4µm to 29±3µm with the increase in Mg content. The interconnectivity between intermetallics also increased from 93±22 µm to 128±25 µm.

6.2.4.2 Intermediate Mg content alloys

Like low Mg content alloys, α-AlFeSi and β-AlFeSi in these alloys were also observed in their regular morphologies i.e. flower-like and platelet/rod-like morphologies respectively. However, α-AlFeSi and β-AlFeSi were not observed for Mg> 1.2wt% alloys and, Mg_2Si and $Al_{13}Fe_4$ were the major phases in these alloys. Fig. 6.34 shows the different features observed in these alloys. α-AlFeSi was again generally dendritic and this increased in nature with the Mg content. I-DAS decreased further from 1.2±0.1µm to 1.1±0.1µm as the Mg content was increased. The length of the α-AlFeSi petals increased sharply to 51±6µm for 1.2 wt% Mg and the size of the β-AlFeSi platelets increased to 42±4µm in the

1.2 wt% Mg alloy. β-AlFeSi platelets or α-AlFeSi petals were rarely observed for the 1.6 wt% Mg or 2.0 wt% Mg alloys.

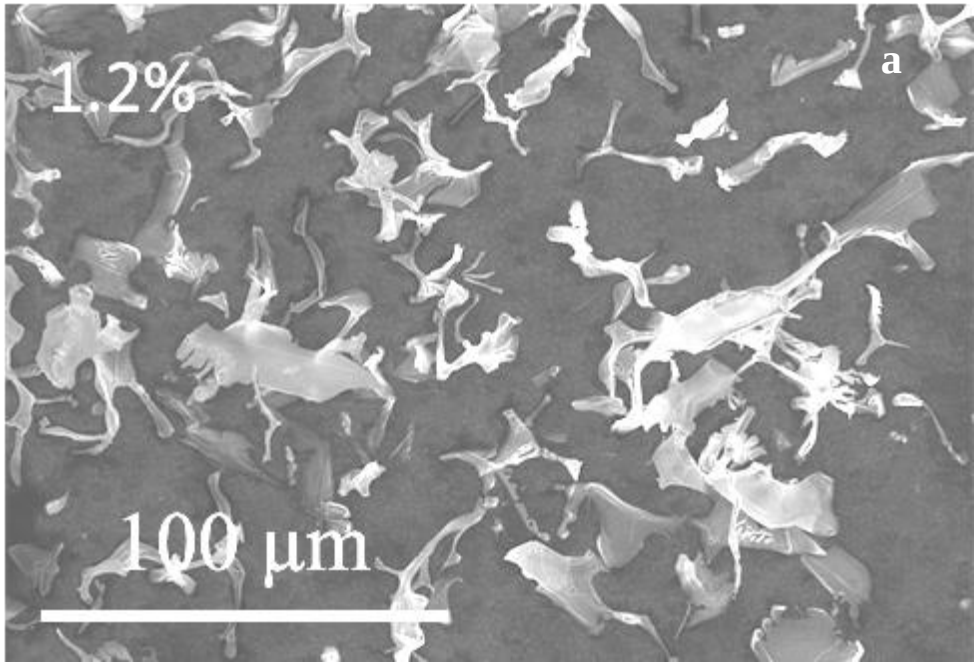

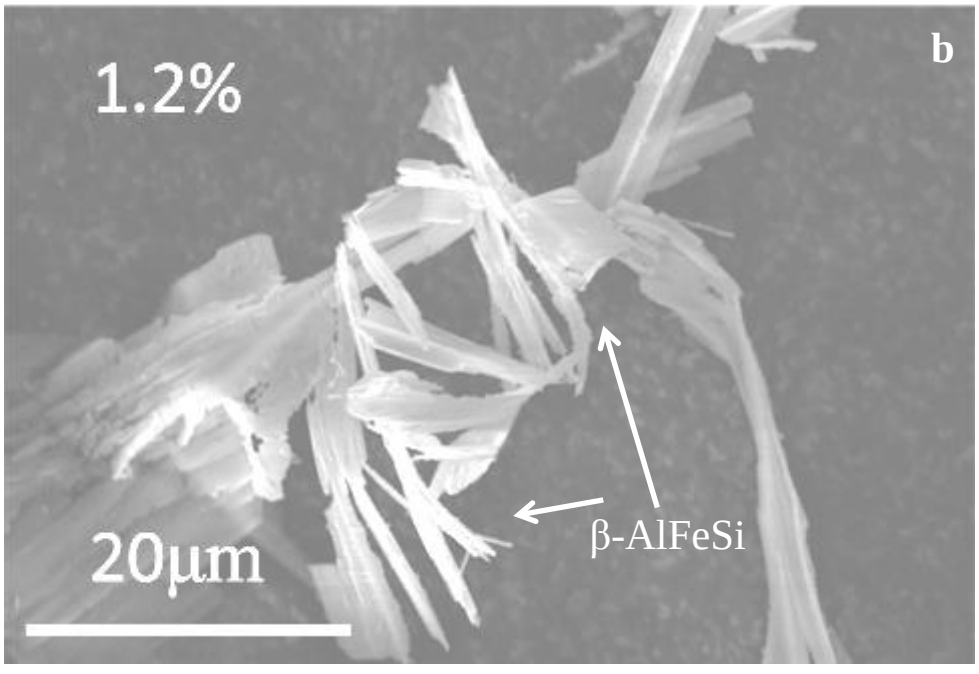

Continued overleaf…

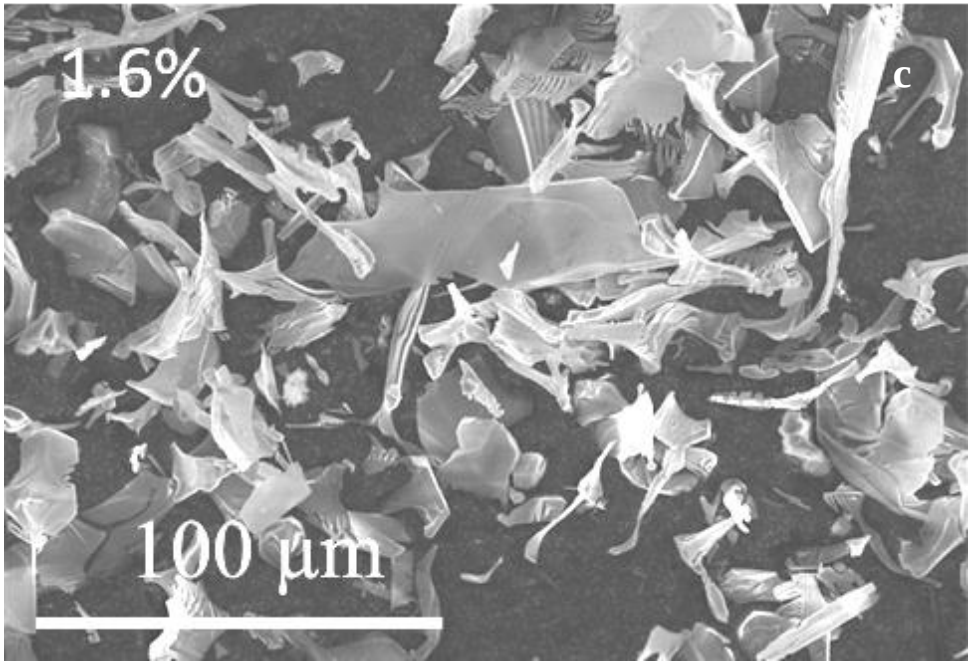

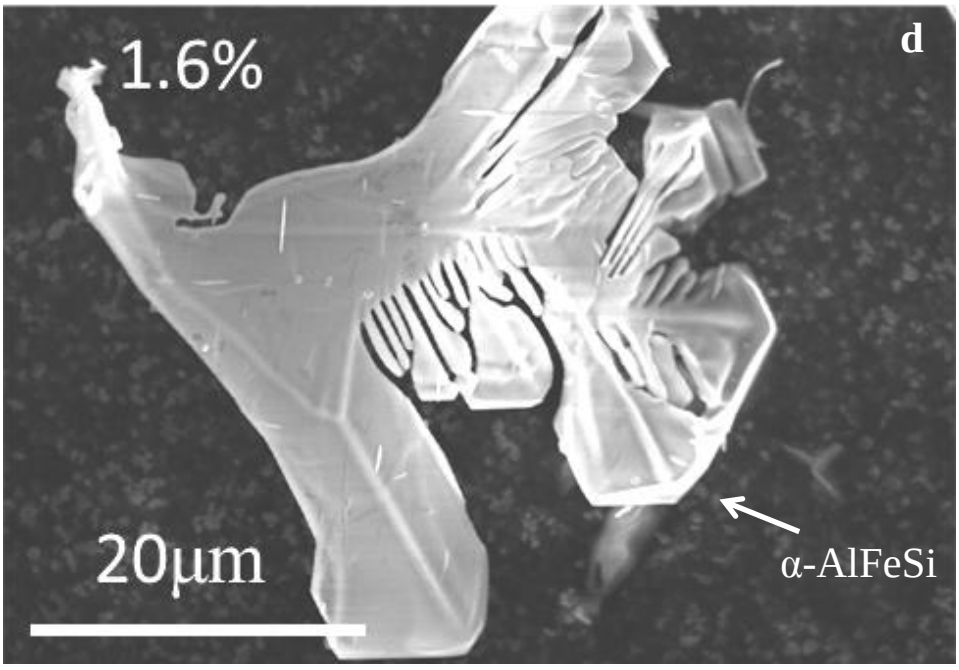

Continued overleaf…

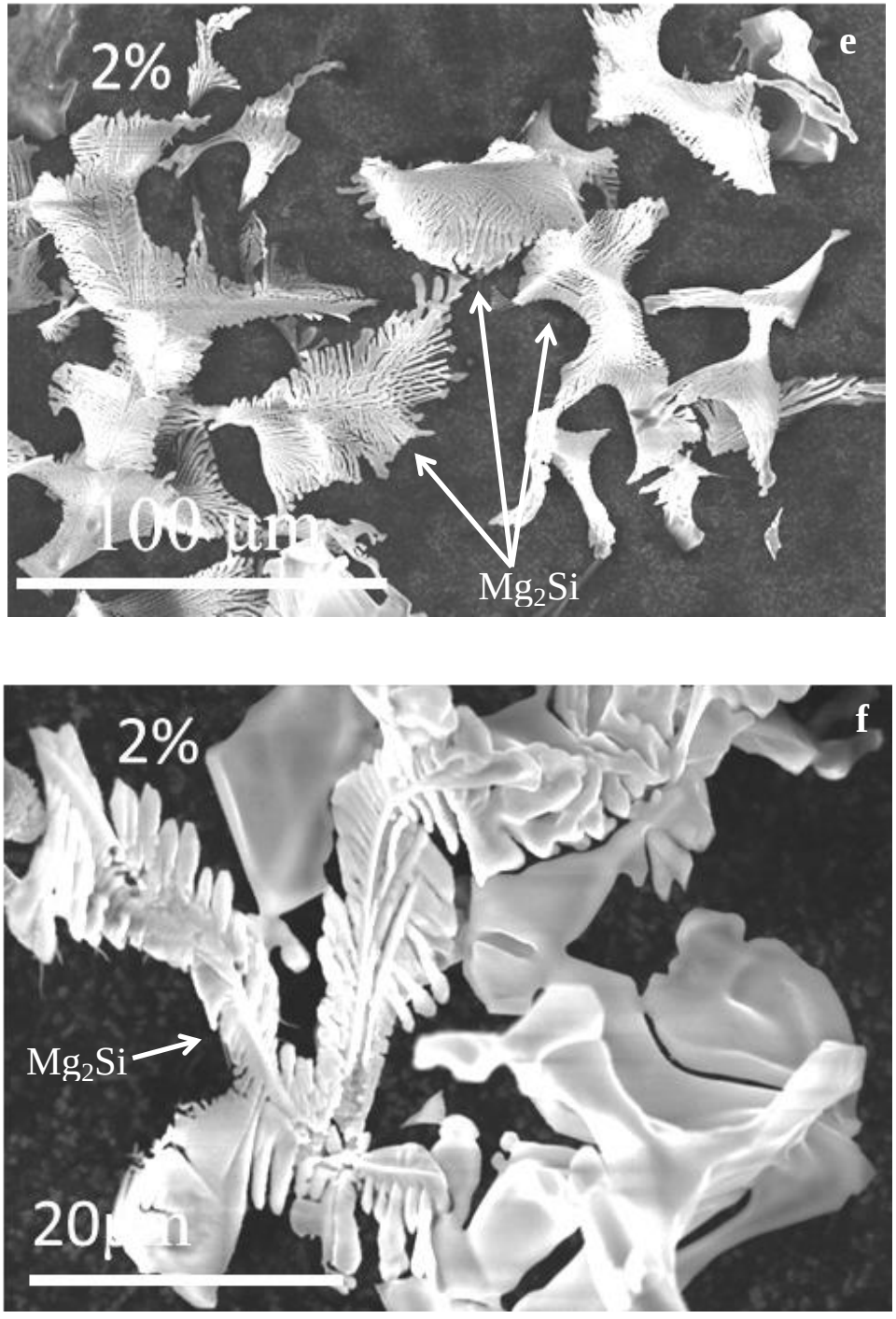

Fig. 6.34 SE micrographs showing the extracted intermetallics of a) & b) 1.2 wt% Mg, c) & d) 1.6 wt% Mg and e) & f) 2.0 wt% Mg

The interconnectivity between intermetallics also increased sharply from 152±29µm to 298±54µm. There was a step increase in the interconnectivity when Mg content was increased from 1.2 wt% to 1.6 wt%. Mg_2Si and $Al_{13}Fe_4$ phases were more frequently observed as compared to low Mg content alloys and were the dominant phases in the 1.6 wt% and 2.0 wt% Mg alloy.

6.2.4.3 High Mg content alloys

Fig. 6.35 shows the different features observed in these alloys. Like 2 wt% Mg alloy, Mg_2Si and $Al_{13}Fe_4$ were the major phases in these alloys. α-AlFeSi and β-AlFeSi were completely absent. Mg_2Si was observed with a dendritic morphology whereas $Al_{13}Fe_4$ was observed to have platelet/rod-like morphology as shown by white arrows in Fig. 6.35e.

Mg_2Si and $Al_{13}Fe_4$ were highly interconnected and the high level of interconnectivity indicates that they have grown in the direction of primary aluminium (α-Al). In general, these phases were observed to have cooperative growth features with very fine dendrites of Mg_2Si and α-AlFeSi/$Al_{13}Fe_4$ as shown in Fig. 6.36. Fig. 6.36b shows the EDX spectrum which was inconclusive as all the elements were present. This can be attributed to a combination of Mg_2Si and $Al_{13}Fe_4$. On the other hand the EDX in Fig. 6.36d was useful to mark Mg_2Si particles and $Al_{13}Fe_4$ needles more precisely.

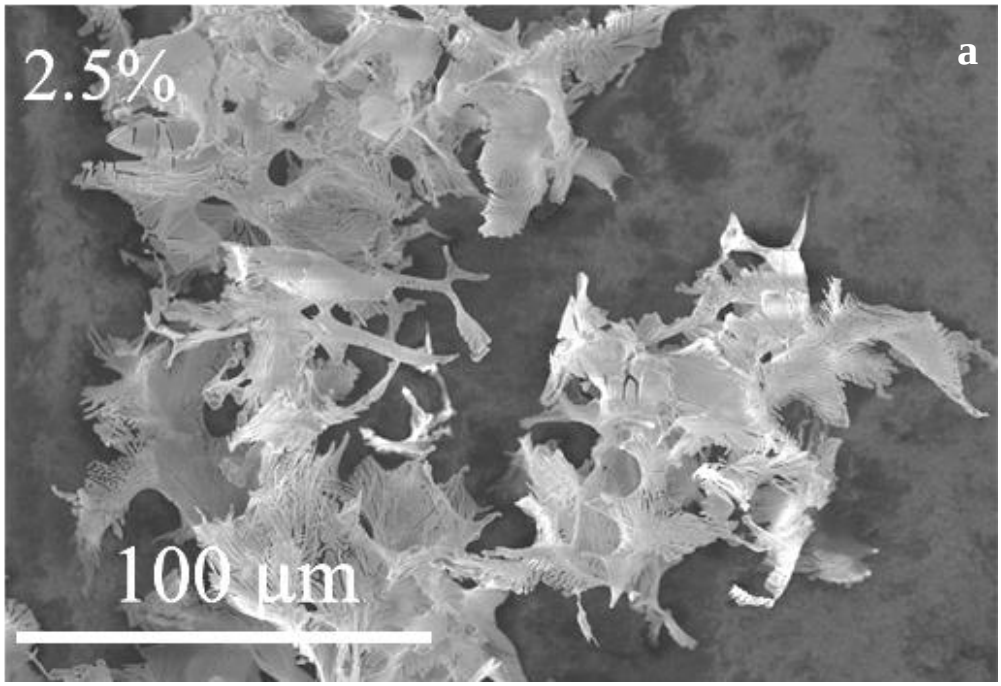

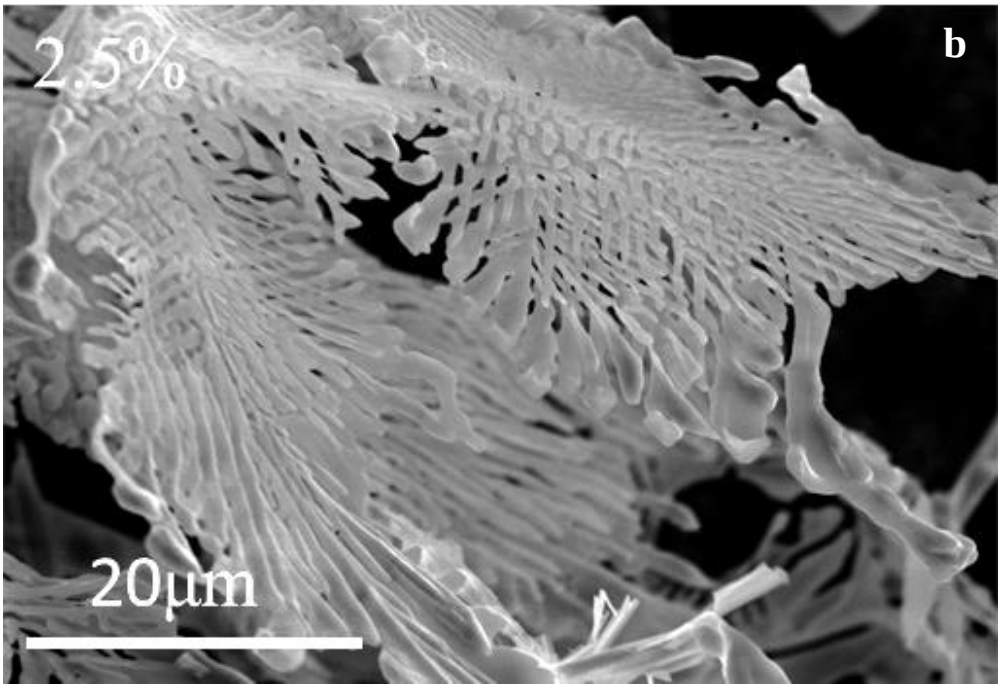

Continued overleaf…

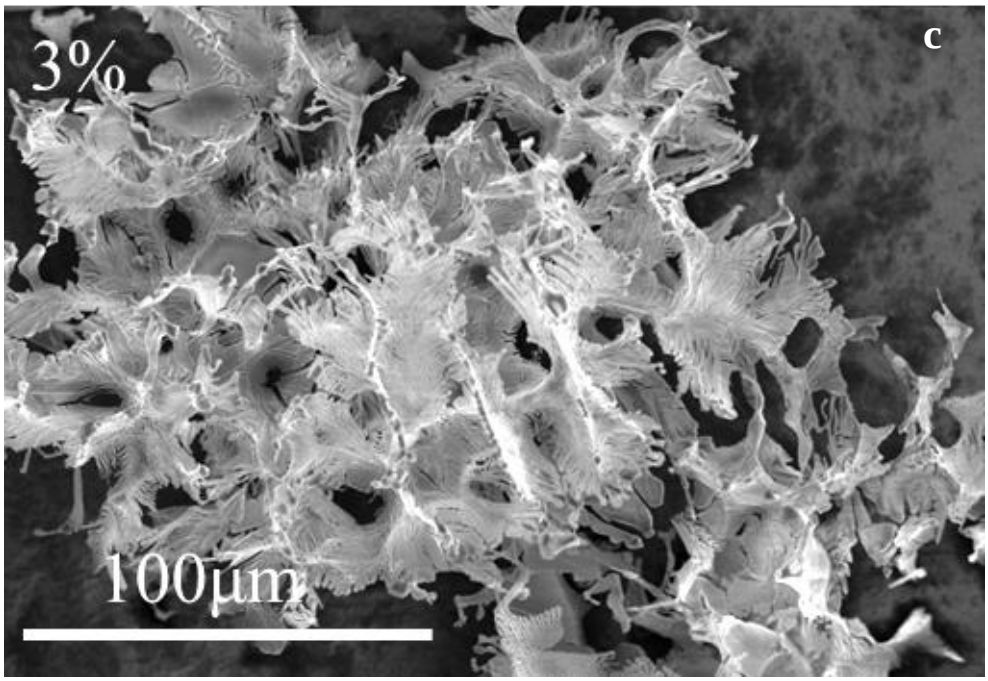

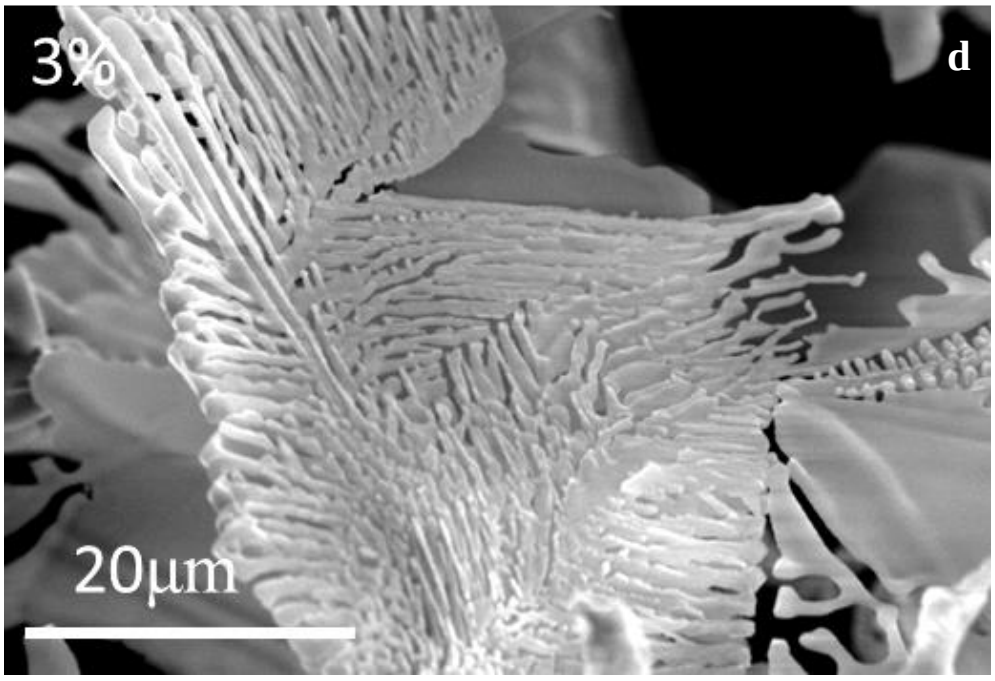

Continued overleaf…

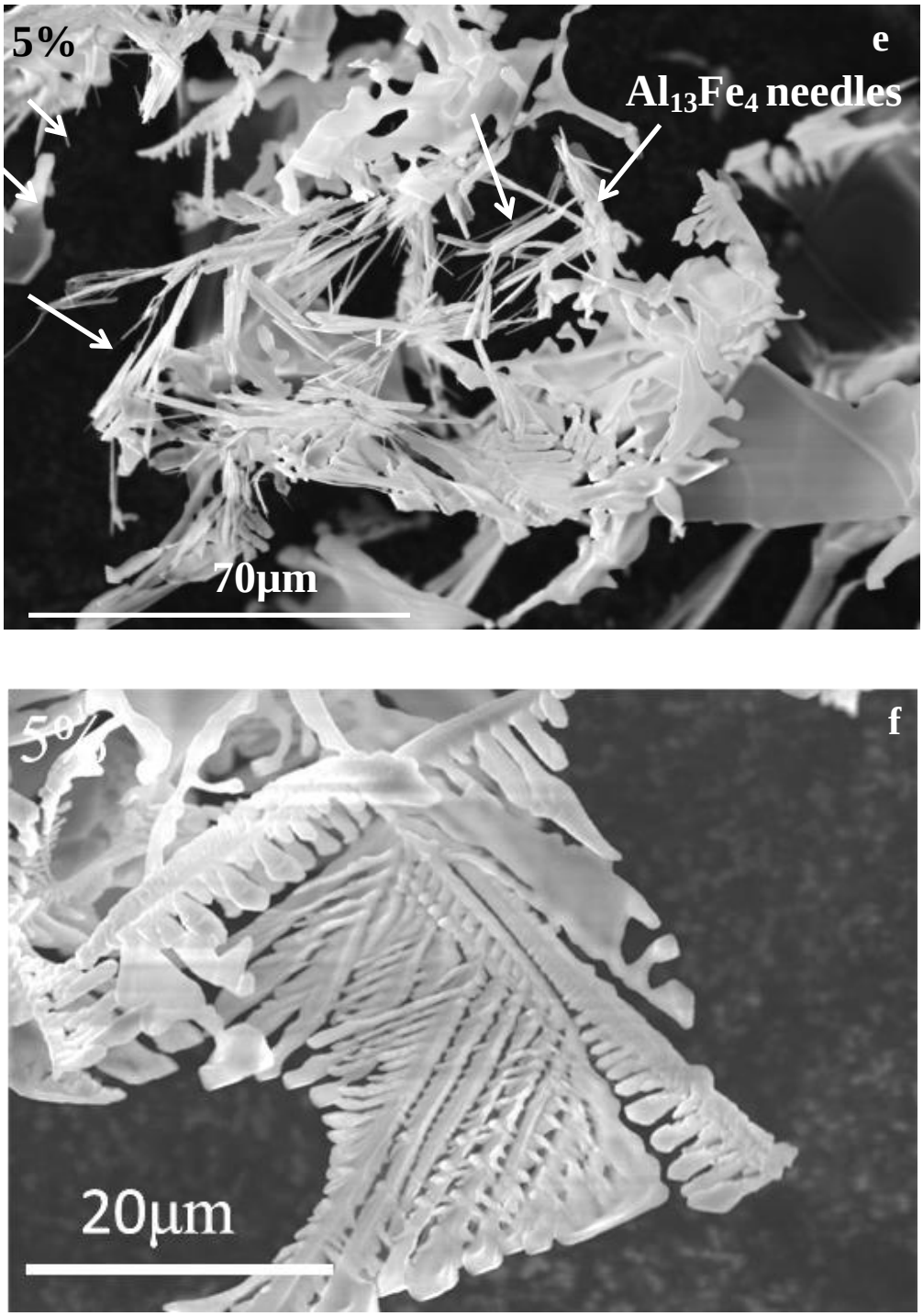

Fig 6.35 SE micrographs showing the extracted intermetallics of a) & b) 2.5 wt% Mg, c) & d) 3.0 wt% Mg and e) & f) 5.0 wt% Mg.

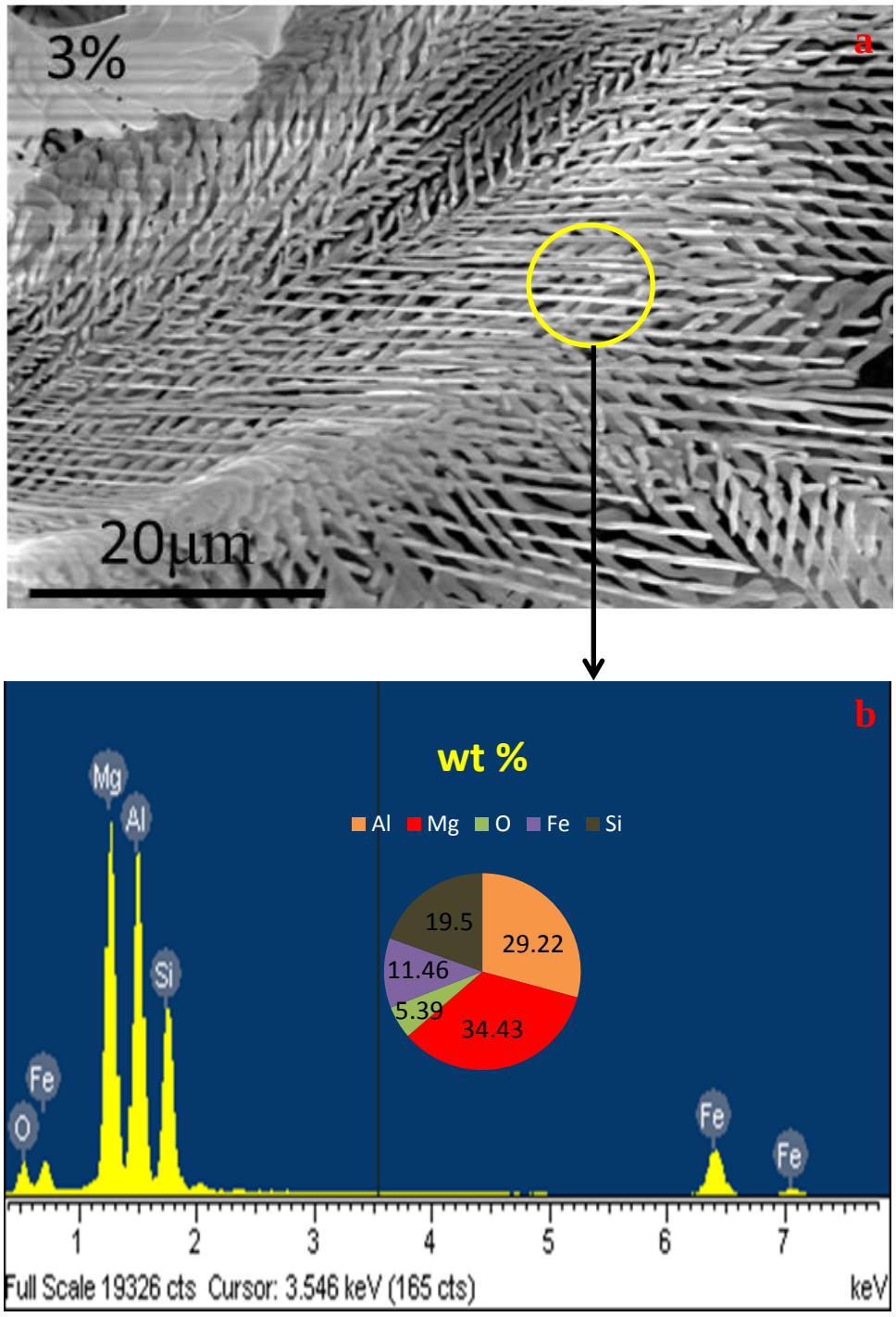

Continued overleaf…

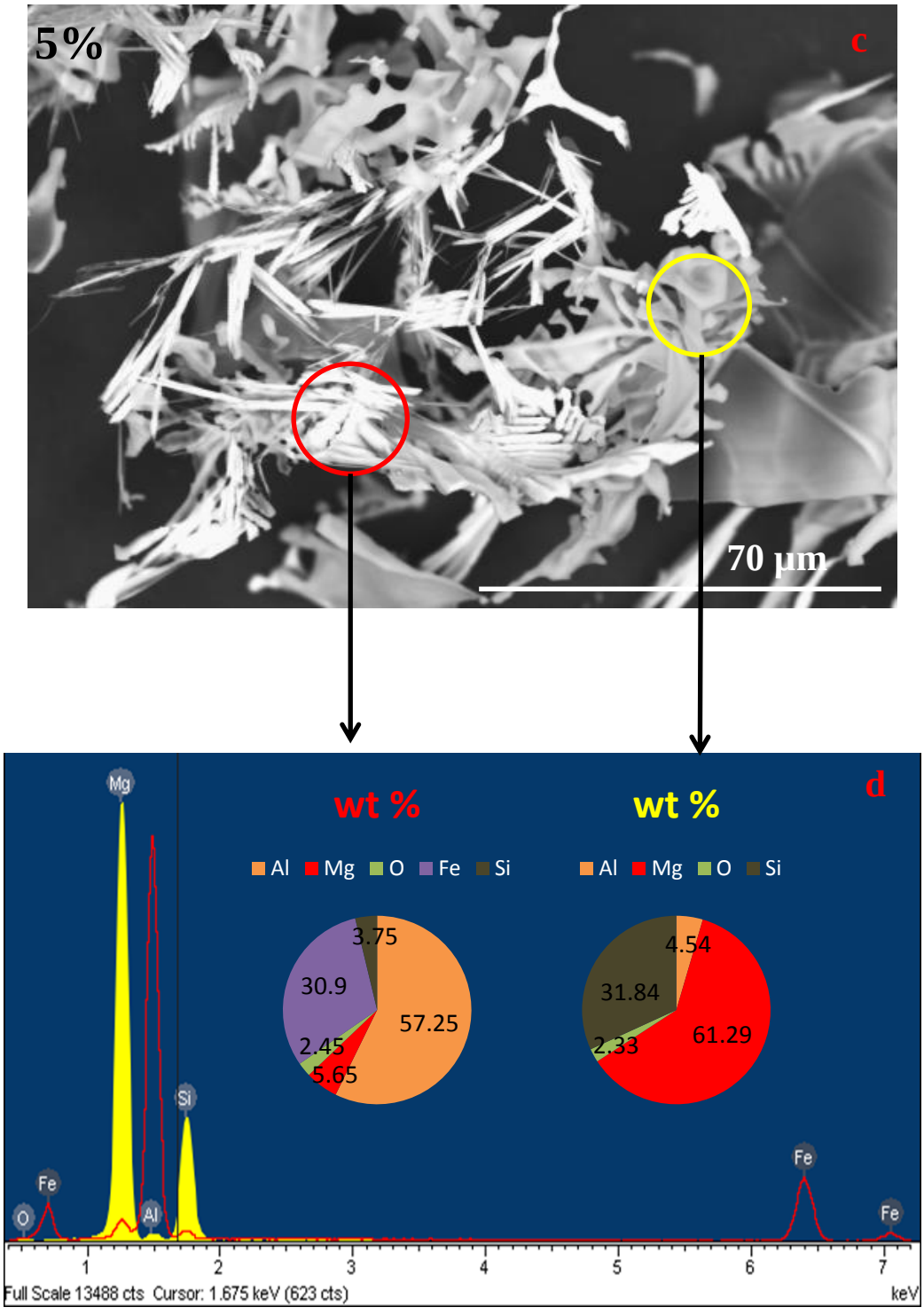

Continued overleaf…

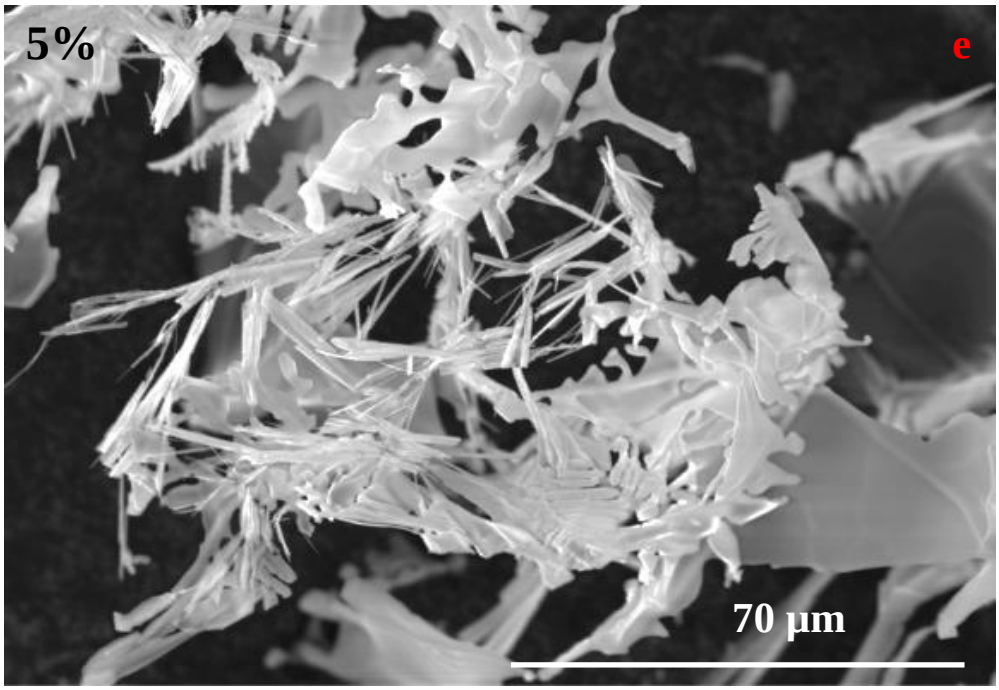

Fig 6.36 SE micrograph of extracted intermetallics showing a) fine dendritic structure of 3.0 wt% Mg alloy, b) EDX spectrum showing the composition of the fine dendrites, c) BSE image showing Fe-rich regions (bright sections), d) EDX spectrum confirming the presence of $Al_{13}Fe_4$ and Mg_2Si and e) SE micrograph of same area (as image c)) showing $Al_{13}Fe_4$ and Mg_2Si in 5 wt% Mg alloy.

The extracted particles from the 3.0 wt% and 5.0 wt% Mg alloys were highly interconnected and had very similar morphologies with few isolated Mg_2Si and $Al_{13}Fe_4$ particles, which was not the case with other alloys. Also, the I-DAS measured in the 2.5 wt% Mg alloy reduced to 1±0.1µm, however the reduction in I-DAS from 3.0 wt% to 5.0 wt% was negligible and within error limit i.e. from 0.9±0.1µm in both the alloys, which shows that addition of further Mg will not have a significant effect on intermetallic morphology. A number of Mg_2Si

particles were found to be associated with MgO. The association of Mg_2Si particles with MgO particles is discussed in detail in section 6.4.2.2.

6.2.5 X-Ray Diffraction

Fig. 6.37a shows the XRD patterns from the extracted particles from the samples with different Mg contents. The major peaks observed belonged to α-AlFeSi, β-AlFeSi, Mg_2Si and $Al_{13}Fe_4$. Reference patterns using JCPDS data for various compounds are also shown along with the XRD patterns to ease the peak analysis as a few of them were overlapping. Also, Fig. 6.37b and 6.37c shows zoom in XRD patterns to clearly indicate the peaks. Al_2O_3, MgO and spinel were present in very small amount which could not be detected by XRD. Regression analysis was used to calculate the relative weight fractions of α-AlFeSi and β-AlFeSi (100 - α-AlFeSi weight fraction) **(Lui, 05)**. Fig. 6.30 shows the variation of relative weight fraction of α-AlFeSi with the change in Mg wt%.

6.2.5.1 Low Mg content alloys

High α-AlFeSi (44.15^o, 42^o, 43.01^o, 22.22^o, 36.5^o, 45.9^o, 26.4^o) and β-AlFeSi (17.1^o, 20.89^o, 28.92^o, 34.99^o, 24.1^o, 46.63^o) peaks were observed in all the low Mg content alloys which indicated that they were the two dominant intermetallic phase present, which can be correlated with SEM analysis. For 0 wt% Mg, no peaks were observed for Mg_2Si due to the absence of Mg. On the other hand, small peaks of Mg_2Si (40.13^o, 24.3^o) were observed for 0.4 wt% Mg and

0.8 wt% Mg. No peaks of $Al_{13}Fe_4$ were present in these alloys. The relative weight fraction of α-AlFeSi increased marginally with increase in Mg content however not significant taking into account an error of ±10%. The relative weight fraction of α-AlFeSi calculated was 70%, 65% and 75% for 0 wt% Mg, 0.4 wt% Mg and 0.8 wt% Mg respectively which is within the calculation error limit.

6.2.5.2 Intermediate Mg content alloys

Majority of the peaks belonged to α-AlFeSi (44.15^o, 42^o, 43.01^o, 22.22^o, 36.5^o, 45.9^o, 26.4^o) whereas only few β-AlFeSi (17.1^o, 46.63^o) peaks were observed in the intermediate Mg content alloys. Both α-AlFeSi and β-AlFeSi were not as dominant as in the low Mg content alloys. Mg_2Si (40.13^o, 24.3^o, 47.43^o, 58.04^o, 63.83^o) was the dominant intermetallic phase present, as was observed during SEM analysis. For 1.2 wt% Mg, significant peaks were observed for Mg_2Si, α-AlFeSi and β-AlFeSi phases. Similar feature was observed in 1.6 wt% Mg alloy, where high peaks were observed for Mg_2Si and α-AlFeSi but not for β-AlFeSi phases, Mg_2Si being the dominant one. It is interesting to note that the dominance of Mg_2Si increases with the increase in Mg content. In the XRD graph of 2.0 wt% Mg, Mg_2Si was relatively more dominant than α-AlFeSi. No peaks for β-AlFeSi phase were observed for 2.0 wt% Mg. Small peak of $Al_{13}Fe_4$ (43.15^o) was also observed in 2 wt% Mg alloy and not in 1.2 wt% or 1.6 wt% alloys. No peaks of oxides were observed due to their small fraction and XRD detection limit. The relative weight fraction of α-AlFeSi increased with the Mg

content. The relative weight fraction of α-AlFeSi for intermediate Mg content alloys was calculated to be 80% and 85% for 1.2 wt% Mg and 1.6 wt% Mg respectively, which is a slight increase as compared to the low Mg content alloys but within the error limit of ±10%.

6.2.5.3 High Mg content alloys

Few α-AlFeSi (44.15^o, 42^o, 22.22^o) peaks were observed in the high Mg content alloys and were much smaller as compared to other Mg content alloys. No β-AlFeSi peaks were observed for these alloys. Mg_2Si (40.13^o, 24.3^o, 47.43^o, 58.04^o, 63.83^o) and $Al_{13}Fe_4$ (25.1^o, 27.26^o, 43.15^o) were the major phases present, as was observed during SEM analysis. For 2.5 wt% Mg, significantly high peaks were observed for Mg_2Si. Small peaks of α-AlFeSi and $Al_{13}Fe_4$ were also observed. Similar features were observed in 3.0 wt% Mg and 5.0 wt% Mg alloys, where Mg_2Si was the dominant phase. Small peaks of α-AlFeSi and $Al_{13}Fe_4$ were also observed. The relative weight fraction of α-AlFeSi decreased with the increase in Mg content. The relative weight fraction of α-AlFeSi was similar to other alloys i.e. 85%, 80% and 70% for the 2.5 wt% Mg, 3.0 wt% Mg and 5.0 wt% Mg alloys respectively. However it is important to note that no β-AlFeSi peaks were observed for these alloys so the calculations might have higher error.

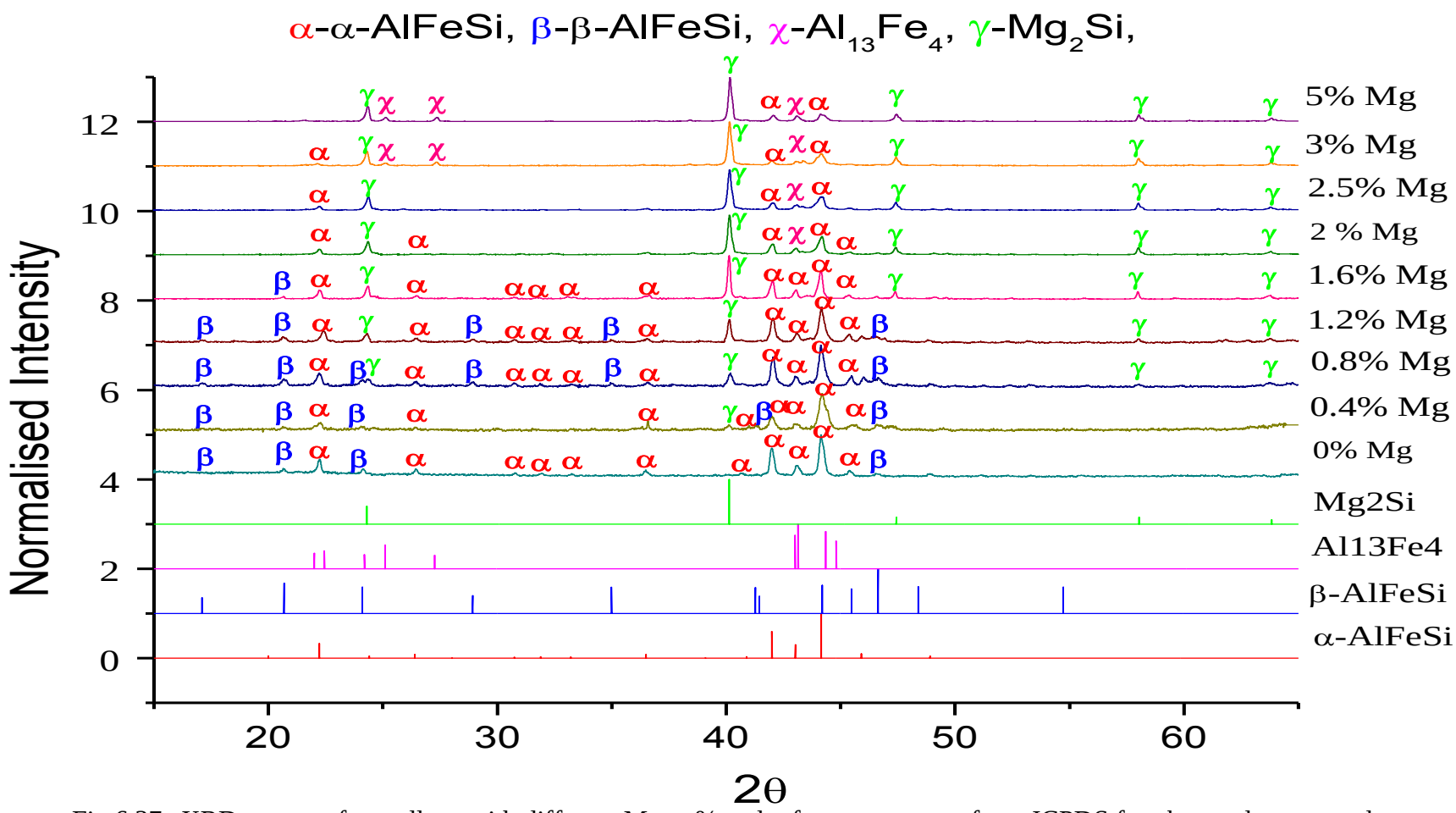

Fig 6.37a XRD patterns from alloys with different Mg wt% and reference patterns from JCPDS for observed compounds.

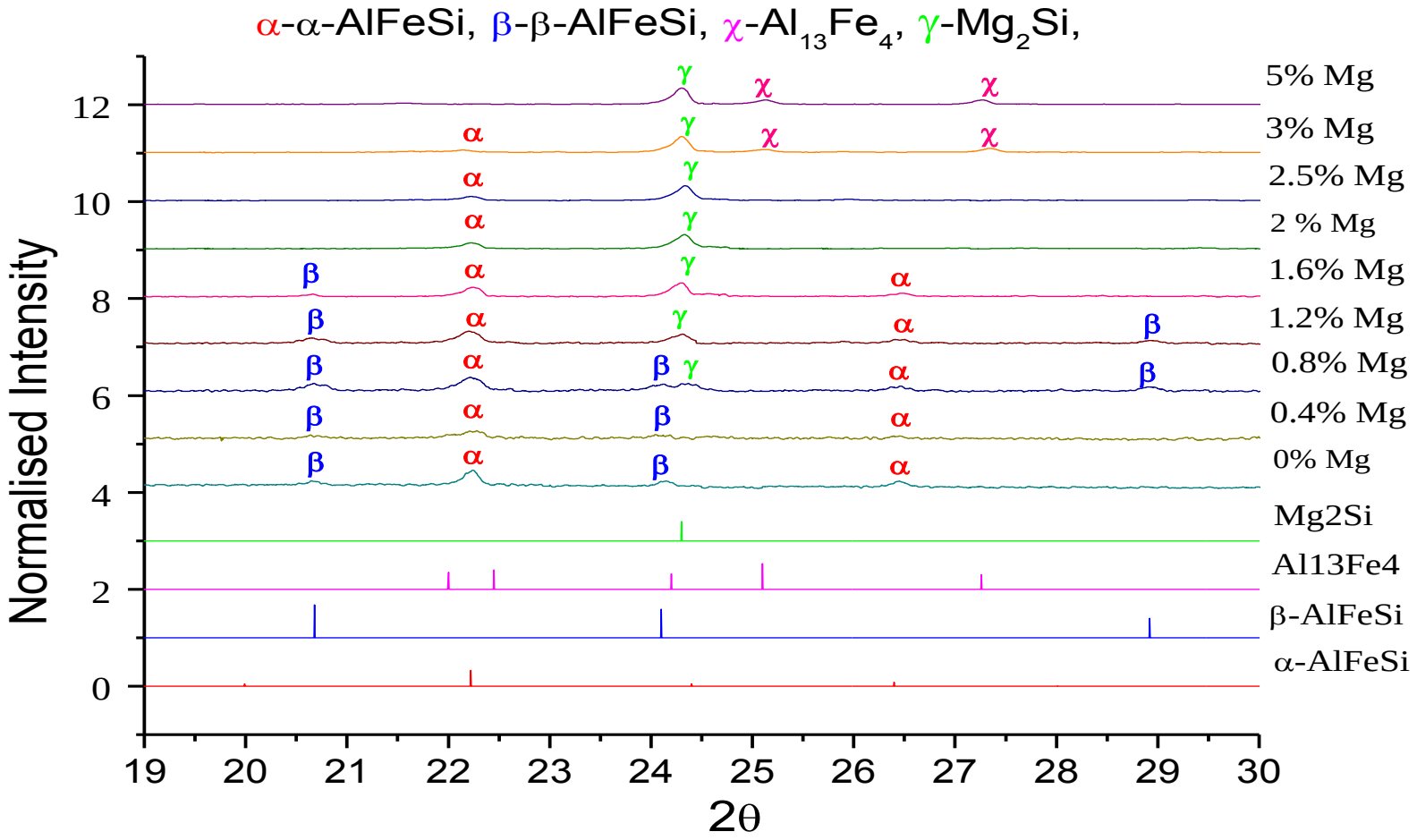

Fig 6.37b Zoom in XRD patterns from alloys with different Mg wt% and reference patterns for 2θ=20 to 2θ=30.

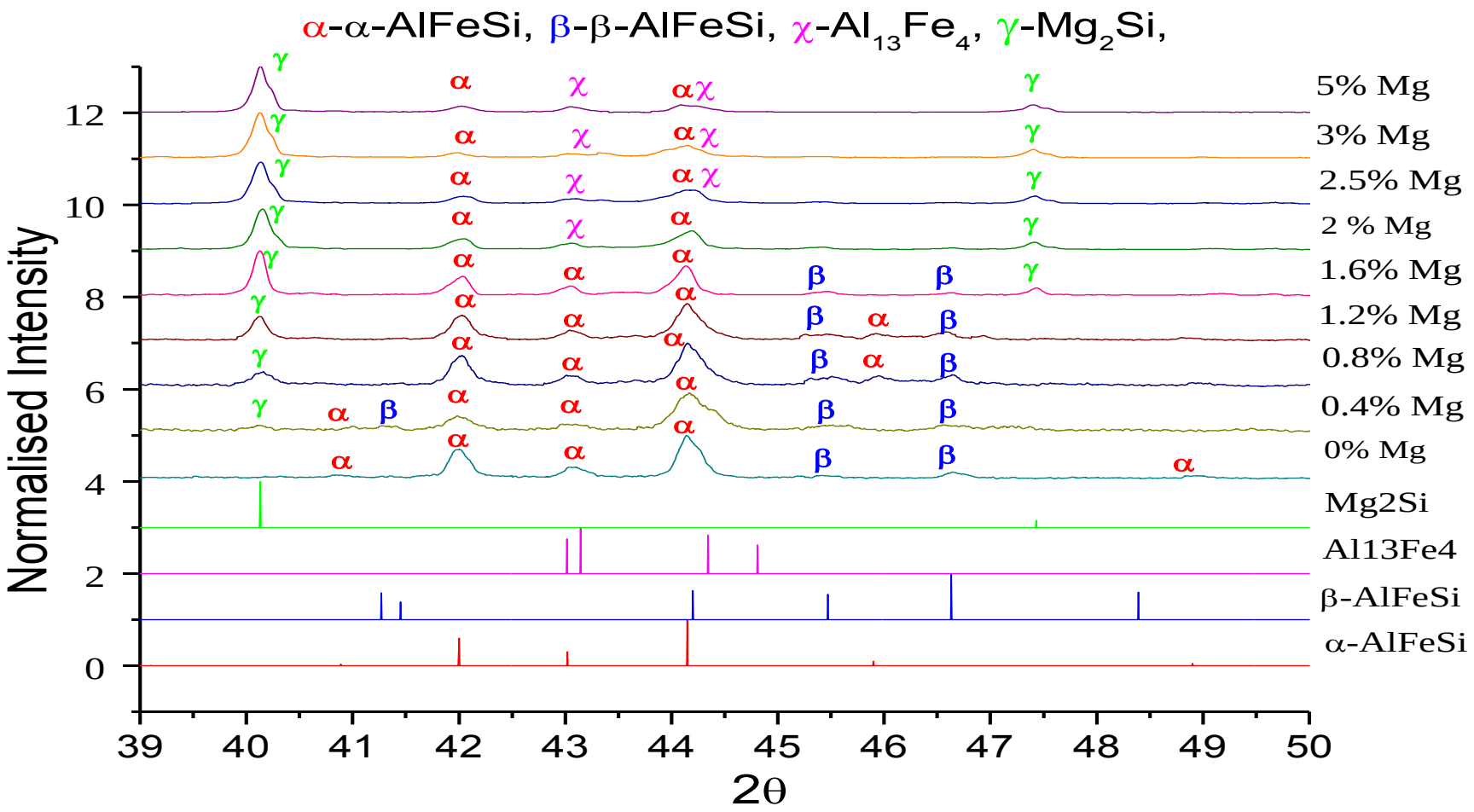

Fig 6.37c Zoom in XRD patterns from alloys with different Mg wt% and reference patterns for 2θ=40 to 2θ=50.

Table 6.3 Summary of the 2D and 3D morphologies of major phases observed in TP1 cast alloys

Phase	2D morphology	3D morphology
α-AlFeSi	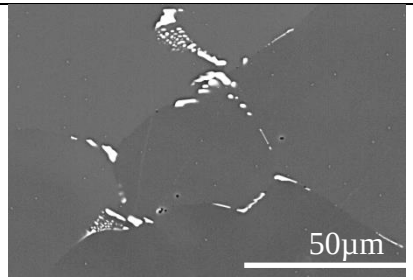	
β-AlFeSi	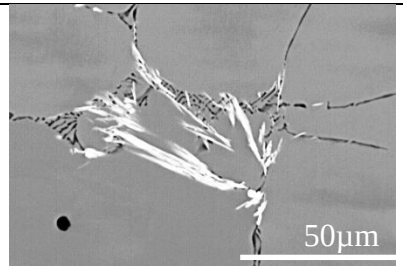	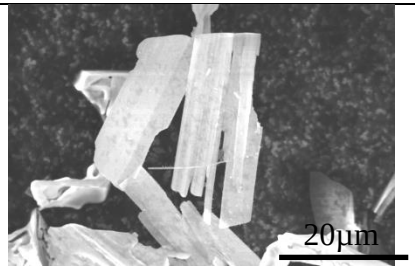
Mg_2Si	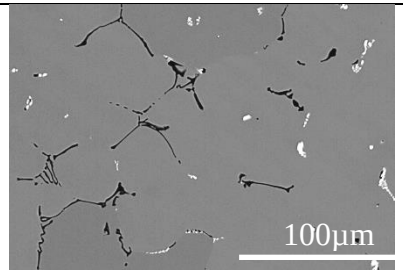	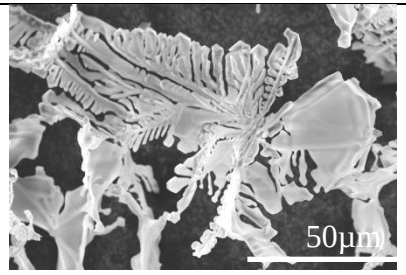

6.3 Influence of Mg on oxide and oxide bi-film formation

The negative effect of oxides on the mechanical properties of Al alloys is well known **(Lessiter, 93), (Doutre et al., 85) & (Cao, 01)**. However, the effect of oxides on intermetallics requires in-depth investigation to reach any conclusion. In order to do so, it is very important to correlate both the 2D and 3D morphology of oxides in the melt.

6.3.1 Oxide bi-films

Spinel was observed more frequently in the low Mg content alloys (0.1 wt% and 0.4 wt%), in comparison to high Mg content alloys (1.3 wt% and 5.1 wt%) where MgO was dominant. Mixed clusters of MgO and spinel were also a common feature in the 0.4% and 1.3% Mg alloys. This is because as the Mg content was increased, the oxide phase in equilibrium with the liquid changes from Al_2O_3 (0% Mg) to $MgAl_2O_4$ (≤1% Mg) and finally to MgO (>1% Mg) **(Cochran et al., 77), (Field et al., 87)** and **(Shimizu et al., 96)**. AlFeSi intermetallics were also observed underneath the layer of oxides as confirmed by backscatter images, which supports the theory of nucleation of intermetallics on the wet surface of the oxide bi-film. Nucleation of β-AlFeSi on oxide bi-films was suggested in previous studies **(Narayanan et al., 94)** and **(Samuel et al., 01)**, however only small quantities of β-AlFeSi phase were detected by XRD.

Furthermore, as different oxides have different nucleating capabilities, the nature of the oxide bi-film formed in these alloys may not be compatible for the promotion of β-AlFeSi. The relative wt % of α-AlFeSi and β-AlFeSi was calculated using regression analysis and α-AlFeSi was found to be present at three times the amount of β-AlFeSi in low Mg content alloys and four times for high Mg contents. Other researchers **(Narayan et al., 95)** have proposed the formation of β-AlFeSi on oxide bi-films (for Al-6Si-3.2Cu-0.3Mg-0.15Fe alloy), whereas α-AlFeSi was observed to dominate over β-AlFeSi in this study as the Mg content / oxide bi-films increased (for Mg<1.2 wt%). However, this might be due to the high Si content which stabilises the β-AlFeSi phase **(Belov et al., 05)**. Apart from the oxides, many cracks were also observed frequently associated with the oxides particularly for Mg>1.2 wt% alloys.

The width of these cracks was proposed to be the distance between the two dry surfaces of an oxide bi-film **(Cao et al., 03)**. EDX analysis also confirmed them to be oxides. Some oxide bi-films (cracks) were also observed passing through the middle of the Fe-rich intermetallics. As we increased the Mg content in the alloy, oxide bi-films were found to be the dominant feature along with the lather-like structure of MgO. The lather-like structure of MgO was readily found on the edges of oxide bi-films. This may be because MgO is the dominant phase on the wet surface of the oxide bi-film for high Mg content (>1%) **(Field et al., 87)** and **(Huang et al., 00)**.

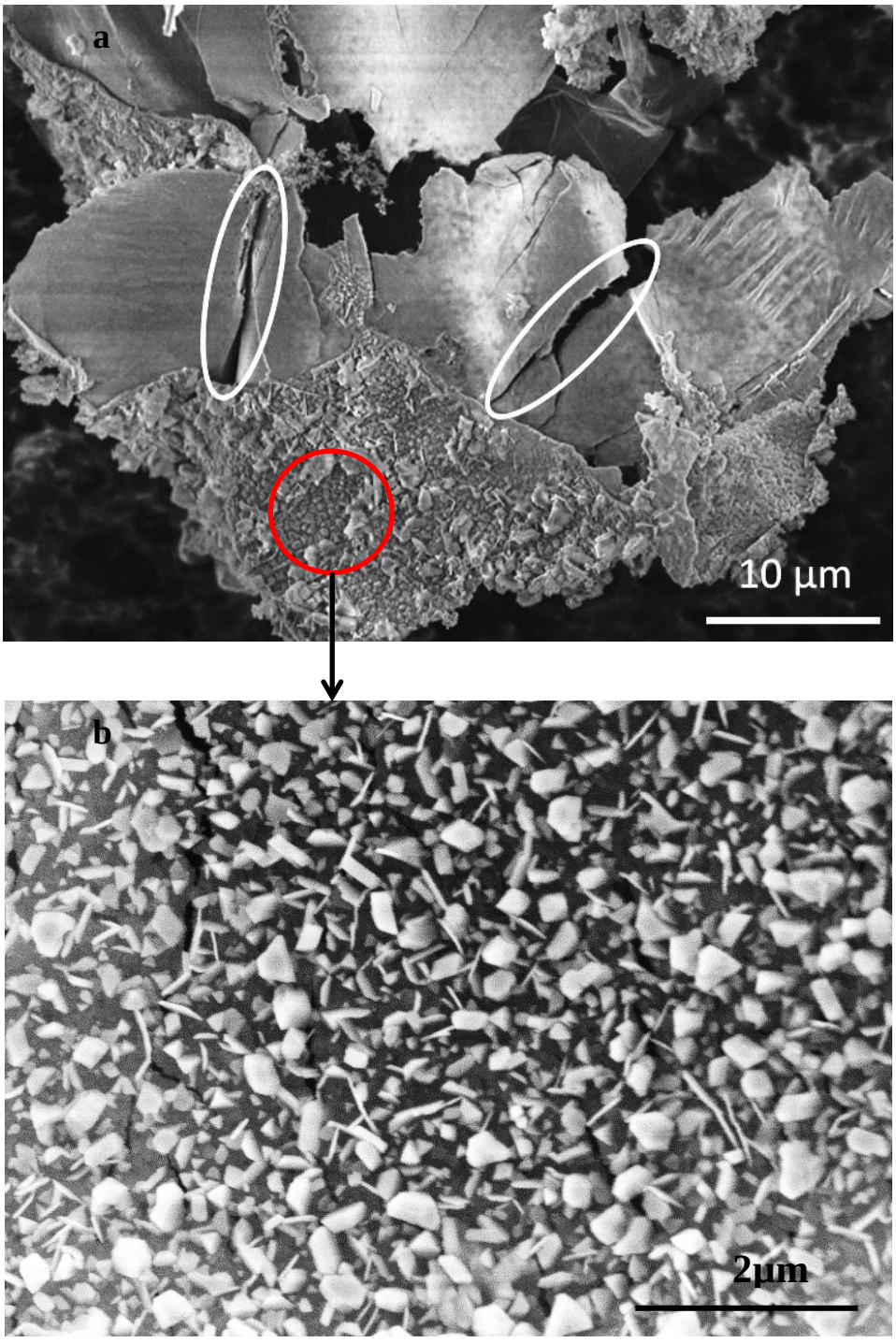

Fig 6.38 SE micrographs showing a) dry and wet surfaces of the oxide bi-film with the presence of crack-like features on the dry surface and b) magnified image of the wet surface showing the faceted and needle-like particles for 0.1 wt% Mg.

On analysing the extracted particles, the dry and wet surfaces of the oxide bi-film were observed. The oxide bi-films stretch from ~70-100μm in length and 3-5μm in thickness. A number of gaps were also observed as shown in Fig. 6.38a. These gaps appear as crack-like features which in reality are distances between two dry surfaces (facing each other) of the oxide bi-film which correspond to the thickness of the oxide film.

However, these gaps could also correspond to the actual cracks present in the oxide bi-film as observed in 2D micrographs. On a closer examination of the wet surface, it was observed that it has a layer of mixture of spinel (faceted) and Al_2O_3 (needle-like) particles (see Fig. 6.38b). The presence of cracks on the dry surface of the oxide bi-film is a good indicator of the strain generated from oxide particle attachment and growth **(Kubaschewski et al., 53)** and **(Gulbransen, 47)**. Also, the Mg oxides that attached to the wet surface of the oxide bi-film changed from spinel to spinel and MgO, and finally to only MgO as the Mg content was increased.

From the calculated equilibrium phase diagram for Al-Mg-O system **(Salas et al., 95)**, it can be concluded that spinel formation is favourable for low Mg content (Mg<1wt%) and MgO formation is preferred for high Mg content (Mg>1wt%). The other common feature associated with the oxide bi-film was the presence of ripples on the dry surface of the oxide bi-film along with a crack

propagating through it as shown in Fig. 6.10d. The ripples could be formed due to the strain developed by the non-uniform attachment of spinel particles on the wet surface of the oxide bi-film at higher temperature when the bi-film is relatively ductile, whereas the crack could be due to the dominance of the brittle nature of the oxide bi-film as the film thickness grows over time, together with the overloading of the spinel particles on the wet surface as the temperature is reduced (Fig. 6.10b, Fig. 6.38a, and Fig. 6.38b).

Two main types of oxide dominated in this study because of their thermodynamic stability i.e. MgO and spinel. Earlier studies **(Simensen et al., 81)** also observed MgO and spinel as the dominant oxides for lower Mg content alloys. γ-Al_2O_3 was also observed but only as a minor phase due to the shift in equilibrium towards Mg-rich oxides.

Previous studies on Al-Mg alloys have shown that oxidation of Mg alloys forms MgO before spinel. However, if the melt is held for sufficient time, MgO is converted to spinel as it has greater thermodynamic stability **(Haginoya et al., 83)**. However, it has also been demonstrated that MgO is much more favourable over spinel for Mg > 2.5 wt% due to its higher thermodynamic stability **(Kim et al., 96) (Xie et al., 05).** For low Mg wt% alloys, the majority of the MgO was converted to spinel. As a result, the MgO layer initially formed was broken during the holding time. Hence, MgO particles

were nanoscale in size and had spherical morphology due to minimization of the surface energy.

The melt is initially covered with amorphous aluminium oxide layer. Mg directly reacts with the oxygen diffused through this layer to form MgO as well as by reducing aluminium oxide **(Gulbransen, 47)**. The growth of the MgO nanoparticles formed causes stress due to the difference in thermal expansion coefficients at temperatures above 450^{o}C **(Doherty et al., 63)** and **(Kofstad, 66)**. As a result, microcracks are created in the continuous aluminium oxide film **(Shimizu et al., 98)** and **(Zayan, 90)**. As the Mg content is increased, more nanoscale MgO particles are formed. Hence more microcracks are created which result in more space for oxygen to diffuse through the aluminium oxide layer. The increase in the oxygen diffusion rate results in the formation of more MgO nanoparticles rather than the growth of previous ones. As a result, the size of MgO nanoparticles decreased with the increase in Mg content.

Spinel was observed frequently on the wet surface of the oxide bi-films for low Mg content alloys (Mg<1 wt%), whereas a mixture of spinel and MgO or only MgO was observed for high Mg content alloys (Mg>1 wt%). This is because as the Mg content increases, the segregation of Mg metal at the surface of the liquid increases **(Haginoya et al., 83)**. Hence, the tendency to form MgO increases.

On one hand spinel was more frequently observed as individual particles with faceted morphology, whereas MgO was always found in clusters with spherical morphology. This may be related to their size, as the nanoscale size of MgO may be responsible for their existence in clusters so that they can reduce the surface energy, whereas the spinel was a few microns in size. The average diameter of an oxide cluster for 0.1 wt% Mg sample was 45µm with standard deviation of 11µm, whereas for 0.5 wt% Mg sample it was 59µm with a standard deviation of 17µm. The increase in cluster size can be explained by the reduction in size of the MgO particles i.e. as the size of MgO particles reduced their tendency to form bigger clusters increased to achieve lower surface energy.

Oxide bi-films were frequently observed in the 2D sample of the high Mg content alloys i.e. 1.3 wt% and 5.1 wt%. However, after extraction no oxide bi-films were observed. This may be because as the Mg content was increased, the bi-films got more strained from the oxides attaching underneath, hence the cracks generated are more in number and bigger in size, thus making it harder for the oxide bi-film to stay intact at lower temperatures. As a result, the oxide broke down after extraction i.e. removal of Al matrix and stuck to the surface of the intermetallics as shown in Fig. 6.14 and Fig. 6.16. The other possible reason for oxide breakdown could be electrostatic attraction after extraction. However, this can also happen during prefil experiment as described in section 6.1.2.5.

6.3.2 Oxides

Since Mg has high affinity for oxygen, the Mg containing Al alloys will oxidise easily under normal casting conditions. Due to the high segregation tendency of Mg, it is expected that a thin MgO layer will form first, which leads to the growth of $MgAl_2O_4$, as it is thermodynamically more stable **(Haginoya et al., 83)** and **(Salas et al., 95)**. They also reported $MgAl_2O_4$ as the dominant oxide for high Mg contents in binary alloys. However, in this investigation, at high Mg content in quaternary alloys (Al-Fe-Si-Mg) MgO was the dominant oxide. The oxides formed in this study were of very small volume fraction, as detected by XRD. Earlier studies showed that the oxides formed are 1-5 ppm in concentration **(Simensen, 85)**, which explains why only a few oxide particles were observed in SEM analysis of extracted particles. As a result, prefil experiments were conducted to increase the density of the oxides and hence increase the probability of observing oxides and oxide bi-films for these alloy compositions, as described in detail in section 6.1. As the Mg content was increased, the amount of Mg-rich oxides generated in the melt increased. $MgAl_2O_4$ was the major oxide formed at low Mg levels (Mg $\leq$ 0.8 wt%), whereas both MgO and $MgAl_2O_4$ were favourable for Mg levels (0.8 wt% < Mg < 3.0 wt%). However, for Mg $\geq$ 3.0 wt%, MgO was the dominant oxide. Table 6.4 shows the summary of the observed oxides and phases for different alloy compositions.

The dominance of MgO at high Mg content is because of rapid diffusion of Mg to the surface to form a thick layer of MgO via reaction (1). MgO combines with the thin layer of Al_2O_3 formed initially to form small fractions of $MgAl_2O_4$ through reaction (3). For low Mg content, $MgAl_2O_4$ growth occurs via reaction (4) due to the diffusion of Al through cracks that develop during the conversion of $MgAl_2O_4$ to MgO **(Murthy et al., 95)**. However, at high Mg content, reaction (4) slows down significantly and the liquid Al is not able to diffuse through the thick MgO layer to form $MgAl_2O_4$. As a result, Al is consumed by the other solute elements (Fe and Si) to form intermetallics. Also, excess Mg in the liquid diffuses faster than Al to react with oxygen to form more MgO through reaction (1).

$Mg + ½\ O_2 \rightarrow MgO$…….. .(1)

$2Al + 3/2\ O_2 \rightarrow Al_2O_3$……(2)

$MgO + A1_2O_3 \rightarrow MgAl_2O_4$……(3)

$4MgO + 2A1 \rightarrow MgAl_2O_4 + 3Mg$…… .(4)

Also, XRD traces demonstrated a shift in the nature of the oxide from $MgAl_2O_4$ at low Mg content alloys to MgO at high Mg content alloys. This shift is consistent with the microscopy results in this study.

6.3.2.1 MgO nucleating the α-AlFeSi intermetallic

Fine MgO particles were observed on a few occasions to be at the most probable nucleation point of the α-AlFeSi intermetallic.

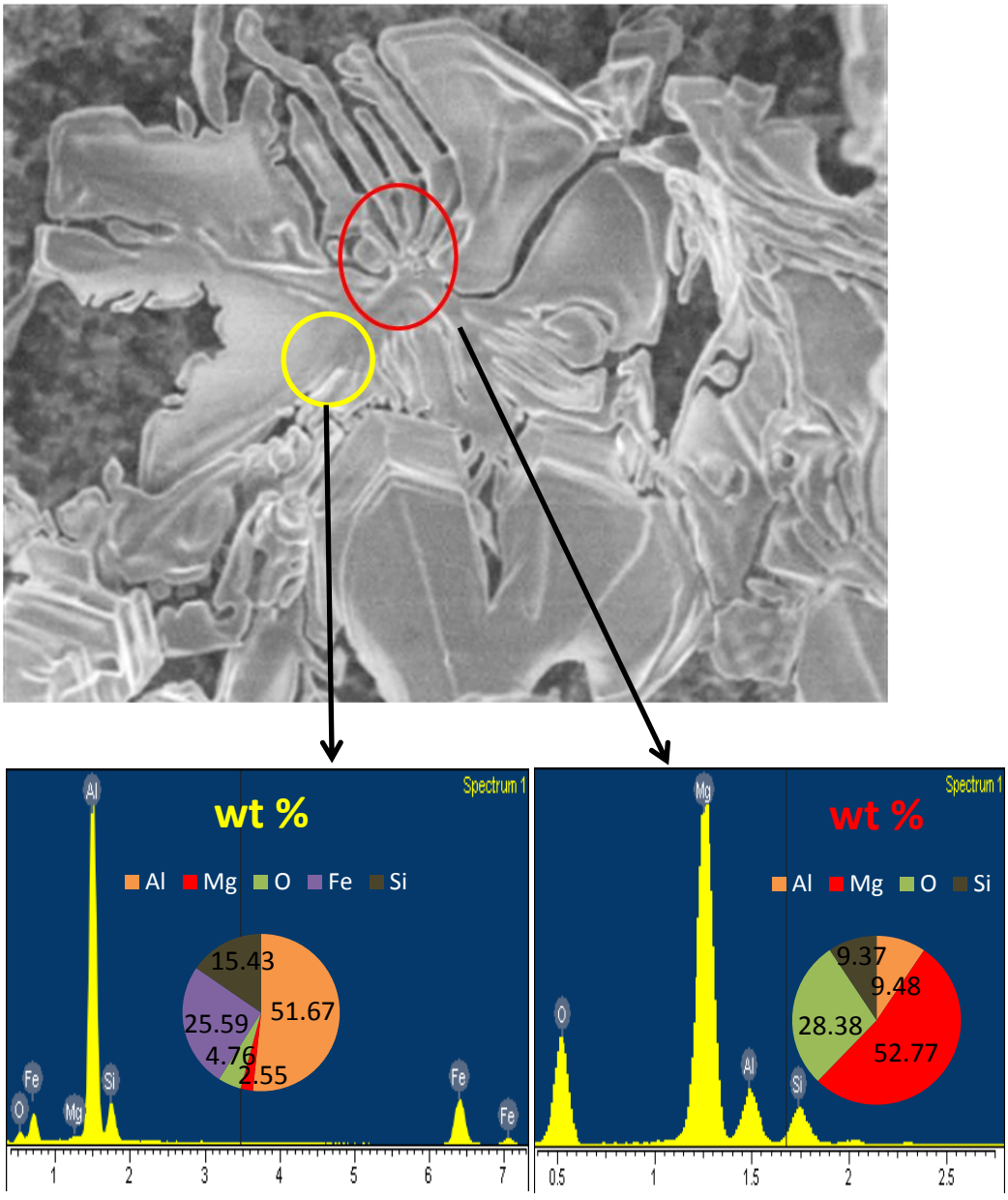

Fig 6.39 SEM micrograph and EDX analysis showing the presence of MgO at the most probable nucleation point of the α-AlFeSi intermetallic particle.

Fig. 6.39 shows one such observation. EDX analysis was used to confirm the identity of the oxide particle and the intermetallic. The flower-like geometry also supported the EDX analysis i.e α-AlFeSi intermetallic (Fe:Si=1.6). No such relation was observed with β-AlFeSi intermetallic. This will be discussed in detail in section 6.4.2.1.

6.3.3 Relation between crack-like feature and oxide films

A number of random cracks were also observed in the 2D microstructures. Similar features have been reported earlier **(Cao et al., 03)**. It was suggested that the crack widths are similar to the distance between the dry surfaces of an oxide film.

Section 6.1.2 discussed the 3D morphology and ductile and brittle nature of the oxide film. It was proposed that the oxide film is subjected to high strain as the number of oxide particles attached to it increases and the nature of the oxide film changes from ductile to brittle as it thickens with time. It is because of this brittle nature that cracks can easily propagate in the oxide film under high strain. Hence, the observation of crack-like features in the ductile matrix of 2D microstructures could also be a real crack on the underside of the oxide film on which the intermetallics appeared to have nucleated.

Table 6.4 Summary of the alloy compositions and observed phases and oxides

Alloy Composition				Relative fraction of phases				Relative fraction of oxides			
Al%	Fe%	Si%	Mg%	$Al_{13}Fe_4$	β-AlFeSi	α-AlFeSi	Mg_2Si	Oxide Bi-films	Γ-Al_2O_3	MgO	Spinel
98.79	0.31	0.52	0.13								
98.46	0.29	0.51	0.52								
97.62	0.32	0.51	1.33								
93.82	0.29	0.49	5.15								

Some Quite a lot Dominant Absent

6.4 Effect of Mg on the cast microstructure

6.4.1 Effect of oxides on α-Al grains

The increase in oxide content with Mg can be correlated with grain refinement, as shown in the anodised images in Fig. 6.21. Earlier studies have demonstrated the high efficiency of Mg-rich oxides in nucleating primary-Al, using lattice mismatch **(Cao et al., 03)** and **(Li, 11)**. It was suggested that (001) planes of $MgAl_2O_4$ are more favourable for the nucleation of primary-Al because of small lattice misfit **(Li et al., 12)**. However, for the oxide particles to be effective for nucleation, they also need to have the right size and distribution **(Greer et al., 00)**.

In low Mg content alloys, oxides were observed to exist as films and not as individual particles. Hence, the grain size was not reduced significantly as there were not sufficient nucleation sites, whereas for high Mg content a significant grain refinement was noted. This can be attributed to the observation that with the increase in Mg content, MgO particles reduce in size and increase in number as shown in section 6.1.2. These refined MgO particles act as nucleation sites for α-Al **(Cao et al., 03)** and cause a reduction in grain size. It was also suggested that oxides are naturally dispersed in Al - 5.0 wt% Mg alloys due to the surface tension reduction and agitation while pouring the melt, which leads to a refined microstructure without any need for melt shearing **(Li, 11)**. However, the reduction in surface tension cannot explain the dispersion of the oxide films.

The dispersion of small oxide particles can be chiefly associated with the changing behaviour of oxide films. With the increase in Mg content, the oxide films grow bigger and thicker **(Huang et al., 00)**. As the density of the oxide particles attached to the wet surface increases, the strain on the oxide film increases, which changes the behaviour of oxide films from ductile to brittle. Fig. 6.10d shows the ripple and crack features on oxide films which are direct evidence of the ductile and brittle natures respectively. Consequently, any agitation during pouring/stirring can break the oxide films easily and disperse the oxide particles in the melt.

Also, the tendency for the oxide films to break and disperse in the melt gradually increases with the Mg content, which leads to a gradual change in the grain structure. As a result, there are plenty of nucleation sites for high Mg content alloys which lead to the gradual transition from columnar grain structure to equiaxed. However, it is important to note that there was no significant increase in the grain refinement for Mg $\geq$ 3.0 wt%. This could be because of two counteracting effects. As the number of inoculant particles in the melt was increased, the density of grains also increased. This results in recalescence and lowers the number of inoculant particles participating in nucleation. This effect is balanced by the extra number of inoculant particles available, thus only a small increase in grain size.

However, it is also important to consider another competing effect at the same time, as grain refinement can also be achieved by increasing solute content i.e. via grain growth restriction. As the amount of solute in the melt increases, they cause obstruction in the grain growth of α-Al. As a result, deeper undercooling can be achieved which allows more activated inoculant particles for nucleation thus reducing the grain size. Growth restriction factor is denoted by Q and is calculated by equation (1) for single component systems **(Greer et al., 00)**.

$Q = m\ C_0\ (k-1)$……………………………………………………………….(1)

where,

C_0 – bulk solute content

m – liquidus slope

k – equilibrium partition coefficient

For simplicity Q for multi component systems is calculated by adding the Q's for all the different solute in the system. In this study Q increases linearly with the increase in Mg content (C_0) as the Q from all other elements were kept constant. This increase in growth restriction factor (Q) could also contribute to α-Al grain refinement. However, for accurate calculation of the growth restriction factor (Q) in high component systems (quaternary or higher in this thesis) requires complex modelling/calculations and hence is out of the scope of this study.

6.4.2 Effect of oxides on secondary phase

6.4.2.1 Nucleation of AlFeSi intermetallics

The role of oxides in nucleating intermetallics has been investigated for a couple of decades. The secondary electron images and backscattered electron images shown in Fig. 6.3, Fig. 6.4 and Fig. 6.28 clearly show the presence of intermetallics underneath the wet surface of the oxide film. Similar features were observed by **Cao et al**, who showed the presence of AlFeSi intermetallics on the wet surfaces of oxide films. Section 6.1.2 analysed the 3D morphology of the oxide films which showed the direct evidence of the presence of Mg oxides on the wet surface of the oxide film as well as the change in the nature of the oxide particles associated with the oxide film with the increase in Mg content.

A number of AlFeSi intermetallics (α-AlFeSi) were observed to be associated with MgO particles. These oxide particles were present at the location which appeared to be the nucleating site of the intermetallic. For example in Fig. 6.37, MgO was detected at the centre of the flower-like structure of α-AlFeSi. It is geometrically reasonable to assume that all the petal-like features for that intermetallic originated from the central point which is rich in MgO. The type of oxide and intermetallic were confirmed using EDX. This is the first clear evidence of an oxide acting as a potent nucleating substrate for Fe-rich intermetallics. It is interesting to note that α-AlFeSi has a minimum in its relative volume fraction for the 0.4 wt% Mg alloy (Fig. 6.30) which might be attributed to the presence of high spinel. Also, with the increase in Mg wt%, the

relative fraction of α-AlFeSi increases which might be because of the increase in the amount of MgO.

Disregistry calculations showed (100), (110) and (111) as favourable planes for MgO to nucleate α-AlFeSi **(Cao et al., 03)**, whereas similar calculations cannot be performed for β-AlFeSi intermetallics due to their complex geometry. Previous studies **(Narayanan et al., 94)** and **(Samuel et al., 03)** also proposed the importance of oxides in nucleating α-AlFeSi and β-AlFeSi intermetallics on the wet surface of the oxide film.

6.4.2.2 The potency of MgO particles to act as nucleating sites for Mg_2Si

Interfacial free energy and lattice matching between the solid and the substrate are two important factors in heterogeneous nucleation **(Cao et al., 03)**. The nucleating substrate with better lattice matching with the solid is likely to have higher potency (see section 2.4.3 for details). However, it is important to note that the local chemistry also play a decisive role in governing the potency of a substrate i.e. a substrate with good lattice match with the solid may not be potent if the local chemistry is unfavourable **(Eskin, 08).** Hence, in order to find the potency of MgO to nucleate Mg_2Si, the planar disregistry needs to be calculated. Since Mg_2Si is the last phase to form, its nucleation temperature will be lower than 660^oC. The nucleation temperature for Mg_2Si is taken to be 600.1^oC as calculated thermodynamically using MTDATA, which was observed to be constant with varying Mg content. The crystal structure for both MgO and

Mg_2Si is FCC. The lattice parameters at 600.1^oC for MgO and Mg_2Si can be calculated using the lattice parameter from the JCPDS files (MgO-00-045-0946, Mg_2Si–00-034-0458) and coefficient of thermal expansion at room temperature.

In order to calculate the planar disregistry, a low index plane was chosen for both substrate and nucleated solid for eg. $(100)_{MgO}$ and $(100)_{Mg2Si}$. Low indexed directions were chosen in that plane for eg. $[001]_{MgO}$ and $[001]_{Mg2Si}$. The $d[hkl]_{MgO}$ and $d[hkl]_{Mg2Si}$ values were calculated using the lattice parameter, crystal structure and coefficient of thermal expansion. In this case $d[001]_{MgO}$ and $d[001]_{Mg2Si}$ were 0.421 nm and 0.635 nm respectively. If the difference between the d-spacings for substrate and nucleated solid is greater than 50% of the d-spacing for the substrate, then d-spacings for the substrate and nucleated solid are multiplied by positive integers to see if multiples of the d-spacing give a lower misfit. These integers represent the number of times substrate/nucleated lattice are repeated to get the lowest planar disregistry possible.

For example, the difference between $d[001]_{MgO}$ and $d[001]_{Mg2Si}$ is 0.635 – 0.421 = 0.214. However, the difference after multiplying by positive integers is much less i.e. 2 x 0.635 – 3 x 0.421= 0.007. This means that the lowest disregistry for the $(100)_{MgO}$ and $(100)_{Mg2Si}$ along the $[001]_{MgO}$ and $[001]_{Mg2Si}$ is achieved when the lattices are repeated 3 times and 2 times respectively. These disregistries are calculated along the three sets of directions for the given plane and their average value is calculated. However, it is

important to note that the higher the multiplying integers are, the higher is the unlikeliness of it actually acting as a nucleant substrate. This is because of high energy caused by the intermediate unmatched phases.

The planar disregistry for various planes/directions between MgO and Mg_2Si is shown in Table 6.2. Good lattice matching was observed for all the directions of (100) and (111) planes as evidenced by their smaller planar disregistry values. The average misfit value for the three directions of (100) and (111) planes are 0.51 and 0.44 respectively. However, it should be noted that segregation of other solute elements can affect the potency of the nucleating substrates.

Table 6.2 Planar disregistry for various planes/directions between MgO and Mg_2Si

Match planes	$[hkl]_s$	$[hkl]_n$	$d[hkl]_s$	$d[hkl]_n$	f %
(100)s//(100)n	[001]	[001]	3 X 0.421	2 X 0.635	0.55
	[011]	[011]	3 X 0.596	2 X 0.898	0.44
	[010]	[010]	3 X 0.421	2 X 0.635	0.55
(100)s//(110)n	[001]	[001]	3 X 0.421	2 X 0.635	0.55
	[011]	[-111]	3 X 0.596	2 X 1.1	18.72
	[010]	[-110]	2 X 0.421	0.898	6.23
(100)s//(111)n	[001]	[-1-12]	3 X 0.421	1.549	18.46
	[011]	[-312]	4 X 0.596	2.376	0.33
	[010]	[-110]	4 X 0.421	1.796	6.23
(110)s//(100)n	[001]	[001]	3 X 0.421	2 X 0.635	0.55
	[-1-12]	[011]	3 X 0.516	2 X 0.898	13.8
	[-110]	[010]	2 X 0.298	0.635	6.14
(110)s//(110)n	[001]	[001]	3 X 0.421	2 X 0.635	0.55
	[-111]	[-111]	3 X 0.73	2 X 1.1	0.46
	[-110]	[-110]	3 X 0.516	2 X 0.898	13.8
(110)s//(111)n	[1-10]	[-1-12]	2 X 0.596	1.549	23.05
	[1-11]	[-101]	2 X 0.73	1.796	18.71
	[001]	[-110]	2 X 0.421	0.898	6.23
(111)s//(100)n	[-1-12]	[001]	0.516	0.635	18.74
	[-312]	[011]	0.788	0.898	12.25
	[-110]	[010]	0.596	0.635	6.14
(111)s//(110)n	[-1-12]	[-110]	1.032	0.898	14.92
	[-101]	[-111]	1.191	1.1	8.27
	[-110]	[001]	0.596	0.635	6.14
(111)s//(111)n	[-101]	[-101]	3 X 0.596	2 X 0.898	0.44
	[-211]	[-211]	3 X 1.032	2 X 1.555	0.45
	[-110]	[-110]	3 X 0.596	2 X 0.898	0.44

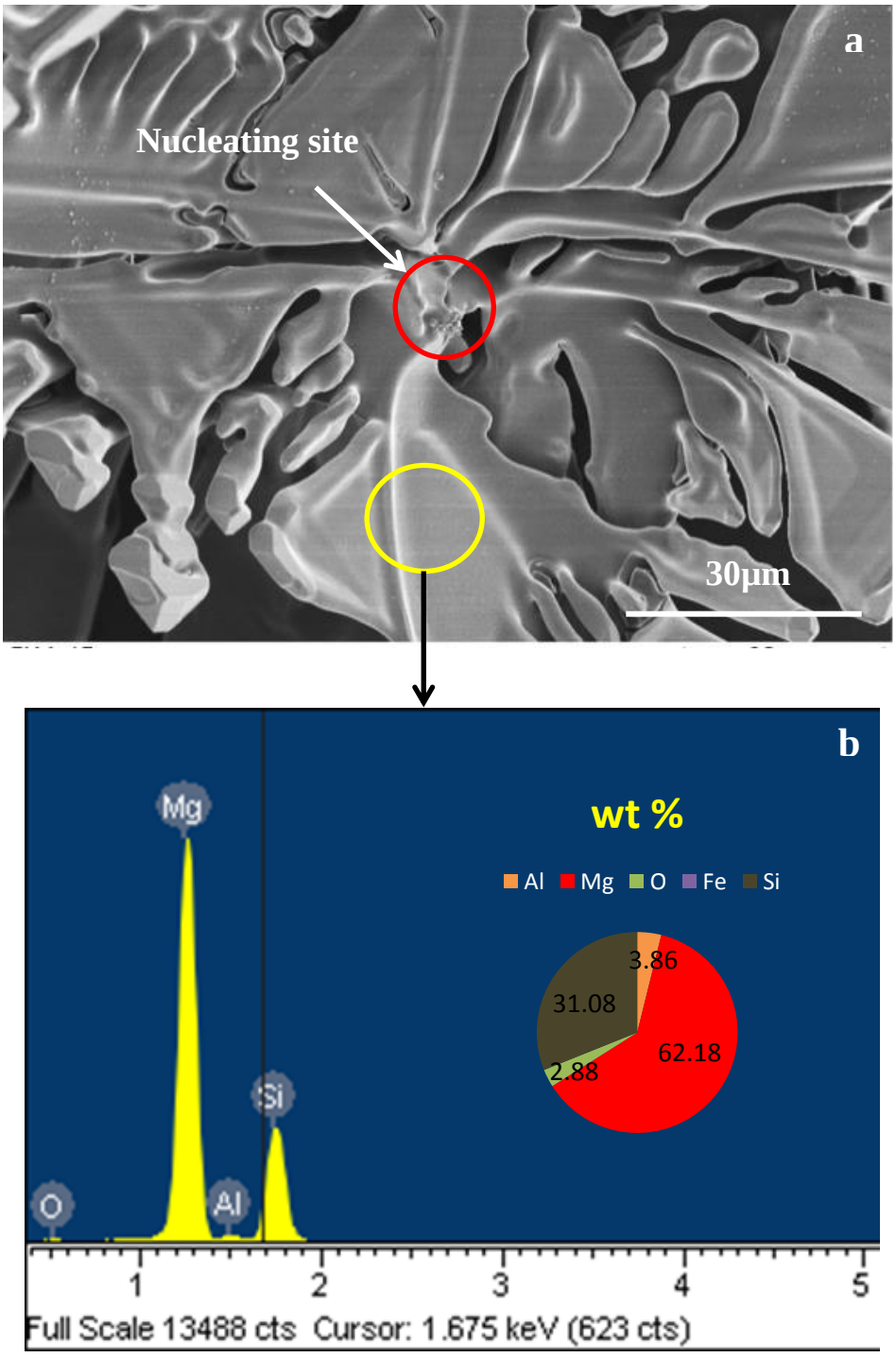

Continued overleaf…

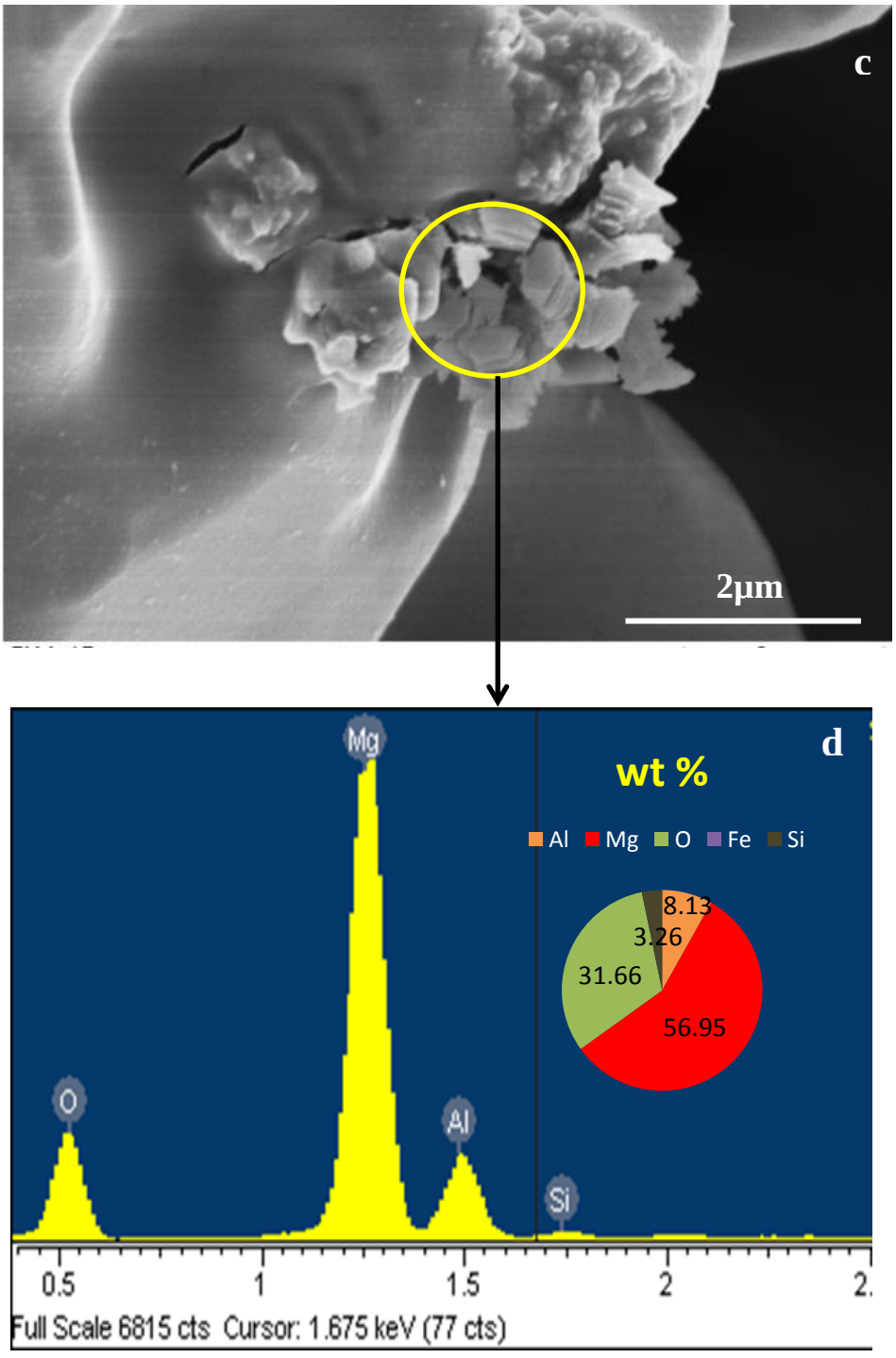

Fig. 6.40 SEM micrographs showing a) Mg_2Si particle, c) MgO particles at the most probable nucleating site of the Mg_2Si particle, b) and d) EDX specta confirming the presence of Mg_2Si and MgO.

Fig. 6.40 shows the presence of MgO (Mg/O>1) at the probable nucleating site of an Mg_2Si particle. A nucleating agent is effective if it has the correct size and distribution of particles in the melt along with suitable solidification conditions. As the Mg content was increased, Mg_2Si became thermodynamically favourable and there was an increase in the volume fraction of Mg_2Si formed as shown in Fig. 6.27.

Also, the 3D morphological analysis showed a high density of Mg_2Si for high Mg content alloys. Around 30 Mg_2Si particles were analysed and approximately 70% of them were found to be associated with MgO particles. Hence, the SEM observation and lattice matching calculation together strongly suggest the high potential of MgO as a nucleating substrate for Mg_2Si in high Mg content alloys.

6.4.2.3 Morphology of the intermetallics

On increasing the Mg content, it was observed that the size of the intermetallics was increased i.e. the length of the petals of α-AlFeSi and the length of the maximum faceted side of β-AlFeSi increased with an increase in Mg content as shown in Fig. 6.33 and Fig. 6.34 respectively. The increase in the size of the intermetallics can be associated with the agglomeration of oxides. As the Mg content increased, the tendency of oxide particles to form bigger clusters increases, which make them possibly less potent sites for an intermetallic. As a result, fewer nucleations sites are available for intermetallics. Hence, each particle can grow for longer time before it interacts with another particle which

results in features like larger petals and increase in interconnectivity between the intermetallics as shown in Fig. 6.31. This is also due to increase in liquid the fraction from where the intermetallics nucleate and grow. From the MTDATA calculations (Fig. 5.2) it can be seen that the semi solid region increases with the increase in Mg content. Also the intermetallics starts to form at a much earlier stage when there is more liquid fraction. Therefore the intermetallics have more space to grow lengthier and bigger with the increase in Mg content.

The fraction of remaining liquid during intermetallic nucleation should also govern the size of the intermetallics. As this fraction increases the size of the intermetallics should also increase. The fraction of remaining liquid at intermetallic nucleation temperature was calculated using the MTDATA. However, no correlation can be made between the variation in the remaining liquid and the size of the intermetallic.

Fe-rich intermetallics in particular, were observed to have a coupled eutectic growth mechanism with Mg_2Si for the high Mg content (Mg > 2 wt%) alloys as shown in Fig. 6.37. This can be explained by the behaviour of the solidification front. As Mg takes away Si from the melt due to its high affinity towards Si to form Mg_2Si, the neighbouring melt becomes rich in Al and Fe which favours the formation of $Al_{13}Fe_4$. Both these compounds assist the formation of each other and result in the fine dendritic structure (Fig. 6.37). The dendritic nature of the intermetallics also increased with the Mg content. I-DAS was observed to

decrease with the Mg content as shown in Fig. 6.32. As the Mg content was increased, the severity of Si depletion from the neighbouring melt also increased which did not allow the dendrites to grow further and resulted in finer dendrites.

6.4.3 Effect of Mg on the formation of secondary phases

Theoretical calculations using MTDATA in chapter 5 showed the changes in the secondary phases with the variation in Mg wt%. Mg:Si plays a critical role in deciding the stability and formation of secondary phases. Both theoretical calculations and experimental observations showed that at low Mg wt%, AlFeSi phases dominated the secondary phases, whereas at high Mg wt%, Mg_2Si dominated. This can be attributed to the Mg:Si ratio **(Chakrabarti et al., 04)**.

At low Mg wt%, there is enough Fe and Si in the solute for the formation of AlFeSi intermetallics and only a small amount of Fe and Si is absorbed to form $Al_{13}Fe_4$ and Mg_2Si. However, at high Mg content, it was the nucleation temperature of secondary phases which was the deciding factor. Generally AlFeSi compounds form before $Al_{13}Fe_4$ and Mg_2Si, but at high Mg wt% the nucleation temperature of $Al_{13}Fe_4$ and Mg_2Si goes higher than that of AlFeSi. As a result, $Al_{13}Fe_4$ and Mg_2Si nucleate first and absorb the Fe and Si in the liquid. Then due to a lack of Si and Fe content in the liquid, formation of AlFeSi intermetallics is hindered. Previous studies showed the formation of only β-AlFeSi in 0.4 wt% Mg content alloy **(Caceres et al., 99)**, which also correlates with the phases predicted by MTDATA. However, it is interesting to note that

the calculated relative fraction of β-AlFeSi with respect to α-AlFeSi reached a maximum for 0.4 wt% Mg in this study.

7. Conclusions

1. Homogenisation has a significant impact on the microstructure of the Al alloy and Fe bearing intermetallics in particular. A considerable reduction in the size of the intermetallics and interconnectivity between them was observed in the homogenised alloy with respect to the as-cast alloy which can be attributed to the spheroidising effect. Also, the ratio of α-AlFeSi : β-AlFeSi measured was much higher in the homogenised alloy.

2. The influence of cooling rate on the 3D morphology of Fe bearing intermetallics in an AA6063 Al alloy has been analysed. The 3D analysis suggests cooling rate not only influences the Al grain size but also controls the Fe bearing intermetallic phase selection and intermetallic size, morphology and interconnectivity. The relative fraction of β-AlFeSi phases increases as the cooling rate decreases. The sizes of the petals and dendrite type α-AlFeSi particles were smaller at higher cooling rates. Large plates of β-AlFeSi were observed at low cooling rates. At low cooling rate the Fe intermetallic particles were intact and well interconnected.

3. Grain size analysis proved the effectiveness of the TP-1 (38mm from the bottom of the TP-1 mould) to simulate the grain structure of DC billet, when fresh grain refiner was added. However, it failed to simulate the 2D and 3D morphologies of the α-AlFeSi and β-AlFeSi intermetallics. Though the relative

fractions of α_c-AlFeSi and β-AlFeSi were similar using the two different solidification processes, the difference between the sizes of the intermetallics, intermetallic interdentritic arm spacing and interconnectivity between intermetallics suggest a different mechanism of formation of intermetallic phases as compared to DC casting. In order to get comparable intermetallic microstructures, more of the solidification conditions should be similar, not just the cooling rate.

4. Theoretical calculation using MTDATA showed the presence of both α-AlFeSi and β-AlFeSi for low Mg content alloys (Mg<1.2 wt%). However, they shifted to $Al_{13}Fe_4$ and Mg_2Si for high Mg content alloys (Mg≥1.6 wt%).

5. Combined Prefil and extraction experiments were utilised to concentrate the inclusions and study the 2D and 3D morphology of mainly oxides and oxide bi-films of different Mg containing alloys. 3D morphology of the oxide bi-films were observed for the first time. Spinel was mainly observed at the wet surface of the oxide bi-film for low Mg content alloys, wheras MgO was dominant on the wet surface for high Mg content alloys. Also, the parallel gaps between the two dry surfaces of a folded oxide bi-films gives rise to the cracks observed in the 2D micrographs. However, the cracks observed on the surface of the extracted oxide bi-films are due to the high strain from the particles attached on the wet surface or due to stress induced by extraction process itself. of the oxide bi-film. Also, the oxide bi-films became more brittle as the Mg content was

increased. As a result, the oxide bi-films can be broken up / dispersed relatively easily.

6. Spinel dominated in the low Mg content alloys. Also, the tendency to form MgO increased with an increase in Mg content. Spinel was observed as octahedral particles whereas MgO was observed as spherical particles. The size of the MgO particles was in the range of 150nm-350nm and reduced with the increase in Mg content.

7. Hexagonal rods of Al_2O_3 (aspect ratio > 1.8) and TiB_2 (aspect ratio < 1.8) were also observed.

8. Addition of Mg leads to significant grain refinement from 402±39μm in 0 wt% Mg to 291±38μm in the 5.0 wt% Mg alloy of TP1 samples. SDAS also reduced notably from 109±9μm in the 0 wt% Mg alloy to 45±3μm in the 5 wt% Mg alloy.

9. In prefil samples, MgO was observed for the first time at the centre/most probable nucleation site of α-AlFeSi in 0.5 wt% Mg alloy. MgO was also observed at the most probable nucleation point of Mg_2Si particles in 5.1 wt% Mg alloy with planar disregistry calculations showing (100) and (111) as the

favourable planes. Spinel was not observed to be associated with Fe bearing intermetallics in prefil or TP1 samples.

10. In both prefil and TP1 samples, α-AlFeSi and β-AlFeSi were the dominating phases for low Mg content alloys (Mg wt% < 1.6), whereas, $Al_{13}Fe_4$ and Mg_2Si phases dominated as the Mg content increased (Mg wt% > 1.6).

This research work demonstrated that inclusions (MgO in particular) have the potency to nucleate α-AlFeSi in script form in 6xxx Al alloys. It is well known in industry that α-AlFeSi in script form causes problems like poor surface quality in 6xxx series extruded products. This research would prove helpful to explain the unexpected occurrence of script α-AlFeSi in commercial alloys and the importance of good melt filtering process to achieve correct level of melt cleanliness. As discussed earlier, there is not enough information available on the effect of inclusions on the extrusion alloys and this project provides valuable evidence on the effect of oxide inclusions (MgO) on intermetallic phase formation.

The other existing problem in the extrusion of 6xxx alloys with high Mn content is poor surface quality due to pick-up defect and excessive die lines. It is possible to add MgO deliberately to these alloys for the formation of fine α-AlFeSi particles due to an increase in number of nucleation sites (as both Mn

and MgO promotes α-AlFeSi) and may result in reducing the defects and better surface quality. This project also showed the importance of the 3D analysis as 2D micrographs show an incomplete picture and might give rise to misleading conclusions.

8. Future work

This research has shown promising results and high potential to have a significant impact on the extrusion of 6xxx Al alloys. A lot more research opportunities are opened in this area to improve the 6xxx Al alloy extrusion process. For example:

1. Further work needs to be done to optimise the conditions for oxide formation inside the melt and to improve the efficiency of nucleation of intermetallics on them. i.e. the alloying elements, composition, the holding time, temperature, dispersion etc.

2. This study mainly investigated Mg oxides whereas other oxides might also have the potential to nucleate Fe bearing intermetallics which needs to be investigated as well.

3. TEM analysis of particles appearing to nucleate on oxides will also provide valuable information and help in the selection of oxides for nucleating a specific intermetallic.

4. It will be interesting to investigate the combined effect of Mn and MgO on the α-AlFeSi intermetallic phase formation and on extrusion quality.

5. Further research can be done on different Al alloy systems, both cast and wrought alloys.

6. It will be interesting to investigate the influence of addition of ex-situ formed oxide particles on the intermetallic phase selection in 6xxx series extrusion alloys.

7. Though there is considerable literature on the β-AlFeSi to α-AlFeSi transformation during homogenisation, the actual mechanism of transformation is still unknown. Therefore it will be interesting to investigate this transformation mechanism through a combination of 3D and in-situ studies.

References:-

(Adam et al., 72) C. McL. Adam and L.M. Hogan, Austral. Inst. Met. 17, 1972, 81-90.

(Akhtar et al., 09) S. S. Akhtar, A. F. M. Arif, B. S. Yilbas, Journal of Manufacturing Science and Engineering, Oct. 2009, Vol. 131 (5), p.p. 054502 (1-7).

(Alexander et al., 02) D.T.L. Alexander, A.L. Greer, Acta. Mater., 2002, 50, 2571– 83.

(Alexander et al., 04) D. T. L. Alexander, A. L. Greer, Philosophical Magazine, Oct. 2004, Vol. 84, No. 28, 3051–3070.

(Aliravci et al., 98) C.A. Aliravci, M.O. Pekgüleryüz, Calphad, 1998, 22, 147–l55

(Allen et al., 96) C.M. Allen, K.A.Q. O'Reilly, B. Cantor and P.V. Evans, Material Science Forum, 1996, 217–222, 678–84.

(Allen et al., 98) C.M. Allen, K.A.Q. O'Reilly, B. Cantor, and P.V. Evans, Progress in Material Science, 1998, vol. 43, 89-170.

(Allen et al., 99) C.M. Allen, K.A.Q. O'Reilly, P.V. Evans, and B. Cantor: Acta Materialia, 1999, vol. 47, 4387-4403

(Allen et al., 00) C. M. Allen, K. A. Q. O'Reilly, B. Cantor and P.V. Evans and D. J. Bristow, Acta Mater., 2000, 48, 2823-2835.

(Allen et al., 01) C.M. Allen, K.A.Q. O'Reilly, and B. Cantor: Acta Mater., 2001, vol. 49, pp. 1549-63.

(Altenpohl et al., 98) D.G. Altenpohl, 'Aluminium: Technology, Applications and Environment', Minerals, Metals, and Materials Society, Warrendale, Pennsylvania, 1998.

(Aucote et al., 78) J. Aucote, D.W.E., Effects of excess silicon addition on ductility of Al-0.95%Mg2Si Alloy, Materials Science and Technology, 1978. 12(2): p. 57-63.

(Backerud et al., 86) L. Backerud, E. Krol, J. Tamminen, Solidification Characteristics of Aluminium Alloys, Vol. 1: Wrought Alloys, 1986.

(Bakhtiarani et al., 11) Bakhtiarani, F.N. and R. Raiszadeh, The behaviour of double oxide film defects in Al-4.5 wt% Mg melt. Journal of Materials Science, 2011. 46(5): p. 1305-1315.

(Bale et al, 90) C. W. Bale, G Eriksson, Canada Metal. Quart., 1990, Vol 29, 105-132

(Barekar et al., 09) N. S. Barekar, N. Hari Babu, B. K. Dhindaw, Z. Fan, J. of Mat. Pro. and Perf., Vol 18 (9), 2009, 1230-1240.

(Belov et al., 05) N. A. Belov, D.G. Eskin, A.A. Aksenov, "Multicomponent Phase Diagrams: Applications for Commercial Aluminium Alloys", Amsterdam:Elsevier, 2005.

(Birol, 98) Y. Birol, Z. Metallkd., 1998, Vol 89, pp. 501-506.

(Birol, 04) Y. Birol, Journal of Materials Processing Technology, 2004, 148, 250–258.

(Birol, 08) Y. Birol, J Mater Sci, 2008, 43, 4652–4657.

(Bichsel et al., 81) H. Bichsel, A. Reid, and J. Langerweger: Aluminium, 1981, 57, (12), 787-791.

(Bongo et al., 14) A-A. Bogno, A. Maitre, H. Henein and Ch.-A. Gandin, Conference of Metallurgists Proceedings, Canadian Institute of Mining, Metallurgy and Petroleum, 2014

(Bramfitt, 70) B. Bramfitt: Metall. Trans., 1970, vol. 1, pp. 1987-95.

(Brusethaug et al., 87) Brusethaug S, Porter D, Vorren O., Int. Light Metals Congr. Proc., Vienna, Austria, 1987, p. 472-477.

(Burden et al., 74) M. H. Burden and J. D. Hunt, Journal of Crystal Growth, 1974, vol. 22, 109-116.

(Caceres et al., 99) C.H. Caceres, C.J. Davidson, J.R. Griffiths, and Q.G. Wang, Metal. and Mat. Trans A, vol 30A, Oct 1999, 2611-2618.

(Campbell et al., 03) J. Campbell, The New Metallurgy of Cast Metals, 2nd Ed., Oxford, Butterworth Heinemann, 2003, 151-156.

(Cantor et al., 97) B. Cantor, Mater. Sci. Eng. A, 1997, 226-228, 151-156

(Cao, 01) Ph.D. Thesis, University of Birmingham, United Kingdom, 2001

(Cao et al., 03) X. Cao and J. Campbell, Metall. Mater. Trans. A, 2003, 34A, 1409-1420.

(Cao et al., 05) X. Cao and J. Campbell, Canadian Metallurgical Quarterly, 2005, Vol 44, No 4 pp 435-448.

(Carroll, 99) L. M. Carroll, D. Phil. Thesis, 1999, University of Oxford.

(Cefalu et al., 03) S.A. Cefalu, M.J.M. Krane, Mater. Sci. Eng. A, 2003, vol. 359, pp. 91-99.

(Chakrabarti et al., 99) Chakrabarti, D., Y. Peng, and D.E. Laughlin. Precipitation in Al-Mg-Si alloys with Cu additions and the role of the Q'and related phases. in Materials Science Forum. 2002. Transtec Publications; 1999.

(Chakrabarti et al., 04) D.J. Chakrabarti, David E. Laughlin, Progress in Materials Science, 2004, 49, 389–410.

(Chen, 99) X. G. Chen, Light Metals, 1999, 803-809.

(Cheng et al., 11) Cheng Wei-Jen, Wang Chaur-Jeng, Applied Surface Science, 2011, Vol 257, pp 4637–4642.

(Claves et al., 04a) S.R. Claves, W.Z. Misiolek, and J.R. Michael, Mat. Sci. Forum, Vol. 28, 2004, pp. 1334-1340.

(Claves et al., 04b) S.R. Claves, A.R. Bandar, W.Z. Misiolek, J.R. Michael, Microsc Microanal, 2004, 10 (Suppl 2), pp 1139-1139.

(Cochran et al., 77) C.N. Cochran, D.L. Belitskus, D.L. Kinosz, Metallurgical and Materials Transactions B, vol 8B, 1977, 323-332.

(Cooper, 67) M. Cooper, Acta Crystallography., 1967, 23, 1106-1107.

(Dai et al., 03) X. Dai, X. Yang, J. Campbell, J. Wood, Mater. Sci. Eng. A, 2003, 354, 315–325.

(Davidson, 06) I. Davidson, D. Phil. Thesis, 2006, University of Oxford

(Davis et al., 93) J.R. Davis (Ed.), Al and Al-Alloys, ASM Specialty Handbook, ASM International, 1993.

(Davis, 99) J.R. Davis (Ed.), Corrosion of Al and Al-Alloys, ASM International, 1999.

(Dinsdale et al., 89) A.T. Dinsdale, S.M. Hodson, T.I. Barry, J.I. Taylor, 'Computer software in chemical and extractive metallurgy', Pergamon press, Oxford, 1989, 59-74

(Dispinar et al., 04) D. Dispinar, J. Campbell, International journal of Cast Metals Research, July 2004, Vol. 17, No. 5, pp 1-8.

(Dispinar, 05) D. Dispinar, PhD Thesis, University of Birmingham, Birmingham, 2005.

(Dix et al., 32) E.H. Dix, G.F. Sager, B.P. Sager, Transactions of the American Institute of Mining and Metallurgical Engineers, 1932, vol. 99, 119-131.

(Doherty et al., 63) P.E. Doherty, R.S. Davis, Journal of Applied Physics, Vol 34(3), 1963, 619-628.

(Dons, 01) A.L. Dons, Jour. Light Met. 1, 2001, 133-149

(Doutre et al., 85) Doutre, D, Gariepy B, Martin J. P and Dube, G. Aluminum Cleanliness Monitoring: Methods and Applications in Process Development and Quality Control. Light Metals 1985; New York; USA; Feb. 1985. pp. 1179-1195.

(Drits et al., 77) M.E. Drits, E.S. Kadaner, E.M. Padezhnova, L.L. Rokhlin, Z.A. Sviderskaya, N.I. Turkina, Phase Diagrams of Aluminium and Magnesium Based Systems, Editor Abrikosov, N.Kh. Nauka, Moscow, 1977.

(Dutta et al., 02) B. Dutta and M. Rettenmayr, Materials Science and Technology, 2002, vol. 18, 1428-1434.

(Du et al., 05) Q. Du, D.G.Eskin, L. Katgerman, Mater. Sci. Eng. A, 2005, vol. 413-414, pp. 144-150.

(Enright et al., 96) P.G. Enright, I.R.Hughes, Foundryman Magazine, IBF Publications, Birmingham, 1996, 390-395

(Enright, 87) P.G. Enright, U.S. Patent No. 4,917,728, April 29, 1987

(Eskin et al., 04) D.G.Eskin, J. Zuidema, V.I. Savran, L. Katgerman, Mater. Sci. Eng A, 2004, vol. 384, pp. 232-244.

(Eskin et al., 05) D.G.Eskin, V.I. Savran, L. Katgerman, Metall. Mater. Trans. A, 2005, vol. 36A, pp. 1965-1976.

(Eskin, 08) Dmitry G. Eskin**,** Physical Metallurgy of Direct Chill Casting of Aluminum Alloys, CRC press, 2008.

(Fan et al., 09a) Z. Fan, Y. Wang, M. Xia, S. Arumuganathar, Acta Materialia, 57, 2009, 4891-4901.

(Fan et al., 09b) Z. Fan, M. Xia, H. Zhang, G. Liu, J. B. Patel, Z. Bian, I. Bayandorian, Y. Wang, H. T. Li and G. M. Scamans, International Journal of Cast Metals Research, 2009, Vol 22 (1-4), 103-107.

(Fang et al., 07) X. Fang, G. Shao, Y.Q. Liu, Z. Fan, Materials Science and Engineering A 445–446, 2007, 65–72.

(Field et al., 87) D.J. Field, G.M. Scamans, E.P. Butler, Metallurgical and Materials Transactions A, vol 18A, 1987, 463-472.

(Flemings, 74) M.C. Flemings, Solidification Processing, McGraw-Hill, New York, 1974

(Gabathuler et al., 92) J.P.Gabathuler, D.Barras, 2nd International Conference on Semisolid Processing of Alloys and Composites, MIT/Boston, USA, 1992, pp. 33–46.

(Gale et al., 04) W.F. Gale, T.C. Totemeier (Eds.), Smithells Metals Reference Book, 8th Ed., Elsevier, 2004.

(Garratt et al., 03) A.J. Garratt-Reed, D.C Bell, Energy Dispersive X-ray Analysis in the Electron Microscope, Bio Scientific publishers (Microscopy Handbooks).

(Grandfield et al., 93) J.F. Grandfield, Aluminium Melt Treatment and Casting, M Nilmani (TMS), 1993, 351.

(Grazyna et al., 05) Grazyna Mrowka-Nowotnik, Jan Sieniawski, Journal of Materials Processing Technology 162–163, 2005, 367–372.

(Greer et al., 00) A. L. Greer, A. M. Bunn, A. Tronche, P. V. Evans, D. J. Bristow, Acta Mater., Vol 48, 2000, 2823−2835.

(Griger et al., 96) A. Griger, V. Stefaniay, J Mater Sci, Vol 31, 1996, 6645–52.

(Grishkovets et al., 83) Y. G. Grishkovets, L. V. Budanova, D. A. Morgacheva, Metallovedenie i Termicheskaya Obrabotka Metallov, August, 1983, No. 8, 37-39.

(Gruzleski, 00) Gruzleski, J.E., AFS: Des Plaines, IL, USA, 2000, pp. 117–130.

(Gulbransen, 47) E. A. Gulbransen, Transactions of the Electrochemical Society, Vol. 91, 1947, 573-604.

(Gupta et al., 01) A. K. Gupta, D. J. L., S. A. Court, Precipitation hardening in Al-Mg-Si alloys with and without excess Si. Materials Science and Engineering A, 2001. 336: p. 11-17.

(Gustafsson et al., 86) G. Gustafsson, T. Thorvaldsson and G. L. Dunlo, Metallurgical Transactions A, Volume 17 A, January 1986, 45-52.

(Haghayeghi et al., 10) R. Haghayeghi, E.J. Zoqui, N.R. Green, H. Bahai, Journal of Alloys and Compounds 502, 2010, 382–386

(Haginoya et al., 83) I. Haginoya, T. Fukusako, Trans. Jpn. Inst. Metals, 1983, 24, 613-619.

(Hamerton et al., 00) R. G. Hamerton, H. Cama, M. W. Meredith, Mater. Sci. Forum, 2000, 331-337, 143-154.

(Hanliang et al., 09) Hanliang Zhu, Xinquan Zhang, Malcolm J. Couper, Arne K. Dahle, Materials Chemistry and Physics 113, 2009, 401–406.

(Hansen et al., 98) V. Hansen, B. Hauback, M. Sundberg, C. Romming, J. Gjonnes, Acta Cryst., 1998, B54, 351-357.

(Hsu, 99) C. Hsu, D. Phil. Thesis, Oxford University, UK, 1999.

(Hsu et al., 01) C. Hsu, K.A.Q. O'Reilly, B. Cantor, R. Hamerton, Mater. Sci. Eng. A, 2001, vols. 304-305, 119-124.

(Huang et al., 00) L.W. Huang, W.J. Shu, T.S. Shih, AFS Transactions, Vol 108, 2000, 547-560.

(Janecek et al., 04) M. Janecek, M. Slamova, M. Cieslar, Kovove Materialy, Vol. 42, No.3 2004, 173-184.

(Jarrett et al., 03) M. Jarrett, B. Neilson and E. Manson-Whitton: "Solidification and Casting" (ed. Brian Cantor and Keyna O'Reilly), 2003, The Institute of Physics, 3-25.

(Kashyap et al., 93) K.T. Kashyap, S. Murali, K.S. Raman, and K.S.S. Murthy: Mater. Sci. Technol., 1993, vol. 9, pp. 189-203.

(Khafri et al., 05) M. Aghaie-Khafri, R. Mahmudi, Journal of Materials Processing Technology, 169, 2005, 38–43.

(Khalifa et al., 05) W. Khalifa, F.H. Samuel, J.E. Gruzleski, H.W. Doty, S. Valtierra, Meta. & Mat. Trans.A Vol 36A, April 2005, 1017-1032.

(Kim, 14) KeeHyun Kim, Metallogr. Microstruct. And Anal., Vol. 3, No. 3, 2014, pp 233-237.

(Kofstad, 66) P. Kofstad, High Temperature Oxidation of Metals, John Wiley & Sons, Wiley New York, Vol. 584. 1966.

(Kral et al., 04) M.V. Kral, H.R. McIntyre, M.J. Smillie, Scripta Materialia 51, 2004, 215–219.

(Kubaschewski et al., 53) Von O. Kubaschewski and B.E. Hopkins, Rabald (Ed.), Oxidation of metals and alloys, Butterworths Scientific Publications London, 1953.

(Kuijpers et al., 02a) N.C.W. Kuijpers, W.H. Kool, S. van der Zwaag, Mater. Sci. Forum 396–402, 2002, 675–680.

(Kuijpers et al., 02b) N.C.W. Kuijpers, J. Tirel, D.N. Hanlona, S. van der Zwaag, Materials Characterization 48, 2002, 379– 392.

(**Kuijpers et al., 03)** N.C.W. Kuijpers, W.H. Kool, P.T.G. Koenis, K.E. Nilsen, I. Todd, S. Van Der Zwaag, Materials Characterization 49, 2003, 409– 420

(**Kuijpers et al., 04)** N.C.W.Kuijpers, Kinetics of the β-AlFeSi to α-Al(FeMn)Si transformation in Al–Mg–Si alloys, Ph.D. Thesis, TUDelft, 2004.

(Kuijpers et al., 05) N.C.W. Kuijpers, F. J. Vermolen, C. Vuik, P.T.G. Koenis, K.E. Nilsen, S. van der Zwaaga, Materials Science and Engineering A, 2005, 394, 9-19.

(Kumar et al., 14) S. Kumar, N. Hari Babu, G.M. Scamans, Z. Fan and K.A.Q. O'Reilly, Metall. And Mat. Trans. A, Vol 45A, Issue 3, 2014, 2842-2854.

(Kurz et al., 92) W. Kurz and D.J. Fischer, Fundamentals of solidification, Aedermannsdorf: Trans Tech publications, Switzerland, 3rd Ed., 1992.

(Langsrud, 90) Y. Langsrud: Key Engineering Materials, 1990, 44/45, 95-116

(Lassance, 06) D. Lassance, Ph.D. Thesis, Presses Universitaires de Louvain, Louvain, Belgium, March 2006.

(Laue et al., 76) K. Laue, H. Stenger, Extrusion: Process Machinery Tooling, ASM International, Vol. 3, 1976, 465-475.

(Lavrent et al., 04) Lavrent'ev L.G., Korolyuk V.N., and Usova L.V., J. Anal. Chem., 2004, Vol. 59, pg. 600

(Legarth, 96) J.B. Legarth, Journal of Clean Production, Vol. 4, 1996, 97–104.

(Lessiter, 93) Lessiter, M J. Understanding Inclusions in Aluminum Castings. Modern Casting (USA). Vol. 83, no. 1, pp. 29-31. Jan. 1993

(Li, 11) H.T. Li, IOP Conf. Series: Materials Sci and Eng., Vol. 27, 2011, pp 012047 (1-4)

(Li et al., 12) H.T. Li, Y. Wang and Z Fan, Acta Materilia, Vol. 60, 2012, 1528-1537

(Liu et al., 86) P. Liu, T. Thorvaldsson, G.L. Dunlop, Materials Science and Technology, 2, 1986, pp. 1009-1018.

(Liu et al., 99) Y.L. Liu, S.B. Kang, H.W. Kim, Materials Letters, vol. 41, 1999, 267–272.

(Lodgaard et al., 00) L. Lodgaard, N. Ryum, Mater. Sci. Eng. A, Vol 283, 2000, 144-152.

(Lorimer et al., 66) G.W. Lorimer, R.B. Nicholson, Acta Metall. 14, 1966, 1009-1013.

(Lozano et al., 14) Juan Asensio-Lozano, Beatriz Suárez-Peña and George F. Vander Voort, Materials, 2014, 7, 4224-4242.

(Lu et al., 05) L. Lu and A.K. Dahle, Metallurgical and Materials Transactions A, Volume 36A, March 2005, 819-835.

(Lui, 05) A. Lui, Thesis, 2005, University of Oxford.

(Maggs et al., 95) S.J. Maggs, R.F. Cochrance, S.C. Flood, and P.V. Evans, TMS Annual Meeting, Las Vegas, NV, 1995, 1039-1047.

(Mahta et al., 05) M. Mahta, M. Emamy, A. Daman, A. Keyvani and J. Campbell, Int. J. cast metals, 2005, Vol. 18 No 2 pp. 73-79.

(Mckay et al., 00) B.J. Mckay, P. Cizek, P. Schumacher, and A.Q. O'Reilly: in Light Metals 2000, R. Peterson, ed., TMS, Warrendale, PA, 2000, pp. 833-38.

(Merchant et al., 66) H.D. Merchant, T.Z. Kattamis, and J.G. Morris.- In Continuous Casting of Non-Ferrous Metals and Alloys, H. D Merchant, D. E Tyler and C. H. Chia, TMS Pub. 1-66, 1966.

(Meredith et al., 97) M. W. Meredith, A. L. Greer and P. V. Evans, *Proc. of the 4th Inter. Conf. on Solidification Processing*, ed. J. Beech and H. Jones, University of Sheffield, 1997, 541-545.

(Meredith et al., 98) M. W. Meredith, A. L. Greer and P. V. Evans, Light Metals, 1998, 977-982.

(Merdith et al., 99) M. W. Meredith, A. L. Greer, P. V. Evans and R. G. Hamerton, Light Metals, 1999, 811-817.

(Meyveci et al., 10) Ahmet Meyveci, Ismail Karacan, Ugur Calıgülü, Hülya Durmus, Journal of Alloys and Compounds 491, 2010, 278–283.

(Miller et al., 06) D.N. Miller, L. Lu, and A.K. Dahle, Metal. & Mat. Trans. B Vol. 37B, Dec 2006, 873-878.

(Minoda et al., 98) Minoda T, Hayakawa H, Yoshida H. Proceedings of 6th International Conference on Aluminium Alloys (ICAA-6. Toyohashi (Japan): The Japan Institute of Light Metals, 1998, p. 339– 44.

(Minoda et al., 00) Minoda T, Hayakawa H, Yoshid AH, Mater Sci Technol , 2000, 7, 13–7.

(Mondolfo, 76) L.F. Mondolfo, Aluminium Alloys Structure and Properties, Butterworths, London, 1976, p. 787-805.

(Mulazimoglu et al., 96) M.H. Mulazimoglu, A. Zaluska, J.E. Gruzleski, F. Paray, Metallurgical and Materials Transactions A, 27A, 1996, pp. 929-936.

(Murali et al., 92) S. Murali, K.S. Raman, and K.S.S. Murthy: Mater. Sci. Eng., 1992, vol. A151, pp 1-10.

(Murali et al., 96) S. Murali, K.S. Raman and K.S.S. Murthy, Materials Science Forum, Vols 217-222, 1996, pp. 207-212.

(Murat et al., 03) Murat, S. and James, T.T.l., Physical Metallurgy and the Effect of Alloying Additions in Aluminum Alloys, Aluminium Handbook, 2003.

(Musulin et al., 90) I. Musulin, O.C. Celliers, Minerals Metal and Material Society (TMS), Warrendle, PA, 1990, Vol. 119, 951-954.

(Nadella et al., 08) R. Nadella, D.G.Eskin, L. Katgerman, Metall. Mater. Trans. A, Vol. 39A, 2008, 1206–1212.

(Naiyu et al., 06) Naiyu Sun, Burton R. Patterson, Jaakko P. Suni, Eider A. Simielli, Hasso Weiland, Lawrence F. Allard, Materials Science and Engineering A, 416, 2006, 232–239.

(Narayan et al., 95) L. Anantha Narayanan, F.H. Samuel, J.E. Gruzleski, Metall. Mater. Trans. 26A, 1995, 2161.

(Nayan et al., 10) Niraj Nayan, S. V. S. Narayana Murty, Govind, M. C. Mittal, P. P. Sinha, Metal Science and Heat Treatment, Vol. 52, Nos.3–4, 2010, pp. 171 – 178.

(Nilsen et al., 00) Nilsen KE, Koenis PTG. Proceedings of 7th International Aluminum Extrusion Technology Seminar, vol. 2. Chicago: Aluminum Extruders Council, 2000, 69–75.

(Oka et al., 96) T. Oka, M. Yanagawa, M. Hirano, "The Effect of Homogenisation Heat Treatment Practice on the Productivity of Al-Mg-Si System Alloy", *Proceedings of the 6th International Aluminium Extrusion Technology Seminar*, 1996, 157-161.

(Onrulu et al., 94) Onurlu S, Tekin A, J Mater Sci, 1994, Vol 29, 1652–5.

(Osada, 04) Yoshio Osada, X-Ray Spectrom. 2004, Vol. 33, 321–325.

(Paray et al., 96) F. Paray, B. Kulunk and J. Gruzleski: Mater. Sci. Technol., 1996, Vol. 12(4), 315-322.

(Parson et al., 89) N.C. Parson, H.L. Yiu, Light Alloys, 1989, pp 713-724.

(Parson et al., 02) N.C. Parson, J.D. Hankin, K.P. Hicklin, US Patent 6,440,359, 2002.

(Pennors et al., 98) A. Pennors, A.M. Samuel, F.H. Samuel and H.W. Doty, AFS transactions 98, 105, 251-264.

(Polmear, 81) I. J. Polmear, Light Alloys: Metallurgy of Light Alloys, Edward Arnold, London, 1981.

(Precth et al., 87) W. Precth and J. P. Pickens, Metall. Trans. A, 18, 1987, 1603 – 1611.

(Puga et al., 09) H. Puga, J. Barbosa, D. Soares, F.Silva, S. Ribeiro, Journal of Materials Processing Technology 209, 2009, 5195–5203

(Quentero et al., 86) O. Quintero-Sayago, C. Hurtado, and S. Ramirez.- In Alloy Theory and Phase Equilibria, D. Farkas and D.F. Dyment Editors, ASM Pub. 1986, 81-90.

(Ramanan et al., 08) R. Ramanan, N. C. Parson, Proceedings of the 9th International Extrusion Technology Seminar, Vol 2, 2008.

(Reiso, 84) O. Reiso, "The Effect of Composition and Homogenisation Treatment on Extrudability of AlMgSi Alloys*",* Proceedings of the 3rd International Aluminium Extrusion Technology Seminar, 1984, 31-40.

(Reiso, 04) O. Reiso, Extrusion of AlMgSi Alloys, Materials Forum, Vol. 28, 2004, 32-46.

(Roth et al., 60) W. Roth, Verfahren zum Gießen von Metallblöcken mit Ausnahme solcher aus Leichtmetallen, 1960, BRD Patent 974203, filed 1936.

(Salas et al., 95) O. Salas, V. Jayaram, K.C. Vlach, C.G. Levi, R Mehrabian, Jour. Amer. Cera. Soc., 78(3), 1995, 609-22

(Samaras et al., 07) S.N. Samaras, G.N. Haidemenopoulos, Journal of Materials Processing Technology 194, 2007, 63–73.

(Scamans et al., 09) G. Scamans, Z. Fan, Metal Bulletin's17th International Recycled Aluminium Conference, 24-25 November, 2009, Bilbao, Spain, pp 29-31

(Schwartz et al., 00) A Schwartz, M Kumar and B Adams, Electron Backscatter Diffraction in Materials Science, Springer, 2000

(Haro-Rodriguez et al., 11) S. Haro-Rodríguez, R. E. Goytia-Reyes, D. K. Dwivedi, V. H. Baltazar-Hernandez, Horacio Flores-Zuniga, M. J. Perez-Lopez, Materials and Design 32, 2011, 1865–1871.

(Sha et al., 00) G. Sha, K. A. Q. O'Reilly, B. Cantor, J. Worth, R. Hamerton, Material Science Forum 2000, 304– 306, 253– 8.

(Sha, 01) G. Sha: D. Phil. Thesis, 2001, University of Oxford

(Sha et al., 01) G. Sha, K. O'Reilly, B. Cantor, J. Worth, R. Hamerton, Materials Science and Engineering A304–306, 2001, 612–616.

(Sha et al., 03) G. Sha, K. A. Q. O'Reilly, B. Cantor, J.M. Titchmarsh and R.G. Hamerton, Acta Materialia, 2003, 51, 1883-1897.

(Shabestari et al., 02) S.G. Shabestari, M. Mahmudi, M. Emamy, J. Campbell, International Journal of Cast metals Research, Vol 15, 2002, 17-24.

(Shabestari, 04) S.G. Shabestari, Materials Science and Engineering A, 2004, vol. 383, 289-298.

(Shimizu et al., 96) K. Shimizu, G.M. Brown, K. Kobayashi, P. Skeldon, G.E. Thompson, G.C. Wood, Microscopy of Oxidation 3, 1996, 396-405.

(Shimizu et al., 98) K.S himizu, G.M. Brown, K. Kobayashi, P. Skeldon, G.E. Thompson, and G. C. Wood, Corrosion Science, vol. 40, no. 4-5, 1998, 557–575.

(Shinzato et al., 05) Shinzato, M.C., Hypolito, R., 2005, Waste Management 25, 37–46.

(Silva et al., 04) M.S. Silva, C. Barbosa, O. Acselrad, L.C. Pereira, J. of Mat. Eng. and Perf., 2004, vol. 13, pp. 129-134

(Simensen et al., 97) C. Simensen and T.L. Rolfsen: Z. Metallkunde., 1997, vol. 88, pp. 142-46

(Skjerpe, 87) P. Skjerpe, Metallallurgical Transactions A., 1987, vol. 18A, pp. 189-200. 4

(Spittle et al., 83) J. A. Spittle and A. A. Cushway, Metals Technology, 1983, vol. 10, 6–13.

(Springer Handbook, 05) W. Martienssen and H. Warlimont**,** Springer Handbook of Condensed Matter and Materials Data, 2005

(Sun et al., 67) C. Y. Sun and L. F. Mondolfo, J. Inst. Met., 1967, vol. 95, pp 384.

(Sweet et al., 11) L. Sweet, S.M. Zhu, S.X. Gao, J.A. Taylor, and M.A. Easton, Metall. & Mat. Trans. A Vol. 42A, July 2011, 1737-1749.

(Tanihata et al., 99) H. Tanihata, T. Sugawara, K. Matsuda, S. Ikeno, J. Mater Sci, 1999, 34, 1205–10.

(Taylor, 04) A. J. Taylor, 35th Australian Foundary Institute National Conference, Adelaide, Australia, 2004, 148-157.

(Terzi et al., 10) S. Terzi, J.A. Taylor, Y.H. Cho, L. Salvo, M. Suéry, E. Boller and A.K. Dahle, Acta Materialia, 2010, vol. 58, 5370-5380.

(Tian et al., 02) C. Tian, J. Law, J. Van der Touw, M. Murray, J.Y. Yao, D. Graham, D. StJohn, Journal of materials processing technology, 122, 2002, 82-93.

(TP1, 90) Standard test procedure for aluminium alloy grain refiners, AA TP-1, The Aluminium Association, 1990.

(TP1, 12) Standard test procedure for aluminium alloy grain refiners, AA TP-1, The Aluminium Association, 2012.

(Tromberg et al., 92) E. Tromborg, A. L. Dons, and L. Arnberg, Proceedings of the Third International Conference on Aluminium Alloys, 1992, pp. 270–275.

(Turchin et al., 05) A.N. Turchin, D.G. Eskin, L. Katgerman, Mater. Sci. Eng. A 413–414, 2005, 98-104.

(Tzamtzis et al., 10) S. Tzamtzis, H. Zhang, N. Hari Babu, Z. Fan, Materials Science and Engineering A 527, 2010, 2929–2934.

(Valle et al., 98) A. Valle, P. L. Orsetti Rossi, R. Tosta, Proceedings of the 6th International Conference on Aluminium Alloys, vol. 4. Toyohashi (Japan): Japan Institute of Light Metals, 1998, p. 2123– 8

(Verran et al., 08) G. O. Verran and U. Kurzawa, 2008, Conservation & Recycling 52, 731-736

(Veki et al., 85) M. Veki, S. Horie, T. Nakamura, and J. Mech, Work Technol., 11(3), 355 – 364, 1985.

(Vermolen et al., 98) F. Vermolen, K. Vuik, S. Zwaag, Mat. Sci. and Eng., A254, 1998, 13-32.

(Vives, 92) C. Vives, Proceedings of 2nd International Conference on Semisolid Alloys and Composites, MIT/Boston, USA, 1992, pp. 436–439.

(Voronov et al., 46) S.M. Voronov, "Continuous Casting of Round Billets from Light Alloys, Selected Works on Light Alloys (1946)", Moscow:Oborongiz, 1957, 336-362.

(Vusanovic et al., 05) I. Vusanovic, B. Sarler, M.J.M. Krane, Mater. Sci. Eng., 2005, vol. 413-414, pp. 217-222.

(Wang et al., 95) L. Wang, M. Makhlouf and D. Apelian, Int. Materials Reviews, Vol. 40 1995, 221-238.

(Westengen et al., 82) H. Westengen, Z. Metallkunde, 1982, vol. 73, pp. 360-368.

(Williams et al., 05) David B. Williams, C. Barry Carter, Transmission Electron Microscopy: A Textbook for Materials Science, 6th edition, 2005

(www.abb.com) ABB Prefil-Footprinter Brochure, April 2015

(www.substech.com) Substances and Technology website, DC casting, April 2015

(Yi et al., 04) J.Z. Yi, Y.X. Gao, P.D. Lee, T.C. Lindley, Mater. Sci. Eng. A 386, 2004, 396.

(Yongzhi et al., 10) Z. Yongzhi, X. Zhengbing, H. Juan, Z. Jianmin, Chinese Journal of Mech. Eng. Vol. 23, No. 3, 2010, 305-311.

(Zajac, et al., 93) S. Zajac, B. Hutchinson, A. Johanson, L.O. Gullman, R. Lagneborg, J. Physique 3, 1993, vol. 7, 251-254.

(Zajac et al., 94) S. Zajac, B. Hutchinson, A. Johansson, L.O. Gullman, Mater. Sci. Tech. 10, 1994, 323–333.

(Zajac et al., 96) Zajac S, Gullman LO, Johansson A, Bengtsson B., Mat Sci Forum 1996, 217– 222, 1193–98.

(Zajac et al., 02) S. Zajac, B. Bengtsson, Ch. Jonsson, Mater. Sci. Forum, 396–402, 2002, pp. 399–404.

(Zayan, 90) M.H. Zayan, Oxidation of Metals, Vol. 34 (5-6), 1990, 465-472.

(Zuo et al., 11) Y. Zuo, H. Li, M. Xia, B. Jiang, G. M. Scamans, Z. Fan, Scripta Materialia 64, 2011, pp. 209–212.

Appendix I

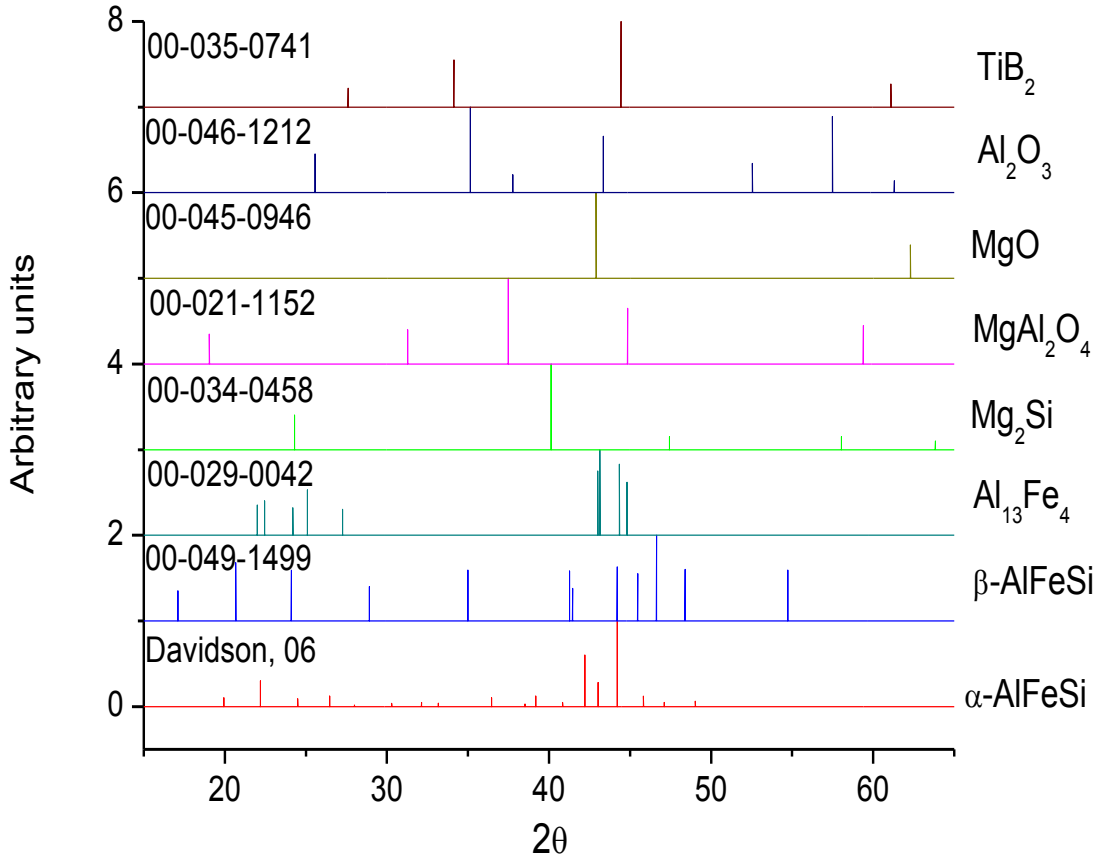

Fig. I XRD traces of all the compounds with their JCPDS reference code

Appendix II

Calculation showing the material used for preparation of the base alloy for TP1 experiments with different Mg content:

12 kgs of high purity Al (99.95 Al) was taken. Let's assume the amount of Al-80Fe alloy added was x kg and the amount of Al-50Si alloy added was y kg. In order to obtain the composition of Al-0.4Si-0.2Fe, the following equations must hold true:

$0.4/100 = (0.5 * y) / (12+x+y)$

$0.2/100 = (0.8 * x) / (12+x+y)$

On solving these equations we get the value of x = 30.2 gms and y = 96.6 gms.